



**Swansea
University**
Prifysgol
Abertawe

Medical School
Ysgol Feddygaeth

**‘Targeting iron metabolism in cancer
to induce ferroptosis:
a type of programmed cell death’**

Rhiannon Paige Beadman



Swansea University

2023

Submitted to Swansea University in fulfilment of the requirements for the
Degree of ‘Doctor of Philosophy in Medical and Health Care Studies’

Abstract

Cancer patients undergo a number of procedures in order to eradicate tumours. Although cancer patients are often highly responsive to initial treatment, acquired resistance can lead to a relapse in disease. Due to increased metabolism to sustain rapid proliferation, cancer cells are vulnerable to the induction of ferroptotic cell death; a form of programmed cell death dependent on iron and the accumulation of lipid peroxides. Cancer cells are known to evade ferroptosis through the upregulation of the key enzyme glutathione peroxidase IV (GPX4), which therefore provides a potential therapeutic target. This study used ferroptosis inducers: Erastin and RSL3, which inhibit GPX4 indirectly and directly respectively. A novel ferroptosis-inducing iron oxide nanoparticle was also synthesised for this study.

This study used a panel of cancer cell lines: breast, colon, lung and three ovarian cancers which modelled different chemotherapy sensitivities. Ferroptosis was characterised by the accumulation of lipid peroxides and changes in GPX4. Ferroptosis was confirmed after the addition of a lipid peroxide scavenger, which rescued against Erastin and RSL3 induced ferroptotic cell death. Autophagy induction was also investigated to determine the role autophagy regulators may play in ferroptotic induction.

Overall, cancer cells were more susceptible to RSL3-induced ferroptotic cell death. Autophagy was induced and inhibited through the activation and inhibition of AMPK, respectively, resulting in changes in ferroptotic induction in the cancer cells, which requires further investigation. Furthermore, the ferroptosis-inducing iron oxide nanoparticles induced cancer cell death, which was characteristic of ferroptosis. Therefore, ferroptosis could be exploited as a therapeutic target for cancer nanotherapy.

Declarations & Statements

This work has not previously been accepted in substance for any degree and is not being concurrently submitted in candidature for any degree.


Signed..... (candidate)


Date 31/03/23

This thesis is the result of my own investigations, except where otherwise stated. Other sources are acknowledged by footnotes giving explicit references. A bibliography is appended.

Signed 
..... (candidate)

Date 31/03/23

I hereby give consent for my thesis, if accepted, to be available for photocopying and for inter-library loan, and for the title and summary to be made available to outside organisations.

Signed 
..... (candidate)

Date 31/03/23

The university's ethical procedures have been followed and, when appropriate, that ethical approval has been granted.

Signed 
..... (candidate)

Date 31/03/23

Contents

Acknowledgments.....	0
List of Tables	1
List of Figures.....	2
List of Abbreviations	17
Chapter 1: Introduction	21
1.1 Cancer.....	22
1.2 Breast Cancer.....	23
1.3 Lung Cancer	24
1.4 Colorectal cancer	25
1.5 Melanoma	26
1.6 Ovarian Cancer	27
1.7 Cancer Metabolism	28
1.8 Iron Metabolism	30
1.8.1 Iron Metabolism – The Fenton Reaction.....	33
1.9 Ferroptosis.....	35
1.9.1 Erastin	39
1.9.2 RSL3	40
1.9.3 Nanoparticles and ferroptosis.....	41
1.10 Autophagy	42
1.11 Apoptosis.....	47
1.11.1 Extrinsic Pathway	48
1.11.2 Intrinsic Pathway.....	48
1.12 Cancer Therapy Resistance.....	50
1.13 Nanomedicine.....	50
1.14 Aims and Hypotheses.....	51
Chapter 2: Materials and Methods	54
2.1 Panel of cancer cell lines	55
2.1.1 4T1 Cell Culture	58
2.1.2 MC-38 Cell Culture	58
2.1.3 LC-2 Cell Culture	58
2.1.4 B16-F10 Cell Culture.....	59
2.1.5 PEO1 Cell Culture	59
2.1.6 PEO4 Cell Culture	59
2.1.7 OVCAR8 Cell Culture.....	59
2.2 Cell Growth and Maintenance.....	60
2.3 Cell Cryopreservation.....	60
2.4 Resurrecting Cells From Liquid Nitrogen.....	61
2.5 Inducers of Ferroptosis.....	61
2.6 Inhibitors of Ferroptosis.....	61
2.7 MTT ((3-(4, 5-dimethylthiazol-2-yl)-2, 5- diphenyltetrazolium bromide)) assay.....	61

2.8 Western Blot Analysis	62
2.8.1 Protein extraction	62
2.8.2 Protein Assay.....	62
2.8.3 SDS Page.....	63
2.8.4 Image J	66
2.9 Flow cytometric analysis	66
2.9.1 Cell viability by Deep Red Anthraquinone 7 – DRAQ7.....	66
2.9.2 Intracellular Staining	66
2.9.3 Lipid peroxidation	67
2.10 Experimental Design and Statistical Analysis	68
<i>Chapter 3: Characterising ferroptosis in a panel of cancer cell lines</i>	69
3.1 Introduction.....	70
3.2 Hypothesis and Aims.....	78
3.3 Materials and Methods.....	79
3.3.1 MTT ((3-(4, 5-dimethylthiazol-2-yl)-2, 5- diphenyltetrazolium bromide)) assay.....	79
3.3.2 Western Blot	79
3.3.3 Flow cytometric analysis of cell viability by DRAQ7	80
3.3.4 Flow cytometric analysis of intracellular staining	82
3.3.5 Flow cytometric analysis of lipid hydroperoxides in live cells.....	83
3.3.6 Statistics	84
3.4 Results	85
Treating a panel of cancer cells with Erastin or RSL3 induced ferroptosis, reducing cell viability	85
3.5 Discussion	103
3.6 Conclusion	105
<i>Chapter 4: mTORC1/2 and the AMPK pathway link to ferroptosis.....</i>	106
4.1 Introduction.....	107
4.2 Aims and Hypothesis.....	116
4.3 Materials and Methods.....	117
4.3.1 MTT ((3-(4, 5-dimethylthiazol-2-yl)-2, 5- diphenyltetrazolium bromide)) assay.....	117
4.3.2 Western Blot	117
4.3.3 Statistics	118
4.4 Results	118
4.4.1 Investigating mTOR and ferroptosis in a panel of cancer cell lines.....	118
4.4.2 Investigating AMPK and ferroptosis in a panel of cancer cell lines.....	120
4.5 Discussion	160
4.6 Conclusion	164
<i>Chapter 5: Nanoparticle Development.....</i>	165
5.1 Introduction.....	166
5.2 Aims and Hypothesis.....	174
5.3 Materials and Methods.....	175
5.3.1 Synthesis of mIONP-DLin.....	175
5.3.2 MTT ((3-(4, 5-dimethylthiazol-2-yl)-2, 5- diphenyltetrazolium bromide)) assay.....	175
5.3.1 Flow cytometric analysis of cell viability by Deep Red Anthraquinone 7 – DRAQ7.....	176
5.3.2 Western Blot	177

5.3.3 Flow cytometric analysis of intracellular staining	178
5.3.4 Statistics	180
5.4 Results	180
5.4.1 Characterising the B16F10 melanoma cell line	181
5.4.2 Development of Iron oxide nanoparticles: Phase one	199
5.4.1 Development of Iron oxide nanoparticles: Phase two	204
5.4.1 Development of Iron oxide nanoparticles: Phase three.....	210
5.5 Discussion	216
5.6 Conclusion	219
<i>Chapter 6: General discussion and conclusions</i>	220
6.1 Discussion	221

Acknowledgments

I acknowledge the generous funding received towards my PhD from the Engineering and Physical Sciences Research Council (EPSRC).

Undertaking this PhD has been a truly life-changing experience and it would not have been possible without the help and support from so many people.

Firstly, I would like to express my sincere gratitude to my first supervisor Dr James Cronin for his continuous support, patience and motivation over the past four years. I am extremely grateful that you took me on as a student and continued to have faith in me over the years, especially when I did not believe in myself.

Thank you to my second supervisor Professor Martin Sheldon, who provided words of wisdom when I needed them. For your continuous guidance, insightful comments and encouragements. I could not have imagined having better advisors and mentors for my PhD.

I greatly appreciated the support received through the collaborative work undertaken with Swansea University Chemistry department, in the synthesis of nanoparticles. Thank you to Professor Juan Mareque-Rivas, Marc Bilbao-Asensio and Joel Crane.

I would also like to say a heartfelt thankyou to my family for always believing in me. Most importantly, thank you to my nan for being my guardian angel, for without you this PhD would not have been possible.

Finally, to my friends at Swansea university; Carmen Tse, Rhiannon Gould, Samantha Llewellyn, Emma Stanton, Emma Lucas, Molly Raikes, Tyler Joseph, Laura Baker and the rest of ILS1 4th and 2nd floor for all their help and emotional support throughout my PhD.

List of Tables

Table 1: The main features that distinguish between ferroptosis, apoptosis and autophagy.....	36
Table 2: Polyacrylamide gel recipe for one gel	63
Table 3: List of antibodies used for western blots.....	65
Table 4: IC50 values from MTT assay for all cancer cell lines treated with Erastin.	86
Table 5: IC50 values from DRAQ7 assay for all cancer cell lines treated with Erastin.	88
Table 6: IC50 values from MTT assay for all cancer cell lines treated with RSL3.	94
Table 7: IC50 values from DRAQ7 assay for all cancer cell lines treated with RSL3.	95
Table 8: The five particles synthesised for different ratios of PEG to linoleic acid (LA).....	205

List of Figures

- Figure 1.1: The hallmarks of cancer.** The schematic conceptualises the ideal conditions required for malignant tumour growth and progression (Hanahan & Weinberg, 2011). Hanahan and Weinberg, 2011, created a framework which helps to understand the diversity of tumour development. There are six hallmark capabilities, two enabling characteristics and two emerging hallmarks. The biological capabilities include; sustaining proliferative signaling, evading growth suppressors, inducing angiogenesis, activating invasion and metastasis, resisting cell death and enabling replicative immortality. The two enabling characteristics are; genome instability and mutation and tumour-promoting inflammation. Over the last decade two general emerging hallmarks; avoiding immune destruction and deregulating cellular energetics (Hanahan & Weinberg, 2011). 23
- Figure 1.2: Signalling pathways associated with the regulation of cancer metabolism.** PI3K activated AKT which in turn activated mTOR. Tumour cells activate mTORC1 in order to induce anabolic pathways for nucleotide, protein and lipid synthesis. The activation of HIF also results in metabolic changes; activation of glutaminolysis and inactivation of mitochondrial pyruvate dehydrogenase complex. p53 inhibits glycolysis but indirectly activates mTORC1. Myc also promotes anabolic pathways for tumour growth and proliferation (Created with BioRender.com). 30
- Figure 1.3: Cellular iron homeostasis.** Transferrin bound iron (Fe^{3+}) can be imported into the cell via endocytosis after binding to TFR1 (also known as CD71). Within the endosome Fe^{3+} is converted to Fe^{2+} by STEAP3 before being transported to the cytosol by DMT1. Non-transferrin bound iron can be imported into the cell by DMT1 after conversion of Fe^{3+} to Fe^{2+} . All iron transported into the cell becomes available within the labile iron pool (LIP), the available iron may remain available or be stored in the ferritin complex by PCBP1 or transported to the mitochondria for the biosynthesis of iron-sulphur clusters (Fe-S). When iron is required NCOA4 breaks down the ferritin complex (ferritinophagy) and iron can be released from the cell via FPN1 after the conversion of Fe^{2+} to Fe^{3+} via hepcidin (HEPC; Created with BioRender.com). 33
- Figure 1.4: Schematic overview of the Fenton Reaction.** The Fenton reaction is driven by endocytosis of iron via the transferrin receptor protein 1 (TFR1). External ferric iron (Fe^{3+}) binds to transferrin (Tf) and becomes incorporated into the cell via TFR1. The change in the pH within the endosome causes the iron to be released from transferrin and reduced ferrous iron. The ferrous iron is then free to react with hydrogen peroxide (H_2O_2) resulting in free radicals. The free radicals are able to react with lipids within the cell membrane, which can induce a cell death pathway known as ferroptosis. Cancer cells can convert the ferrous iron back to ferric iron to be stored in the ferritin complex for when iron is later required (Created with BioRender.com). 35
- Figure 1.5: Schematic overview of the ferroptosis pathway.** Cancer cells are able to evade ferroptosis through the upregulation of GPX4. System Xc^-

imports cystine and exports glutamate, which is essential for the production of glutathione (GSH). GPX4 and GSH catalyse the reduction of lipid peroxides to lipid alcohols, enabling cell survival (Created with BioRender.com)..... 37

Figure 1.6: Schematic overview of how FINs induce ferroptosis in cancer cells. Ferroptosis may be induced through the inhibition of system X_C^- by Erastin or the inhibition of GPX4 directly by RSL3 (Created with BioRender.com)..... 40

Figure 1.7: Schematic overview of how iron oxide nanoparticles interact with cancer cells The internalisation of nanoparticles is random but the uptake of nanoparticles into the cell can be achieved through phagocytosis, endocytosis and direct trans-membrane transport. The internalised iron oxide nanoparticles undergo the Fenton reaction; where ferrous iron is free to react with hydrogen peroxide (H_2O_2) resulting in free radicals. The free radicals react with lipids within the cell membrane, resulting in ferroptotic cell death (Created with BioRender.com)..... 42

Figure 1.8: Schematic of the three defined types of autophagy. (a) Macro-autophagy, (b) Chaperone-mediated autophagy and (c) Micro-autophagy. In macro-autophagy the autophagosome fuses with the lysosome for the degradation of cytoplasmic cargo. In chaperone-mediated autophagy, a chaperone protein (Hsc70) enables the translocation of proteins across the lysosomal membrane for the degradation of cytoplasmic cargo. Micro-autophagy requires the invagination of the lysosomal membrane for the degradation of cytoplasmic cargo (From BioRender.com). 44

Figure 1.9: Schematic of the macro-autophagy pathway which is important in cancer regulation. The isolation membrane is triggered and continues to expand to form an autophagosome. The autophagosome is responsible for engulfing target cargos such as dead organelles. which can be recycled. Once the membrane has fused together the autophagosome fuses with lysosome to form an autolysosome, which is essential for the degradation and recycling of internal cargo (From BioRender.com). 46

Figure 1.10: Schematic of the extrinsic and intrinsic pathways of apoptosis. The extrinsic pathway is initiated by the binding of transmembrane death receptors with death ligands. Bound to the death receptor is an adaptor molecule that contains a death domain (DD) and a death effector domain (DED). Further found to DED are pro-caspase 8. The combination of these bound molecules results in the formation of the death inducing signalling complex (DISC). Once DISC is formed, caspase 8 is autocatalytically activated and subsequently transmits the death signal to effector caspases, which induce apoptosis. The intrinsic pathways is initiated by stress or other stimuli which cause the release of cytochrome-c from the inner mitochondrial space. Cytochrome-c within the cytoplasm results in the activation of caspase-9 and subsequently transmits the death signal to effector caspases, which induce apoptosis. Abbreviations: FasL, fatty acid synthetase ligand; TNF, tumour necrosis factor; TRAIL, TNF related apoptosis inducing ligand; TNR1, tumour necrosis factor receptor 1; FADD, Fas-associated death domain protein; TRADD, TNF receptor-associated death domain protein (From BioRender.com). 49

Figure 2.1: Representative phase contrast microscopy image of 4T1 cancer cell populations.	55
Figure 2.2: Representative phase contract microscopy image of MC38 cancer cell populations.	55
Figure 2.3: Representative phase contract microscopy image of LC2 cancer cell populations.	56
Figure 2.4: Representative phase contract microscopy image of B16F10 cancer cell populations.	56
Figure 2.5: Representative phase contrast microscopy of (a) PEO1, (b) PEO4 and (c) OVCAR8 cancer cell populations.	57
Figure 3.1: Schematic overview of the induction of ferroptosis in cancer cells after treatment with known inducers. Cancer cells are able to evade ferroptosis through the upregulation of GPX4. System X _C ⁻ imports cystine and exports glutamate, which is essential for the production of glutathione (GSH). GPX4 and GSH catalyse the reduction of lipid peroxides to lipid alcohols, enabling cell survival. Ferroptosis can be induced in cancer cells by Erastin, RSL3, IFN γ and iFSP1. Erastin binds to system X _C ⁻ to indirectly inhibit GPX4, whereas RSL3 directly binds to GPX4. IFN γ has been found to inhibit to the expression of the two system X _C ⁻ subunits. FSP1 blocks the production of lipid peroxides by using ubiquinone, the final product of the mevalonate pathway (Created in BioRender.com).	71
Figure 3.2: Schematic of glucose and glutamine metabolism in cancer cells. Cancer cells increase uptake of glucose to drive glycolysis in order to produce ATP. Under restricted glucose conditions cancer cells utilise glutamine in order to maintain ATP production and therefore proliferation (Adapted from BioRender.com).	72
Figure 3.3: Schematic of how CD8⁺ T cells interact with tumour cells to prevent the induction of ferroptosis. The immune checkpoint blockade results in the activation of T cells, which results in the release of IFN γ . IFN γ causes the downregulation of system X _C ⁻ and therefore drives ferroptosis in tumour cells (Created in BioRender.com).	75
Figure 3.4: Schematic of activated CD8⁺ T Cell IFNγ release resulting in ferroptotic cancer cell death. INF γ released from activated CD8 ⁺ T cells results in the activation of the JAT/STAT1 pathway, which consequently activates interferon regulatory factor 1 (IRF1). IRF1 inhibits the expression of SLC7A11 and SLC3A2, resulting in the inhibition of system X _C ⁻ and ultimately inducing ferroptotic cancer cell death. IRF1 also binds to the promotor region of acyl-coenzyme A (CoA) synthetase long-chain family member 4 (ACSL4), which ultimately produces arachidonic acid (AA) filled phospholipids, under the influence of IFN γ . The polyunsaturated phospholipids are prone to lipid peroxidation and consequently induce ferroptotic cancer cell death (Created in BioRender.com).	77
Figure 3.5: Gating strategy to determine cell viability using DRAQ7. The total population was first selected, gating out the debris such as dead cells. The singlets were selected using a FSC-H vs FSC-A dot plot. A histogram visualising the percentage positive cells was used to determine cell viability (% dead). Left histogram shows the unstained sample results and the right histogram shows the vehicle sample results.	81

Figure 3.6: Gating strategy to determine intracellular GPX4 levels by MFI of Alexa Fluor 488. The total population was first selected, gating out the debris such as dead cells. The singlets were selected using a FSC-H vs FSC-A dot plot. A histogram visualising the MFI for Alexa Fluor 488 was then created. An unstained sample (blue histogram) shows the background of the sample. The stained sample (red histogram), demonstrates the presence of GPX4 with Alexa Fluor 488 signals. 83

Figure 3.7: Gating strategy to determine lipid hydroperoxide levels by MFI of Liperfluo. The total population was first selected, gating out the debris such as dead cells. The singlets were selected using a FSC-H vs FSC-A dot plot. A histogram visualising the MFI for Liperfluo was then created. An unstained sample (blue histogram) shows the background of the sample. The positive control (red histogram), cumene hydroperoxide demonstrates the presence of lipid peroxides with Liperfluo signals. 84

Figure 3.8: Effect of Erastin on cell viability, determined by MTT. The panel of cancer cell lines (a) 4T1; (b) MC-38; (c) LC-2; (d) PEO1; (e) PEO4; (f) OVCAR8 were cultured in media containing vehicle (v) or the individual concentrations of Erastin. Cell viability was evaluated using MTT assay after 24 h. Data was presented as mean (SEM) from three independent cell passage experiments and analysed using 2-way ANOVA; * $p < 0.05$, ** $p < 0.01$, *** $p < 0.001$, **** $p < 0.0001$ 86

Figure 3.9: Effect of Erastin on cell viability, determined by DRAQ7. The panel of cancer cell lines (a) 4T1; (b) MC-38; (c) LC-2; (d) PEO1; (e) PEO4; (f) OVCAR8 were cultured in media containing vehicle (v) or the individual concentrations of Erastin. Cell death was assessed by flow cytometry using DRAQ7 after 24 h. Data was presented as mean (SEM) from three independent cell passage experiments and analysed using 1-way ANOVA; * $p < 0.05$, ** $p < 0.01$, *** $p < 0.001$, **** $p < 0.0001$ 87

Figure 3.10: Effect of Erastin on cell size (FSC-A). The panel of cancer cell lines (a) 4T1; (b) MC-38; (c) LC-2; (d) PEO1; (e) PEO4; (f) OVCAR8 were cultured in media containing vehicle (v) or the individual concentrations of Erastin. Cell size was determined from the DRAQ7 data. Data was presented as mean (SEM) from three independent cell passage experiments and analysed using 1-way ANOVA; ** $p < 0.01$, **** $p < 0.0001$ 89

Figure 3.11: SLC7A11 western blots for panel of cancer cell lines. SLC7A11 was observed at 55 kDa and the housekeeping protein Lamin-B1 was observed at 66 kDa. 90

Figure 3.12: The rescue effect of Liproxstatin-1 treatment against the ferroptosis inducer, Erastin. The panel of cancer cell lines (a) 4T1, (b) MC-38, (c) LC-2, (d) PEO1, (e) PEO4, (f) OVCAR8 were cultured in media containing vehicle (v) or liproxstatin-1 or Erastin. Cells were treated with liproxstatin-1 for 30 min prior to treatment with Erastin for 24 h. Cell viability was evaluated using MTT assay after 24 h. Data was presented as mean (SEM) from three independent cell passage experiments and analysed using 2-way ANOVA; * $p < 0.05$, ** $p < 0.001$, *** $p < 0.001$ 91

Figure 3.13: Liperfluo staining for lipid peroxidation to quantify the rescue effect of Liproxstatin-1 treatment against the ferroptosis inducer, Erastin. (a) PEO1; (b) PEO4; (c) PEO1 representative flow histograms and (d) PEO4 representative flow histograms. The cancer cell

lines were cultured in media containing vehicle (v) or liproxstatin-1 or Erastin. Cells were treated with liproxstatin-1 for 30 min prior to treatment with Erastin (5 μ M and 10 μ M) for 24 h. Cell viability was evaluated using MTT assay after 24 h. Data was presented as mean (SEM) from three independent cell passage experiments and analysed using 2-way ANOVA; * p <0.05, ** p <0.001, ***<0.001..... 92

Figure 3.14: Effect of RSL3 on cell viability, determined by MTT. The panel of cancer cell lines (a) 4T1; (b) MC-38; (c) LC-2; (d) PEO1; (e) PEO4; (f) OVCAR8 were cultured in media containing vehicle (v) or the individual concentrations of RSL3. Cell viability was evaluated using MTT assay after 24 h treatment. Data was presented as mean (SEM) from three independent cell passage experiments and analysed using 2-way ANOVA; * p <0.05, ** p <0.01, ***<0.001, ****<0.0001..... 93

Figure 3.15: Effect of RSL3 on cell viability, determined by DRAQ7. The panel of cancer cell lines (a) 4T1; (b) MC-38; (c) LC-2; (d) PEO1; (e) PEO4; (f) OVCAR8 were cultured in media containing vehicle (v) or the individual concentrations of RSL3. Cell death was assessed by flow cytometry using DRAQ7 after 24 h. Data was presented as mean (SEM) from three independent cell passage experiments and analysed using 1-way ANOVA; * p <0.05, ** p <0.01, ***<0.001, ****<0.0001..... 95

Figure 3.16: Effect of RSL3 on cell size (FSC-A). The panel of cancer cell lines (a) 4T1; (b) MC-38; (c) LC-2; (d) PEO1; (e) PEO4; (f) OVCAR8 were cultured in media containing vehicle (v) or the individual concentrations of RSL3. Cell size was determined from the DRAQ7 data. Data was presented as mean (SEM) from three independent cell passage experiments and analysed using 1-way ANOVA; ** p <0.01, ***<0.001, ****<0.0001..... 96

Figure 3.17: GPX4 western blots for panel of cancer cell lines. GPX4 was observed at 22 kDa and the housekeeping protein Lamin-B1 was observed at 66 kDa. 97

Figure 3.18: Intracellular staining for GPX4 at different concentrations of Erastin and RSL3. The PEO1 ovarian cancer cell line was cultured in media containing vehicle or the individual concentrations of (a) Erastin; (b) representative flow histogram of Erastin data; (c) RSL3 and (d) representative flow histogram of RSL3 data. Intracellular GPX4 was determined by flow cytometry and visualised as median fluorescent intensity (MFI). Data was presented as mean (SEM) from three independent experiments and analysed using 2-way ANOVA; * p <0.05, ** p <0.001. 98

Figure 3.19: The rescue effect of Liproxstatin-1 treatment against the ferroptosis inducer, RSL3. The panel of cancer cell lines (a) 4T1; (b) MC-38; (c) LC-2; (d) PEO1; (e) PEO4; (f) OVCAR8 were cultured in media containing vehicle (v) or liproxstatin-1 or RSL3. Cells were treated with liproxstatin-1 for 30 min prior to treatment with RSL3 for 24 h. Cell viability was evaluated using MTT assay after 24 h. Data was presented as mean (SEM) from three independent cell passage experiments and analysed using 2-way ANOVA; * p <0.05, ** p <0.01, ***<0.001, ****<0.0001..... 99

Figure 3.20: The effect of cotreatment with IFN γ and Erastin. The panel of cancer cell lines (a) 4T1; (b) MC-38; (c) LC-2; (d) PEO1; (e) PEO4; (f) OVCAR8 were cultured in media containing vehicle (v) or IFN γ or Erastin or IFN γ plus Erastin. Cells were treated with IFN γ for 30 min prior to treatment

with Erastin for 24 h. Cell viability was evaluated using MTT assay after 24 h. Data was presented as mean (SEM) from three independent cell passage experiments and analysed using 2-way ANOVA; * $p < 0.05$, ** $p < 0.001$, *** < 0.001 101

Figure 3.21: The effect of cotreatment with IFN γ and RSL3. The panel of cancer cell lines (a) 4T1; (b) MC-38; (c) LC-2; (d) PEO1; (e) PEO4; (f) OVCAR8 were cultured in media containing vehicle (v) or IFN γ or Erastin. Cells were treated with IFN γ for 30 min prior to treatment with Erastin for 24 h. Cell viability was evaluated using MTT assay after 24 h. Data was presented as mean (SEM) from three independent cell passage experiments and analysed using 2-way ANOVA; * $p < 0.05$, ** $p < 0.001$, *** < 0.001 102

Figure 4.1: Schematic of AMPK activation in cells. AMPK is composed of three subunits; α , β and γ . LKB1 is responsible for the phosphorylation of AMPK at Thr172. The activation of AMPK results in the activation of catabolic pathways such as fatty acid oxidation and glycolysis. AMPK activation also induces autophagy. The activation of AMPK results in the inhibition of anabolic pathways such as fatty acid and cholesterol synthesis. AMPK activation also inhibits mTORC. AMPK is activated by AICAR and inhibited by Compound C (Created in BioRender.com)..... 108

Figure 4.2: Schematic structure of mTORC1 and mTORC2. Both complexes contain mTOR, DEPTOR and mLST8. Unique to mTORC1 is RAPTOR and PRAS40, whereas mTORC2 contains RICTOR, mSIN1 and PROTOR (Adapted from BioRender.com)..... 110

Figure 4.3: Schematic of cellular metabolism...... 112

Figure 4.4: Schematic overview of the Glutaminolysis Pathway. The pathway results in the generation of glutathione (GSH) or α -ketoglutarate (α -KG). Glutamine is incorporated into the cell via the transporter ASCT2. Glutamine is converted to glutamate by the glutaminases, GLS1 and GLS2. Glutamate is either converted into α -KG to fuel the TCA cycle or used to biosynthesise GSH, the reducing substrate of GPX4 activity (Created in BioRender.com)..... 114

Figure 4.5: Schematic overview of the Transsulfuration Pathway. The pathway results in the generation of cysteine from methionine. Homocysteine is converted to cystathionine by cystathionine β -synthase (CBS) before generating cystine by cystathionine γ -lyase (CSE). Cysteine is then condensed to synthesis glutathione by glutamate-cysteine ligase enzyme (GCL; Created in BioRender.com)..... 115

Figure 4.6: Synergistic effect of mTOR inhibitors Rapamycin and Torin-1 with the ferroptosis inducer Erastin. The panel of cancer cell lines (a) 4T1, (b) MC-38, (c) LC-2, (d) PEO1, (e) PEO4, (f) OVCAR8 were cultured in media containing vehicle or Rapamycin or Torin-1 or Erastin. Cells were treated with Rapamycin or Torin-1 30 min prior to treatment with Erastin for 24 h. Cell viability was evaluated using MTT assay after 24 h. Data was presented as mean (SEM) from three independent experiments and analysed using 2-way ANOVA; * $p < 0.05$, ** $p < 0.001$, *** < 0.001 119

Figure 4.7: Synergistic effect of mTOR inhibitors Rapamycin and Torin-1 with the ferroptosis inducer RSL3. The panel of cancer cell lines (a) 4T1, (b) MC-38, (c) LC-2, (d) PEO1, (e) PEO4, (f) OVCAR8 were cultured in

media containing vehicle or Rapamycin or Torin-1 or RSL3. Cells were treated with Rapamycin or Torin-1 30 min prior to treatment with RSL3 for 24 h. Cell viability was evaluated using MTT assay after 24 h. Data was presented as mean (SEM) from three independent experiments and analysed using 2-way ANOVA; * $p < 0.05$, ** $p < 0.001$, *** $p < 0.001$ 120

Figure 4.8: Synergistic effect of AMPK inhibitor Compound C and AMPK activator AICAR with the ferroptosis inducer Erastin. The panel of cancer cell lines (a) 4T1, (b) MC-38, (c) LC-2, (d) PEO1, (e) PEO4, (f) OVCAR8 were cultured in media containing vehicle or compound C or AICAR or Erastin. Cells were treated with Compound C or AICAR 30 min prior to treatment with Erastin for 24 h. Cell viability was evaluated using MTT assay after 24 h. Data was presented as mean (SEM) from three independent experiments and analysed using 2-way ANOVA; * $p < 0.05$, ** $p < 0.001$, *** $p < 0.001$ 121

Figure 4.9: Synergistic effect of AMPK inhibitor Compound C and AMPK activator AICAR with the ferroptosis inducer RLS3. The panel of cancer cell lines (a) 4T1, (b) MC-38, (c) LC-2, (d) PEO1, (e) PEO4, (f) OVCAR8 were cultured in media containing vehicle or compound C or AICAR or RSL3. Cells were treated with Compound C or AICAR 30 min prior to treatment with RSL3 for 24 h. Cell viability was evaluated using MTT assay after 24 h. Data was presented as mean (SEM) from three independent experiments and analysed using 2-way ANOVA; * $p < 0.05$, ** $p < 0.001$, *** $p < 0.001$ 122

Figure 4.10: GPX4 western blot for 4T1 breast cancer cells. The breast cancer cells were treated with vehicle or compound C or AICAR for 30 min prior to treatment with Erastin or RSL3 for 4 h, and GPX4 analysed by western blot. Representative western blot for GPX4 and β -actin are shown. Data are presented as mean (SEM) of three independent experiments and analysed using 1-way ANOVA; * $p < 0.05$, ** $p < 0.001$, **** $p < 0.0001$ 123

Figure 4.11: GPX4 western blot for MC38 colon cancer cells. The colon cancer cells were treated with vehicle or compound C or AICAR for 30 min prior to treatment with Erastin or RSL3 for 4 h, and GPX4 analysed by western blot. Representative western blot for GPX4 and β -actin are shown. Data are presented as mean (SEM) of three independent experiments and analysed using 1-way ANOVA; * $p < 0.05$, ** $p < 0.001$, **** $p < 0.0001$ 124

Figure 4.12: GPX4 western blot for LC2 lung cancer cells. The colon cancer cells were treated with vehicle or compound C or AICAR for 30 min prior to treatment with Erastin or RSL3 for 4 h, and GPX4 analysed by western blot. Representative western blot for GPX4 and β -actin are shown. Data are presented as mean (SEM) of two independent experiments..... 125

Figure 4.13: P70S6K western blot for 4T1 breast cancer cells. The breast cancer cells were treated with vehicle or compound C or AICAR for 30 min prior to treatment with Erastin or RSL3 for 4 h, and the phosphorylation of ribosomal protein S6 kinase 1 (P-P70-S6K) and total ribosomal protein S6 kinase (T-P70-S6K), were analysed by western blot. Representative western blot for P-P70-S6K, T-P70-S6K and β -actin are shown. Data was presented as mean (SEM) from two independent experiments and analysed using 1-way ANOVA; * $p < 0.05$, ** $p < 0.001$, **** $p < 0.0001$ 127

Figure 4.14: P70S6K western blot for MC38 colon cancer cells. The colon cancer cells were treated with vehicle or compound C or AICAR for 30 min prior to treatment with Erastin or RSL3 for 4 h, and the phosphorylation of ribosomal protein S6 kinase 1 (P-P70-S6K) and total ribosomal protein S6 kinase (T-P70-S6K), were analysed by western blot. Representative western blot for P-P70-S6K, T-P70-S6K and β -actin are shown. Data was presented as mean (SEM) from one independent experiment for P-P70-S6K and two independent experiments for T-P70-S6K. 128

Figure 4.15: P70S6K western blot for LC2 lung cancer cells. The lung cancer cells were treated with vehicle or compound C or AICAR for 30 min prior to treatment with Erastin or RSL3 for 4 h, and the phosphorylation of ribosomal protein S6 kinase 1 (P-P70-S6K) and total ribosomal protein S6 kinase (T-P70-S6K), were analysed by western blot. Representative western blot for P-P70-S6K, T-P70-S6K and β -actin are shown. Data was presented as mean (SEM) from one independent experiment for P-P70-S6K and two independent experiments for T-P70-S6K and analysed using 1-way ANOVA; * $p < 0.05$, ** $p < 0.001$, **** $p < 0.0001$ 129

Figure 4.16: ULK1 western blot for 4T1 breast cancer cells. The breast cancer cells were treated with vehicle or compound C or AICAR for 30 min prior to treatment with Erastin or RSL3 for 4 h, and the expression of SER555, SER757 and ULK1, were analysed by western blot. Representative western blot for SER555, SER757, ULK1 and β -actin are shown. Data was presented as mean (SEM) from one independent experiment. 131

Figure 4.17: ULK1 western blot for MC38 colon cancer cells. The colon cancer cells were treated with vehicle or compound C or AICAR for 30 min prior to treatment with Erastin or RSL3 for 4 h, and the expression of SER757 and ULK1, were analysed by western blot. Representative western blot for SER757, ULK1 and β -actin are shown. Data was presented as mean (SEM) from one independent experiment. 132

Figure 4.18: AMPK western blot for 4T1 breast cancer cells. The breast cancer cells were treated with vehicle or compound C or AICAR for 30 min prior to treatment with Erastin or RSL3 for 4 h, and the phosphorylation of AMPK (P-AMPK) and total AMPK (T-AMPK), were analysed by western blot. Representative western blot for P-AMPK, T-AMPK and β -actin are shown. Data was presented as mean (SEM) from two independent experiments... 134

Figure 4.19: AMPK western blot for MC38 colon cancer cells. The colon cancer cells were treated with vehicle or compound C or AICAR for 30 min prior to treatment with Erastin or RSL3 for 4 h, and the phosphorylation of AMPK (P-AMPK) and total AMPK (T-AMPK), were analysed by western blot. Representative western blot for P-AMPK, T-AMPK and β -actin are shown. Data was presented as mean (SEM) from one independent experiment for P-AMPK and two independent experiments for T-AMPK. 135

Figure 4.20: AMPK western blot for LC2 lung cancer cells. The lung cancer cells were treated with vehicle or compound C or AICAR for 30 min prior to treatment with Erastin or RSL3 for 4 h, and the phosphorylation of AMPK (P-AMPK) and total AMPK (T-AMPK) were analysed by western blot. Representative western blot for P-AMPK, T-AMPK and β -actin are shown.

Data was presented as mean (SEM) from one independent experiment for P-AMPK and two independent experiments for T-AMPK. 136

Figure 4.21: BECN1 western blots for 4T1 breast cancer cells. The breast cancer cells were treated with vehicle or compound C or AICAR for 30 min prior to treatment with Erastin or RSL3 or 4 h, and the BECN1 (Beclin-1) was analysed by western blot. Representative western blot for Beclin-1 and β -actin are shown. Data was presented as mean (SEM) from three independent experiments and analysed using 1-way ANOVA. 137

Figure 4.22: BECN1 western blots for mc38 colon cancer cells. The colon cancer cells were treated with vehicle or compound C or AICAR for 30 min prior to treatment with Erastin or RSL3 or 4 h, and the BECN1 (Beclin-1) was analysed by western blot. Representative western blot for Beclin-1 and β -actin are shown. Data was presented as mean (SEM) from three independent experiments and analysed using 1-way ANOVA. 138

Figure 4.23: BECN1 western blot for LC2 lung cancer cells. The lung cancer cells were treated with vehicle or compound C or AICAR for 30 min prior to treatment with Erastin or RSL3 or 4 h, and the BECN1 (Beclin-1) was analysed by western blot. Representative western blot for Beclin-1 and β -actin are shown. Data was presented as mean (SEM) from two independent experiments. 139

Figure 4.24: LC3B western blot for 4T1 breast cancer cells. The breast cancer cells were treated with vehicle or compound C or AICAR for 30 min prior to treatment with Erastin or RSL3 or 4 h, and LC3B-I and LC3B-II were analysed by western blot. Representative western blot for LC3B-I, LC3B-II and β -actin are shown. Data was presented as mean (SEM) from two independent experiments. 140

Figure 4.25: LC3B western blot for MC38 colon cancer cells. The colon cancer cells were treated with vehicle or compound C or AICAR for 30 min prior to treatment with Erastin or RSL3 or 4 h, and LC3B-I and LC3B-II were analysed by western blot. Representative western blot for LC3B-I, LC3B-II and β -actin are shown. Data was presented as mean (SEM) from two independent experiments. 141

Figure 4.26: LC3B western blot for LC2 lung cancer cells. The lung cancer cells were treated with vehicle or compound C or AICAR for 30 min prior to treatment with Erastin or RSL3 or 4 h, and LC3B-I and LC3B-II were analysed by western blot. Representative western blot for LC3B-I, LC3B-II and β -actin are shown. Data was presented as mean (SEM) from two independent experiments. 142

Figure 4.27: The effect of glutaminase inhibitor, compound 968 and Erastin. The panel of cancer cell lines (a) 4T1; (b) MC-38; (c) LC-2; (d) PEO1; (e) PEO4; (f) OVCAR8 were cultured in media containing vehicle (v) or C968 (10 μ M) or Erastin (2.5 μ M). Cells were treated with C968 for 30 min prior to treatment with Erastin for 24 h. Cell viability was evaluated using MTT assay after 24 h. Data was presented as mean (SEM) from three independent cell passage experiments and analysed using 2-way ANOVA, * $p < 0.05$, ** $p < 0.001$, *** $p < 0.001$ 143

Figure 4.28: The effect of glutaminolysis inhibitor, compound 968 and RSL3. The panel of cancer cell lines (a) 4T1; (b) MC-38; (c) LC-2; (d) PEO1;

(e) PEO4; (f) OVCAR8 were cultured in media containing vehicle (v) or C968 (10 μ M) or RSL3 (0.625 μ M). Cells were treated with c968 for 30 min prior to treatment with RSL3 for 24 h. Cell viability was evaluated using MTT assay after 24 h. Data was presented as mean (SEM) from three independent cell passage experiments and analysed using 2-way ANOVA; *p<0.05, **p<0.001, ***<0.001, ****<0.0001..... 144

Figure 4.29: GPX4 and BECN1 western blots for 4T1 breast cancer cells. The breast cancer cells were treated with vehicle or C968 for 30 min prior to treatment with Erastin or RSL3 or 4 h, and GPX4 and BECN1 were analysed by western blot. Representative western blot for GPX4, BECN1 and β -actin are shown. Data was presented as mean (SEM) from three independent experiments and data was analysed with a 1-way ANOVA. 145

Figure 4.30: GPX4 and BECN1 western blots for MC38 colon cancer cells. The colon cancer cells were treated with vehicle or C968 for 30 min prior to treatment with Erastin or RSL3 or 4 h, and GPX4 and BECN1 were analysed by western blot. Representative western blot for GPX4, BECN1 and β -actin are shown. Data was presented as mean (SEM) from three independent experiments and data was analysed with a 1-way ANOVA; *p<0.05, ***<0.001. 147

Figure 4.31: GPX4 and BECN1 western blots for LC2 lung cancer cells. The lung cancer cells were treated with vehicle or C968 for 30 min prior to treatment with Erastin or RSL3 or 4 h, and GPX4 and BECN1 were analysed by western blot. Representative western blot for GPX4, BECN1 and β -actin are shown. Data was presented as mean (SEM) from three independent experiments 148

Figure 4.32: P70S6K and ULK1 western blots for 4T1 breast cancer cells. The breast cancer cells were treated with vehicle or C968 for 30 min prior to treatment with Erastin or RSL3 or 4 h, and phosphorylated P70S6K (P-P70-S6K), total P70S6K (T-P70-S6K), SER757, SER555 and ULK1 were analysed by western blot. Representative western blot for P-P70-S6K, T-P70-S6K, SER555, SER757, ULK1 and β -actin are shown. Data was presented as mean (SEM) from two independent experiments for P70S6K and one independent experiment for ULK1. 150

Figure 4.33: P70S6K and ULK1 western blots for MC38 colon cancer cells. The colon cancer cells were treated with vehicle or C968 for 30 min prior to treatment with Erastin or RSL3 or 4 h, and phosphorylated P70S6K (P-P70-S6K), total P70S6K (T-P70-S6K), SER757 and ULK1 were analysed by western blot. Representative western blot for P-P70-S6K, T-P70-S6K, SER757, ULK1 and β -actin are shown. Data was presented as mean (SEM) from two independent experiments for P70S6K and one independent experiment for ULK1. 152

Figure 4.34: P70S6K western blots for LC2 lung cancer cells. The lung cancer cells were treated with vehicle or C968 for 30 min prior to treatment with Erastin or RSL3 or 4 h, and phosphorylated P70S6K (P-P70-S6K) and total P70S6K (T-P70-S6K) were analysed by western blot. Representative western blot for P-P70-S6K, T-P70-S6K, and β -actin are shown. Data was presented as mean (SEM) from one independent experiments for P-P70S6K and two independent experiment for T-P70S6K. 153

Figure 4.35: AMPK and LC3B western blots for 4T1 breast cancer cells. The breast cancer cells were treated with vehicle or C968 for 30 min prior to treatment with Erastin or RSL3 or 4 h, and phosphorylated AMPK (P-AMPK), total AMPK (T-AMPK), LC3B-I and LC3B-II were analysed by western blot. Representative western blot for P-AMPK, T-AMPK, LC3B-I, LC3B-II and β -actin are shown. Data was presented as mean (SEM) from two independent experiments. 155

Figure 4.36: AMPK and LC3B western blots for MC38 colon cancer cells. The colon cancer cells were treated with vehicle or C968 for 30 min prior to treatment with Erastin or RSL3 or 4 h, and phosphorylated AMPK (P-AMPK), total AMPK (T-AMPK), LC3B-I and LC3B-II were analysed by western blot. Representative western blot for P-AMPK, T-AMPK, LC3B-I, LC3B-II and β -actin are shown. Data was presented as mean (SEM) from two independent experiments. 157

Figure 4.37: AMPK and LC3B western blots for LC2 lung cancer cells. The lung cancer cells were treated with vehicle or C968 for 30 min prior to treatment with Erastin or RSL3 or 4 h, and phosphorylated AMPK (P-AMPK), total AMPK (T-AMPK), LC3B-I and LC3B-II were analysed by western blot. Representative western blot for P-AMPK, T-AMPK, LC3B-I, LC3B-II and β -actin are shown. Data was presented as mean (SEM) from one independent experiment for AMPK and two independent experiments for LC3B. 159

Figure 5.1: Gating strategy to determine cell viability using DRAQ7. The total population was first selected, gating out the debris such as dead cells. The singlets were selected using a FSC-H vs FSC-A dot plot. A histogram visualising the percentage positive cells was used to determine cell viability (% dead). Left histogram shows the unstained sample results and the right histogram shows the vehicle sample results. 177

Figure 5.2: Gating strategy to determine intracellular GPX4 levels by MFI of Alexa Flour 488. The total population was first selected, gating out the debris such as dead cells. The singlets were selected using a FSC-H vs FSC-A dot plot. A histogram visualising the MFI for Alexa Flour 488 was then created. An unstained sample (blue histogram) shows the background of the sample. The stained sample (red histogram), demonstrates the presence of GPX4 with Alexa Fluor 488 signals. 179

Figure 5.3: Effect of (a) Erastin and (b) RSL3 on mouse melanoma cell viability. The B16-F10 skin melanoma cell line was cultured in media containing vehicle, (a) Erastin or (b) RSL3 for 24 h. Cell viability was evaluated using MTT assay after 24 h. Data was presented as mean (\pm SEM) from three independent cell passages and analysed using 2-way ANOVA, * $p < 0.05$, ** $p < 0.01$, *** $p < 0.001$, **** $p < 0.0001$ 181

Figure 5.4: Effect of Erastin and RSL3 on cell viability, determined by DRAQ7. The B16-F10 skin melanoma cell line was cultured in media containing vehicle, (a) Erastin or (b) RSL3 for 24 h. Cell death was assessed by flow cytometry using DRAQ7 after 24 h. Data was presented as mean (SEM) from three independent cell passage experiments and analysed using 1-way ANOVA; ** $p < 0.01$, *** $p < 0.001$, **** $p < 0.0001$ 182

Figure 5.5: Effect of Erastin and RSL3 on cell size (FSC-A). The panel of cancer cell lines (a) 4T1; (b) MC-38; (c) LC-2; (d) PEO1; (e) PEO4; (f)

OVCAR8 were cultured in media containing vehicle (v) or the individual concentrations of Erastin. Cell size was determined from the DRAQ7 data. Data was presented as mean (SEM) from three independent cell passage experiments and analysed using 1-way ANOVA; **p<0.01, ****<0.0001..... 183

Figure 5.6: GPX4 and SLC7A11 western blots for B16F10 cancer cells. GPX4 was observed at 22 kDa, SLC7A11 was observed at 55 kDa and the housekeeping protein Lamin-B1 was observed at 66 kDa 184

Figure 5.7: The rescue effect of Liproxstatin-1 treatment against the ferroptosis inducers, Erastin and RSL3. The mouse melanoma cells were cultured in media containing vehicle (v) or liproxstatin-1 (100 nM) or Erastin (2.5 μ M) or RSL3 (0.625 μ M). Cells were treated with liproxstatin-1 for 30 min prior to treatment with Erastin or RSL3 for 24 h. Cell viability was evaluated using MTT assay after 24 h. Data was presented as mean (SEM) from three independent cell passage experiments and analysed using 2-way ANOVA, **p<0.001, ****p<0.0001..... 185

Figure 5.8: The effect of cotreatment with IFN γ and Erastin or RSL3. The mouse melanoma cells were cultured in media containing vehicle (v) or IFN γ (10ng/ml) or Erastin (2.5 μ M) or RSL3 (0.625 μ M) or IFN γ plus Erastin or IFN γ plus RLS3. Cells were treated with IFN γ for 30 min prior to treatment with Erastin or RSL3 for 24 h. Cell viability was evaluated using MTT assay after 24 h. Data was presented as mean (SEM) from three independent cell passage experiments and analysed using 2-way ANOVA, ****p<0.0001.... 186

Figure 5.9: Synergistic effect of (a) mTOR inhibitors Rapamycin and Torin-1, (b) AMPK inhibitor Compound C and AMPK activator AICAR, with the ferroptosis inducers Erastin and RSL3..... 188

Figure 5.10: GPX4 and BECN1 western blots for B16-F10 melanoma cells. The melanoma cells were treated with vehicle or compound C or AICAR for 30 min prior to treatment with Erastin or RSL3 or 4 h, and GPX4 and BECN1 were analysed by western blot. Representative western blot for GPX4, BECN1 and β -actin are shown. Data was presented as mean (SEM) from three independent experiments and data was analysed with a 1-way ANOVA..... 189

Figure 5.11: P70S6K and ULK1 western blots for B16-F10 melanoma cells. The melnom cells were treated with vehicle or compound C or AICAR for 30 min prior to treatment with Erastin or RSL3 or 4 h, and phosphorylated P70S6K (P-P70-S6K), total P70S6K (T-P70-S6K), SER757, SER555 and ULK1 were analysed by western blot. Representative western blot for P-P70-S6K, T-P70-S6K, SER555, SER757, ULK1 and β -actin are shown. Data was presented as mean (SEM) from one or two independent experiments..... 191

Figure 5.12: AMPK and LC3B western blots for B16-F10 melanoma cells. The melanoma cells were treated with vehicle or compound C or AICAR for 30 min prior to treatment with Erastin or RSL3 or 4 h, and phosphorylated AMPK (P-AMPK), total AMPK (T-AMPK), LC3B-I and LC3B-II were analysed by western blot. Representative western blot for P-AMPK, T-AMPK, LC3B-I, LC3B-II and β -actin are shown. Data was presented from one independent experiment. 193

Figure 5.13: The effect of glutaminase inhibitor, compound 968 and the ferroptosis inducers, Erastin and RSL3. The mouse melanoma cells were

cultured in media containing vehicle (v) or Compound 968 (10 μ M) or Erastin (2.5 μ M) or RSL3 (0.625 μ M). Cells were treated with Compound 968 for 30 min prior to treatment with Erastin or RSL3 for 24 h. Cell viability was evaluated using MTT assay after 24 h. Data was presented as mean (SEM) from three independent cell passage experiments and analysed using 2-way ANOVA, * p <0.05, ** p <0.01, *** p <0.001, **** p <0.0001..... 194

Figure 5.14: GPX4 and BECN1 western blots for B6-F10 melanoma cells. The melanoma cells were treated with vehicle or C968 for 30 min prior to treatment with Erastin or RSL3 or 4 h, and GPX4 and BECN1 were analysed by western blot. Representative western blot for GPX4, BECN1 and β -actin are shown. Data was presented as mean (SEM) from three independent experiments and data was analysed with a 1-way ANOVA. ... 195

Figure 5.15: P70S6K and ULK1 western blots for B16-F10 melanoma cells. The melanoma cells were treated with vehicle or C968 for 30 min prior to treatment with Erastin or RSL3 or 4 h, and phosphorylated P70S6K (P-P70-S6K), total P70S6K (T-P70-S6K), SER757, SER555 and ULK1 were analysed by western blot. Representative western blot for P-P70-S6K, T-P70-S6K, SER555, SER757, ULK1 and β -actin are shown. Data was presented as mean (SEM) from one or two independent experiments. 196

Figure 5.16: AMPK and LC3B western blots for B16-F10 melanoma cells. The melanoma cells were treated with vehicle or C968 for 30 min prior to treatment with Erastin or RSL3 or 4 h, and phosphorylated AMPK (P-AMPK), total AMPK (T-AMPK), LC3B-I and LC3B-II were analysed by western blot. Representative western blot for P-AMPK, T-AMPK, LC3B-I, LC3B-II and β -actin are shown. Data was presented from one independent experiment. 198

Figure 5.17: Illustration of Ferumoxytol. With an iron oxide core (dark purple) and a dextrose coating (light purple). 199

Figure 5.18: Illustration of the PEGylated SPION. With an iron oxide core (dark purple), oleic acid (green) and PEG (pink)..... 199

Figure 5.19: Effect of Erastin in combination with (a) Ferumoxytol or (b) PEGylated iron oxide nanoparticles on cell viability (absorbance at 570 nm) in mouse melanoma cells. Mouse melanoma cells were cultured in media containing vehicle (v) or the individual concentrations of Erastin for 24 h followed by 24 h treatment of iron oxide nanoparticles. Cell viability was evaluated using MTT assay. Data was presented as mean (\pm SEM) from three independent cell passages and analysed using 2-way ANOVA, * p < 0.05, ** p <0.01, *** p <0.001..... 201

Figure 5.20: Illustration of stage one Linoleic acid nanoparticles. With an iron oxide core (dark purple), hydrophobic linoleic acid (blue) and oleic acid (green). 202

Figure 5.21: Effect of Erastin in combination with linoleic acid coated iron oxide nanoparticles on cell viability (absorbance at 570 nm) in mouse melanoma cells. Mouse melanoma cells were cultured in media containing vehicle (v) or the individual concentrations of Erastin for 24 h followed by 24 h treatment of iron oxide nanoparticles coated in linoleic acid. Cell viability was evaluated using MTT assay. Data was presented as mean

(±SEM) from three independent cell passages and analysed using 2-way ANOVA, *p < 0.05, **p<0.01, ***p<0.001, ****p<0.0001.....203

Figure 5.22: Illustration of next generation stabilised Linoleic acid nanoparticles. With an iron oxide core (dark purple), hydrophobic linoleic acid (blue), oleic acid (green) and PEG (pink).....204

Figure 5.23: Effect of PEGylated linoleic acid iron oxide nanoparticles on cell viability (absorbance at 570 nm) of mouse melanoma cells. Particle 1 to Particle 5 show increasing concentration of linoleic acid. Particle 1; 100:0 (PEG:LA), Particle 2; 75:25, Particle 3; 60:40, Particle 4; 50:50 and Particle 5 40:60. Mouse melanoma cells were cultured in media containing vehicle (v) or complete media for 24 h followed by 24 h treatment of PEGylated linoleic acid iron oxide nanoparticles (500 nM). Cell viability was evaluated using MTT assay. Data was presented as mean (±SEM) from three independent cell passages and analysed using 2-way ANOVA, *p < 0.05, **p<0.01, ***p<0.001.....206

Figure 5.24: Effect PEGylated linoleic acid iron oxide nanoparticles in combination with Erastin at 1.25 µM on cell viability of mouse melanoma cells. Particle 1 to Particle 5 show increasing concentration of linoleic acid. Particle 1; 100:0 (PEG:LA), Particle 2; 75:25, Particle 3; 60:40, Particle 4; 50:50 and Particle 5; 40:60. Cell viability was evaluated using MTT assay after 24 h treatment of Erastin followed by 24 h treatment of PEGylated linoleic acid iron oxide nanoparticle (500 nM). Data was presented as mean (±SEM) from three independent cell passages and analysed using 2-way ANOVA, *p < 0.05, **p<0.01.....207

Figure 5.25: Effect of PEGylated Linoleic acid nanoparticles in combination with Erastin (2,5 µM) on cell viability on (a) chemo-sensitive (PEO1) and (b) chemo-resistant (PEO4) ovarian cancer cells. Cell viability was evaluated using MTT assay after 24 h treatment of Erastin (2.5 µM) followed by 24 h treatment of nanoparticle (500 nm). Data was presented as mean (±SEM) from three independent cell passages and analysed using 2-way ANOVA, *p < 0.05, **p<0.01, ***p<0.001.....209

Figure 5.26: Illustration of citric acid coated iron oxide nanoparticle. With an iron oxide core (dark purple) and citric acid (blue).....210

Figure 5.27: Effect of iron oxide nanoparticles on GPX4 expression in mouse melanoma cells. (a) Mouse melanoma cells were cultured in media containing vehicle or iron oxide nanoparticle (500 nm): mIONP-COOH (PEGylated), IONP-Cit (Citric acid coated) or mIONP-DLin (Linoleic acid coated) for 24 h. GPX4 expression was determined by flow cytometry. Data was presented as mean (±SEM) from three independent cell passages and analysed using 2-way ANOVA, *p<0.05, **p<0.001, ***<0.001. (b) B16F10 incubated with vehicle or iron oxide nanoparticle (500 nm): mIONP-COOH, IONP-Cit or mIONP-DLin for 24 h, Representative flow cytometric profiles for intracellular GPX4 with Alexa Flour488 signals.....211

Figure 5.28: Effect of iron oxide nanoparticles on cell viability in a panel of cancer cell lines. The panel of cancer cell lines (a) 4T1, (b) MC-38, (c) LC-2, (d) PEO1, (e) PEO4, (f) OVCAR8 were cultured in media containing vehicle or Erastin or RSL3 for 24 h prior to treatment with iron oxide nanoparticle (500 nm): mIONP-COOH (PEGylated), IONP-Cit (Citric acid

coated) or mIONP-DLin (Linoleic acid coated). Cell viability was evaluated using MTT assay after a further 24 h. Data was presented as mean (\pm SEM) from three independent cell passages and analysed using 2-way ANOVA, * $p < 0.05$, ** $p < 0.001$, *** $p < 0.001$ 213

Figure 5.29: Effect of iron oxide nanoparticles on GPX4 expression in a panel of cancer cell lines. The panel of cancer cell lines (a) 4T1, (b) MC-38, (c) LC-2, (d) PEO1, and (e) PEO4, were cultured in media containing vehicle or iron oxide nanoparticle (500 nm): mIONP-COOH (PEGylated), IONP-Cit (Citric acid coated) or mIONP-DLin (Linoleic acid coated) for 24 h. GPX4 expression was determined by flow cytometry. Data was presented as mean (\pm SEM) from two or three independent cell passages and analysed using 2-way ANOVA, * $p < 0.05$, ** $p < 0.001$, *** $p < 0.001$ 214

Figure 5.30: Effect of iron oxide nanoparticles on mitochondrial superoxide levels in a panel of cancer cell lines. The panel of cancer cell lines (a) 4T1, (b) MC-38, (c) LC-2, (d) PEO1, (e) PEO4, (f) OVCAR8 were cultured in media containing vehicle or iron oxide nanoparticles (500 nm): mIONP-COOH (PEGylated), IONP-Cit (Citric acid coated) or mIONP-DLin (Linoleic acid coated) for 24 h. Mitochondrial superoxide quantity was determined via flow cytometry using MitoSOX. Data was presented as mean (\pm SEM) from three independent cell passages and analysed using 2-way ANOVA, * $p < 0.05$, ** $p < 0.001$, *** $p < 0.001$ 215

Figure 1: The rescue effect of Liproxstatin-1 treatment against the ferroptosis inducers; Erastin and RSL3. The panel of cancer cells lines were cultured in media containing Vehicle or Liproxstatin1 (25nM-1000nM) or Erastin (2.5 μ M) or RSL3 (0.625 μ M). Cells were treated with Liproxstatin-1 for 30 min prior to treatment with Erastin or RSL3 for 24 h. Cell viability was evaluated using MTT assay after 24 h. 254

List of Abbreviations

α -KG – Alpha-ketoglutarate
4E-BP – Eukaryotic translation initiation factor 4E-binding protein
AA – Arachidonic acid
ABAM – Antibiotic antimycotic solution
ACC1 – Acetyl-CoA carboxylase 1
ACSL4 – Acyl-CoA synthetase long-chain family member 4
AICAR - 5-aminoinidazole-4-carboxamide ribonucleotide
AIMF1 – Apoptosis-inducing factor mitochondrial-associated-1
AIMF2 – Apoptosis-inducing factor mitochondrial-associated-2
AKT – Protein kinase B
AMP – Adenosine monophosphate
AMPK – AMP-activated protein kinase
APAF-1 – Apoptotic protease-activating factor-1
ATG13 – Autophagy related protein 13
ATP – Adenosine triphosphate
BCL-2 – B-cell lymphoma 2
BMP – Bone morphogenic protein
BRCA1 – Breast Cancer Gene-1
BRCA2 – Breast Cancer Gene-2
BSA – Bovine serum albumin
CAMKK β - Calmodulin-dependent protein kinase kinase- β
CKD – Chronic kidney disease
CoA – Acetyl-Coenzyme A
Compound C - 6-[4-(2-piperidin-1-ylethoxy) phenyl]-3-pyridin-4-ylpyrazolo
[1,5-a]pyrimidine
CTLA-4 – Cytotoxic T lymphocyte associated protein 4
DC – Detergent compatible
ddH₂O – Double distilled water
DEPTOR – DEP domain-containing mTOR interacting protein
DISC – Death-inducing signalling complex
DMEM – Dulbecco's modified eagle medium
DMSO – Dimethyl sulfoxide
DMT1 – Divalent metal transporter-1
DNA – Deoxyribonucleic acid
ECM – Extracellular matrix
EPR – Enhanced permeability and retention
ER - Estrogen receptor
Erastin – Eradicator of RAS and ST-expressing
ERK8 – Extracellular signal-regulated kinase 8
ETC – Electron transport chain
EU – European Union
FADD – Fas-associated death domain
FasL – Fatty acid synthetase ligand
FBS- Foetal bovine serum
Fe²⁺ - Ferrous iron
Fe³⁺ - Ferric iron
FINs – Ferroptosis-inducing compounds

FIP200 – Focal adhesion kinase family interacting protein of 200 kDa
FPN1 – Ferroportin-1
FPP - Farnesyl pyrophosphate
FSP1 – Ferroptosis suppressor protein-1
FTL – Ferritin light chain
GCL – Glutamate-cysteine ligase
GDH – Glutamate Dehydrogenase
GLS – Glutaminase Enzyme
GLUT1 - Glutamine transporter-1
GPX4 – Glutathione peroxidase-4
GRAS – Generally regarded as safe
GSH – Glutathione
GSS – Glutathione synthetase
GSSG – Glutathione disulphide
H₂O₂ – Hydrogen peroxide
HEPC – Hepcidin
HER2 – Epidermal growth factor receptor-2
HIF1 – Hypoxia-inducible factor
HIPK2 – Homeodomain interacting protein kinase 2
HMGCR – 3-hydroxy-3-methylglutaryl-CoA reductase
HMOX1 – Heme Oxygenase 1
HRT – Hormone Replacement Therapy
IFN_γ - Interferon gamma
IONP – Iron Oxide Nanoparticle
IONVs – Iron oxide-loaded nanovaccines
IRF1 – Interferon regulatory factor 1
IRP2 – Iron regulatory protein 2
JAK – Janus kinase
LA – Linoleic acid
LAMP-2A – Lysosomal-associated membrane protein 2A
LDH – Lactate Dehydrogenase
LIP -Labile iron pool
LKB1 – Liver kinase B1
LOX – Lipoxygenases
LPCAT3 - Lysophosphatidylcholine acyltransferase 3
MEFs – Mouse embryonic fibroblasts
mLST8 – Mammalian lethal with Sec-13 protein 8
MNK1 – MAP kinase-interacting serin/threonine protein kinase 1
MRI – Magnetic resonance imaging
mSIN1 – MAP kinase interacting protein 1
mTOR – Mammalian target of rapamycin
mTORC1 – Mechanistic target of rapamycin complex 1
mTORC2 – Mechanistic target of rapamycin complex 2
MUFA – Monounsaturated fatty acid
MVA – Mevalonate
NCOA4 – Nuclear receptor coactivator-4
NRF2 – Nuclear factor-like 2
NSCLC – Non-small cell lung cancer
OA – Oleic acid

OXPHOS – Oxidative phosphorylation
PBS – Phosphate buffered saline
PD-1 – Programmed death-1
PD-L1 – Programmed death-ligand 1
PDH – Pyruvate Dehydrogenase
PEG – Polyethylene glycol
PI3K – Phosphoinositide 3-kinase
PIC – Protease inhibitor cocktail
PIC2 – Phosphatase inhibitor cocktail 2
PIC3 – Phosphatase inhibitor cocktail 3
PKC – Protein kinase C
PR – Progesterone receptor
PRAS40 – Proline-rich AKT substrate of 40 kDa
PROTOR - Protein observed with RICTOR
PUFA – Polyunsaturated fatty acids
PVA – Polyvinyl alcohol
PVDF – Polyvinylidene difluoride
PVP – Polyvinyl pyrrolidone
RAPTOR – Regulatory-associated protein of mammalian target of rapamycin
RES – Reticuloendothelial system
RHEB – RAS-homologue enriched in brain
RICTOR – Rapamycin-insensitive companion of mTOR
ROS – Reactive oxygen species
RSL3 – RAS selective lethal 3
S6K – Ribosomal protein S6 kinase
SAS – Sulfasalazine
SCLC – Small cell lung cancer
SDS-PAGE – Sodium dodecyl sulphate-polyacrylamide gel electrophoresis
SEM – Standard error of mean
SPIONs – Superparamagnetic Iron Oxide Nanoparticle
STAT1 – Signal transducer and activator of transcription 1
STEAP3 – Six transmembrane epithelial antigen of prostate-3
TCA – Tricarboxylic acid
TFR1 – Transferrin receptor protein-1
Thr172 – Threonine residue
TME – Tumour Microenvironment
TNBC – Triple-negative breast cancer
TNF - Tumour necrosis factor
Torin-1 - 1-[4-[4-(1-Oxopropyl)-1-piperazinyl]-3-(trifluoromethyl)phenyl]-9
(3-quinolinyl)-benzo[h]-1,6-naphthyridin-2(1H)-one
TRADD – TNF receptor-associated death domain
TRAIL – TNF-related apoptosis-inducing ligand
TSC – Tuberous sclerosis complex
UK - United kingdom
ULK1 – Unc-51-like kinase 1
UV – Ultraviolet
VDACs – Voltage dependent anion channels

VPS34 – Vacuolar protein sorting-associated protein 34
WIPI2 – WD repeat domain phosphoinositide-interacting protein 2
ZMP – AICAR monophosphate

Chapter 1: Introduction

1.1 Cancer

Cancer is recognised as more than 200 forms and is now estimated to affect 1 in 2 people within the United Kingdom (UK) during their lifetime (Cancer Research UK, 2021). It is estimated that 4 in 10 cancer cases can be prevented just through changes in lifestyle such as, cessation of smoking, keeping active, moderate alcohol intake and balanced diet (Cancer Research UK, 2021).

The majority of cancers (90-95%) are caused by environmental factors, with the remaining as a result of inherited genetics (Cancer Research UK, 2021). Cancer is a disease characterised by disruptions in normal cellular functions (Hanahan & Weinberg, 2011). Cancer development is triggered by dysregulation in the pathways that control the cells most fundamental processes, resulting in thousands of point mutations, translocations, amplifications and deletions (Cairns et al., 2016). The accumulation of genetically altered cells (abnormal cells) results in uncontrollable growth and invasion of surrounding tissues or metastasis to nearby organs for progression of the tumour (Yokota, 2000). Tumour growth and metastatic capabilities can be conceptualised into 'ten hallmarks' as determined by Hanahan & Weinberg 2011; **Figure 1.1**. This study will use a representative panel of cancer cells: Breast, Lung, Colorectal, Melanoma and Ovarian cancers.

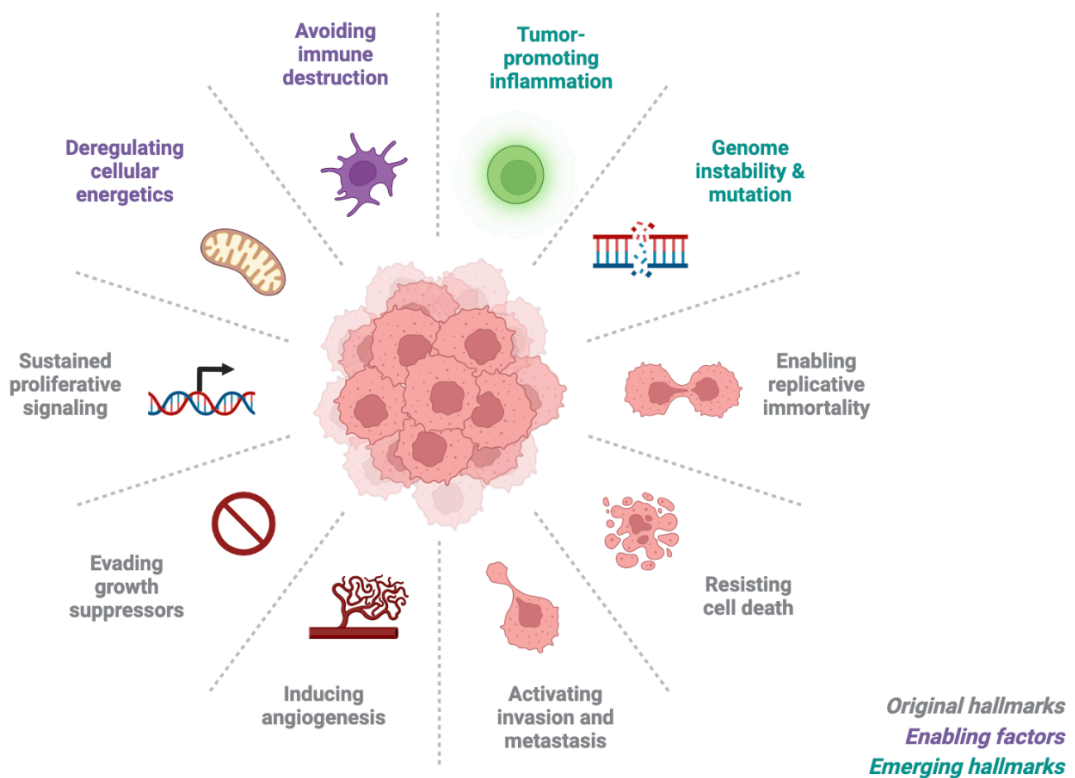


Figure 1.1: The hallmarks of cancer. The schematic conceptualises the ideal conditions required for malignant tumour growth and progression (Hanahan & Weinberg, 2011). Hanahan and Weinberg, 2011, created a framework which helps to understand the diversity of tumour development. There are six hallmark capabilities, two enabling characteristics and two emerging hallmarks. The biological capabilities include; sustaining proliferative signaling, evading growth suppressors, inducing angiogenesis, activating invasion and metastasis, resisting cell death and enabling replicative immortality. The two enabling characteristics are; genome instability and mutation and tumour-promoting inflammation. Over the last decade two general emerging hallmarks; avoiding immune destruction and deregulating cellular energetics (Hanahan & Weinberg, 2011).

1.2 Breast Cancer

Breast cancer is the most common form of cancer in the UK, with around 55,900 people diagnosed each year. The majority (70%) of breast cancers originate in the cells that line the milk ducts, which is known as invasive breast cancer. A further 15% of breast cancers originate in the lobules, known as invasive lobular breast cancer. Inflammatory breast cancer originates in the small lymph vessels of the breast, this form of cancer is rare, contributing to around 5% of breast cancer cases. Triple negative breast cancers (TNBC) contribute to 10% of breast cancer cases (Cancer Research, UK, 2023).

Breast cancer may then metastasise to surrounding organs via the nearby lymph vessels (Cancer Research, UK, 2023). For all breast cancer stages combined around 85% of breast cancer patients survive 5-years, however the 5-year survival rate for stage IV breast cancer is only 25% (Cancer Research, UK, 2023). Within this study a model for TNBC was used; these cancer cells test negative for oestrogen receptors (ER), progesterone receptors (PR) and epidermal growth factor receptor 2 (HER2; nedeljkovic & Damjanovic, 2019). TNBC is characterised as an aggressive, highly metastatic cancer, which results in poor prognosis. There is currently no targeted therapy for TNBC, therefore patients undergo chemotherapy treatment, however this form of cancer is resistant to current available treatment programmes (Cleator et al., 2007). A number of factors can contribute to the development of breast cancer: obesity, oral contraception and hormone replacement therapy (HRT), along with other factors that cannot be controlled: age, ethnicity, cancer history and family history (Dolle et al., 2009; Cancer Research, UK, 2021). Furthermore, several factors have been associated with improving clinical outcomes of breast cancer: breastfeeding, diet and activity and preventative surgery based on family history (Cancer Research, UK, 2021).

1.3 Lung Cancer

Lung cancer is the third most common cancer in the UK: around 48,500 people are diagnosed each year in the UK (Cancer Research UK, 2021). Lung cancer can develop in any part of the respiratory system. For all lung cancer stages around 15% of lung cancer patients survive 5-years; however, the 5-year survival rate for stage IV lung cancer is 10% (Cancer Research, UK, 2021).

Histologically, nearly 15% of lung cancer cases are small cell lung cancer (SCLC), whilst the majority (85%) of lung cancer cases are non-small cell lung cancer (NSCLC). Within this study an NSCLC cell line was used. Most patients with NSCLC are diagnosed at advanced stages of the disease, resulting in poor prognosis. The current treatment regime for late-stage NSCLC is chemotherapy and palliative care (Scheff & Schneider, 2013).

Tobacco smoking contributes to more than 90% of lung cancer cases. A life-time smoker has a 20-fold increased risk of developing lung cancer in comparison to a non-smoker (Alberg & Samet, 2003). A study by Peto et al., 2000, showed that cessation of tobacco smoking can reduce lung cancer incidence by half. Other causative factors that can contribute to lung cancer development include air pollution, lung disease and family history (Cancer Research, UK, 2021).

1.4 Colorectal cancer

Bowel cancer is the fourth most common cancer in the UK, with around 42,900 people diagnosed in the UK each year (Cancer Research UK, 2021). Colorectal cancer comes under the umbrella term 'bowel cancer' and is determined by the cancer origin: either the colon or rectum. For all colon cancer stages around 60% of colon cancer patients survive 5-year; however, the 5-year survival rate for stage IV colon cancer is 10%. There is no effective therapy for advanced colorectal carcinoma (Cancer research UK, 2021; Rodriguez-Bigas et al., 2006).

Colon cancer originates in the mucosal wall before growing outwards; the depth of the tumour determines the stage of cancer. Unfortunately, two thirds of colon cancer cases are diagnosed at late stages of the disease (Corvino et al., 2015). Late diagnosis is attributed to high tumour heterogeneity, which also makes effective treatment difficult (Rodrigues-Bigas et al., 2006; Yang et al., 2019).

In recent years, colon cancer morbidity and mortality rates have increased due to changes in diet and the environment. Other factors increasing the risk of bowel cancer are obesity, benign polyps, ulcerative colitis, and Crohn's disease (Cancer research UK, 2021). A preventative measure for colon cancer is through regular screenings, which enables the early detection of polyp

formation. Colon screening is available in the UK for males and females from 50 years of age (Cancer research UK, 2021).

1.5 Melanoma

Skin melanoma is the fifth most common cancer in the UK, with around 16,700 people diagnosed in the UK each year (Cancer Research UK, 2021). Skin melanoma originates from the melanocytes with the most common form being, superficial spreading melanoma (around 70%). At early stages of the diseases, surgical removal of the melanoma cells results in a 99% survival rate. However, after metastasis there is only a 20% 5-year survival rate (Jerant et al., 2000). For all skin melanoma cancer stages around 90% of melanoma cancer patients survive 5-years, however the 5-year survival rate for stage IV skin melanoma is only 30% (Cancer Research, UK, 2021). The incidence rate of melanoma cancer is increasing but there is still no successful treatment. The cancer is highly aggressive and becomes resistant to chemotherapy (Tentori et al., 2013).

Melanoma originates from melanocytes within the basal layer of the epidermis and migrate through the basement membrane and into the dermis due to altered extracellular matrix (ECM) expression. Melanocytes are tightly regulated by keratinocytes and the microenvironment, however homeostasis dysregulation results in the continuous proliferation of melanocytes, consequently forming melanomas. Melanomas are able to overcome regulations by down-regulating receptors for keratinocytes, upregulating receptors for melanoma interactions and alter ECM expression in order to lose anchorage to the basement membrane (Hass et al., 2005).

In the UK 85% of skin melanomas are attributed to too much ultraviolet (UV) radiation exposure (Cancer Research, UK, 2020). Gene mutations (RAS/RAF/MEK/BRAF) are other contributing factors to the development of skin melanomas along with age, skin colour, moles, body weight and family history (Veierød et al., 2010; Tímár et al., 2016).

1.6 Ovarian Cancer

Ovarian Cancer is the 6th most common cancer in women with around 7,400 cases diagnosed in the UK each year (Cancer Research UK, 2021). The prognosis of the disease is dependent on the stage of development. However, the majority of women are diagnosed at advanced stages of the disease due to the vague and indistinctive symptoms, including weight gain, abdominal or pelvic pain, abdominal swelling and vaginal bleeding (Cancer Research UK, 2021). For all ovarian cancer stages around 25% of ovarian cancer patients survive 5-years, a worse outcome than breast cancer (Kipps et al., 2013). The current 5-year survival rate of women with stage IV ovarian cancer is 15% (Cancer Research UK, 2019). The majority of women undergo chemotherapy, to which they initially respond well but then become therapy resistant within 18 months, leaving surgery and palliative care as the only treatment options. There has been no change in the survival rate of ovarian cancer for over 50 years, therefore it is of paramount importance that novel therapies are identified (Kurman & Shih, 2010).

Alternative treatments for ovarian cancer involve the use of PARP inhibitors, a class of pharmacological agents targeting the poly ADP ribose polymerase (PARP) enzyme. PARP1, characterised by its poly ADP-ribose activity, becomes activated in response to DNA damage. In this activated state, it adds branched PAR chains, facilitating the recruitment of other repair protein and promoting the repair of DNA single-strand breaks, PARP inhibitors were the first approved cancer drugs that selectively targeted DNA damage response, particularly in BRCA1/2 mutated ovarian and breast cancers. Inhibiting PARP1 results in the formation of double-stranded DNA breaks which ultimately results in cell death (D.Andrea, 2018; Franzese et al., 2019).

The risk of developing ovarian cancer increases when women undergo menopause. Many women attempt to reduce the symptoms of menopause through HRT, however there is an increased risk of ovarian cancer with

oestrogen replacement therapy when used for more than 10 years (Lacey et al., 2002). Other factors impose a greater risk for the development of ovarian cancer: inherited gene mutations such as breast-cancer susceptibility genes 1/2 (*BRCA1* and *BRCA2*), smoking, obesity, and previous cancer such as breast cancer. Women who have previously had breast cancer are twice as likely to develop ovarian cancer, which has been found to be three times more lethal than breast cancer alone (Visintin et al., 2008). A number of factors have been associated with improving clinical outcomes of ovarian cancer, the use of oral contraceptive, breastfeeding and the number of successful full-term pregnancies (McLaughlin et al., 2007).

1.7 Cancer Metabolism

Cancer cells are required to alter their metabolism to enable continuous rapid proliferation (**Figure 1.2**; DeBerardinis & Chandel, 2016). This is achieved through a shift towards aerobic glycolysis (known as the Warburg effect), which shows a shift from adenosine triphosphate (ATP) generation from oxidative phosphorylation (OXPHOS) to glycolysis under aerobic conditions (Brand & Harmfisse, 1997). Subsequently, cancer cells must increase their uptake of glucose by increasing the expression of the glucose transporter 1 (*GLUT1*). The increased uptake of glucose results in an increased production of lactate, which can be used to fuel the tricarboxylic acid (TCA) cycle. Tumour metastasis and therapy resistance is also attributed to high levels of lactate in the tumour microenvironment (TME), which causes extracellular acidification, resulting in a TME of pH 6-6.5 (Estrella et al., 2013; Garcia-Canaveras et al., 2019).

The metabolic shift towards glycolysis is also advantageous within hypoxic conditions associated with the poor blood supply observed within solid tumours. Under these conditions, glutamine is utilised to form α -ketoglutarate (α -KG) to fuel the TCA cycle (Wise et al., 2008; DeBerardinis & Chandel, 2016). Glutamine is metabolised into α -KG via glutaminolysis, which involved two deamination steps (Xiao et al., 2016). Firstly, glutamine is

converted to glutamate and ammonia, by the glutaminase enzyme (GLS), before conversion to α -KG by glutamate dehydrogenase (GDH). Cancer cells become glutamine addicted due to changes in metabolism as a result of oncogenic levels of MYC, resulting in increased glutaminolysis and glycolysis (Wise et al., 2008; Stine et al., 2015).

Cancer cell metabolism becomes adapted to hypoxia via the hypoxia-inducible factor (HIF-1), and as a result of this adaptation cancer cells acquire both invasive and metastatic properties but also resistance to chemotherapy and radiotherapy (Semenza 2012; Gorrini et al., 2013). HIF-1 is composed of two subunits HIF-1 α and HIF-1 β , responsible for the upregulation of hypoxic response elements and increased glycolytic flux, of which the alpha subunit expresses a correlation with tumour progression (Petrova et al., 2018).

The anabolic kinase mammalian target of rapamycin (mTOR) drives tumour growth through mutations within the phosphoinositide 3-kinase (PI3K)-protein kinase B (AKT)-mTOR network (Han et al., 2018). The aberrant activation of this pathway results in the reduction of apoptosis, which therefore enables continuous tumour growth and survival with minimal input from extrinsic growth factors. The PI3K pathway is essential for cell survival, growth, and differentiation. The pathway activates AKT, which has a number of downstream effects, including the activation of mTOR. The activation of the network is essential for protein, lipid, and nucleic acid biosynthesis. PI3K signalling pathway activates fatty acid uptake alongside the inactivation of fatty acid oxidation (DeBerardinis & Candel, 2016). Under nutrient deprivations, AMP-activated protein kinase (AMPK) activates fatty acid oxidation to stimulate ATP production (**Figure 1.2**).

The tumour suppressor *TP53* is frequently mutated and deleted in 50% of cancer and is the most commonly mutated gene within all types of cancer (Freed-Pastor & Prives, 2016). The role of p53 in cancer metabolism is to regulate glycolysis, though the suppression of GLUT1, resulting in reduced

conversion of glucose to pyruvate, the end product of glycolysis. Pyruvate can either be converted to lactate by lactate dehydrogenase (LDH) or to acetyl-coenzyme A (CoA) by pyruvate dehydrogenase (PDH; Kruiswijk et al., 2015). Therefore, the loss of the tumour suppressor p53 results in increased glycolytic flux (Deberardinis & Chandel, 2016).

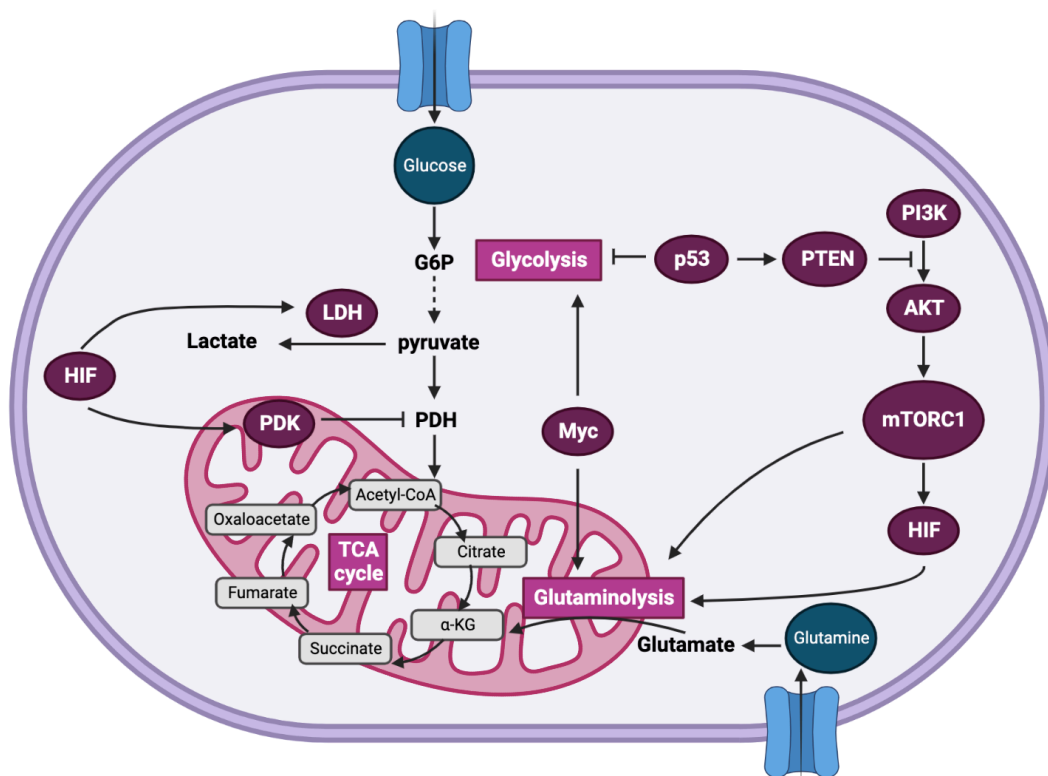


Figure 1.2: Signalling pathways associated with the regulation of cancer metabolism. PI3K activated AKT which in turn activated mTOR. Tumour cells activate mTORC1 in order to induce anabolic pathways for nucleotide, protein and lipid synthesis. The activation of HIF also results in metabolic changes; activation of glutaminolysis and inactivation of mitochondrial pyruvate dehydrogenase complex. p53 inhibits glycolysis but indirectly activates mTORC1. Myc also promotes anabolic pathways for tumour growth and proliferation (Created with BioRender.com).

1.8 Iron Metabolism

Elemental iron is a fundamental micronutrient in mammalian cells, with a number of important roles especially within metabolic processes, such as

oxygen transportation, deoxyribonucleic acid (DNA) and ATP biosynthesis and the function of the electron transport chain (ETC; Dong et al., 2019). The presence of iron is essential for cell function, however high levels can potentially be toxic due to free radical formation and consequently can lead to cell death (Britton et al., 1994). Alternatively, iron deficiency can result in detrimental cellular processes and eventually cell death. Therefore, complex iron regulatory mechanisms are undertaken in order to maintain iron homeostasis, resulting in a balance between iron uptake, transport, storage and utilisation (Wallace, 2016).

Iron is an essential element absorbed from the diet in two forms; haem and non-haem, which are recycled and conserved by the body. A daily diet contains between 10-20 mg of iron, from which 1-2 mg is absorbed and transported; 75% to haemoglobin, 10-20% is stored in the ferritin complex, whilst 5-15% is available for other iron processes such as respiration and metabolism (Trumbo et al., 2001; Abbaspour et al., 2014). Around 1-2 mg of iron may be lost per day through menstruation, epidermal desquamation, urination, and bowel movements (Hunt et al., 2009). Iron absorption can be influenced by dietary factors such as ascorbic acid and citrate, which result in increased iron uptake by chelating iron within the duodenum (Conrad & Schade, 1968).

Iron is present in two forms within the body: ferrous iron (Fe^{2+}) and ferric iron (Fe^{3+}). There are two main mechanisms in which iron is incorporated into the cell. The first mechanism uses the divalent metal transporter 1 (DMT1) to import Fe^{2+} ; the second mechanism results in endocytosis of iron, where Fe^{3+} binds to transferrin before being incorporated into the cell via the transferrin receptor (TFR1; also known as CD71), or alternatively iron is endocytosed via the CD44/hyaluronate (Hyal) pathway. Upon maturation of the endocytic vesicle, Fe^{3+} is released from transferrin and is further reduced to Fe^{2+} by the six-transmembrane epithelial antigen of prostate 3 (STEAP3). Fe^{2+} translocates to the cytosol via DMT1, where iron becomes freely available within the labile iron pool (LIP; Pantopoulos, 2004). The LIP can be utilised by

mammalian cells for multiple processes, otherwise excess iron may be stored within the ferritin complex or exported from the cell via ferroportin-1 (FPN1), under control of the liver hormone hepcidin (HEPC). HEPC is a peptide hormone secreted from the liver, which directly binds to FPN1 in response to iron levels, hypoxia, and inflammation (Pantopoulos, 2004). FPN1 is the exclusive iron export protein expressed on the basolateral membranes of enterocytes, hepatocytes, macrophages, and adipocytes. When serum iron levels are too high HEPC expression is increased, HEPC then binds to FPN1 and becomes internalised resulting in the degradation of FPN1 and prevention of iron flux. Iron deficient conditions results in decreased HEPC expression, thus enabling FPN1 to transport iron into the blood (Waldvogel-Abramowski et al., 2014).

All of the incorporated iron found within the cytosol of the cells can either remain available within the LIP or be transported to the mitochondria for the formation of iron-sulphur (Fe-S) clusters or be stored within the ferritin complex. If the LIP needs replenishing, ferritin is degraded by a process known as ferritinophagy, which is activated by the nuclear receptor coactivator 4 (NCOA4; Pantopoulos, 2004; Santana-Codina & Mancias, 2018). NCOA4 is an autophagy cargo receptor that binds to ferritin in autophagosomes and delivers them to lysosomes for degradation (Wallace, 2016). The breakdown of ferritin is initiated during ferroptosis (discussed later). Once ferritin is broken down, the cargo iron undergoes oxidation controlled by HEPC before it can be released from the cell via FPN1 and contribute to the LIP (**Figure 1.3**; Wallace, 2016).

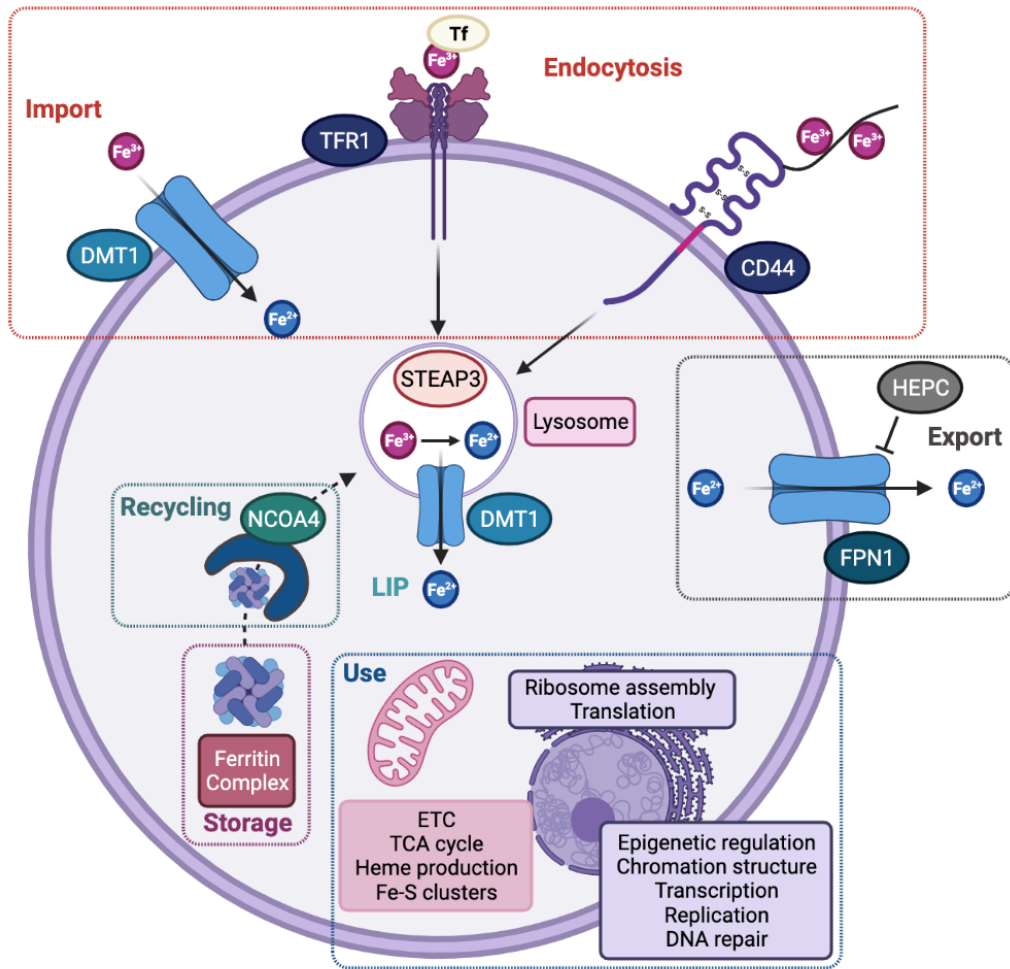


Figure 1.3: Cellular iron homeostasis. Transferrin bound iron (Fe^{3+}) can be imported into the cell via endocytosis after binding to TFR1 (also known as CD71). Within the endosome Fe^{3+} is converted to Fe^{2+} by STEAP3 before being transported to the cytosol by DMT1. Non-transferrin bound iron can be imported into the cell by DMT1 after conversion of Fe^{3+} to Fe^{2+} . All iron transported into the cell becomes available within the labile iron pool (LIP), the available iron may remain available or be stored in the ferritin complex by PCBP1 or transported to the mitochondria for the biosynthesis of iron-sulphur clusters (Fe-S). When iron is required NCOA4 breaks down the ferritin complex (ferritinophagy) and iron can be released from the cell via FPN1 after the conversion of Fe^{2+} to Fe^{3+} via hepcidin (HEPC; Created with BioRender.com).

1.8.1 Iron Metabolism – The Fenton Reaction

Excessive iron results in an increased accumulation of reactive oxygen species (ROS) driven by the Fenton reaction. The production of ROS is a result of the ability of iron to switch between oxidised and reduced forms (Manz et al., 2016). The Fenton Reaction is driven by free Fe^{2+} which catalyses the conversion of hydrogen peroxide (H_2O_2) into free radicals; $\text{HO}\cdot$. The free

radicals produced from the Fenton reaction can react with lipids within the cell membrane to form lipid peroxides (Orino et al., 2001). Lipid peroxide accumulation can result in a programmed cell death pathway known as ferroptosis.

The Fenton reaction equation:



Cancer cells are able to evade the Fenton reaction through the production of the ferritin complex (Orino et al., 2001). Ferritin is a hollow protein, which sequesters free Fe^{3+} . There are two functionally and genetically distinct subunits of the ferritin complex; L-ferritin (19 kDa) and H-ferritin (21 kDa), which are found in varying ratios in different cell types (Wang et al., 2006). The heavy subunit is involved in the ferroxidase activity of the complex, whereas the light subunit is responsible for iron storage within the ferritin core (Yang & Chasteen, 1999). The ferritin complex is predominantly known as an iron storage protein, but new observations have found that this complex is also associated with iron accessibility, transcriptional regulation, and DNA protection from iron-induced oxidative damage. The Fenton reaction is driven by the endocytosis of iron via TFR1 (Gao et al., 2015; Xie et al., 2016; Wang et al., 2016; **Figure 1.4**).

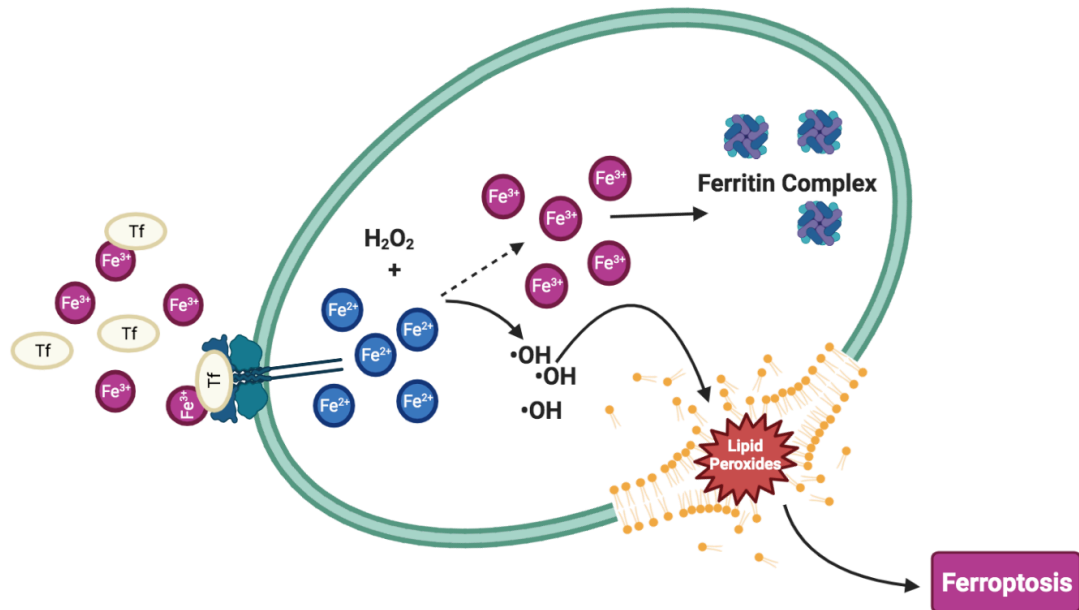


Figure 1.4: Schematic overview of the Fenton Reaction. The Fenton reaction is driven by endocytosis of iron via the transferrin receptor protein 1 (TFR1). External ferric iron (Fe³⁺) binds to transferrin (Tf) and becomes incorporated into the cell via TFR1. The change in the pH within the endosome causes the iron to be released from transferrin and reduced ferrous iron. The ferrous iron is then free to react with hydrogen peroxide (H₂O₂) resulting in free radicals. The free radicals are able to react with lipids within the cell membrane, which can induce a cell death pathway known as ferroptosis. Cancer cells can convert the ferrous iron back to ferric iron to be stored in the ferritin complex for when iron is later required (Created with BioRender.com).

1.9 Ferroptosis

In order to maintain tissue homeostasis, it is vital that cells undergo a form of programmed cell death when necessary (Cao & Dixon, 2016; Stockwell et al., 2017). Various types of programmed cell death have been identified, including; apoptosis, necroptosis and ferroptosis. Autophagy also plays a central role in the breakdown of cells (Su et al., 2019).

Polyunsaturated fatty acids (PUFAs) scavenge ROS to counter cell damage induced by the elevated levels of ROS detected in almost all cancers (Liou & Storz, 2010). Lipids are converted into lipid peroxides by oxidative degradation via the addition of a free radical (Halliwell & Chirico, 1993); consequently, inducing ferroptotic programmed cell death. Ferroptosis is a type of non-apoptotic programmed cell death, which is dependent on iron and characterised by the accumulation of toxic lipid peroxides (Stockwell et al.,

2017). Characteristic changes of cells undergoing ferroptotic cell death include the rounding up of cells and a decreased volume of mitochondria but increase in mitochondrial membrane density (Stockwell et al., 2017). The distinguishing differences between ferroptosis, apoptosis and autophagy are explained in **Table 1**.

Table 1: The main features that distinguish between ferroptosis, apoptosis and autophagy.

Cell Death	Ferroptosis	Apoptosis	Autophagy
Biochemical	Reduced glutathione (GSH) biosynthesis, lipid peroxide accumulation	Activation of a caspase cascade	Increased lysosomal activity
Morphological	Increased mitochondrial membrane density, rounding up of cells, vanishing of mitochondria crista	Blebbing of the plasma membrane, nuclear reduction, and fragmentation	Double-membraned autolysosome
Genes	<i>GPX4</i> , <i>SLC7A11/SLC3A2</i> (system X_c^-), <i>NFE2L2</i> (NRF2), <i>TFR3</i>	<i>CASP3</i> , <i>TP53</i> , <i>FAS</i> , <i>BCL2</i> , <i>BAX</i>	<i>ATG5</i> , <i>ATG7</i>
Regulators	GPX4, System X_c^- , mevalonate (MVA) pathway, p62-KEAP1-NRF2	Death receptor, mitochondrial, endoplasmic reticulum, caspase cascade, p53, Bcl-2	P13K-AKT-mTOR, MAPK-ERK1/2, mTOR
Inducers	Erastin, RSL3, FIN56, sorafenib, SAS	FASL, DCC, UNC5B	Rapamycin
Inhibitors	DFO, Vitamin E, Ferrostatin-1, Liproxstatin-1	XIAP, IAP2, NAIP	Hydrochloroquine, VPS34

Ferroptosis involves the import of cystine and export of glutamate via the system X_c^- in a 1:1 ratio (also known as xCT; Bannai, 1986). The system X_c^- is a heterodimeric amino acid transporter, composed of a light chain SLC7A11 and a heavy chain SLC3A2, which are covalently linked by a disulphide bridge

(Huang et al., 2005). Imported cystine is reduced to cysteine, the glutamate-cysteine ligase (GCL) enzyme condenses cysteine with available glutamate to form gamma-glutamylcysteine. This dipeptide is further condensed with glycine by the enzyme glutathione synthetase (GSS), resulting in the formation of glutathione (GSH; Stockwell et al., 2017). The enzyme glutathione peroxidase IV (GPX4) uses GSH to convert lipid peroxides into their equivalent alcohols, through the reduction of GSH to glutathione disulphide (GSSG). A schematic overview of the ferroptosis pathway can be seen in **Figure 1.5**.

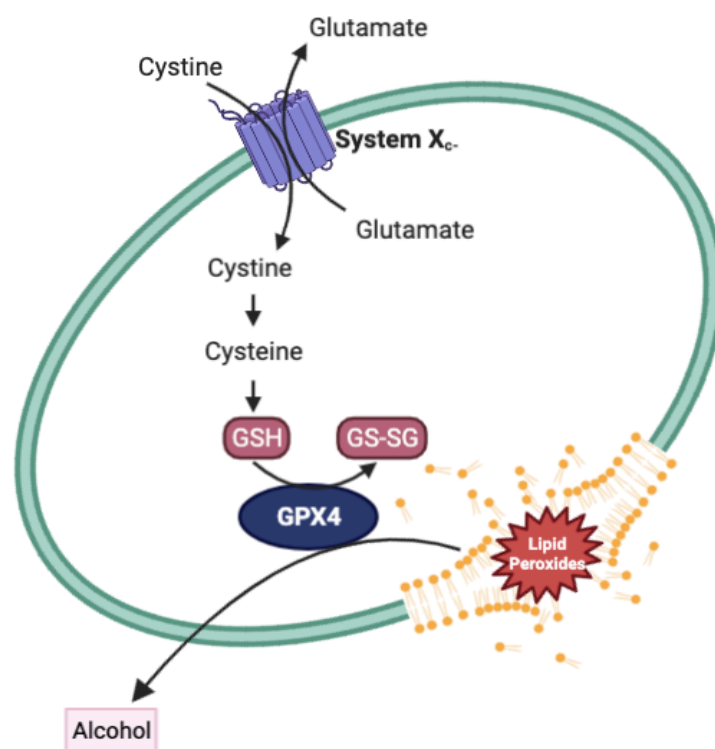


Figure 1.5: Schematic overview of the ferroptosis pathway. Cancer cells are able to evade ferroptosis through the upregulation of GPX4. System X_c⁻ imports cystine and exports glutamate, which is essential for the production of glutathione (GSH). GPX4 and GSH catalyse the reduction of lipid peroxides to lipid alcohols, enabling cell survival (Created with BioRender.com).

The presence of iron is essential for ferroptotic induction as the addition of iron chelators suppresses ferroptosis (Yang & Stockwell, 2008). The ability of iron to switch between oxidised and reduced forms results in an increased accumulation of lipid peroxidation (Cao & Dixon, 2016; Manz et al., 2016). As mentioned, ferroptosis is regulated by iron and ROS and is characterised by the accumulation of lipid peroxides (Stockwell et al., 2017). ROS are generated

by the Fenton reaction and enzyme-catalysed reactions involving a number of metabolic enzymes and PUFAs such as arachidonic acid (AA; Gorrini et al., 2013; Coscia et al., 2016). PUFAs are highly susceptible to lipid peroxidation due to the presence of a bis-allylic carbon, the protons are vulnerable to free hydrogen ions, which are essential for the implementation of ferroptosis. The interaction between the two results in alkyl-radicals to further react with oxygen to result in peroxy-radicals. These radicals are then free to react with PUFAs causing a continual chain reaction of lipid peroxidation (Yang et al., 2016; Coscia et al., 2016). Lipid peroxidation is mediated by the activity of lipoxygenases (LOXs); non-heme iron-containing enzymes, now thought to be key regulator of ferroptosis due to their activity contributing to an increased accumulation of hydroperoxides. LOXs catalyse the deoxygenation of PUFAs (such as AA and linoleic acid (LA)) resulting in the formation of hydroperoxides (Shintoku et al., 2017).

Cancer cells are able to evade ferroptosis through the upregulation of GPX4 and via the transsulfuration pathway. This pathway enables cancer cells to biosynthesise cysteine from methionine and therefore maintain GSH production under depleted cystine conditions (Stockwell et al., 2017). Ferroptosis can be induced in cancer cells using ferroptosis-inducing compounds (FINs), which are classified based on how they induce ferroptosis in the cell. The I class inhibits System X_C^- and therefore depletes GSH production. Class II FINs induce ferroptosis through the direct inhibition of the central regulator enzyme GPX4, whereas class III FINs indirectly inhibit GPX4. Finally, the class IV FINs induce ferroptosis through the excessive activation of heme oxygenase 1 (HMOX1), which consequently increases LIP (Sun et al., 2020).

The flavoprotein apoptosis-inducing factor mitochondria-associated 2 (AIFM2) was recognised as a p53-responsive gene, which induced apoptosis. However due to close similarity to apoptosis-inducing factor mitochondria-associated 1 (AIFM1) AIFM2 was re-named to ferroptosis suppressor protein 1 (FSP1). The expression of FSP1 complements the loss of GPX4 and therefore can be

recognised as a glutathione-independent ferroptosis suppressor (Santoro, 2020; Doll et al., 2019; Bersuker et al., 2019).

Prototypic ferroptosis-inducing biochemical inhibitors used in this study to induce ferroptosis include **Eradicator of RAS** and **ST**-expressing cells (Erastin) and RAS selective lethal 3 (RSL3). These inhibitors trigger ferroptotic cell death (Dächert et al., 2016).

1.9.1 Erastin

Erastin is a class one FIN, which irreversibly binds to the light chain SLC7A11 of system X_C^- . Consequently, Erastin deprives cells of cysteine, which results in the depletion of GSH synthesis, resulting in an increase in lipid peroxides and consequently ferroptotic cell death (Cao & Dixon, 2016; Stockwell et al., 2017; Sato et al., 2018; **Figure 1.6**). However, it has been shown that the inhibition of system X_C^- can result in the upregulation of *SLC7A11* gene, consequently causing Erastin resistance. The transsulfuration pathway also results in Erastin resistance, as cysteine can be synthesised from methionine (Dixon et al., 2012; Stockwell et al., 2017).

The inhibitory effect of Erastin on the system X_C^- has been shown to be as lethal as the FDA approved drugs: sulfasalazine (SAS) and sorafenib (Cao & Dixon, 2016). SAS has previously been used to target the system X_C^- in primary brain tumours, with some success (Robert et al., 2015). In order to inhibit system X_C^- , SAS is required at a concentration of 100 μM , which exhibits an IC_{50} of 26.1 μM , whereas Erastin has been found to be more efficient at inhibiting system X_C^- and is required at a concentration of 10 μM , which exhibits an IC_{50} of 1.4 μM (Gout et al., 2001; Dixon et al., 2012; Stockwell et al., 2017).

1.9.2 RSL3

RAS selective lethal 3; RSL3 is a class II FIN, which directly binds to and inactivates GPX4. RSL3 covalently binds to the selenocysteine containing active site of GPX4, which results in an increase in lipid peroxides and consequently ferroptotic cell death (Dixon et al., 2012; **Figure 1.6**).

There are two identified lipid metabolism-associated genes that are known to promote RLS3-induced ferroptosis within cancer cells. They include acyl-CoA synthetase long-chain family member 4 (ACSL4) and lysophosphatidylcholine acyltransferase 3 (LPCAT3). ACSL4 is involved in the acylation of fatty acids, such as AA, and LPCAT3 inserts the acylated fatty acid into the phospholipid membrane (Dixon et al., 2015). Once these PUFAs are embedded into the cell membrane they become prone to peroxidation and thus trigger ferroptosis (Sun et al., 2020). A study undertaken by Doll et al., found that the deletion of these genes within cancer cells abrogated the ability of the cells to undergo ferroptosis, even with the addition of RSL3 (Doll et al., 2017).

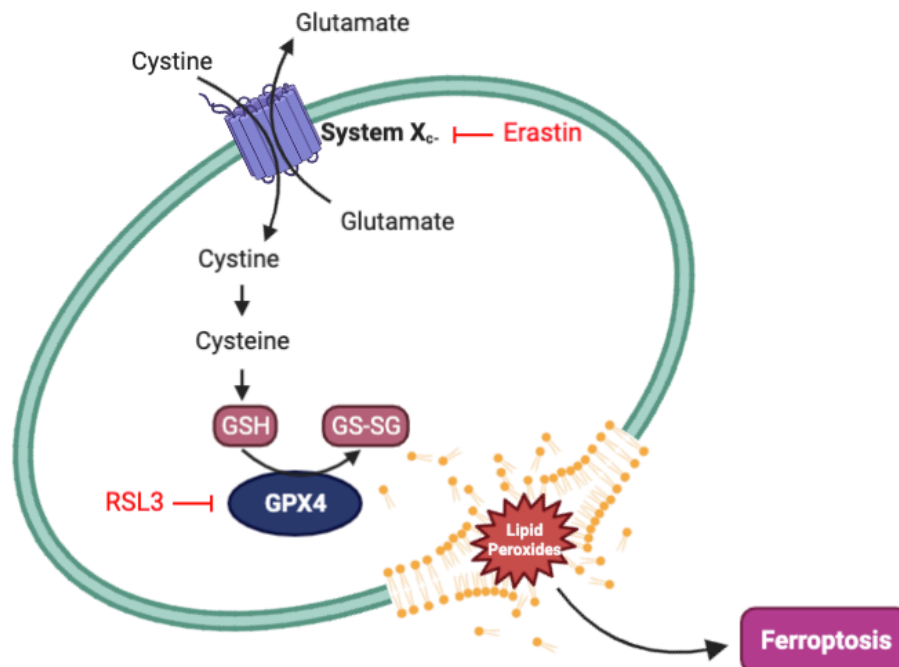


Figure 1.6: Schematic overview of how FINs induce ferroptosis in cancer cells. Ferroptosis may be induced through the inhibition of system X_c⁻ by Erastin or the inhibition of GPX4 directly by RSL3 (Created with BioRender.com).

1.9.3 Nanoparticles and ferroptosis

Current ferroptotic activators (Erastin and RSL3) are unable to circulate throughout the body, with Erastin displaying poor solubility (crystalline solid) and poor metabolic stability (Feng & Stockwell, 2018); and little is presently known about the pharmacokinetics of RSL3 (Feng & Stockwell, 2018); therefore, alternative inducers are required. However, the addition of chemical groups into the aniline ring of Erastin has improved the stability and solubility of the compound for *in vivo* use whilst also maintaining the lethality of Erastin. For example, Yang et al (2015) injected fibrosarcoma cells into nude mice prior to treatment with piperazine Erastin (PE), they observed a reduction in tumour growth and also no off target effects, even at the highest doses of PE (60mg/kg). Yang et al (2015) also used RSL3 *in vivo*, which showed to prevent tumour growth and caused tumour reduction.

Many reports have shown that iron oxide nanoparticles can be cytotoxic to human cancer cells (Huang et al., 2019). Therefore, the use of such nanoparticles may be utilised in the treatment of numerous cancer types. Indeed, therapies that interfere with key regulators of iron metabolism and cellular iron trafficking are currently in clinical development and represent a promising new class of therapeutic agents (Crielaard et al., 2017). Studies have shown that ferroptosis can be induced in a range of cancers by iron oxide nanoparticles (SPIONs). Therefore, iron addiction maybe cancers' 'Achilles heel' and a novel therapeutic target.

The delivery of SPIONs to the target tumour site is a complex process that is dependent on the physio-chemical characteristics of the nanoparticles and protein-particle interactions (Rees et al., 2019). The internalisation of the nanoparticles is also dependent upon these factors, but the most researched and common ways for internalisation are through phagocytosis, endocytosis and direct trans-membrane transport (Lesniak et al., 2012). The internalisation of nanoparticles is random, and the acquired dose can be described by well-defined probability distribution functions (Summers et al., 2011; **Figure 1.7**).

Once iron oxide nanoparticles are internalised, they are able to exploit the TME in order to eradicate established tumours. The iron oxide nanoparticles undergo Fenton chemistry, resulting in the conversion of H_2O_2 into toxic ROS (Ruiz-de-Angulo et al., 2020, **Figure 1.7**).

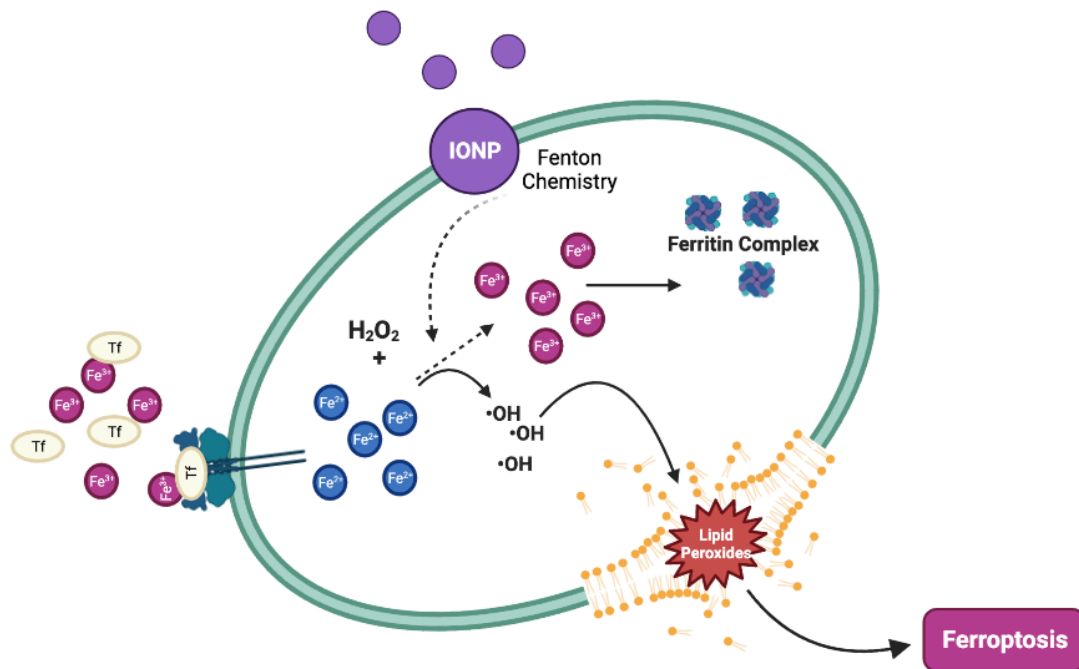


Figure 1.7: Schematic overview of how iron oxide nanoparticles interact with cancer cells The internalisation of nanoparticles is random but the uptake of nanoparticles into the cell can be achieved through phagocytosis, endocytosis and direct trans-membrane transport. The internalised iron oxide nanoparticles undergo the Fenton reaction; where ferrous iron is free to react with hydrogen peroxide (H_2O_2) resulting in free radicals. The free radicals react with lipids within the cell membrane, resulting in ferroptotic cell death (Created with BioRender.com).

1.10 Autophagy

First described in the 1950s, autophagy is derived from the Greek meaning 'eating of self', the process is essential for maintaining cellular homeostasis by removing and recycling dysfunctional components (Rabinowitz & White, 2010). Autophagy is a form of nonselective degradation but also enables the cell to adapt to a variety physiological and pathophysiological changes. The process of autophagy enables cells to survive under stressful conditions, most importantly amino acid starvation. Amino acids are important regulators of

cellular metabolism as they provide building blocks for proteins (Kuma & Mizushima, 2010).

There are three main types of autophagy: macro-autophagy, chaperone-mediated autophagy, and micro-autophagy, but they all have the same end point, the degradation of cytosolic components (Glick et al., 2010, **Figure 1.8**). Macro-autophagy is the result of an autophagosome that fuses with the lysosome for the degradation of cytoplasmic cargo. Chaperone-mediated autophagy is the translocation of proteins across the lysosomal membrane. The proteins bind to chaperone proteins, such as Hsc-70, to form a complex, which can be transported into the lysosome by lysosome membrane receptor lysosomal-associated membrane protein 2A (LAMP-2A). Micro-autophagy involves the invagination of the lysosomal membrane, to directly take up cytosolic components (Glick et al., 2010; Feng et al., 2014; Oku & Sakai, 2018).

Macro-autophagy (henceforth known as autophagy) is the main focus within this study. Autophagy is initiated by an isolation membrane (also known as a phagophore), which forms a cup-shape to engulf intra-cellular cargo. The phagophore continues to expand until it forms a double-membraned autophagosome, which continues to mature and subsequently fuses with lysosomes to generate autolysosomes. Lysosomal acid proteases degrade the internal cargo, from which amino acids and other useful by-products are exported into the cytoplasm where they can be utilised (Glick et al., 2010; Lane et al., 2013).

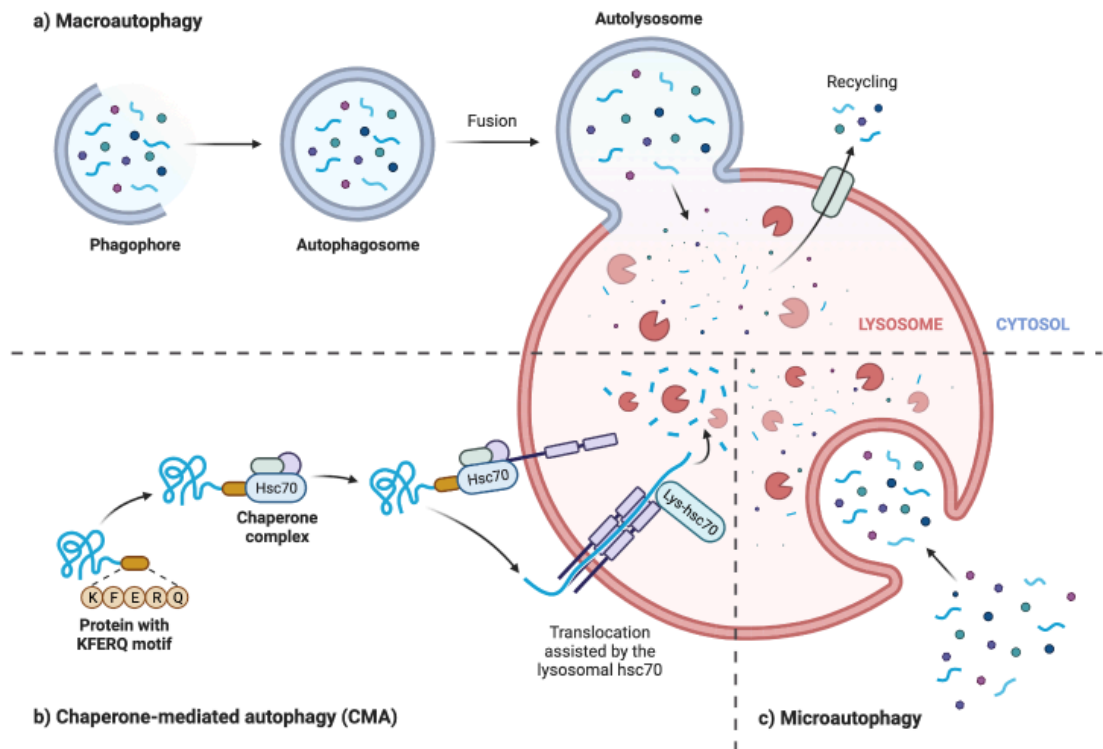


Figure 1.8: Schematic of the three defined types of autophagy. (a) Macro-autophagy, (b) Chaperone-mediated autophagy and (c) Micro-autophagy. In macro-autophagy the autophagosome fuses with the lysosome for the degradation of cytoplasmic cargo. In chaperone-mediated autophagy, a chaperone protein (Hsc70) enables the translocation of proteins across the lysosomal membrane for the degradation of cytoplasmic cargo. Micro-autophagy requires the invagination of the lysosomal membrane for the degradation of cytoplasmic cargo (From BioRender.com).

Autophagy has been found to play an important role in the prevention of tumour development but also tumour progression (Qu et al., 2003; Rosenfeldt & Ryan, 2011). The link between autophagy and cancer is through the *BECLIN-1* gene, which has been found to be monoallelically deleted in 40-75% of breast, ovarian and prostate cancer cases (Russell et al., 1990; Saito et al., 1993; Gao et al., 1995; Qu et al., 2003). Koneri et al., 2007 transfected colon cancer cells with low expression of *BECN1* with the *BECN1* gene to show an inhibition in cancer growth.

The ULK1 (unc-51-like kinase 1) complex is responsible for the initiation of autophagy and is regulated by starvation conditions resulting in ULK1 dephosphorylation and activation by the inhibition of the mechanistic target of rapamycin kinase complex 1 (mTORC1) or through the activation of the energy sensor AMP-activated protein kinase (AMPK, Lane et al., 2017). The ULK1

complex has been shown to form punctate structures close to the endoplasmic reticulum whilst cells are under amino acid starvation (Lane et al., 2017). When amino acids are present mTORC1 becomes activated and thus inhibits autophagy through the phosphorylation of ULK1 at Ser757 (Kim et al., 2011). The deprivation of amino acids results in the deactivation of mTORC1 further resulting in the dephosphorylation of ULK1 and thus the activation of autophagy. mTORC1 also activates downstream effectors such as ribosomal protein S6 kinase (S6K) and the eukaryotic translation initiation factor 4E-binding protein (4E-BP), which contribute towards cell growth and proliferation through the synthesis of proteins, lipids, and nucleotides (Kim et al., 2011; Jossé et al., 2016).

The ULK1 complex is composed of ULK1, autophagy-related protein 13 (ATG13), focal adhesion kinase family interacting protein of 200 kDa (FIP200) and ATG101 (Lane et al., 2017). The ULK1 complex acts upstream of PI3K, consisting of the vacuolar protein sorting-associated protein 34 (VPS34), BECLIN-1, VPS15 and ATG14 (Stjepanovic et al., 2017). The PI3K complex is responsible for the formation and expansion of the phagosome through the activation of WD repeat domain phosphoinositide-interacting protein 2 (WIPI2), which is necessary for the recruitment of the phagophore assembly sites the ATG12-ATG5-ATG16 complex, which is responsible for the elongation of the phagophore membrane; achieved through asymmetric presence of LC3B-II (Polson et al., 2010). Macro-autophagy is initiated by an isolation membrane (also known as a phagophore), which forms a cup-shape to engulf intra-cellular cargo. The phagophore continues to expand until it forms a double-membraned autophagosome, which continues to mature and subsequently fuses with lysosomes to generate autolysosomes. Lysosomal acid proteases degrade the internal cargo, from which amino acids and other useful by-products are exported into the cytoplasm where they can be utilised (Glick et al., 2010; Lane et al., 2013, **Figure 1.9**).

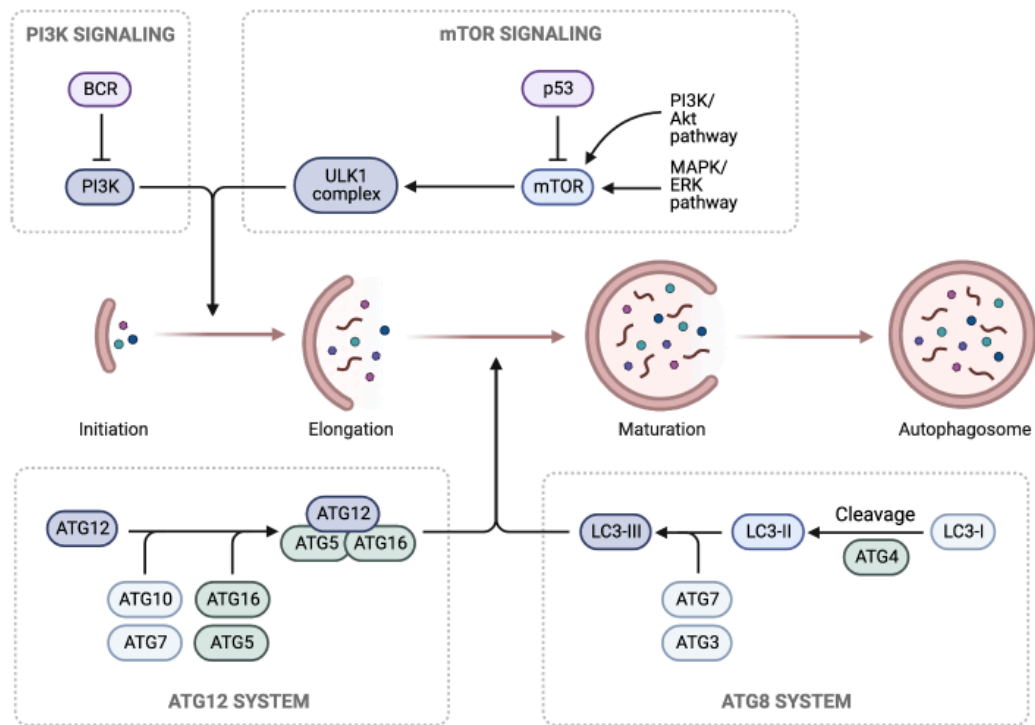


Figure 1.9: Schematic of the macro-autophagy pathway which is important in cancer regulation. The isolation membrane is triggered and continues to expand to form an autophagosome. The autophagosome is responsible for engulfing target cargos such as dead organelles, which can be recycled. Once the membrane has fused together the autophagosome fuses with lysosome to form an autolysosome, which is essential for the degradation and recycling of internal cargo (From BioRender.com).

There are two distinct (functionally and structurally) protein complexes of mTORC; mTORC1 and mTORC2 (Kim et al., 2017). The core components of mTORC1 are mTOR, regulatory-associated protein of mammalian target of rapamycin (Raptor) and mammalian lethal with sec-13 protein 8 (mLST8). mTORC1 activity is controlled by the small GTPase Ras-homologue enriched in brain (RHEB; Yang et al., 2013; Kim et al., 2017). Tuberous sclerosis complex (TSC) is a complex that causes the formation of benign tumours within vital organs caused by mutations in *TSC1* (hamartin) and *TSC2* (Tuberin) genes. These tumours express continued activation of mTORC1 (Tee et al., 2003; Parkhitko et al., 2011). TSC2 is primarily associated with the activation of the small GTPase RHEB; which is required for the activation of mTORC1. The major contributors to the activation of mTORC1 are leucine, glutamine, and arginine (Nicklin et al., 2009).

The activation of AMPK is brought about by low levels of ATP. The activation of AMPK results in the inactivation of mTORC1 through the phosphorylation of raptor (Rabinowitz & White, 2010). AMPK has also been shown to activate mTORC1 through the activation of TSC2 and through the direct phosphorylation of raptor. AMPK also activates autophagy through the direct phosphorylation of ULK1 at a number of residues: Ser317, Ser555 and Ser757 (Bach et al., 2011; Tian et al., 2015).

Recent studies have found that autophagy only restores a limited supply of amino acids. Therefore, other mechanisms must be in place to restore amino acid abundance, such as the release of glutamine. Under certain conditions autophagy is responsible for guiding cells towards ferroptotic cell death (Li et al., 2020). Studies have shown that the PI3K/AKT pathway activates the expression of *NRF2*. The activation of *NRF2* increases the expression of *GCL* and *GSS*, enabling the production of GSH (Wild et al., 1999). The activation of *NRF2* further maintains GSH redox homeostasis through the conversion of GSSG into reduced GSH, catalysed by glutathione reductase (Wild et al., 1999).

1.11 Apoptosis

First described in the 1970s, apoptosis is derived from the Greek meaning 'dropping off', this form of programmed cell death is highly selective and essential within physiological and pathological conditions (Kerr et al., 1972). Excessive apoptosis has been found to induce a number of diseases, such as Parkinson's, Alzheimer's and spinal muscular atrophy (Erekat, 2018). Whereas deficient apoptosis can result in autoimmune diseases and cancer (DNA mutations in p53 and Bcl-2 (B-cell lymphoma 2)). During cancer treatment, chemotherapy results in DNA damage, which can further result in cell death through apoptosis via a p53-dependent pathway (Elmore, 2007). The initiation of apoptosis is dependent on the activation of caspases, a group of cysteine proteases. Caspases can be activated through three pathways;

intrinsic (mitochondrial), extrinsic (death receptor) and the less well-known pathway, intrinsic (endoplasmic reticulum; Elmore, 2007).

1.11.1 Extrinsic Pathway

The extrinsic pathway (**Figure 1.10**) is mediated by death receptors, which include tumour necrosis factor (TNF) receptors, the TNF-related apoptosis-inducing ligand (TRAIL) and fatty acid synthetase ligand (FASL; CD95) receptors. The extrinsic pathway becomes activated when a death ligand binds to one of the death receptors from which intracellular death domains stimulate adaptor proteins, including; TNF receptor-associated death domain (TRADD), Fas-associated death domain (FADD), which associates with procaspase-8 or procaspase-10 resulting in a death-inducing signalling complex (DISC) thus further resulting in the autocatalytic activation of procaspase-8 or -10 (Salvesen, 1999; Czerski & Nunez, 2004; Rampal et al., 2012).

The autocatalytic activation of these procaspases is achieved through aggregation and cleavage of the subunits, which produces caspases capable of transmitting the death signal to the effector executioner caspases within the cytoplasm. Consequently, there is a cascade of activated cytoplasmic caspases-3/6/7 resulting in apoptotic cell death (Czerski & Nunez, 2004). Previous studies have found that the activation of the caspase-3 or -7 is sufficient for the induction of apoptosis (Gray et al., 2010). The procaspases-8 or -10 may otherwise induce apoptosis through the activation of the intrinsic pathway.

1.11.2 Intrinsic Pathway

The intrinsic pathway (**Figure 1.10**) is initiated by internal stimuli, including genetic damage, hypoxia, and oxidative stress, which results in the release of apoptotic mediators such as cytochrome-c (Luo et al., 1998). DNA damage initiates a death signal that results in the transcription of pro-apoptotic BH3-

only proteins. These proteins enable the interaction of pro-apoptotic BCL-2 proteins; BAX and BAK, which are responsible for mediating the induction of apoptosis (Rampal et al., 2012). BAX and BAK aggregate to form pores within the outer mitochondrial membrane, these pores enable the release of cytochrome-c from the inner mitochondrial space. Within the cytoplasm of the cell, cytochrome-c interacts with apoptotic protease-activating factor-1 (APAF-1) facilitating the formation of apoptosomes (Rampal et al., 2012). These structures recruit and activate procaspase 9 through proteolytic cleavage to initiate a caspase cascade, resulting in apoptotic cell death.

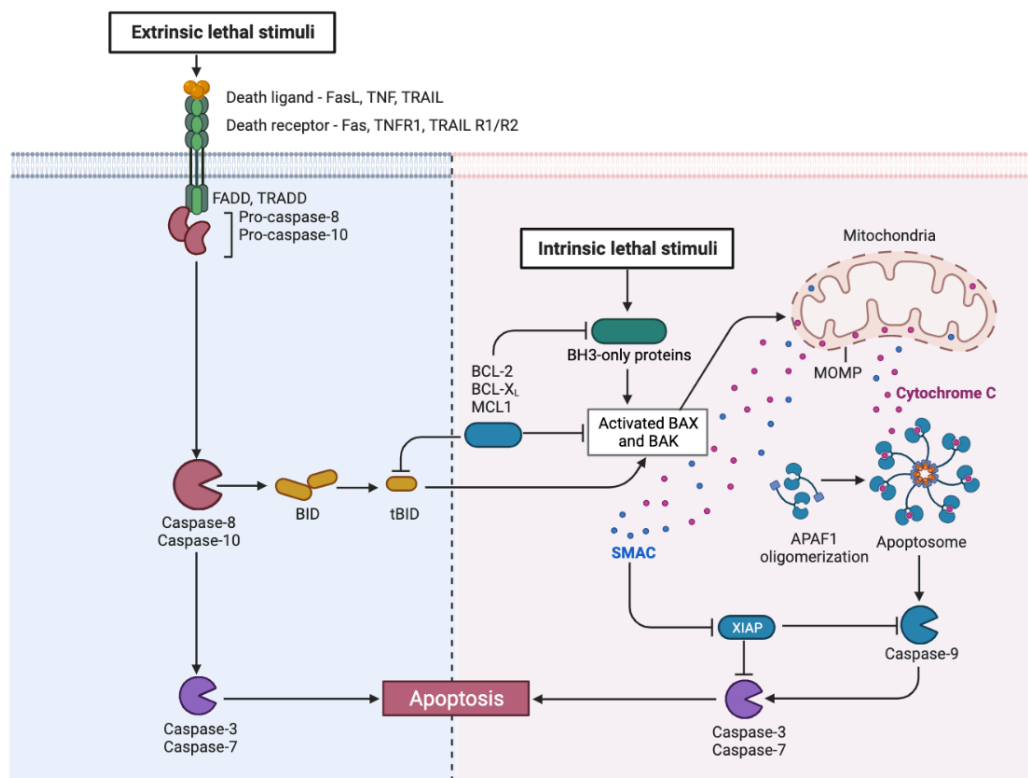


Figure 1.10: Schematic of the extrinsic and intrinsic pathways of apoptosis. The extrinsic pathway is initiated by the binding of transmembrane death receptors with death ligands. Bound to the death receptor is an adaptor molecule that contains a death domain (DD) and a death effector domain (DED). Further found to DED are pro-caspase 8. The combination of these bound molecules results in the formation of the death inducing signalling complex (DISC). Once DISC is formed, caspase 8 is autocatalytically activated and subsequently transmits the death signal to effector caspases, which induce apoptosis. The intrinsic pathways is initiated by stress or other stimuli which cause the release of cytochrome-c from the inner mitochondrial space. Cytochrome-c within the cytoplasm results in the activation of caspase-9 and subsequently transmits the death signal to effector caspases, which induce apoptosis. Abbreviations: FasL, fatty acid synthetase ligand; TNF, tumour necrosis factor; TRAIL, TNF related apoptosis inducing ligand; TNFR1, tumour necrosis factor receptor 1; FADD, Fas-associated death domain protein; TRADD, TNF receptor-associated death domain protein (From BioRender.com).

1.12 Cancer Therapy Resistance

Cancer patients undergo a number of procedures in order to eradicate tumours, such as; surgery, radiotherapy and chemotherapy. Although cancer patients are highly responsive to initial treatment, acquired resistance leads to a relapse in the disease (Cancer Research UK, 2020). Therapeutic resistance is one of the hallmarks of cancer (Hanahan & Weinberg, 2011). The plasticity of cancer cell metabolism impedes on the progress of chemotherapy treatment, therefore new targets are required that take advantage of cancer metabolic vulnerabilities.

The tumour microenvironment (TME) provides resources in order to promote tumour growth and metastasis (Hanahan & Weinberg, 2011). Therefore, the cross-talk between the TME and tumour cells can contribute to therapy resistance. It has been determined that cell-adhesive interactions activate alternative survival pathways in order to evade cytotoxic effects of chemotherapy and radiotherapy (Park et al., 2008; Schwartz et al., 2008; Huang et al., 2011). Intra-tumour heterogeneity and phenotypic differences between primary and metastasised tumours requires the development of personalised cancer therapy.

1.13 Nanomedicine

Nanoparticles are at the forefront of nanotechnology; their size and potential applications make them indispensable. A nanoparticle based delivery system provides an opportunity to overcome the limitations associated with traditional drug therapies (Yao et al., 2020). Nanoparticles can be coated in different moieties and also provide the ability to precisely target the tumour site, therefore, taking advantage of these properties allows a personalised form of therapy (Shah & Dobrovolskaia, 2018).

The size of nanoparticles can range from 1 to 100 nm (Nie, 2010), with some containing an iron oxide core, which may be magnetite (Fe_3O_4), hematite (α -

Fe₂O₃) or maghemite (γ -Fe₂O₃; Couto et al., 2015). The use of iron oxide nanoparticles is encouraging due to the essentiality of iron's role in diverse biological systems.

Nanoparticles have been used in combination with traditional drug therapies with success *in vivo*. Nanoparticle albumin-bound paclitaxel improved the efficacy and tolerability by targeted drug delivery in metastatic breast cancer (Cortes & Saura, 2010). Platinum (Pt(IV)) prodrug-loaded iron oxide nanoparticle (IONP)-filled micelles (mIONP-PL-Pt(IV)) have been shown to suppress melanoma tumour growth (Bilbao-Asensio et al., 2022). Chemotherapy resistance was also overcome in ovarian cancer cells, using cold responsive nanoparticles containing the chemotherapy drug doxorubicin (Wang et al., 2018). Superparamagnetic nanoparticles (SPIONs) loaded with doxorubicin were found to reduce colon solid tumours *in vivo* (Licciardi et al., 2019). Paclitaxel loaded polymeric nanoparticles displayed a greater anti-cancer effect on lung cancer cells in comparison to paclitaxel injection (Hu et al., 2017).

1.14 Aims and Hypotheses

The plasticity of cancer cell metabolism impedes on the progress of chemotherapy treatment, therefore new targets are required that take advantage of cancer metabolic vulnerabilities. The present thesis aimed to explore the induction of ferroptosis, a form of programmed cell death, in therapy-resistant cancer cells.

Ferroptosis can be induced in cancer cells using FINs, therefore in the first experimental chapter of this thesis (*Chapter 3*), we focused on ferroptotic induction in therapy-resistant cancer cell lines. There we tested the hypothesis that therapy-resistant cancer cells are vulnerable to ferroptotic programmed cell death. The first objective was to assay the effect of FINs on cell viability in a panel of cancer cell lines. Cell death was assessed through cell viability and

percentage cell death, using a death stain. The second objective was to determine if ferroptotic induction could be rescued, by assessing cell viability. Immune cells have also been shown to play a role in ferroptotic induction, therefore the third objective was to determine IFN- γ role in ferroptotic induction. The final objective was to determine if any loss in viability is due to ferroptotic induction and not another form of programmed cell death.

In *Chapter 4* we investigated the role of autophagy and apoptosis in ferroptotic induction. The hypothesis of this chapter was that the inhibition of AMPK or mTOR increase ferroptotic cancer cell susceptibility to ferroptotic induction. The first objective was to investigate the role of mTORC1 and mTORC2 in FIN induced ferroptotic cell death, which was assessed through cell viability. The second objective was to investigate the role of AMPK in FIN induced ferroptotic cell death, which was assessed through cell viability. The third objective was to determine the role of glutaminases in ferroptotic induction. This was achieved through the inhibition of GLS1 and GLS2 and cell viability was assessed. The final objective was to determine the link between ferroptosis and autophagy, which was determined by western blotting for death markers.

In *Chapter 5* we explored the use of iron oxide nanoparticles to induce ferroptosis, initially in melanoma cells, which have been shown to metastasise via the lymph in order to evade ferroptotic induction. The hypothesis of this chapter was that therapy-resistant cancer cells are vulnerable to iron oxide nanoparticle-induced ferroptotic programmed cell death. The first objective was to characterise ferroptotic induction in melanoma cancer cells, based off work carried out in *Chapter 3* and *Chapter 4*. The second objective was to determine cancer cell susceptibility to previously established iron oxide nanoparticles, in order to then synthesise an iron oxide nanoparticle with PUFA chains to increase cancer cell susceptibility to ferroptosis. The third objective was to assay the effect of surface modified iron oxide nanoparticles on cell viability and the synergistic effect of combining iron oxide nanoparticles with either Erastin or RSL3. Finally, the fourth objective was to confirm any loss in

viability is due to ferroptotic induction and not another form of programmed cell death.

Chapter 2: Materials and Methods

2.1 Panel of cancer cell lines

Human triple negative breast cancer has been modelled using a mouse tumour-derived cell line 4T1, which were purchased for this thesis from American Type Culture Collection (#CRL-2539; ATCC, Manassas, Virginia, United States; **Figure 2.1**). This model mimics stage IV human breast cancer and has been widely used for research. For experiments, cells were used for a total of 20 passages.

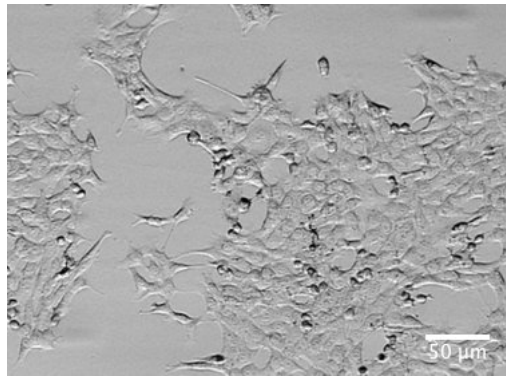


Figure 2.1: Representative phase contrast microscopy image of 4T1 cancer cell populations.

Colon cancer cells, MC-38, were purchased for this thesis from Applied Biological Materials (#T8291; ABM, Richmond, Canada; **Figure 2.2**). The cells were derived from a murine colon adenocarcinoma from a C57BL/6 mouse. For experiments, cells were used for a total of 20 passages.

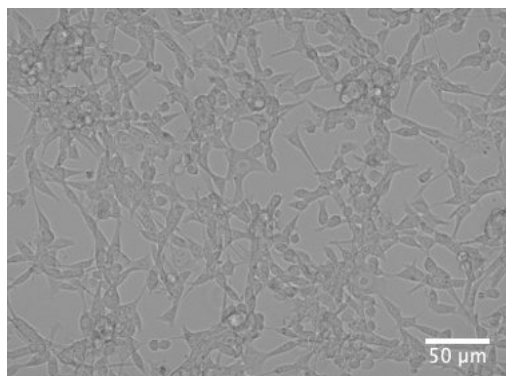


Figure 2.2: Representative phase contract microscopy image of MC38 cancer cell populations.

Non-small cell lung cancer cells, LC-2, were purchased for this thesis from Rikagaku Kenkyujo (#RC0440; RIKEN, Saitama, Japan; **Figure 2.3**). Cells were isolated from a 51 year old woman with moderately differentiated adenocarcinoma within the pleural fluid of the lung. For experiments, cells were used for a total of 20 passages.

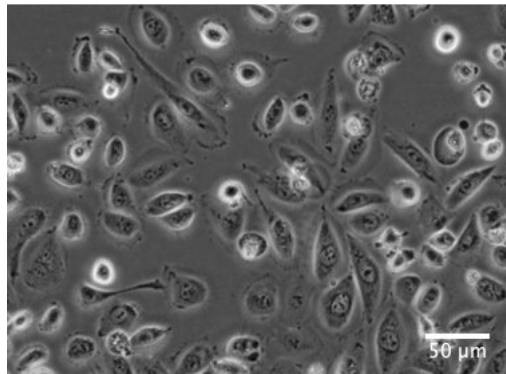


Figure 2.3: Representative phase contract microscopy image of LC2 cancer cell populations.

Skin melanoma cells B16F10 (#CRL-6475, ATCC; **Figure 2.4**) were isolated from the skin tissue of a C57BL/6 mouse. For experiments, cells were used for a total of 20 passages.

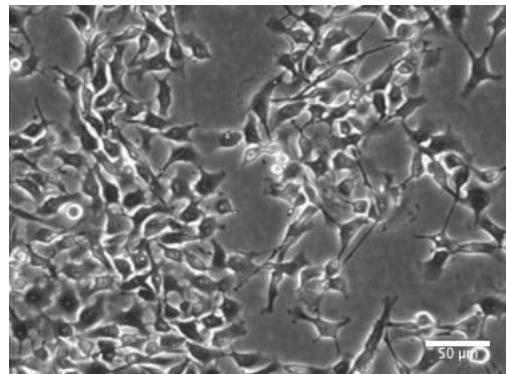


Figure 2.4: Representative phase contract microscopy image of B16F10 cancer cell populations.

Ovarian cancer cells were chosen based on previous proteomic phenotyping data (Coscia et al., 2016). A total of three ovarian cancer cell lines were chosen; PEO1 which were purchased from the European Collection of Authenticated Cell Cultures (#10032308, ECACC, Salisbury, UK; **Figure 2.5 a**); PEO4 (#10032309, ECACC; **Figure 2.5 b**) and OVCAR8 (#CVCL_1629, ATCC; **Figure 2.5 c**). PEO1 cells are derived from a serous adenocarcinoma within peritoneal ascites, this cell line is chemotherapy-sensitive. PEO4 cells were collected from the same patient as PEO1 after the development of clinical chemotherapy-resistance. The patient had previously received cisplatin, 5-fluorouracil and chlorambucil treatment. OVCAR8 were isolated from a 64 year old woman with high grade ovarian serous adenocarcinoma. For experiments, cells were used for a total of 20 passages.

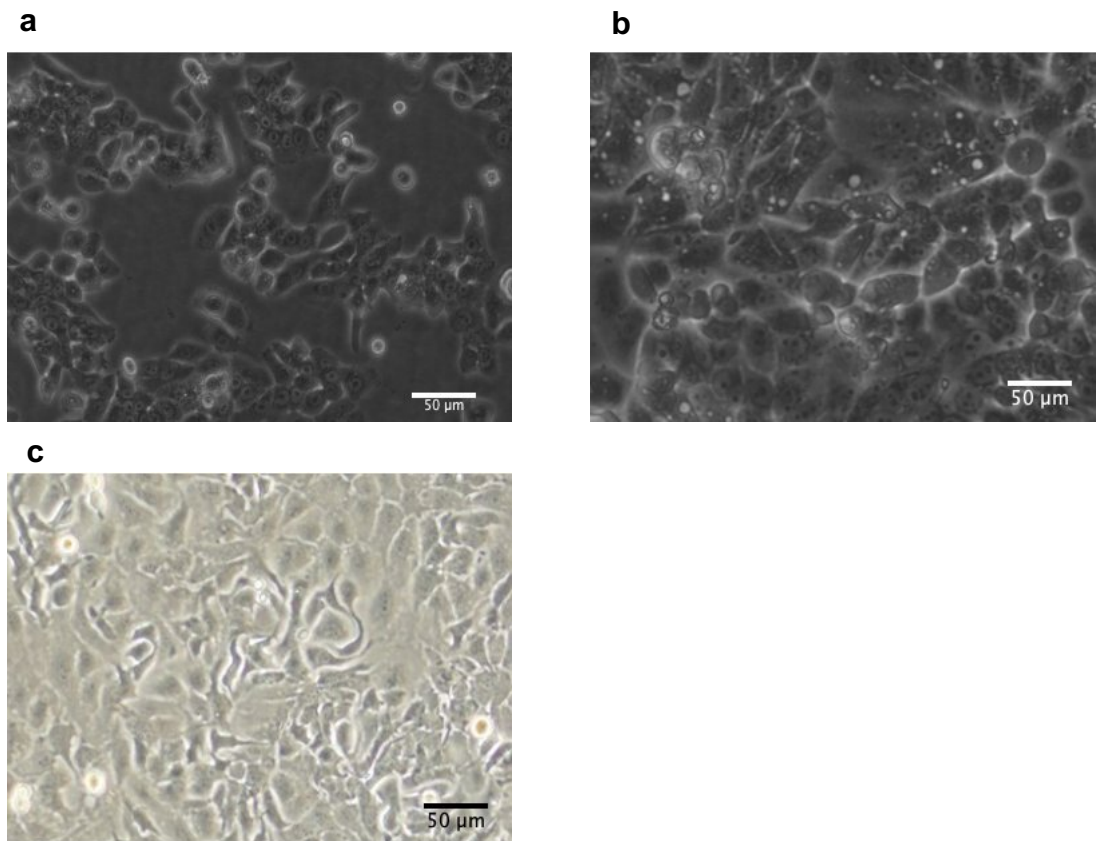


Figure 2.5: Representative phase contrast microscopy of (a) PEO1, (b) PEO4 and (c) OVCAR8 cancer cell populations.

Non-cancerous cells were not used in this study which is critical for understanding any off target effects and toxicity of treatments and therefore is a limitation and should be implemented in future research.

2.1.1 4T1 Cell Culture

4T1 breast cancer cells were routinely cultured in complete medium, comprising of; RPMI-1640 (Thermo Fisher, Cat#31870025), 10% Foetal Bovine Serum (FBS; BIOSERA, Cat#FB-1550/500), Antibiotic Antimycotic solution (ABAM; 100 U/ml penicillin, 0.1 mg/ml streptomycin, 0.25 µg/ml amphotericin B; Sigma, Cat#A5955-100) and L-glutamine (2 mM, Sigma, Cat#G7513-100). Cells were cultured in 75 cm² flasks (Thermo Fisher, Cat#172361) and maintained at 37°C , with 5% CO₂ in air incubator. Cells were mycoplasma tested every 3 months. For experiments, cells were seeded in complete media at a density of 5.0×10^3 cells/well in a Nunc 96-well (Thermo Fisher, Cat#167008) tissue culture plate, unless otherwise stated.

2.1.2 MC-38 Cell Culture

MC-38 colon cancer cells were routinely cultured in complete medium, comprising of; advanced Dulbecco's modified eagle medium (DMEM) (1X, GIBCO, Cat#12491015), 10% FBS, 1% ABAM and 1% L-glutamine. Cells were cultured in 75 cm² flasks and maintained at 37°C , with 5% CO₂ in air incubator. Cells were mycoplasma tested every 3 months. For experiments, cells were seeded in complete media at a density of 5.0×10^3 cells/well in a Nunc 96-well tissue culture plate, unless otherwise stated.

2.1.3 LC-2 Cell Culture

LC-2 lung cancer cells were routinely cultured in complete medium, comprising of 50:50 RPMI 1640:F-12 nutrient mixture (1X, GIBCO, Cat#11765054). Both medias were initially supplemented with 10% FBS, 1% ABAM and RPMI 1640 was further supplemented with 1% L-glutamine. Cells were cultured in 75 cm² flasks and maintained at 37°C , with 5% CO₂ in air incubator. Cells were

mycoplasma tested every 3 months. For experiments, cells were seeded in complete media at a density of 7.5×10^3 cells/well in a Nunc 96-well tissue culture plate, unless otherwise stated.

2.1.4 B16-F10 Cell Culture

B16-F10 skin melanoma cells were routinely cultured in complete medium, comprising of; RPMI-1640, 10% Foetal Bovine Serum, 1 % ABAM and 1% L- glutamine. Cells were cultured in 75 cm² flasks and maintained at 37°C , with 5% CO₂ in air incubator. Cells were mycoplasma tested every 3 months. For experiments, cells were seeded in complete media at a density of 5.0×10^3 cells/well in a Nunc 96-well tissue culture plate, unless otherwise stated.

2.1.5 PEO1 Cell Culture

PEO1 ovarian cancer cells were routinely cultured in complete medium, comprising of; RPMI-1640, 10% Foetal Bovine Serum, 1 % ABAM and 1% L- glutamine. Cells were cultured in 75 cm² flasks and maintained at 37°C , with 5% CO₂ in air incubator. Cells were mycoplasma tested every 3 months. For experiments, cells were seeded in complete media at a density of 7.5×10^3 cells/well in a Nunc 96-well tissue culture plate, unless otherwise stated.

2.1.6 PEO4 Cell Culture

PEO4 ovarian cancer cells were routinely cultured in complete medium, comprising of; RPMI-1640, 10% Foetal Bovine Serum, 1 % ABAM and 1% L- glutamine. Cells were cultured in 75 cm² flasks and maintained at 37°C , with 5% CO₂ in air incubator. Cells were mycoplasma tested every 3 months. For experiments, cells were seeded in complete media at a density of 7.5×10^3 cells/well in a Nunc 96-well tissue culture plate, unless otherwise stated.

2.1.7 OVCAR8 Cell Culture

OVCAR8 ovarian cancer cells were routinely cultured in DMEM (1X; modified with high glucose and L-glutamine and modified without sodium pyruvate and

HEPES, Cat#41965039) supplemented with 10% FBS and 1% ABAM. Cells were cultured in 75 cm² flasks and maintained at 37°C , with 5% CO₂ in air incubator. Cells were mycoplasma tested every 3 months. For experiments, cells were seeded in complete media at a density of 2.5×10^3 cells/well in a Nunc 96-well tissue culture plate, unless otherwise stated.

2.2 Cell Growth and Maintenance

Cell culture manipulations were performed in a Class II laminar flow cabinet using aseptic techniques. Culture media was replenished every 2 to 3 days. Once the cells had reached 80% confluency, the cells were passaged. Cells were washed with phosphate buffered saline (PBS; Gibco, Cat#10010-015) and detached with accutase (Sigma, Cat#A6964-500) for 5 min at 37°C. The accutase was then neutralised with four volumes of pre-warmed complete media.

Subsequently, 100 µl of cell suspension was mixed with 10 ml of diluent (Coulter Isoton II Diluent, Fisher Scientific, Cat#8448011) the number of viable cells per ml was calculated using a Z1 Coulter Particle Counter (Beckman Coulter, High Wycombe, UK). The seeding density was calculated, which was dependent on the condition tested.

2.3 Cell Cryopreservation

Cell stocks were stored in liquid nitrogen. Before freezing, cells must be viable and in an exponential growth phase. Cells were counted following the protocol previously stated in section 2.4. before being centrifuged at 1200 x g for 5 min. The pellet was resuspended in freezing solution (complete media (dependent on the cell line) with 5% dimethyl sulfoxide (DMSO; Sigma, Cat#SHBH9957)), to give a final cell density of 1×10^6 cells per ml. The resuspension was then transferred into a cryovial (ELKAY, Cat#127-T310-200), before being stored at -80°C for at least 24 h prior to liquid nitrogen storage.

2.4 Resurrecting Cells From Liquid Nitrogen

When required, cells were removed from liquid nitrogen and opened in the Class II laminar flow cabinet in order to release pressure before being fast thawed at 37°C. The cells were resuspended in 5 ml of pre-warmed complete media and centrifuged at 600 x g for 5 min. This step was repeated three times to ensure the removal of DMSO (Sigma, Cat#SHBH9957). The pellet was resuspended in pre-warmed complete media in at T25 flask (Corning, Thermo Fisher, Cat#CLS430641U). The cells were then maintained in the incubator at 37°C and 5% CO₂ in air.

2.5 Inducers of Ferroptosis

Erastin (Tocris Bioscience, Cat#5449) and RSL3 (Stratech, Cat#S8155-SEL) were reconstituted in DMSO (Sigma, Cat#SHBH9957) to give a final stock concentration of 10 mM. DMSO was included in all experiments as a vehicle control.

2.6 Inhibitors of Ferroptosis

Liproxstatin-1 (Stratech, Cat#S7699- SEL) was reconstituted in DMSO (Sigma, Cat#SHBH9957) to give a final stock concentration of 10 mM. DMSO was included in all experiments as a vehicle control.

2.7 MTT ((3-(4, 5-dimethylthiazol-2-yl)-2, 5- diphenyltetrazolium bromide)) assay

MTT assays were undertaken in order to assess cell viability after ferroptotic induction. The assay measured the reduction of MTT into an insoluble formazan crystal by the mitochondria of viable cells (Mosmann, 1983). At the end of each experiment, cells were incubated for a further 2 h in the dark with 50 µl of 10 mg/ml MTT (Sigma, Cat#M2128) diluted in complete media. Formazan crystals that formed were dissolved in 100 µl of DMSO (Sigma, Cat#SHBH9957) and incubated for 15 min in the dark at room temperature.

The absorbance was measured at 570 nm using the microplate spectrophotometer system (POLARstar omega, BMG labtech, Offenburg, Germany). Each experimental condition was measured as an average of four technical replicates, which each experiment being performed in triplicate in separate passaged cells.

2.8 Western Blot Analysis

2.8.1 Protein extraction

At the end of the experiment, media was removed and discarded. Cells were then washed with 1ml PBS before adding 100 µl of ice cold lysis buffer. The lysis buffer was made up of 1X RIPA buffer (Sigma Cat#20-188), 0.1% Protease inhibitor cocktail (PIC; Sigma, Cat#P1860), 0.1% phosphatase inhibitor cocktail 2 (PIC2; Sigma, Cat#P5726) and 0.1% phosphatase inhibitor cocktail 3 (PIC3; Sigma, Cat#P0044). Cells were left to lyse on ice for 5 mins before being scraped off the base of the plate. The lysate was then passed through a 20 gauge needle several times before being transferred to 1.5 ml tubes.

2.8.2 Protein Assay

The protein concentration of the samples was determined using the detergent compatible (DC) protein assay. Standards were prepared in duplicate using bovine serum albumin (BSA; Tocris, Cat#5217) dissolved in PBS at concentrations from 0.5 – 5.5 mg/ml and water was used as a blank.

The samples were also plated in duplicate into a 96-well plate at a volume of 5 µl. To each well 25 µl of solution X (2ml reagent A (alkaline copper tartrate solution; Bio-Rad, Cat#5000113) to 40 µl reagent S (surfactant solution; Bio-Rad, Cat#5000115)) was added. To which 200 µl of reagent B (dilute folin reagent, Bio-Rad, Cat#5000114) was added and left to incubate for 10 min at room temperature to enable full colour change. The absorbance was then

measured at 570 nm on a microplate spectrophotometer system (POLARstar omega, BMG labtech, Offenburg, Germany).

A standard curve with lineal regression was deduced from the duplicate standards using Mars analysis. From the curve the protein concentration of each sample could be extrapolated. 10 µg of sample protein was mixed with equal volume of 2x Laemmli buffer (Sigma, Cat#S3401) and analysed by 10% sodium dodecyl sulphate-polyacrylamide gel electrophoresis (SDS-PAGE) unless otherwise stated. Polyacrylamide gels were made in-house as shown in **table 2**.

Table 2: Polyacrylamide gel recipe for one gel

REAGENT	7.5%	10%	12%	15%	Stacking gel
WATER	5 ml	4.2 ml	3.5 ml	2.5 ml	1.75 ml
4X TRIS & SDS (separating buffer)	2.5 ml	2.5 ml	2.5 ml	2.5 ml	0.75 ml (stacking buffer)
30% ACRYLAMIDE	2.5 ml	3.3 ml	4 ml	5 ml	0.5 ml
10% APS	100 µl	100 µl	100 µl	100 µl	50 µl
TEMED	10 µl	10 µl	10 µl	10 µl	3 µl

2.8.3 SDS Page

The protein: Laemmli buffer samples were heated on a thermal cycle for 5 min at 95°C before being loaded onto a 10% SDS-PAGE gel (unless otherwise stated) alongside 5 µl of dual colour ladder (Bio-rad, Cat#1610374) and 10 µl of biotinylated protein ladder (Cell signalling, Cat#7727S) and separated using electrophoresis at 120 V for 60 min. The gel was ran in 1X running buffer (100 ml 10X running buffer (25 mM Tris, 190 mM glycine and 0.1% SDS) with 900 ml ddH₂O).

The SDS-PAGE gel was electro-transferred using the trans-blot turbo system (Bio-Rad) onto polyvinylidene difluoride (PVDF) membrane (Cat#10600023), which was initially activated in 100% methanol for 30 s. The gel, membrane and filter paper were then equilibrated in 1X transfer buffer (100 ml 10X

transfer buffer (25 mM Tris and 190 mM glycine with 20% methanol and 900 ml ddH₂O) for 15 min. The gel was then transferred onto the membrane for 30 min at 25 V.

Membranes were blocked with 5% non-fat dried milk in TBS-tween (100 ml 10X TBS (20 mM Tris, 150 mM NaCl and pH 7.6-8.0) 0.1% Tween 20 and 900 ml ddH₂O) for 1 h at room temperature under agitation. The membranes were then incubated with the relevant primary antibody (**table 3**) overnight at 4°C under agitation. Afterwards, membranes were washed 4 × 5 min with TBS-Tween and incubated with HRP-linked species-specific secondary antibodies in 5% milk in TBS-tween for 1 h at room temperature under agitation. Membranes were washed 4 × 5 min with TBS-Tween before imaging. The membranes were then imaged using BIO-RAD CHEMIDOC apparatus, after exposure to low intensity ECL solution (Bio-Rad, Cat#1705061).

Two house-keeping proteins were chosen in this study; β -actin and Lamin-B1. Both house-keeping proteins were chosen based on their molecular size. Other housekeeping proteins, such as vinculin, were initially considered due to their higher molecular weight. However, the use of vinculin was hindered by issues with the antibody, impacting its suitability for the study. VDAC1, another potential candidate, was excluded from consideration because ferroptosis interferes with mitochondrial function. Furthermore, β -tubulin was deemed unsuitable for this investigation due to its molecular weight being too close to that of the proteins of interest. This close proximity could result in challenges in accurately distinguishing bands on the gel.

Table 3: List of antibodies used for western blots

Antibody target	Species raised in/clonality	Predicted molecular weight (kDa)	Supplier	Product code	RRID
Primary Antibodies					
AMPK α	Rabbit Monoclonal	62	Cell Signalling	5831	AB_331250
p-AMPK α (Thr172)	Rabbit Monoclonal	62	Cell Signalling	2535	AB_10622186
Beclin-1	Rabbit Monoclonal	52	ABCAM	ab21049 8	AB_2810879
Beta-actin	Rabbit Monoclonal	42	ABCAM	ab11577 7	AB_10899528
GPX4	Rabbit Monoclonal	22	ABCAM	ab12506 6	AB_10973901
LC3B	Rabbit Polyclonal	14/16	Cell Signalling	2775	AB_915950
P70S6K	Rabbit Polyclonal	70/85	Cell Signalling	9202	AB_331676
p-P70S6K (The421/Ser424)	Rabbit Polyclonal	70/85	Cell Signalling	9234	AB_2269803
p-ULK1-Ser555	Rabbit Polyclonal	112	ABCAM	ab22953 7	Unavailable
p-ULK1-Ser757	Rabbit Monoclonal	140/150	Cell Signalling	14202	AB_2665508
ULK1	Rabbit Monoclonal	150	Cell Signalling	8054	AB_11178668
Lamin B1	Rabbit Monoclonal	68	Cell Signalling	9087	AB_10896336
Secondary Antibodies					
Rabbit linked	IgG-HRP Goat Polyclonal	N/A	Cell Signalling	7074	AB_2099233

2.8.4 Image J

Immunoblot images were analysed using Fiji ImageJ 2.0 (Schindelin et al., 2012). The target protein expression was standardised to β -actin, phosphorylated proteins were normalized to their equivalent total protein.

2.9 Flow cytometric analysis

Flow cytometry was undertaken for cell viability, intracellular staining and lipid peroxidation.

2.9.1 Cell viability by Deep Red Anthraquinone 7 – DRAQ7

At the end of the experiment, cells were washed with 1 ml PBS (Gibco, Cat#10010-015), and detached by 100 μ l of Accutase (Sigma, Cat#A6964) before being centrifuged at 500 xg for 5 min. The supernatant was discarded, and the cells were resuspended in 100 μ l of fluorescence-activated cell sorting (FACS) buffer (PBS with 0.2% BSA (Tocris, Cat#5217), 0.05% Sodium azide (Sigma, Cat#S2002)). Then 5 μ l of a 1 in 15 dilution of DRAQ7 (Biostatus, Cat#DR71000) was added to each sample before incubation for 15 min at room temperature in the dark. Then, 500 μ l of FACS buffer was added to each sample before being centrifuged at 500 xg for 5 min. The supernatant was discarded and the cell were resuspended in 100 μ l FACS buffer. Using a NovoCyte Flow Cytometer (ACEA Biosciences), cell populations were gated based on the forward and side scatter parameters and the non-single events excluded based on forward area and height scatter parameters (FlowJo, LCC software).

2.9.2 Intracellular Staining

At the end of the experiment, cells were washed with 1 ml PBS (Gibco, Cat#10010-015), and detached by 100 μ l of Accutase (Sigma, Cat#A6964) before being centrifuged at 290 xg for 5 min. Cells were then fixed with 100 μ l of 4% paraformaldehyde solution for 20 min at 4°C and then washed two times in staining buffer PBS (Gibco, Cat#10010-015) and 1% FBS (BIOSERA,

Cat#FB-1550/500)) before centrifugation at 350 xg for 5 min. Cells were then resuspended in 1 ml perm/wash (BD Biosciences, Cat#555028) for 15 min at room temperature, before centrifugation at 350 xg for 5 min. Then, 100 µl of a 1/400 dilution of primary antibody/staining buffer (GPX4; ABCAM, Cat#ab125066) was added to the cells for 1 h at room temperature. Cells were centrifuged at 350 xg for 5 min and washed in staining buffer before 100 µl of a 1/500 dilution of secondary antibody/staining buffer (Anti-rabbit IgG Fab2 Alexa Fluor® 488 molecular probes (Cell signaling technology, Cat#4412S) was added for 30 min at room temperature in the dark. Cells were centrifuged at 350 xg for 5 min and washed in staining buffer before resuspension in 200 µl FACS buffer. Using a NovoCyte Flow Cytometer (ACEA Biosciences), cell populations were gated based on the forward and side scatter parameters and the non-single events excluded based on forward area and height scatter parameters (FlowJo, LCC software).

2.9.3 Lipid peroxidation

For a positive control, cells were incubated with 1 ml cumene hydroperoxide (100 µM; Sigma-Aldrich, Cat#247502) for 2 h at 37°C, 5% CO₂ in air. Cells were then treated with Liperfluo (5 µM; Europa Bioproducts, Cat#DJL248) or DMSO (1%; Sigma, Cat#SHBH9957) vehicle control for 15 min at 37°C, 5% CO₂ in air. Cells were then washed with 1 ml PBS (Gibco, Cat#10010-015), and detached by 100 µl of Accutase (Sigma, Cat#A6964) prior to the addition of 2 ml FACS buffer. Cells were centrifuged at 515 xg, at 4°C, for 7 min before being re-suspended in 200 µl FACS buffer. Using a NovoCyte Flow Cytometer (ACEA Biosciences), cell populations were gated based on the forward and side scatter parameters and the non-single events left out based on forward area and height scatter parameters (FlowJo, LCC software). Differentiation between cells based on lipid peroxidation-positive fluorescent staining using Liperfluo® (530 nm laser).

2.10 Experimental Design and Statistical Analysis

GraphPad prism 9.5.0 (GraphPad Software, San Diego, California, USA) was used for statistical analysis and graph preparation. Each experiment was performed in triplicate, with each replicate using cells from different passage numbers and undertaken on separate days. The mean of each replicate was used for statistical analysis, the data represented as mean +SEM (standard error of the mean). Data was initially analysed for normality using the Shapiro-Wilks test, data was assumed to be normally distributed when $P > 0.05$. Normally distributed data were subjected to a one-way or two-way analysis of variance (ANOVA) followed by a Brown-Forsythe or Dunnett's or Bonferroni post-hoc test; comparing the treatment in relation to the vehicle for $n \Rightarrow 3$. Significance was assumed when $P < 0.05$, which significance presented as follows; * $P < 0.05$, ** $P < 0.01$, *** $P < 0.001$ and **** $P < 0.0001$.

Chapter 3: Characterising ferroptosis in a panel of cancer cell lines

3.1 Introduction

Ferroptosis is a form of non-apoptotic cell death, which is dependent on iron and characterised by the accumulation of lipid peroxides (Stockwell et al., 2017). The induction of ferroptosis could be exploited as a novel therapeutic target in a variety of cancers. Cancer cells are able to evade ferroptosis through the upregulation of GPX4, iron metabolism and lipid metabolism (Chen et al., 2021; Zhang et al., 2022). Other mechanisms of evasion are through the mevalonate pathway (MVA) and the ferroptosis suppressor protein 1 (FSP1; Galadari et al., 2017; Doll et al., 2019; **Figure 3.1**). The expression of FSP1 complements the loss of GPX4 and therefore can be recognised as a glutathione-independent ferroptosis suppressor (Doll et al., 2019). The suppression of ferroptosis by FSP1 is mediated by ubiquinone (coenzyme Q₁₀) produced by farnesyl pyrophosphate (FPP) the final product from the MVA pathway (Galadari *et al.*, 2017). FSP1 inhibits ferroptotic induction by preventing the production of lipid peroxides; FSP1 converts ubiquinone to its oxidised form ubiquinol (a lipophilic radical-trapping antioxidant) in order to prevent lipid peroxidation (Santoro, 2020; Doll et al., 2019; Bersuker et al., 2019).

A number of reagents, drugs and cytokines have been found to play a role in ferroptosis, including Erastin, RSL3 and interferon gamma (IFN γ ; Chen et al., 2021). Erastin initiates the extrinsic pathway of ferroptosis, through the inhibition of system X_C⁻, which is composed of two subunits; a light-chain subunit SLC7A11 and a heavy-chain subunit SLC3A2 (Koppular et al., 2018). Erastin irreversibly binds to SLC7A11, resulting in the cells' inability to import cysteine and therefore the depletion of GSH (Dixon et al., 2012). Subsequently the inhibition of SLC7A11 results in the induction of ferroptosis. Whereas, RSL3 initiates the intrinsic pathway of ferroptosis, through the direct inhibition of GPX4. The small molecule inhibitor covalently binds to the selenocysteine containing active site of GPX4. Consequently, the enzyme is unable to use GSH to eliminate lipid peroxides and therefore results in ferroptotic cell death (Yang et al., 2014: **Figure 3.1**).

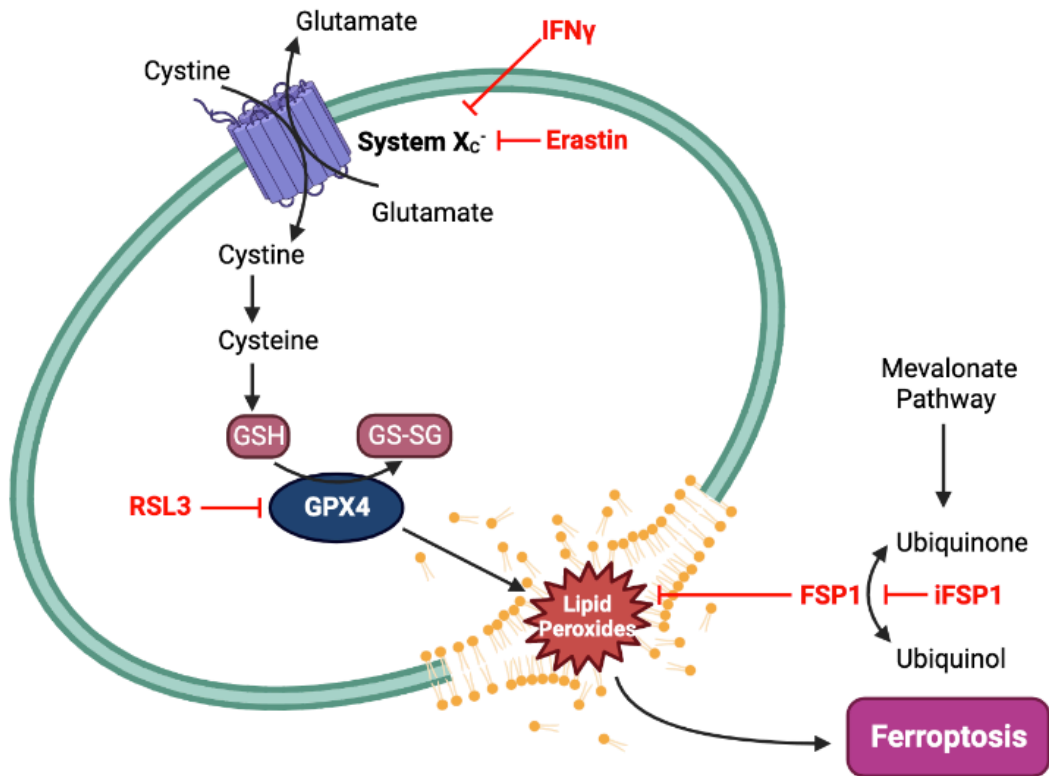


Figure 3.1: Schematic overview of the induction of ferroptosis in cancer cells after treatment with known inducers. Cancer cells are able to evade ferroptosis through the upregulation of GPX4. System X_C⁻ imports cystine and exports glutamate, which is essential for the production of glutathione (GSH). GPX4 and GSH catalyse the reduction of lipid peroxides to lipid alcohols, enabling cell survival. Ferroptosis can be induced in cancer cells by Erastin, RSL3, IFN γ and iFSP1. Erastin binds to system X_C⁻ to indirectly inhibit GPX4, whereas RSL3 directly binds to GPX4. IFN γ has been found to inhibit to the expression of the two system X_C⁻ subunits. FSP1 blocks the production of lipid peroxides by using ubiquinone, the final product of the mevalonate pathway (Created in BioRender.com).

Cancer cells display metabolic dysregulation and therefore undergo metabolic reprogramming in order to survive and proliferate. Tumour cells increase their uptake of glucose and consequently produce more lactate, even when oxygen is replete, known as the Warburg effect (Warburg et al., 1927). Undergoing the Warburg effect enables optimal tumour proliferation, due to increased production of ATP and synthesis of fatty acids, proteins and nucleotides (Xing et al., 2015). However, undergoing aerobic glycolysis does not maximise ATP, and is inefficient in comparison to oxidative phosphorylation (OXPHOS) where 34 more ATP molecules are generated from one glucose molecule (Vander Heiden et al., 2009). The increased uptake of glucose by cancer cells results in the local TME becoming hypoglycaemic (Onozuka et al., 2011).

Due to restricted glucose within the TME, glutamine metabolism provides an alternative carbon source to drive the TCA cycle, in order to generate ATP (**Figure 3.2**). The glutaminolysis pathway metabolises glutamine in order to form α -KG; an important metabolic intermediate within the TCA cycle. Therefore, when glucose is restricted, cancer cells become more reliant on glutamine, this is termed glutamine addiction (Eagle, 1995; Wise & Thompson, 2010).

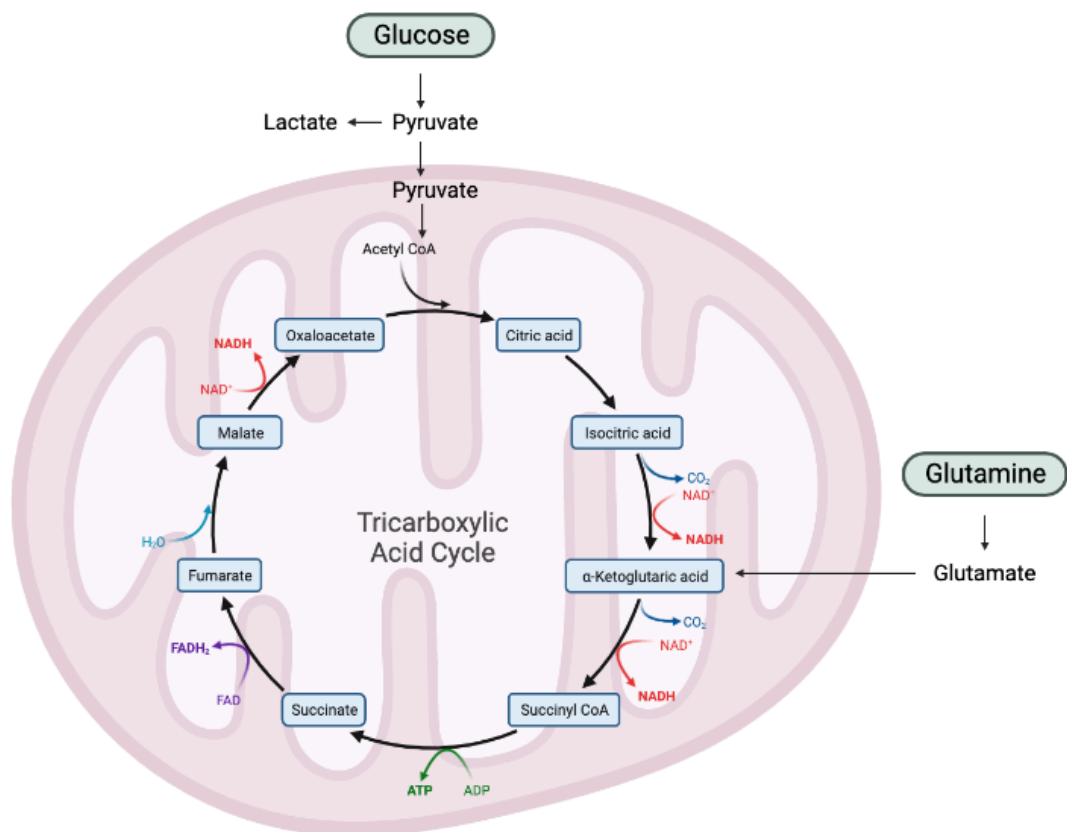


Figure 3.2: Schematic of glucose and glutamine metabolism in cancer cells. Cancer cells increase uptake of glucose to drive glycolysis in order to produce ATP. Under restricted glucose conditions cancer cells utilise glutamine in order to maintain ATP production and therefore proliferation (Adapted from BioRender.com).

Chemotherapy and radiotherapy are currently the main cancer treatments, however the majority of patients relapse, and tumours may become resistant to treatment often through metabolic plasticity (Kurman & Shih, 2010; Desbats et al., 2020). Therefore, new targets are required that take advantage of cancer metabolic vulnerabilities. Immunotherapy is a new treatment method that

reactivates the anti-tumour immune cycle using; immune checkpoint inhibitors, cytokines, tumour-specific vaccines and adoptive cell transfer therapy (Duan et al., 2020; Lin et al., 2021). However, it is currently only 15-25% effective in many different types of advanced cancers (Zhao et al., 2022), including melanoma, NSCLC (Helissey et al., 2016), ovarian cancer (Hamanishi et al., 2015), TNBC (Emens et al., 2015) and colorectal cancer (Le et al., 2015). However, the clinical efficacy of immunotherapies is determined by the 'hotness' or 'coldness' of the tumours, which is determined by the tumour microenvironment. Immune checkpoint inhibitors are only effective against 'hot' tumours due to the high expression of programmed death-ligand 1 (PD-L1), high infiltrating lymphocytes (TILs) and the microsatellite status (MSI-H), Whereas variable and cold tumours have low PD-L1 expression and MSI-L, therefore these tumours must be converted to hot tumours (Wang et al., 2020). Melanoma and lung cancers have high tumour mutation burden (TMB) and are therefore referred to as 'hot tumours' (Alexandrov et al., 2013). Breast, colon and ovarian cancers are referred to as 'cold tumours' (Galon & Bruni, 2019).

Ferroptotic induction in cancer cells has been observed during chemotherapy, radiotherapy and immunotherapy. With a recent study showing that ferroptosis is immunogenic in fibrosarcoma *in vitro* and *in vivo* (Efimova et al., 2020). Therefore, a combination of immunotherapy and ferroptosis could provide a potential strategy to overcome current drug resistance observed in present cancer treatments (Zhao et al., 2021).

Immunotherapies such as immune checkpoint blockade could be an impactful anti-cancer therapy (Wang et al., 2022). Examples of immune checkpoint pathways are, cytotoxic T lymphocyte associated protein 4 (CTLA-4; treatment for patients with advanced melanoma and renal cancer; Cancer Research UK, 2021), programmed death-1 (PD1; treatment for patients with melanoma skin cancer, Hodgkin lymphoma and NSCLC; Cancer Research UK, 2021) and programmed death-ligand 1 (PD-L1; treatment for patients with lung, liver, breast and urinary tract cancers; Wang et al., 2022; Cancer Research UK, 2021). The treatment of metastatic melanoma with a CTLA-4 blocking

antibody, known as ipilimumab was the first successful immunotherapy and approved for treating the disease in 2011 (Robert et al., 2011; Huang & Zappasodi, 2022). Since then, pembrolizumab and nivolumab, PD-1 inhibitors have been approved for metastatic melanoma treatment, but they also show promising results in other solid tumours (Brahmer et al., 2010; Robert et al., 2019; Ascierto et al., 2019). The treatment of metastatic triple negative breast cancer with PD-1 and PD-L1 blocking antibodies, pembrolizumab showed promising results for a first-line therapy (Adams et al., 2019).

In collaboration with Swansea University Chemistry Department, we showed *in vitro* and *in vivo* efficacy with a combination of iron oxide-loaded nanovaccines (IONVs) and an antagonistic anti-PD-L1 antibody. The IONVs were demonstrated to localise to tumour and spleen in an *in vivo* mouse model of melanoma. The IONVs delayed tumour growth; although, all animals eventually developed tumours. Whereas, IONVs in combination with α PD-L1 resulted in 40% of mice being tumour-free 90 days after inoculation with melanoma cancer cells. Furthermore, when mice were rechallenged with melanoma cells they remained tumour-free for 30 days (Ruiz-de-Angulo et al., 2020).

Recent studies have shown that the immune system in conjunction with induction of ferroptosis can prevent tumorigenesis (Wang et al., 2019). Further evidence shows that ferroptosis can be induced to produce a natural tumour suppressive function. Tumour suppressors such as p53, BAP1 and fumarase have been shown to drive ferroptosis under specific conditions, but negative regulators of ferroptosis such as SLC7A11, GPX4 and NRF2 are overexpressed in some tumours to counter this (Wag et al., 2016; Dixon & Stockwell, 2019).

The immune checkpoint blockade works by activating exhausted T cells to drive a natural tumour-selective killing response. A classic subtype of tumour-selective killing T cells are CD8⁺ T cells, which are required for the efficacy of

immunotherapy (Lang et al., 2019). CD8⁺ T cells have been shown to drive ferroptosis in different cancer cells (Wang et al., 2019; **Figure 3.3**).

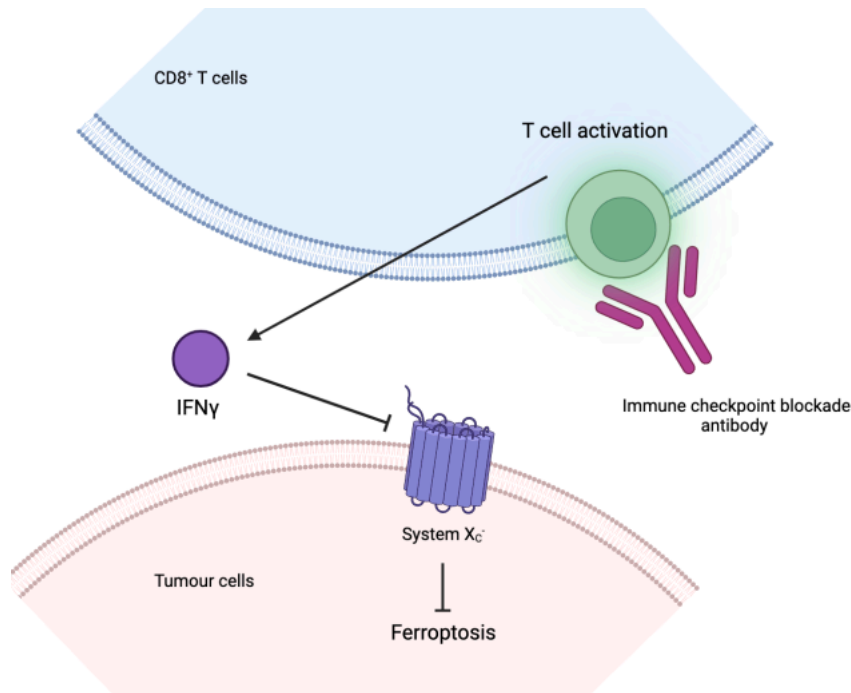


Figure 3.3: Schematic of how CD8⁺ T cells interact with tumour cells to prevent the induction of ferroptosis. The immune checkpoint blockade results in the activation of T cells, which results in the release of IFN γ . IFN γ causes the downregulation of system X_c⁻ and therefore drives ferroptosis in tumour cells (Created in BioRender.com).

Tumour necrosis factor (TNF) and IFN γ are released from cytotoxic T cells. The cytokine IFN γ is responsible for the activation of the Janus kinase (JAK)-signal transducer and activator of transcription 1 (STAT1) pathway, which results in the downregulation of *SLC7A11* and *SLC3A2* and, therefore, induction of ferroptosis (Wang et al., 2019; Lang et al., 2019: **Figure 3.4**). Wang et al., 2019 treated ovarian and melanoma tumours *in vivo* with PD-L1 blockade, which resulted in increased lipid peroxidation and reduced tumour growth. This effect was attenuated after treatment with Liproxstatin-1, a lipid peroxide scavenger. They further treated the tumours with conditioned supernatant from activated CD8⁺ T cells, which also resulted in increased lipid peroxidation. Furthermore, this affect was also attenuated after treatment with anti-IFN γ antibodies but not with anti-TNF antibodies (Wang et al., 2019).

The initiation of the JAK-STAT1 pathway, as a result of IFN γ signalling, induces the upregulation of interferon regulatory factor 1 (*IRF1*). IRF1 represses the expression of *SLC7A11* and *SLC3A2*, the two subunits of system X $_C^-$, thus resulting in ferroptotic cell death. Moreover, IFN γ enhances STAT1 binding to the *SLC7A11* transcription start site (Wang et al., 2019). A study undertaken by Linher-Melvile et al., 2015 found that STAT3 and STAT5 also bind to the promotor region of *SLC7A11*, consequently reducing *SLC7A11* transcription in breast cancer cells (Linher-Melvile 2015). Cancer cell survival and proliferation is dependent on STAT3 and STAT5 activation, with mutations in *STAT3* and *STAT5* resulting in solid tumour formation (Igelmann et al., 2019; **Figure 3.4**).

A recent study by Liao et al., 2022 showed that IFN γ induced ferroptotic cancer cell death is dependent on acyl-coenzyme A (CoA) synthetase long-chain family member 4 (*ACSL4*), not system X $_C^-$. *ACSL4* preferentially catalyses arachidonic acid (AA; a common polyunsaturated fatty acid (PUFA)) to arachidonyl-CoA, which is then esterified into phospholipids (Kagan et al., 2017). Liao et al., 2022 also showed that the expression of *ACSL4* is dependent on the activation of STAT1 by IFN γ . This process resulted in the reprogramming of *ACSL4*-associated-phospholipids by IFN γ , resulting in increased incorporation of AA into C16 and C18 acyl chain-containing phospholipids, resulting in ferroptotic tumour death (Liao et al., 2022; **Figure 3.4**). A common C18 fatty acid is oleic acid (OA), a monounsaturated fatty acid (MUFA) has been shown to inhibit the induction of ferroptosis (Magtanong et al., 2019). Inhibition is achieved through MUFA displacement of PUFAs in membranes (Magtanong et al., 2019). However, Liao et al., 2022 indicated that OA has the potential to induce ferroptosis, when in combination with IFN γ and AA, further indicating alterations in cellular lipid composition may be important in ferroptosis (Liao et al., 2022).

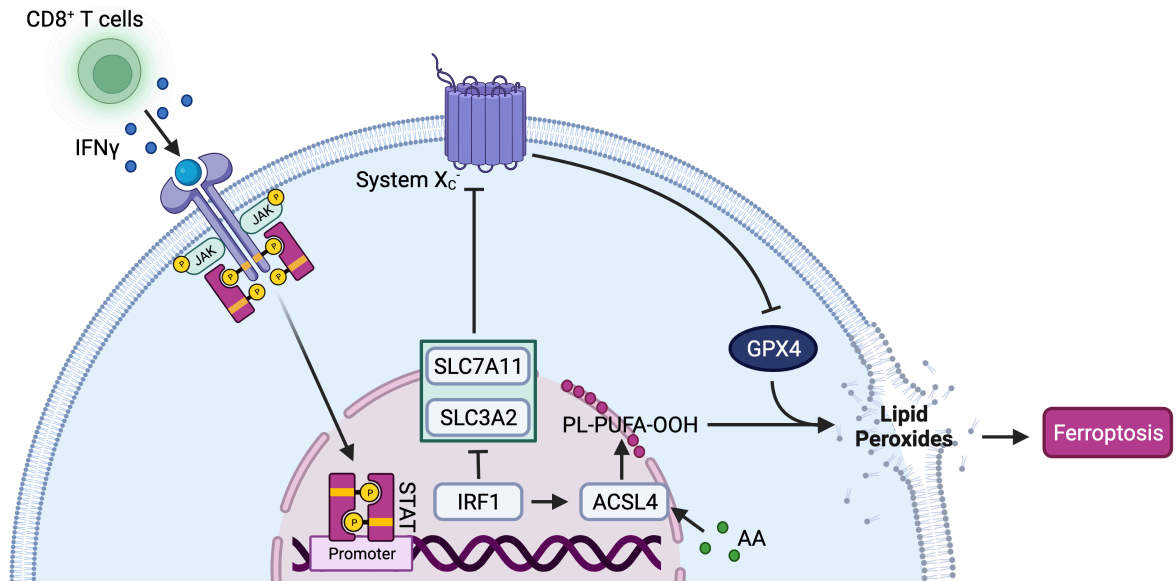


Figure 3.4: Schematic of activated CD8⁺ T Cell IFN γ release resulting in ferroptotic cancer cell death. IFN γ released from activated CD8⁺ T cells results in the activation of the JAK/STAT1 pathway, which consequently activates interferon regulatory factor 1 (IRF1). IRF1 inhibits the expression of SLC7A11 and SLC3A2, resulting in the inhibition of system X_c⁻ and ultimately inducing ferroptotic cancer cell death. IRF1 also binds to the promoter region of acyl-coenzyme A (CoA) synthetase long-chain family member 4 (ACSL4), which ultimately produces arachidonic acid (AA) filled phospholipids, under the influence of IFN γ . The polyunsaturated phospholipids are prone to lipid peroxidation and consequently induce ferroptotic cancer cell death (Created in BioRender.com).

Immunotherapy can also compliment more established cancer therapies. For example, a study undertaken by Lang et al., 2019 demonstrated the importance of immunotherapy in combination with a current cancer treatment, radiotherapy. They showed that CD8⁺ T cells are important for immunotherapy and radiotherapy efficiency, and that they can be used in combination to drive ferroptotic tumour cell death. IFN γ derived from CD8⁺ T cells and radiation resulted in the inhibition of SLC7A11 and increased lipid peroxidation in melanoma, ovarian and fibrosarcoma tumours *in vitro* and *in vivo* (Lang et al., 2019).

3.2 Hypothesis and Aims

Hypothesis: Therapy-resistant cancer cells are vulnerable to ferroptotic programmed cell death.

Aims:

1. To assay the effect of ferroptosis inducers on cell viability in a panel of cancer cell lines.
2. To confirm any loss in viability is due to ferroptotic induction and not another form of programmed cell death.

3.3 Materials and Methods

3.3.1 MTT ((3-(4, 5-dimethylthiazol-2-yl)-2, 5- diphenyltetrazolium bromide)) assay

Cell viability was determined by the MTT assay (Wu et al., 2018). Cells were seeded at the required density, 2.5×10^3 (OVCAR8 ovarian), 5.0×10^3 (4T1 breast and MC-38 colon), 7.5×10^3 (LC-2 lung, PEO1 ovarian and PEO4 ovarian) cells/well in a 96-well plate (Helena Biosciences, Cat#92096) 24 h prior to treatment. Cells were then treated in triplicate with increasing concentrations of Erastin (0, 0.15625, 0.3125, 0.625, 1.25 and 2.5 μM) or RSL3 (0.0390625, 0.078125, 0.15625, 0.3125 and 0.625 μM) diluted in 100 μl of complete media before further incubation for 24 h, 37°C, 5% CO₂ in air. Alternatively, cells were treated with IFN γ (10 ng/ml; R&D Systems, Cat#DY285B) or vehicle for 30 mins prior to addition of Erastin (2.5 μM) or RSL3 (0.625 μM), diluted in 100 μl of complete media before further incubation for 24 h, 37°C, 5% CO₂ in air. At the end of the incubation time an MTT assay was performed as described before (**Chapter 2; Section 2.7**). Briefly, cells were incubated with 10 mg/ml MTT for 2 h at 37°C, formazan crystals were dissolved in DMSO and absorbance was measured at 570 nm using a microplate reader (POLARstar Omega; BMG).

3.3.2 Western Blot

Cells were seeded at the required density, 5.0×10^4 (4T1 breast, MC-38 colon, LC-2 lung, PEO1 ovarian, PEO4 ovarian and OVCAR8 ovarian) cells/well in a 6-well plate (Greiner Cat#657160) 24 h prior to treatment. Cells then underwent protein extraction and quantification using the DC assay, followed by western blot analysis (**Chapter 2; Section 2.8**). Briefly 10 μg /lane of protein was probed overnight to quantify the abundance of GPX4, SLC7A11 and Lamin-B1 (**Table 3**).

3.3.3 Flow cytometric analysis of cell viability by DRAQ7

Cells were seeded in 1 ml of complete media at the required density 4.5×10^4 (4T1, MC38, LC2, PEO1, PEO4 and OVCAR8) cells/well in a 24-well plate (Helena Biosciences, Cat#92024) 24 h prior to treatment. Media was replaced with vehicle control or Erastin (0.625 μ M, 1.25 μ M and 2.5 μ M) or RSL3 (0.15625 μ M, 0.3125 μ M and 0.625 μ M), cells were then further incubated for 24 hrs at 37°C, 5% CO₂ in air. Briefly, cells were detached and resuspended in 100 μ l of FACS buffer. Then 5 μ l of a 1 in 15 dilution of DRAQ7 (Biostatus, Cat#DR71000) was added to each sample before incubation for 15 min at room temperature in the dark. Then, 500 μ l of FACS buffer was added to each sample before being centrifuged at 500 xg for 5 min. The supernatant was discarded and the cell were resuspended in 100 μ l FACS buffer. Using a NovoCyte Flow Cytometer (ACEA Biosciences), cell populations were gated based on the forward and side scatter parameters and the non-single events excluded based on forward area and height scatter parameters (FlowJo, LCC software; **Figure 3.5**).

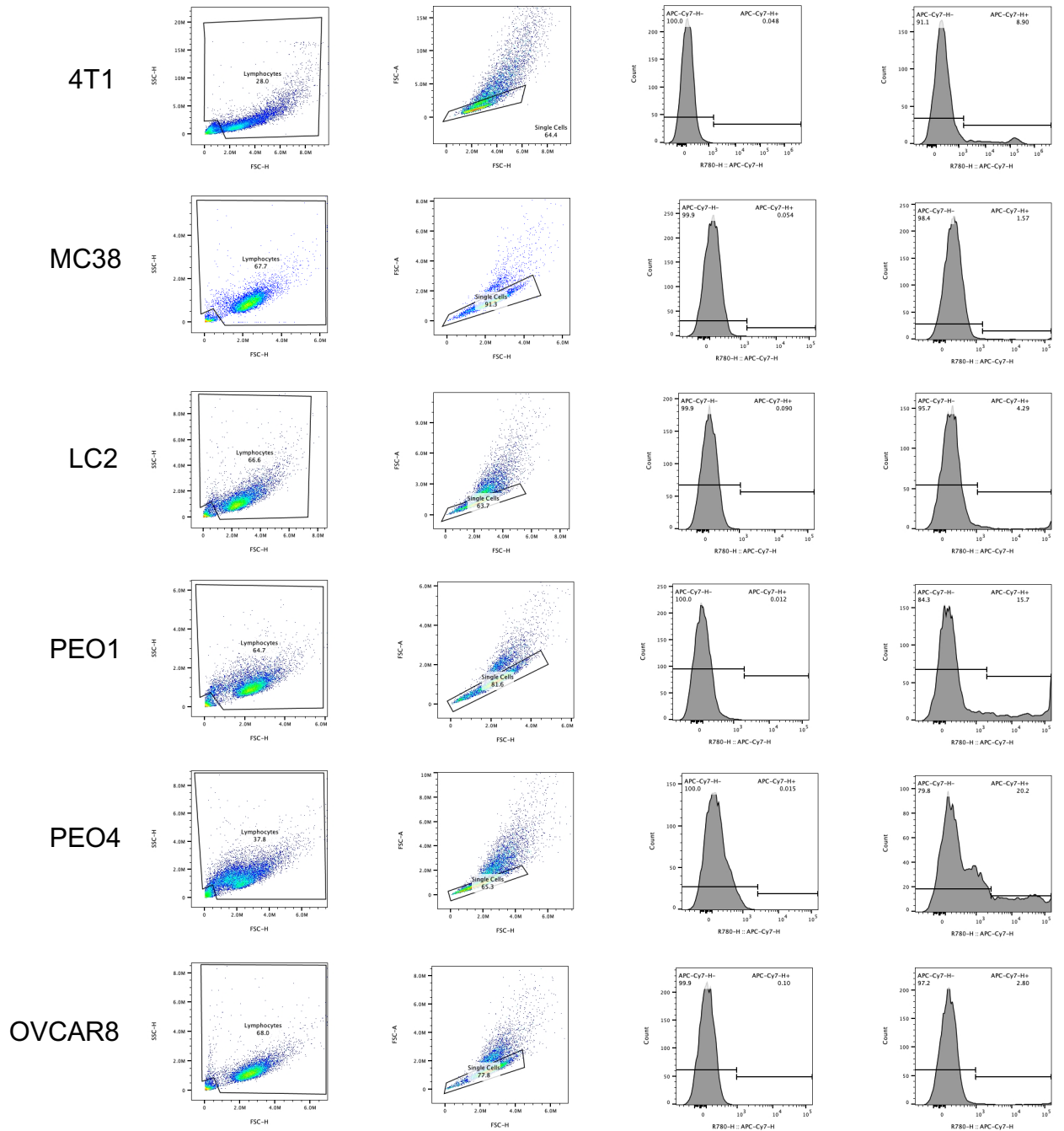


Figure 3.5: Gating strategy to determine cell viability using DRAQ7. The total population was first selected, gating out the debris such as dead cells. The singlets were selected using a FSC-H vs FSC-A dot plot. A histogram visualising the percentage positive cells was used to determine cell viability (% dead). Left histogram shows the unstained sample results and the right histogram shows the vehicle sample results.

3.3.4 Flow cytometric analysis of intracellular staining

Cells were seeded at the required density 2.5×10^4 (OVCAR8 ovarian), 5.0×10^4 (4T1 breast and MC-38 colon), 7.5×10^4 (LC-2 lung, PEO1 ovarian and PEO4 ovarian) cells/well in a 12-well plate (Greiner Cat#665180) 24 h prior to treatment. Media was replaced with DMSO (1% in complete media; Sigma, Cat#SHBH9957) vehicle control or Erastin (0.625 μ M, 1.25 μ M and 2.5 μ M) or RSL3 (0.15625 μ M, 0.3125 μ M and 0.625 μ M), cells were then further incubated for 24 hrs at 37°C, 5% CO₂ in air. Briefly, cells were detached and centrifuged 290 xg for 5 min. Cells were then fixed with 100 μ l of 4% paraformaldehyde solution for 20 min at 4°C and then washed two times in staining buffer PBS (Gibco, Cat#10010-015) and 1% FBS (BIOSERA, Cat#FB-1550/500)) before centrifugation at 350 xg for 5 min. Cells were then resuspended in 1 ml perm/wash (BD Biosciences, Cat#555028) for 15 min at room temperature, before centrifugation at 350 xg for 5 min. Then, 100 μ l of a 1/400 dilution of primary antibody/staining buffer (GPX4; ABCAM, Cat#ab125066) was added to the cells for 1 h at room temperature. Cells were centrifuged at 350 xg for 5 min and washed in staining buffer before 100 μ l of a 1/500 dilution of secondary antibody/staining buffer (Anti-rabbit IgG Fab2 Alexa Fluor® 488 molecular probes (Cell signaling technology, Cat#4412S) was added for 30 min at room temperature in the dark. Cells were centrifuged at 350 xg for 5 min and washed in staining buffer before resuspension in 200 μ l FACS buffer. Using a NovoCyte Flow Cytometer (ACEA Biosciences), cell populations were gated based on the forward and side scatter parameters and the non-single events excluded based on forward area and height scatter parameters (FlowJo, LCC software; **Figure 3.6**).

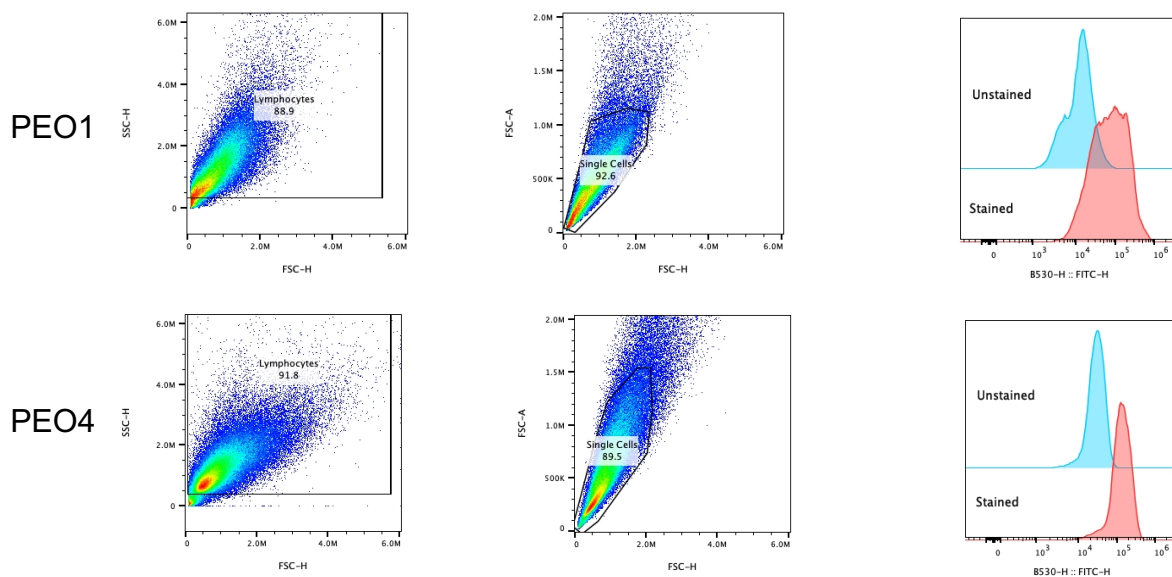


Figure 3.6: Gating strategy to determine intracellular GPX4 levels by MFI of Alexa Fluor 488. The total population was first selected, gating out the debris such as dead cells. The singlets were selected using a FSC-H vs FSC-A dot plot. A histogram visualising the MFI for Alexa Fluor 488 was then created. An unstained sample (blue histogram) shows the background of the sample. The stained sample (red histogram), demonstrates the presence of GPX4 with Alexa Fluor 488 signals.

3.3.5 Flow cytometric analysis of lipid hydroperoxides in live cells

Cells were seeded in 1 ml of complete media at the required density 7.5×10^4 (PEO1 ovarian and PEO4 ovarian) cells/well in a 24-well plate (Helena Biosciences, Cat#92024) 24 h prior to treatment. Media was then replaced with 500 μ l vehicle control (7% H₂O nanopure water in complete media), 500 μ l liproxstatin-1 (at double required concentration; 1000 nM; Cayman chemical Cat#17730) or 500 μ l complete media, and cells were incubated for 30 mins at 37°C, 5% CO₂ in air. Then, 500 μ l Erastin (at double required concentration; Tocris Bioscience, Cat#5449) or 500 μ l complete media was then added to either the vehicle control or liproxstatin-1, cells were then further incubated for 24 hrs at 37°C, 5% CO₂ in air. For a positive control, cells were incubated with 1 ml cumene hydroperoxide (100 μ M; Sigma-Aldrich, Cat#247502) for 2 h at 37°C, 5% CO₂ in air. Cells were then treated with Liperfluo (5 μ M; Europa Bioproducts, Cat#DJL248) or DMSO (1%; Sigma, Cat#SHBH9957) vehicle

control for 15 min at 37°C, 5% CO₂ in air. Cells were then washed with 1 ml PBS (Gibco, Cat#10010-015), and detached by 100 µl of Accutase (Sigma, Cat#A6964) prior to the addition of 2 ml FACS buffer. Cells were centrifuged at 515 xg, at 4°C, for 7 min before being re-suspended in 200 µl FACS buffer. Using a NovoCyte Flow Cytometer (ACEA Biosciences), cell populations were gated based on the forward and side scatter parameters and the non-single events left out based on forward area and height scatter parameters (FlowJo, LCC software, **Figure 3.7**). Differentiation between cells based on lipid peroxidation-positive fluorescent staining using Liperfluo® (530 nm laser).

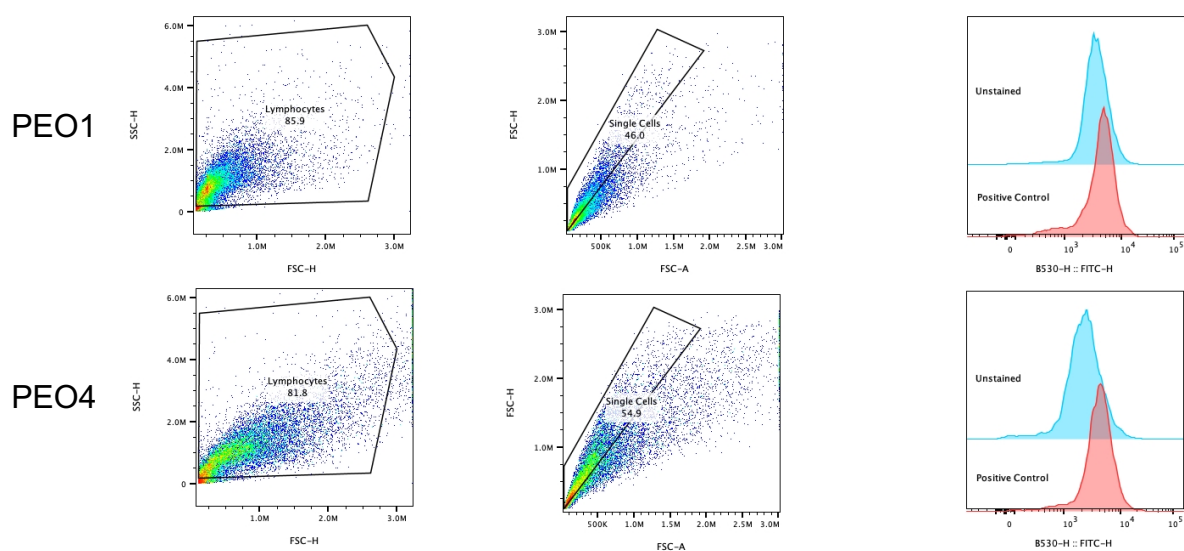


Figure 3.7: Gating strategy to determine lipid hydroperoxide levels by MFI of Liperfluo. The total population was first selected, gating out the debris such as dead cells. The singlets were selected using a FSC-H vs FSC-A dot plot. A histogram visualising the MFI for Liperfluo was then created. An unstained sample (blue histogram) shows the background of the sample. The positive control (red histogram), cumene hydroperoxide demonstrates the presence of lipid peroxides with Liperfluo signals.

3.3.6 Statistics

GraphPad prism 7.0 was used for statistical analysis. Normally distributed data were subjected to a two-way ANOVA with Dunnett's or Bonferroni post-hoc test; comparing the treatment in relation to the vehicle for $n > 3$. Significance was assumed when $P < 0.05$.

3.4 Results

Treating a panel of cancer cells with Erastin or RSL3 induced ferroptosis, reducing cell viability

To assess pan-cancer response to induction of ferroptosis, a panel of breast, colon, lung and three ovarian cancer cell lines were treated with varying concentrations of ferroptosis inducers; Erastin (system X_c^- inhibitor; 0.15625 μ M – 2.5 μ M; **Figure 3.8**) or RLS3 (GPX4 inhibitor; 0.0390625 μ M – 0.625 μ M; **Figure 3.14**), in order to determine cancer cell susceptibility to ferroptotic induction.

Erastin reduced cell viability in a panel of cancer cell lines

Breast (**Figure 3.8 a**) and lung (**Figure 3.8 c**) cancer cells showed a significant reduction in cell viability at the lowest concentration of Erastin (0.15625 μ M) within 24 h treatment. Lung cancer cells showed the lowest IC₅₀ value of 0.07042 μ M (**Table 4**). Whereas colon (**Figure 3.8 b**) cancer showed a significant reduction in cell viability at a four-fold higher concentration (0.625 μ M) of the system X_c^- inhibitor. The ovarian cancer cell lines (**Figure 3.8 d-f**) were more resistant to Erastin at the lower concentrations, in comparison to breast, colon and lung cancer cell lines. The chemo-sensitive PEO1 cells and the chemo-resistant PEO4 ovarian cancer cells (**Figure 3.8 d and e**) showed a 50% reduction in cell viability at the highest concentration (2.5 μ M) of Erastin. Ovarian PEO4 cells showed the highest IC₅₀ value of 2.150 μ M (**Table 4**). Whereas the ovarian cancer cell line OVCAR8 was more susceptible to ferroptotic cell death with Erastin (2.5 μ M: **Figure 3.8 f**), in comparison to PEO1 and PEO4 ovarian cancer cell lines. These results indicate that the panel of cancer cell lines show varied susceptibility to induction of ferroptosis using a type one FIN, such as Erastin.

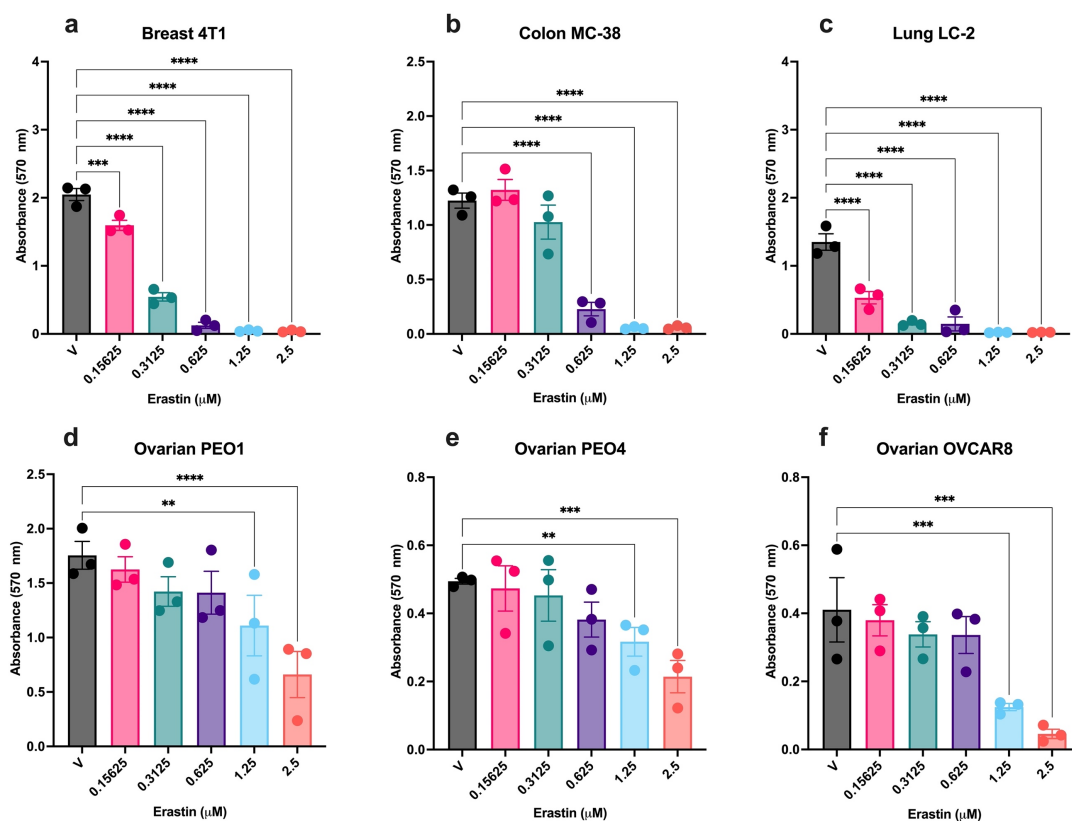


Figure 3.8: Effect of Erastin on cell viability, determined by MTT. The panel of cancer cell lines (a) 4T1; (b) MC-38; (c) LC-2; (d) PEO1; (e) PEO4; (f) OVCAR8 were cultured in media containing vehicle (v) or the individual concentrations of Erastin. Cell viability was evaluated using MTT assay after 24 h. Data was presented as mean (SEM) from three independent cell passage experiments and analysed using 2-way ANOVA; * $p < 0.05$, ** $p < 0.01$, *** $p < 0.001$, **** $p < 0.0001$.

Table 4: IC50 values from MTT assay for all cancer cell lines treated with Erastin.

Cell Line	IC50 Value (μM)
Breast 4T1	0.1655
Colon MC-38	0.4099
Lung LC-2	0.07042
Ovarian PEO1	1.386
Ovarian PEO4	2.150
Ovarian OVCAR8	1.008

The MTT assay, depends on mitochondrial activity, which can be affected by ferroptosis induction. Therefore, cell viability was also assessed by flow cytometry, using a DRAQ7 stain. The ovarian PEO1 (Figure 3.9 d) cancer cells showed a significant increase in cell death at the lowest concentration of Erastin (0.15625 μM) within 24 h treatment. However, the PEO1 ovarian cancer cells showed the highest IC50 value of 113.3 μM (Table 5). Whereas

the ovarian PEO4 cells (**Figure 3.9 e**) showed a significant increase in cell death at double the concentration of (0.3125 μM) of the system X_c^- inhibitor. Both colon (**Figure 3.9 b**) and lung (**Figure 3.9 c**) cancer cell lines showed a significant increase in cell death at 0.625 μM of Erastin, whereas the breast (**Figure 3.9 a**) cancer cells required double the concentration (1.25 μM). The colon cancer cell lines showed the lowest IC₅₀ value of 0.4408 μM (**Table 5**). Finally, the ovarian OVCAR8 (**Figure 3.9 f**) cancer cell lines showed no change in cell death at the lower concentrations of Erastin, but a significant increase in cell death at the highest concentration (2.5 μM) of the system X_c^- inhibitor.

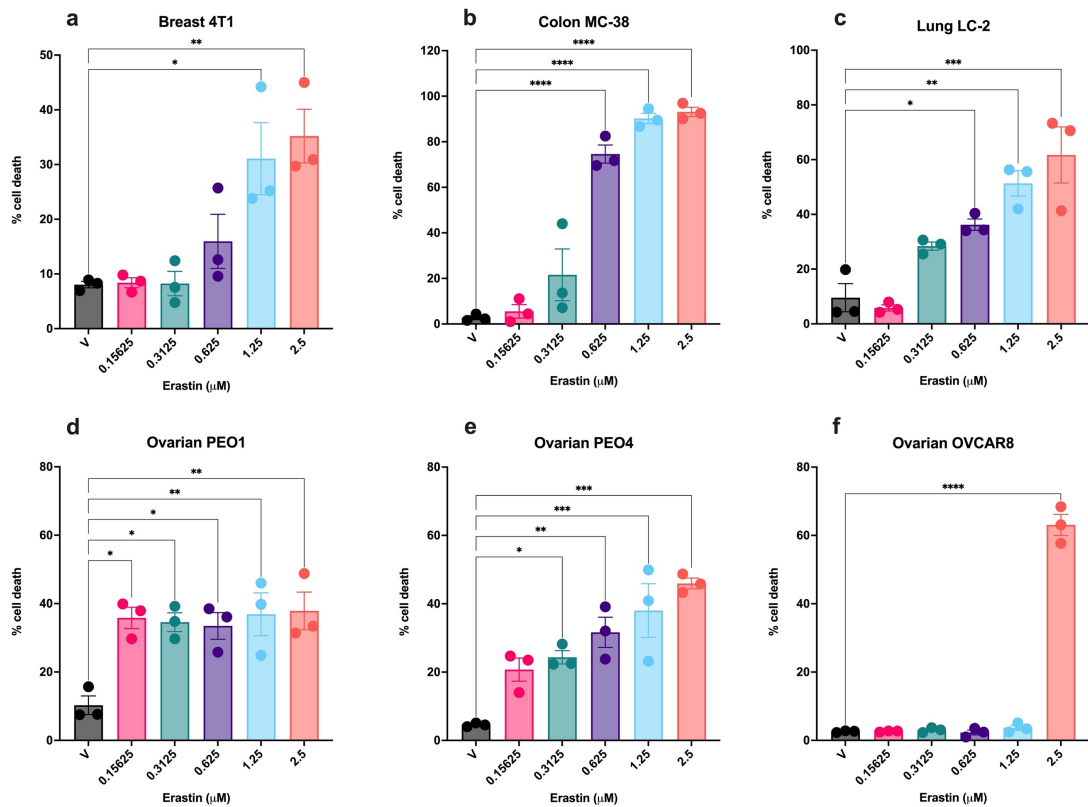


Figure 3.9: Effect of Erastin on cell viability, determined by DRAQ7. The panel of cancer cell lines (a) 4T1; (b) MC-38; (c) LC-2; (d) PEO1; (e) PEO4; (f) OVCAR8 were cultured in media containing vehicle (v) or the individual concentrations of Erastin. Cell death was assessed by flow cytometry using DRAQ7 after 24 h. Data was presented as mean (SEM) from three independent cell passage experiments and analysed using 1-way ANOVA; * $p < 0.05$, ** $p < 0.01$, *** $p < 0.001$, **** $p < 0.0001$.

Table 5: IC50 values from DRAQ7 assay for all cancer cell lines treated with Erastin.

Cell Line	IC50 Value (μM)
Breast 4T1	0.7985
Colon MC-38	0.4408
Lung LC-2	0.5792
Ovarian PEO1	113.3
Ovarian PEO4	7.220
Ovarian OVCAR8	3.630

From the DRAQ7 data, the size of the cancer cells was determined, in order to understand how the cancer cells respond to ferroptotic induction. The shrinking of cells is a key signature of ferroptosis (Yu et al., 2016). Both the breast (**Figure 3.10 a**) and ovarian PEO1 (**Figure 3.10 d**) cancer cells showed no significant changes in cell size after treatment with the concentration range of Erastin. The lung (**Figure 3.10 c**), ovarian PEO4 (**Figure 3.10 e**) and ovarian OVCAR8 (**Figure 3.10 f**) showed a significant decrease in cell size at the highest concentration of Erastin (2.5 μM). The colon (**Figure 3.10 b**) showed a significant decrease in cell size at the three highest concentrations of Erastin (0.625 μM – 2.5 μM).

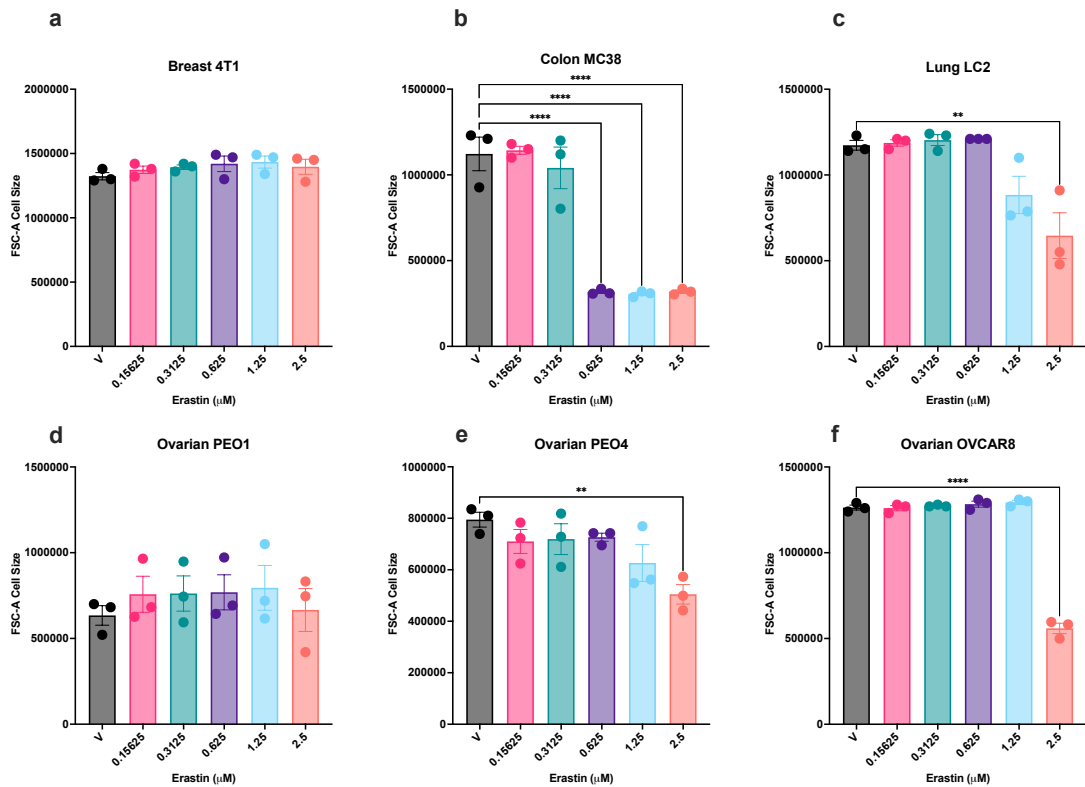


Figure 3.10: Effect of Erastin on cell size (FSC-A). The panel of cancer cell lines (a) 4T1; (b) MC-38; (c) LC-2; (d) PEO1; (e) PEO4; (f) OVCAR8 were cultured in media containing vehicle (v) or the individual concentrations of Erastin. Cell size was determined from the DRAQ7 data. Data was presented as mean (SEM) from three independent cell passage experiments and analysed using 1-way ANOVA; ** $p < 0.01$, **** < 0.0001 .

Erastin inhibits the SLC7A11 light chain component of system Xc⁻, therefore the SLC7A11 protein was next assessed for each cancer cell line by western immunoblotting (**Figure 3.11**). The quantity of SLC7A11 present in each cell line could provide an understanding for the cells' susceptibility to ferroptotic induction by Erastin. There was an observed lower expression of SLC7A11 in the ovarian PEO1 and PEO4 cancer cell lines, in comparison to the other cancer cell lines; breast 4T1, colon MC-38, lung LC-2 and ovarian OVCAR8.

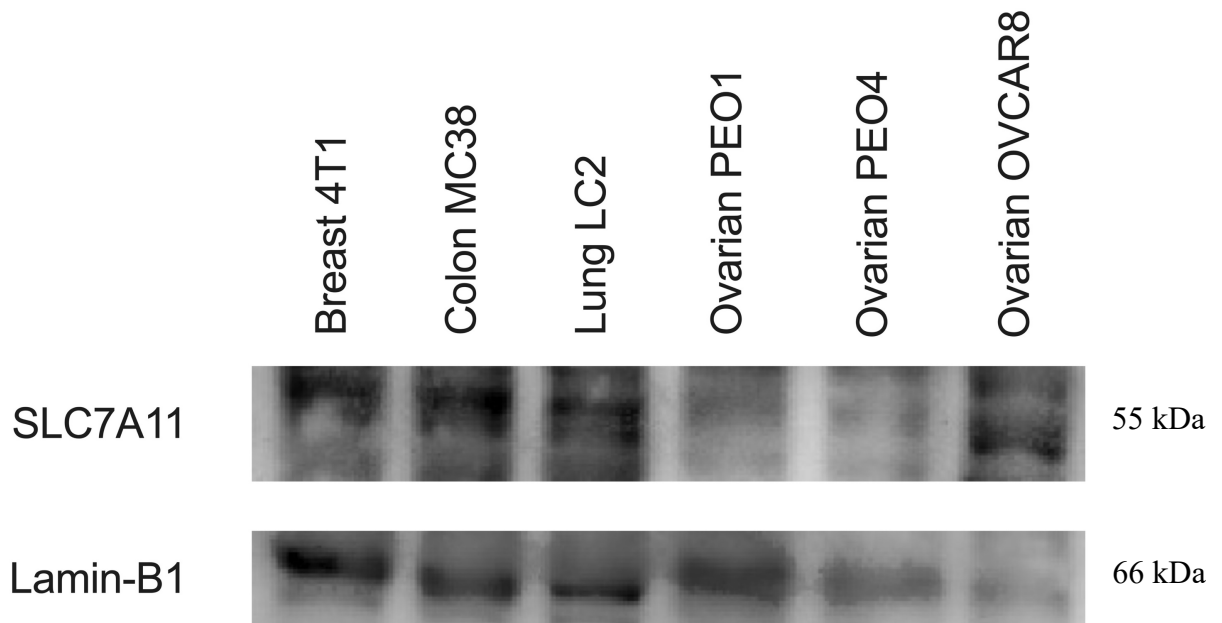


Figure 3.11: SLC7A11 western blots for panel of cancer cell lines. SLC7A11 was observed at 55 kDa and the housekeeping protein Lamin-B1 was observed at 66 kDa.

Lipoxstatin-1 (Lip) is a known lipid peroxide scavenger; therefore, cells were treated with Lip to determine if there was a rescue effect on cell viability. Initially cells were treated with a concentration range from 25 nM to 1000 nM of LIP and 2.5 μ M Erastin (**Appendix, Figure 1**), it was determined that 100nM was sufficient to rescue against ferroptotic induction. Lip 100 nM alone had no effect on cancer cell viability (**Figure 3.12 a-f**). The effect of cotreatment of Lip and Erastin (2.5 μ M) varied across cancer cell lines. There was a significant rescue effect on cell viability in breast cancer cells, whilst the OVCAR8 ovarian cancer cell line showed rescue, which did not reach significance (**Figure 3.12 a and f**). There was no significant effect of the cotreatment in the PEO1 and PEO4 ovarian cancer cell lines; however, the Erastin did not reduce cell viability alone (**Figure 3.12 d**).

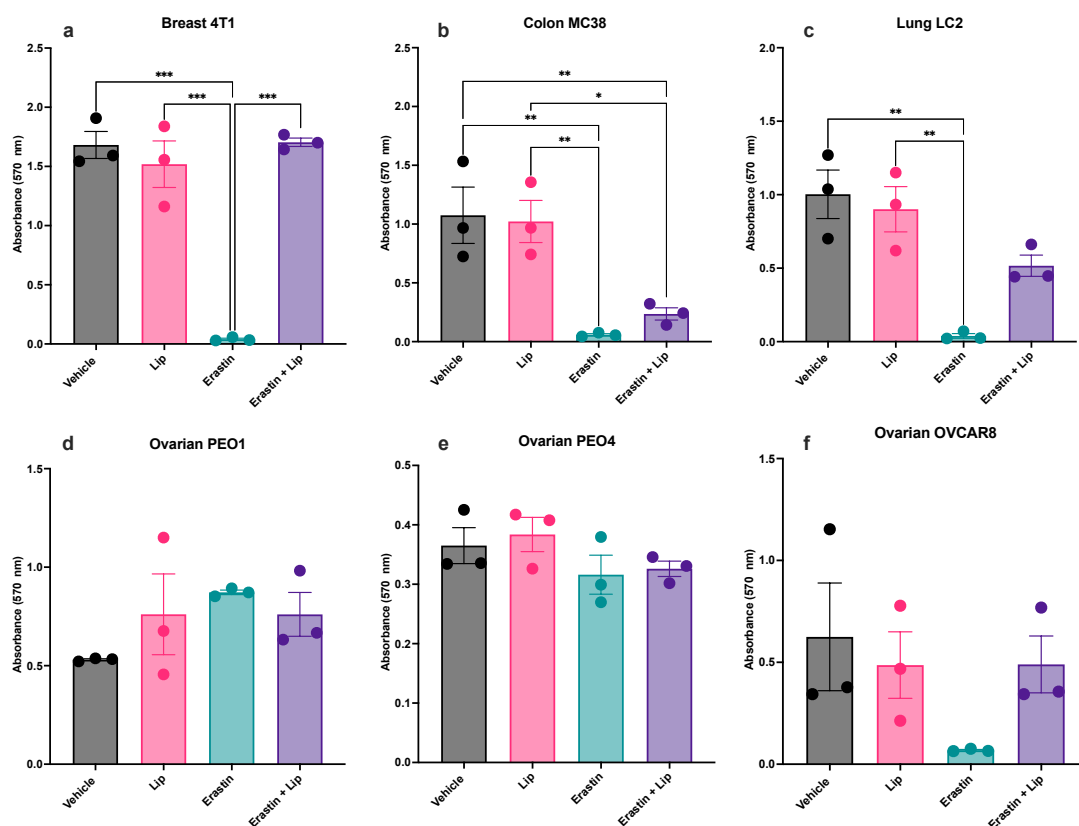


Figure 3.12: The rescue effect of Liproxstatin-1 treatment against the ferroptosis inducer, Erastin. The panel of cancer cell lines (a) 4T1, (b) MC-38, (c) LC-2, (d) PEO1, (e) PEO4, (f) OVCAR8 were cultured in media containing vehicle (v) or liproxstatin-1 or Erastin. Cells were treated with liproxstatin-1 for 30 min prior to treatment with Erastin for 24 h. Cell viability was evaluated using MTT assay after 24 h. Data was presented as mean (SEM) from three independent cell passage experiments and analysed using 2-way ANOVA; * $p < 0.05$, ** $p < 0.001$, *** $p < 0.001$.

To further compare the effect of therapy-resistance on ferroptosis, lipid peroxidation was quantified using Liperfluor by flow cytometry in chemotherapy-sensitive (PEO1) and chemotherapy-resistant (PEO4) ovarian cancer cells (**Figure 3.13**). There were significant increase in lipid peroxidation in both PEO1 and PEO4 cell lines after treatment with 5 μM and 10 μM Erastin. In the PEO1 cell line Lip significantly rescued cells treated with 5 μM and 10 μM Erastin, with the lipid peroxidation levels returning to vehicle concentrations. Lip significantly rescued PEO4 cells treated with the lower concentration of Erastin, with the lipid peroxidation levels returning to vehicle concentration. These results indicate that the two ovarian cancer cell lines exist with high background lipid peroxidation prior to any treatment. Which is

further confirmed by the cumene hydroperoxide positive control having little, if any effect.

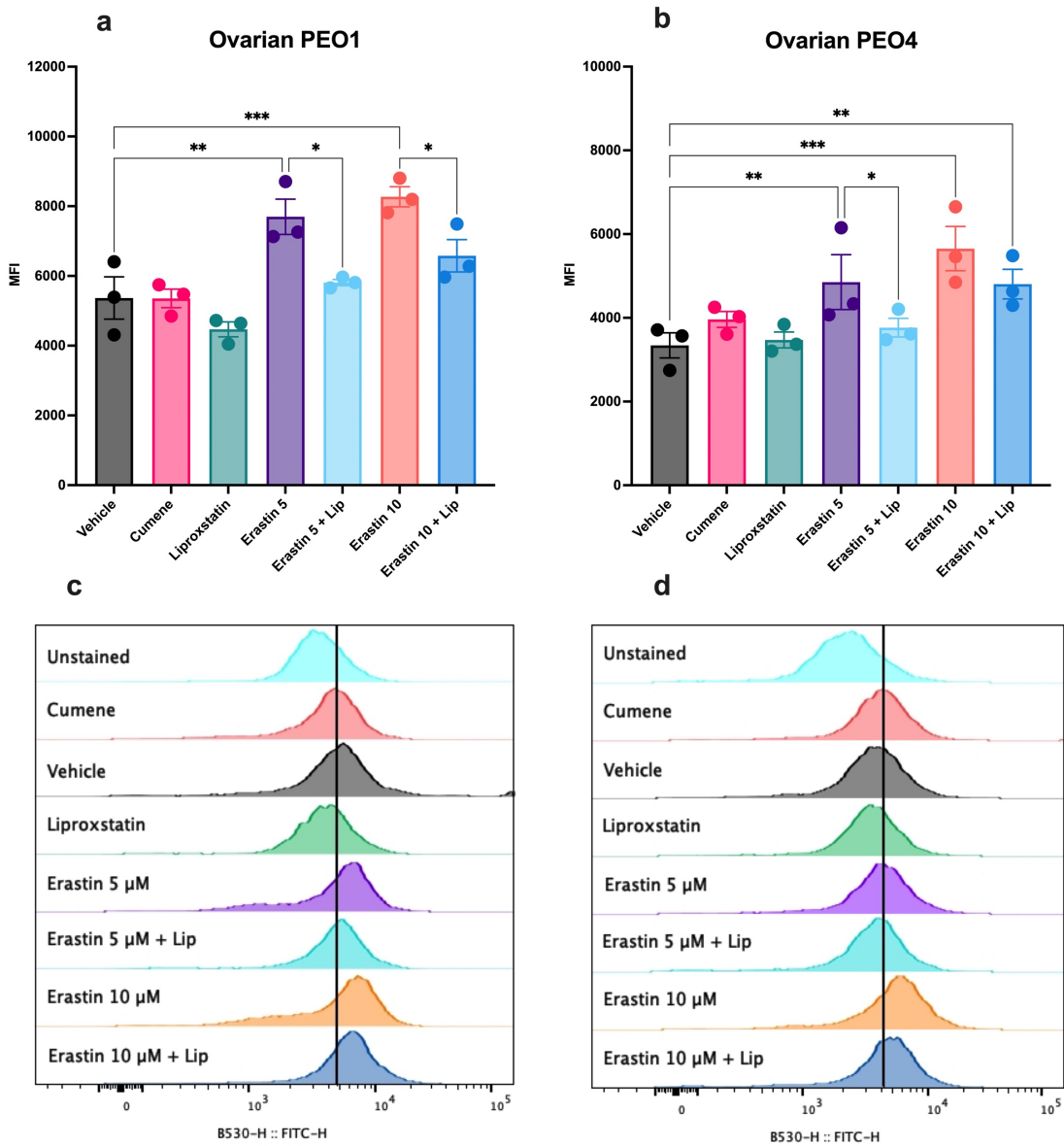


Figure 3.13: Liperflu staining for lipid peroxidation to quantify the rescue effect of Liproxstatin-1 treatment against the ferroptosis inducer, Erastin. (a) PEO1; (b) PEO4; (c) PEO1 representative flow histograms and (d) PEO4 representative flow histograms. The cancer cell lines were cultured in media containing vehicle (v) or liproxstatin-1 or Erastin. Cells were treated with liproxstatin-1 for 30 min prior to treatment with Erastin (5 μ M and 10 μ M) for 24 h. Cell viability was evaluated using MTT assay after 24 h. Data was presented as mean (SEM) from three independent cell passage experiments and analysed using 2-way ANOVA; * $p < 0.05$, ** $p < 0.001$, *** $p < 0.001$.

The GPX4 inhibitor RSL3 significantly reduced cell viability in a panel of cancer cell lines

Colon, lung and the chemo-resistant ovarian cancer cell line PEO4 showed a significant reduction in cell viability at the lowest concentration of the GPX4 inhibitor RSL3 (0.04 μM : **Figure 3.14 b, c and e**). The lung cancer cells showed the lowest IC₅₀ value of 0.009835 μM (**Table 6**). Whereas the other three cell lines (breast, chemo-sensitive ovarian PEO1 and ovarian OVCAR8) showed a significant reduction in cell viability at double the concentration of the inhibitor (0.08 μM ; **Figure 3.14 a, d and f**). The ovarian OVCAR8 cancer cells showed the highest IC₅₀ value of 0.1548 μM (**Table 6**). These results indicate that the panel of cancer cell lines are more susceptible to ferroptosis when treated with a class two FIN, such as RSL3, in comparison to the class one FIN, such as Erastin (**Figure 3.10 a-f and Figure 3.14 a-f**).

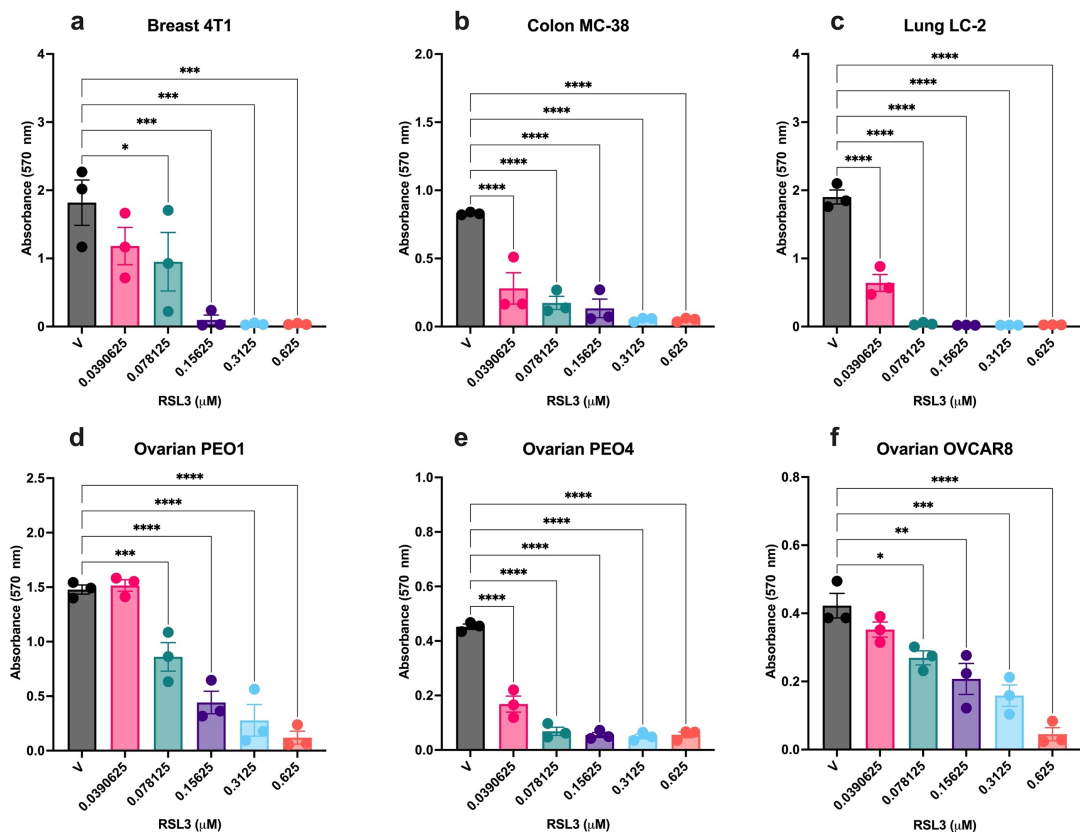


Figure 3.14: Effect of RSL3 on cell viability, determined by MTT. The panel of cancer cell lines (a) 4T1; (b) MC-38; (c) LC-2; (d) PEO1; (e) PEO4; (f) OVCAR8 were cultured in media containing vehicle (v) or the individual concentrations of RSL3. Cell viability was evaluated using MTT assay after 24 h treatment. Data was presented as mean (SEM) from three independent cell passage experiments and analysed using 2-way ANOVA; * $p < 0.05$, ** $p < 0.01$, *** $p < 0.001$, **** $p < 0.0001$.

Table 6: IC50 values from MTT assay for all cancer cell lines treated with RSL3.

Cell Line	IC50 Value (μM)
Breast 4T1	0.07085
Colon MC-38	0.01282
Lung LC-2	0.009835
Ovarian PEO1	0.07326
Ovarian PEO4	0.01423
Ovarian OVCAR8	0.1548

The cell viability was also assessed using a cell stain, DRAQ7. The colon (**Figure 3.15 b**), ovarian PEO1 (**Figure 3.15 d**) and PEO4 (**Figure 3.15 e**) cancer cells showed a significant increase in cell death at the lowest concentration of RSL3 (0.0390625 μM) within 24 h treatment. The PEO1 ovarian cancer cells showed the lowest IC50 value of 0.01049 μM (**Table 7**). Whereas the ovarian OVCAR8 cells (**Figure 3.15 f**) showed a significant increase in cell death at double the concentration of (0.078125 μM) of the GPX4 inhibitor. Both breast (**Figure 3.11 a**) and lung (**Figure 3.11 c**) cancer cell lines showed a significant increase in cell death at 0.15625 μM of RSL3. The lung cancer cells showed the highest IC50 value of 0.4338 μM (**Table 7**).

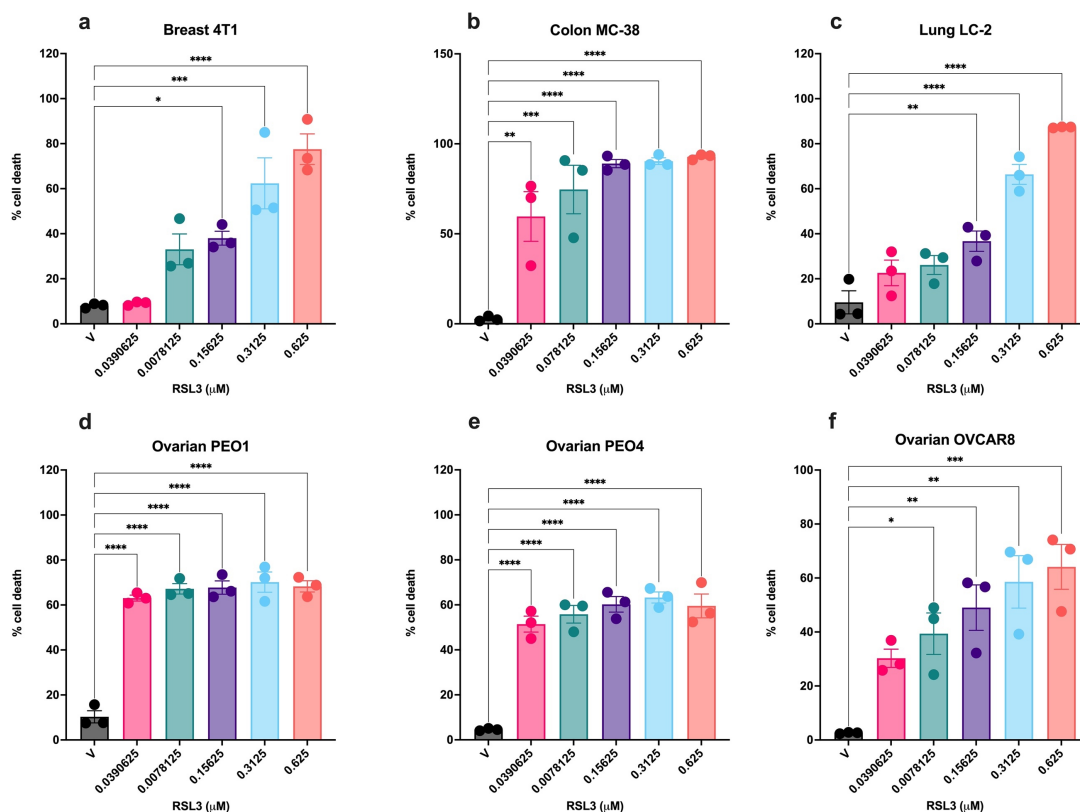


Figure 3.15: Effect of RSL3 on cell viability, determined by DRAQ7. The panel of cancer cell lines (a) 4T1; (b) MC-38; (c) LC-2; (d) PEO1; (e) PEO4; (f) OVCAR8 were cultured in media containing vehicle (v) or the individual concentrations of RSL3. Cell death was assessed by flow cytometry using DRAQ7 after 24 h. Data was presented as mean (SEM) from three independent cell passage experiments and analysed using 1-way ANOVA; * $p < 0.05$, ** $p < 0.01$, *** $p < 0.001$, **** $p < 0.0001$.

Table 7: IC50 values from DRAQ7 assay for all cancer cell lines treated with RSL3.

Cell Line	IC50 Value (μM)
Breast 4T1	0.2121
Colon MC-38	0.02775
Lung LC-2	0.4338
Ovarian PEO1	0.01049
Ovarian PEO4	0.01267
Ovarian OVCAR8	0.07949

From the DRAQ7 data, the size of the cancer cells was determined, in order to understand how the cancer cells respond to ferroptotic induction. The breast (Figure 3.16 a) cancer cell line showed a significant reduction in cell size at the two highest concentrations of RSL3 (0.3125 μM and 0.625 μM). The lung (Figure 3.16 c) cancer cell line showed a significant reduction in cell size at

the highest three concentrations of RSL3 (0.15625 μ M – 0.625 μ M). The ovarian OVCAR8 (**Figure 3.16 f**) showed a significant reduction in cell size at all but the lowest concentration (0.0390625 μ M) of RSL3. The colon (**Figure 3.16 b**), ovarian PEO1 (**Figure 3.16 d**) and ovarian PEO4 (**Figure 3.16 e**) cells showed a significant decrease in cell size at concentrations of RSL3 (0.0390625 μ M – 0.625 μ M).

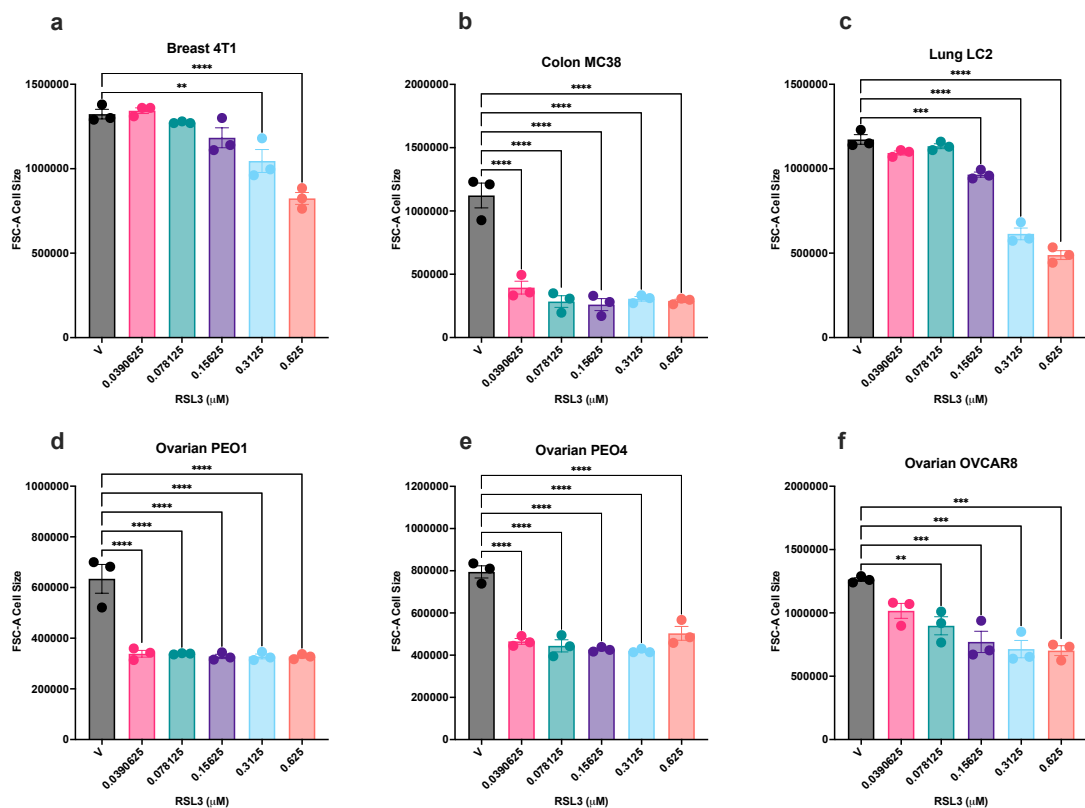


Figure 3.16: Effect of RSL3 on cell size (FSC-A). The panel of cancer cell lines (a) 4T1; (b) MC-38; (c) LC-2; (d) PEO1; (e) PEO4; (f) OVCAR8 were cultured in media containing vehicle (v) or the individual concentrations of RSL3. Cell size was determined from the DRAQ7 data. Data was presented as mean (SEM) from three independent cell passage experiments and analysed using 1-way ANOVA; **p < 0.01, *** < 0.001, **** < 0.0001.

RSL3 inhibits the GPX4 enzyme, which is essential for ferroptotic induction (Yang et al., 2014); therefore the GPX4 protein was next assessed for each cancer cell line by immunoblotting (**Figure 3.17**). The quantity of GPX4 present

in each cell line could provide an understanding for the cells' susceptibility to ferroptotic induction by RSL3. There was an observed lower expression of GPX4 in the ovarian PEO4 cancer cell line, in comparison to the other cell lines; breast 4T1, colon MC38, lung LC2, Ovarian PEO1 and OVCAR8.

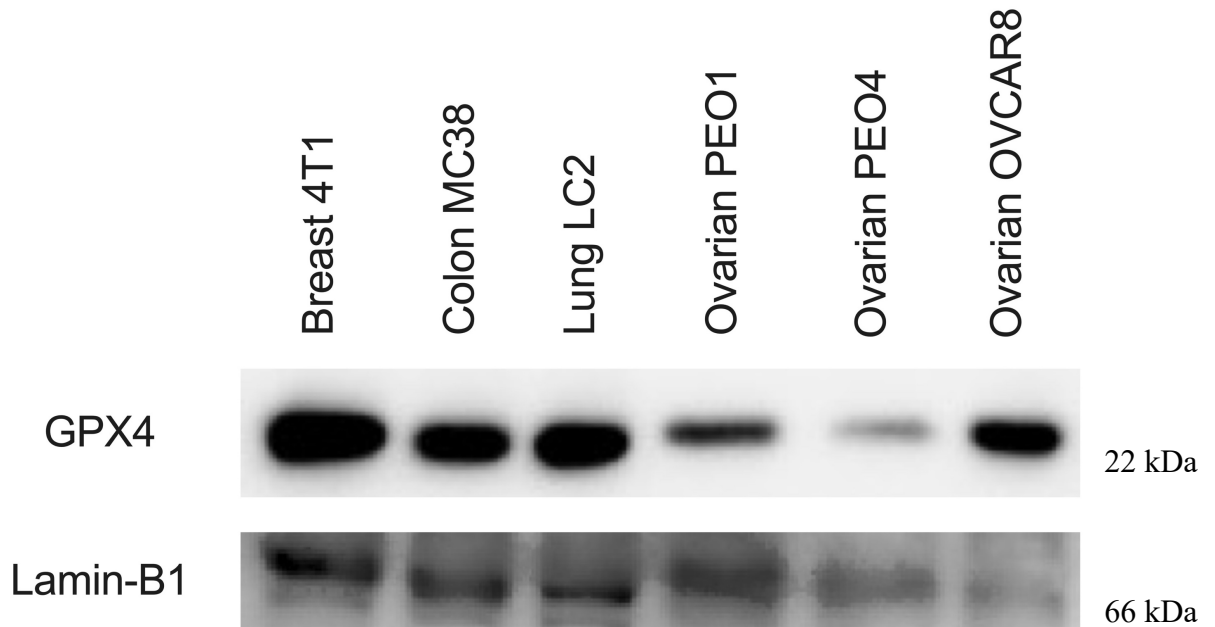


Figure 3.17: GPX4 western blots for panel of cancer cell lines. GPX4 was observed at 22 kDa and the housekeeping protein Lamin-B1 was observed at 66 kDa.

Intracellular GPX4 levels were measured by intracellular staining using flow cytometry in chemotherapy-sensitive (PEO1: **Figure 3.18 a and b**) and chemotherapy-resistant (PEO4: **Figure 3.18 c and d**) ovarian cancer cells. These two cell lines were chosen to model different chemotherapy sensitivities. After treatment with Erastin there was a significant increase in intracellular GPX4 levels in the PEO1 cell line for all concentrations of the inhibitor (**Figure 3.18a**), whereas the PEO4 cell line showed no significant changes (**Figure 3.18c**). There was a significant increase in intracellular GPX4 levels in the PEO1 cell line at the highest concentration of RSL3 (0.63 μ M; **Figure 3.18b**). Whereas, in the PEO4 cell line there was a significant increase in GPX4 at the lowest concentration of RSL3 (0.16 μ M: **Figure 3.18d**).

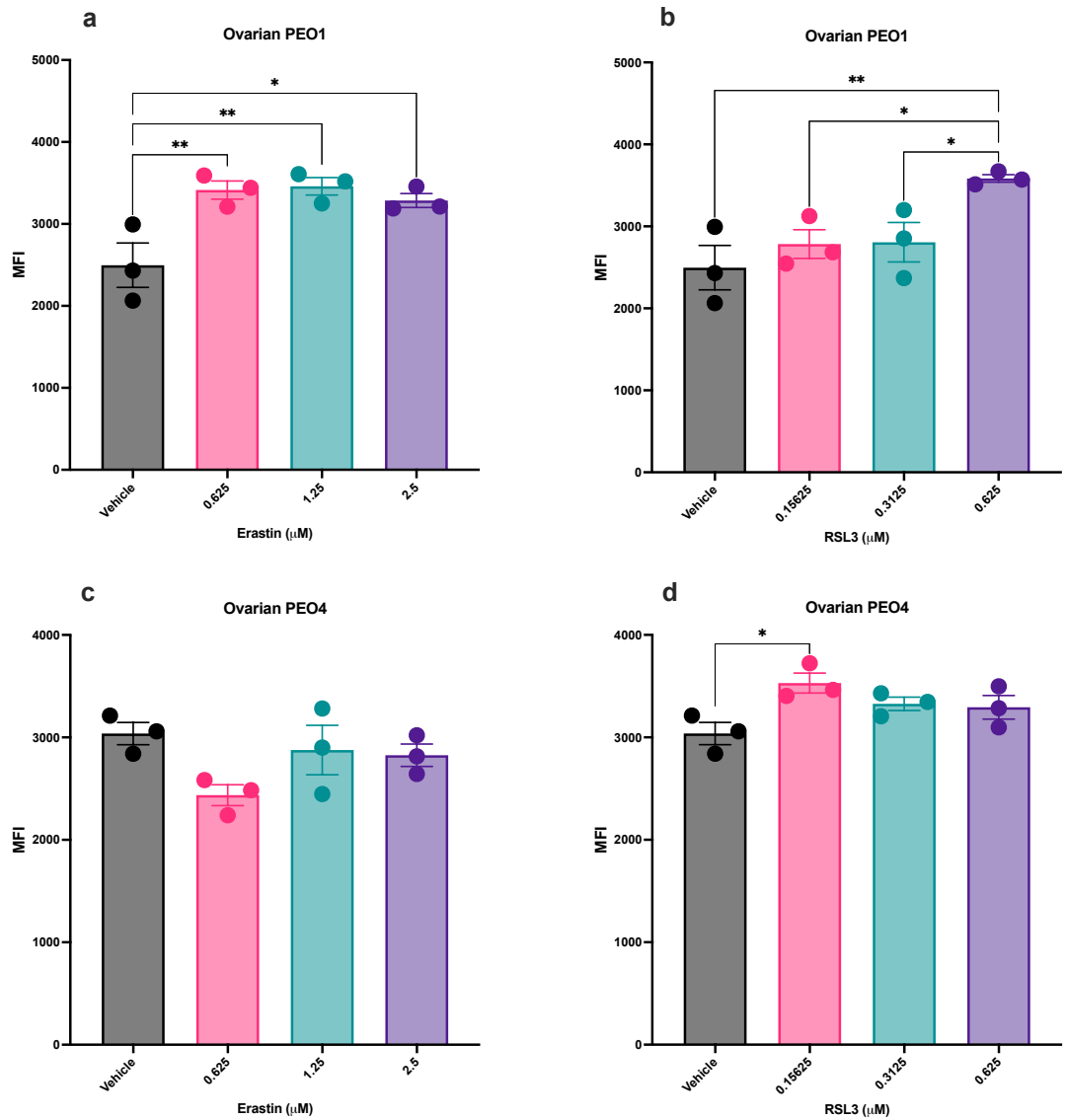


Figure 3.18: Intracellular staining for GPX4 at different concentrations of Erastin and RSL3. The PEO1 ovarian cancer cell line was cultured in media containing vehicle or the individual concentrations of (a) Erastin; (b) representative flow histogram of Erastin data; (c) RSL3 and (d) representative flow histogram of RSL3 data. Intracellular GPX4 was determined by flow cytometry and visualised as median fluorescent intensity (MFI). Data was presented as mean (SEM) from three independent experiments and analysed using 2-way ANOVA; * $p < 0.05$, ** $p < 0.001$.

The lipid peroxide scavenger, Lip was also used to determine if there was a rescue effect on cell viability against RSL3 treatment. Initially cells were treated with a concentration range from 25 nM to 1000 nM of LIP and 0.625 μ M RSL3 (Appendix, Figure 1), it was determined that 100nM was sufficient to rescue against ferroptotic induction. Lip (100 nM) alone had no effect on cancer cell viability. However, cotreatment of Lip and RSL3 (0.625 μ M) resulted in a significant rescue in cell viability in all cancer cell lines (**Figure 3.19 a-f**).

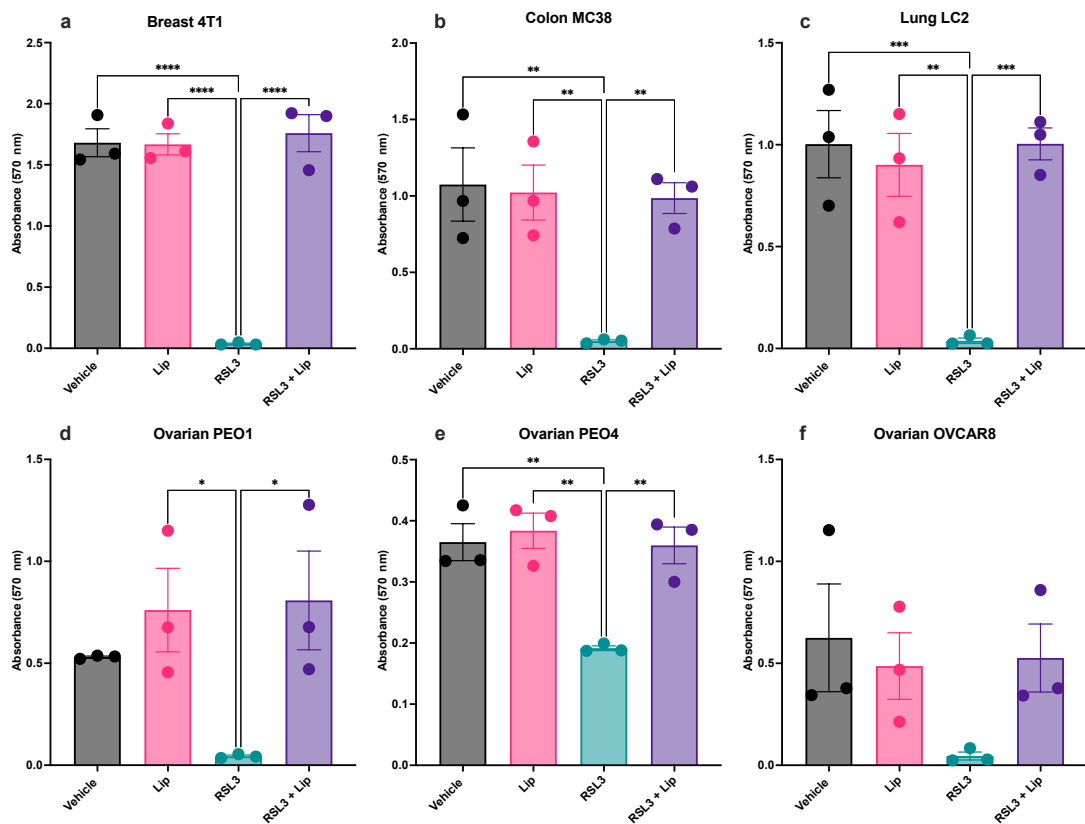


Figure 3.19: The rescue effect of Liproxstatin-1 treatment against the ferroptosis inducer, RSL3. The panel of cancer cell lines (a) 4T1; (b) MC-38; (c) LC-2; (d) PEO1; (e) PEO4; (f) OVCAR8 were cultured in media containing vehicle (v) or liproxstatin-1 or RSL3. Cells were treated with liproxstatin-1 for 30 min prior to treatment with RSL3 for 24 h. Cell viability was evaluated using MTT assay after 24 h. Data was presented as mean (SEM) from three independent cell passage experiments and analysed using 2-way ANOVA; * $p < 0.05$, ** $p < 0.01$, *** $p < 0.001$, **** $p < 0.0001$.

IFN γ is believed to downregulate SLC7A11 and SLC3A2, the two components of system X $_C^-$, resulting in the induction of ferroptosis (Wang et al., 2019). Therefore, the panel of cancer cell lines were treated concurrently with Erastin (2.5 μ M), the known inhibitor of the SLC7A11 component of system X $_C^-$, and IFN γ . A concentration of 10 ng/ml of IFN γ was used for experimental purposes, this concentration has been extensively used previously and has been accepted to be within a physiologically relevant range (Natarajan et al., 2014; Son et al., 2014; Zhou et al., 2022). The *IFNG* gene and IFN γ receptor (IFN γ R1) are conserved between *Homo sapiens* and *Mus musculus* (NCBI).

Treating cancer cells with IFN γ (10 ng/ml) alone significantly reduced cell viability in 4T1 breast and MC38 colon cancer cell lines (**Figure 3.20 a and b**). The effect of Erastin (2.5 μ M) and IFN γ (10 ng/ml) was similar to that of Erastin (2.5 μ M) treatment alone in 4T1 breast, MC38 colon, and PEO4 ovarian cell lines (**Figure 3.20 a, b and d**). Interestingly, cotreating cells with IFN γ (10 ng/ml) and Erastin (2.5 μ M) reversed the loss of cell viability observed with Erastin (2.5 μ M) alone, in the LC2 lung (**Figure 3.20 c**) and OVCAR8 ovarian (**Figure 3.20 d**) cancer cell lines. These results suggest that the effect of IFN γ and ferroptosis susceptibility is dependent on the type of cancer cell line.

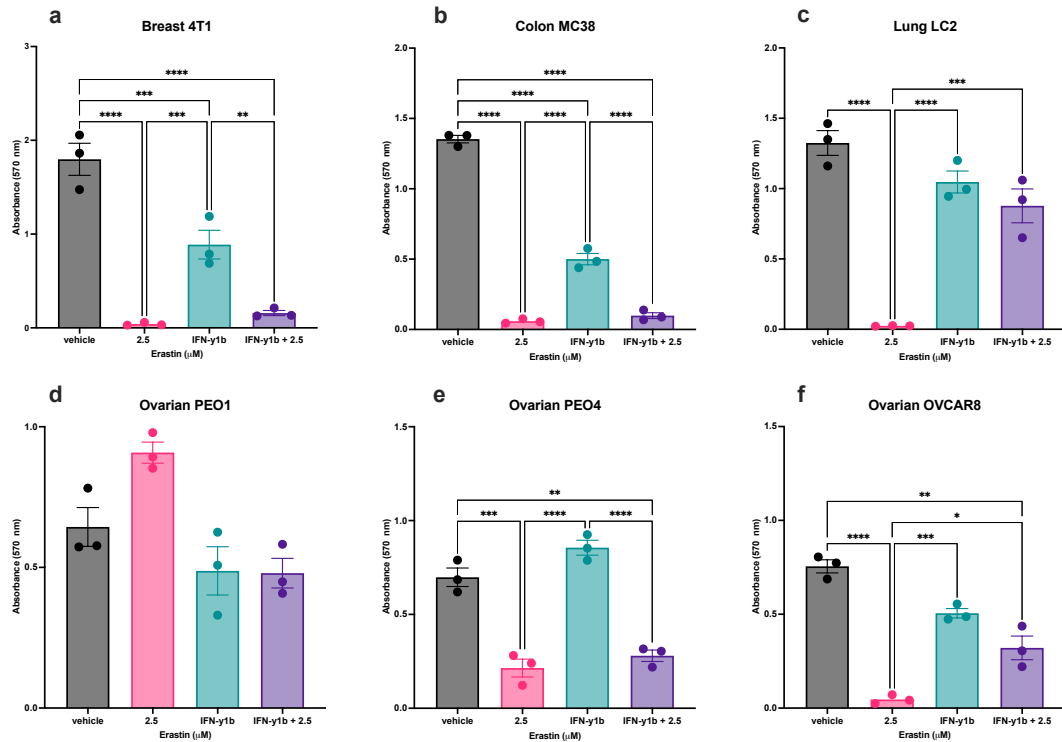


Figure 3.20: The effect of cotreatment with IFN γ and Erastin. The panel of cancer cell lines (a) 4T1; (b) MC-38; (c) LC-2; (d) PEO1; (e) PEO4; (f) OVCAR8 were cultured in media containing vehicle (v) or IFN γ or Erastin or IFN γ plus Erastin. Cells were treated with IFN γ for 30 min prior to treatment with Erastin for 24 h. Cell viability was evaluated using MTT assay after 24 h. Data was presented as mean (SEM) from three independent cell passage experiments and analysed using 2-way ANOVA; * $p < 0.05$, ** $p < 0.001$, *** $p < 0.0001$.

Treatment with IFN γ (10 ng/ml) significantly reduced cell viability in the MC-38 colon and OVCAR8 ovarian cancer cell lines (**Figure 3.21 b and f**). Cotreatment of RSL3 (0.62 μ M) and IFN γ (10 ng/ml) was similar to that of RSL3 (0.625 μ M) treatment alone in MC38 colon, LC2 lung, PEO1 ovarian cancer cell lines (**Figure 3.21 b, c and d**). Whereas there was a significant rescue of cell viability with the co-treatment of RSL3 (0.62 μ M) and IFN γ in 4T1 breast and OVCAR8 Ovarian cancer cell lines (**Figure 3.21 a and f**). These results give further evidence that the effect of IFN γ and ferroptosis susceptibility is dependent on the type of cancer cell line.

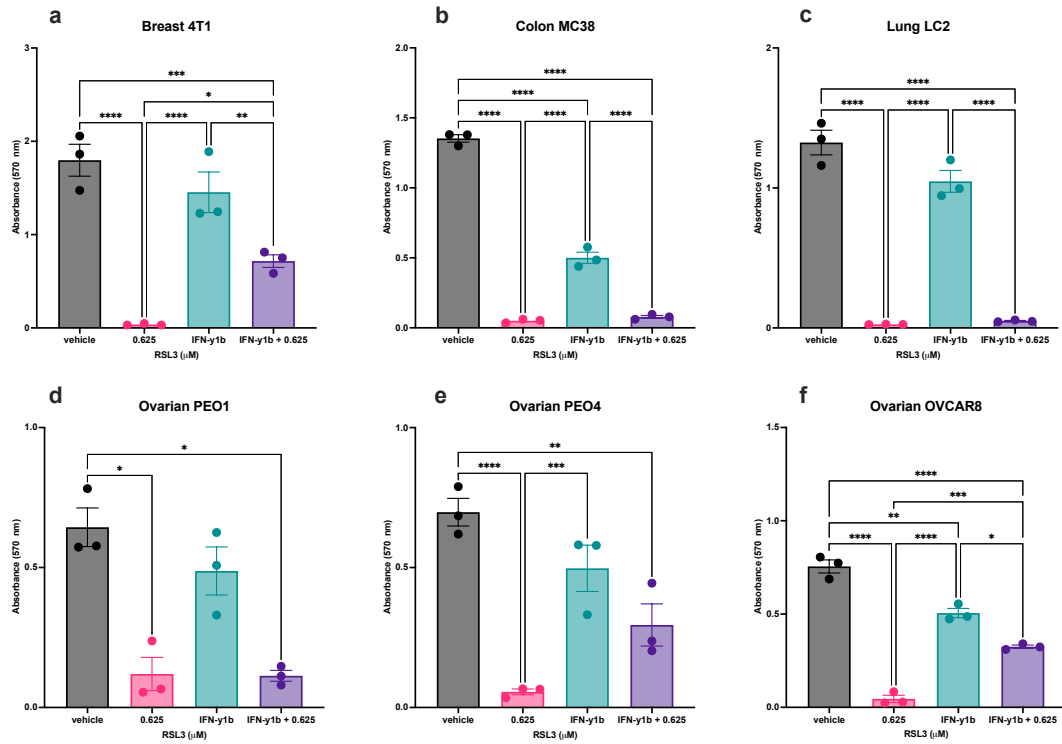


Figure 3.21: The effect of cotreatment with IFN γ and RSL3. The panel of cancer cell lines (a) 4T1; (b) MC-38; (c) LC-2; (d) PEO1; (e) PEO4; (f) OVCAR8 were cultured in media containing vehicle (v) or IFN γ or Erastin. Cells were treated with IFN γ for 30 min prior to treatment with Erastin for 24 h. Cell viability was evaluated using MTT assay after 24 h. Data was presented as mean (SEM) from three independent cell passage experiments and analysed using 2-way ANOVA; * $p < 0.05$, ** $p < 0.001$, *** $p < 0.001$.

3.5 Discussion

Current cancer therapies often become ineffective due to acquired resistance. The ability to evade programmed cell death is one of the hallmarks of cancer (Hanahan & Weinberg, 2011). However, induction of ferroptosis may provide a precision therapy, which could be induced in a number of cancer types. Ferroptosis is a form of non-apoptotic cell death, which is dependent on iron and characterised by the accumulation of lipid peroxides (Stockwell et al., 2017). Cancer cells are known to upregulate the key ferroptotic enzyme GPX4 in order to evade ferroptotic cell death (Chen et al., 2021; Zhang et al., 2022). Non-cancerous cells do not normally have a high abundance of ROS or upregulate GPX4, therefore providing a more specific therapeutic target for cancer treatment than systemic therapies (Liang et al., 2020).

The results from this study indicate that the induction of ferroptosis can be achieved either through the inactivation of system X_c^- by Erastin, resulting in the indirect inhibition of GPX4, or via the direct inhibition of the enzyme by RSL3. The results show that the panel of cancer cells are more susceptible to ferroptotic induction through the direct inhibition of GPX4, using RSL3. RSL3 is reported to only trigger ferroptotic cell death and not alternative cell death pathways (Angeli et al., 2014). However, the underlying mechanism of RSL3 is not fully understood (Li et al., 2021).

Erastin directly inhibits the SLC7A11 component of system X_c^- ; therefore, the susceptibility of cancer cells to Erastin induced ferroptotic induction may be a result of SLC7A11 basal levels. Previous studies have shown that the inhibition of system X_c^- results in compensatory transcriptional upregulation of the light chain subunit *SLC7A11* (Dixon et al., 2012). The western blots indicate that the ovarian PEO1 and PEO4 cancer cell lines have the lowest basal expression of SLC7A11 in the panel of cancer cells, which could indicate why the two cell lines were less susceptible to Erastin induced ferroptotic cell death.

There were observed differences in cancer cell sensitivity to Erastin-induced ferroptosis between the MTT cell viability assay and DRAQ7 cell death stain. Studies have also shown that Erastin binds to voltage-dependent anion channels (VDACs; Yagoda et al., 2007). The transport of ions and metabolites into the mitochondria is facilitated by VDACs. Therefore, cancer cell sensitivity to Erastin is not only dependent on SLC7A11 but also VDAC expression and subsequently effects sensitivity to ferroptotic induction. Therefore, it would have been beneficial to investigate levels of VDAC within the panel of cancer cell lines.

A key characteristic of ferroptotic induction is cell shrinkage, all cancer cells showed a decrease in cell size after treatment with RSL3. Although, changes in cell size are also characteristic of other forms of programmed cell death, therefore further research into characteristic ferroptotic cell death is required, such as GSH production and assessment of apoptosis.

Increased accumulation of lipid peroxides is also characteristic of ferroptosis. Lipid peroxidation was investigated by Liperfluo, which showed increased lipid peroxidation after treatment with Erastin. Erastin-induced lipid peroxidation was reduced after treatment with the lipid peroxide scavenger, Liproxstatin-1. The ability of liproxstain-1 to rescue cell viability in the panel of cancer cells from ferroptosis induced by Erastin or RSL3 indicates that ferroptosis was induced. However, the underlying mechanism is not clearly understood (Feng et al., 2019). Although, liproxstain-1 has been shown to preserve GPX4 whilst downregulating ACSL4, the key enzyme in PUFA formation (Cao et al., 2021; Hou et al., 2022).

The ovarian PEO1 and PEO4 cancer cell lines showed low basal levels of GPX4. However, all the panel of cancer cells showed high susceptibility to RSL3 induced ferroptotic cell death. Generally, GPX4 is downregulated after the induction of ferroptosis (Li et al., 2021; Liu et al., 2022). Surprisingly, the intracellular levels of GPX4 significantly increased in the ovarian cancer cell

lines. Therefore, changes in GPX4 expression could be a coping mechanism in order to evade ferroptotic cell death.

Previous studies have shown that IFN γ induced ferroptotic cancer cell death is dependent on acyl-coenzyme A (CoA) synthetase long-chain family member 4 (ACSL4; Liao et al., 2022). The present chapter shows that IFN γ induced cell death in breast and colon cancer cells, although the mechanism is not understood here. Further research is required to determine the levels of ACSL4 in the panel of cancer cells. Previous studies have also shown that IFN γ facilitates Erastin-induced ferroptotic cell death (Yu et al., 2022); however, in this study we found that IFN γ rescued lung and ovarian OVCAR8 cells from Erastin. Further research into the molecular mechanisms involved in Erastin-induced ferroptosis in the panel of cancer cells is required. Previous studies have also shown IFN γ enhances cell sensitivity to RSL3 induced ferroptotic cell death (Wang et al., 2019). This current chapter showed that IFN γ rescued breast, ovarian PEO4 and OVCAR8 cells from RSL3. Further research into the molecular mechanisms involved in RSL3-induced ferroptosis in the panel of cancer cells is required.

3.6 Conclusion

This study provides support that ferroptosis can be induced in a panel of cancer cells. There was a greater susceptibility to RSL3-induced ferroptosis in the panel of cancer cells. Further research on ferroptosis biomarkers is required in order to enhance ferroptotic therapies for cancer treatment.

Chapter 4: mTORC1/2 and the AMPK pathway link to ferroptosis

4.1 Introduction

Depletion in energy and nutrients in cancer cells activates the adenosine monophosphate-activated protein kinase (AMPK) pathway. AMPK is a heterotrimeric complex, that in humans is formed of three isoforms: AMPK- α (α 1 and α 2), AMPK- β (β 1 and β 2) and AMPK- γ (γ 1, γ 2 and γ 3). Therefore, in humans there are 12 distinct combinations of these isoforms that can be generated, which has been shown to be specific to cell type (Ross et al., 2016; **Figure 4.1**). The α -subunit contains threonine residue (Thr172), which once phosphorylated results in the activation of AMPK. The β -subunit enables association with glycogen and the γ -subunit responds to changes in the ATP:AMP ratio (Hudson et al., 2003; Xiao et al., 2007).

The phosphorylation of Thr172, and therefore the activation of AMPK, can be a result of liver kinase B1 (LKB1) interaction. Studies have shown that the tumour suppressor LKB1 is responsible for the majority of AMPK activation (Shackelford & Shaw, 2009). Another upstream regulator of AMPK is calmodulin-dependent protein kinase kinase- β (CAMKK β , also known as CAMKK2, Hurley et al., 2005). Pharmaceutical compounds are also known to activate AMPK, such as 5-aminoinidazole-4-carboxamide ribonucleotide (AICAR, Corton et al., 1995; **Figure 4.1 and 4.3**). AICAR is incorporated into the cell by adenosine transporters before being phosphorylated by adenosine kinase, which generates an adenosine monophosphate (AMP) analogue: AICAR monophosphate (ZMP). ZMP is then able to bind to the γ -subunit of AMPK, resulting in AMPK activation through phosphorylation at Thr172 by LKB1 (Sullivan et al., 1994; Corton et al., 1995; **Figure 4.1**).

Compound C, also known as dorsomorphin (6-[4-(2-piperidin-1-ylethoxy)phenyl]-3-pyridin-4-ylpyrazolo [1,5-a]pyrimidine) is the only known cell-permeable inhibitor of AMPK (Liu et al., 2014; **Figure 4.1 and 4.3**). However, Compound C also effects other pathways, such as the bone morphogenetic protein (BMP) pathway and also inhibits other kinases, such as ERK8 (extracellular signal-regulated kinase 8), MNK1 (MAP kinase-interacting

serin/threonine-protein kinase 1) and HIPK2 (Homeodomain interacting protein kinase 2, Vogt et al., 2011). Compound C is an ATP-competitive inhibitor of AMPK; however its effect can be reversed (Li & Chen, 2019).

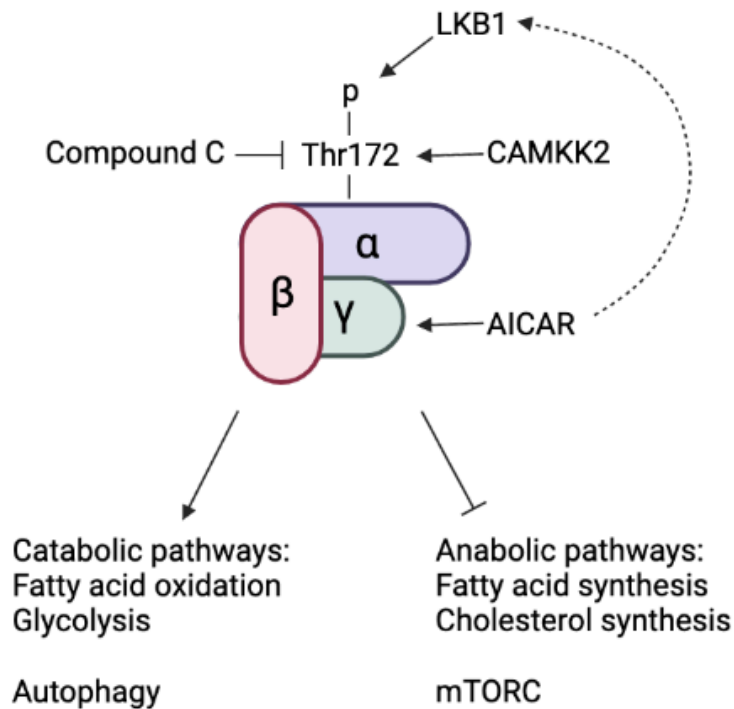


Figure 4.1: Schematic of AMPK activation in cells. AMPK is composed of three subunits; α , β and γ . LKB1 is responsible for the phosphorylation of AMPK at Thr172. The activation of AMPK results in the activation of catabolic pathways such as fatty acid oxidation and glycolysis. AMPK activation also induces autophagy. The activation of AMPK results in the inhibition of anabolic pathways such as fatty acid and cholesterol synthesis. AMPK activation also inhibits mTORC. AMPK is activated by AICAR and inhibited by Compound C (Created in BioRender.com).

The AMPK pathway is triggered after a depletion in intracellular ATP levels and a corresponding increase in AMP levels. Once activated, AMPK inhibits all anabolic pathways that promote cell growth and activates catabolic pathways that generate ATP (Mihaylova & Shaw, 2011; Hardie et al., 2016; **Figure 4.1**). In the short term, AMPK activation results in an increased uptake of glucose and promotion of fatty acid oxidation. In the long term, AMPK activation results in oxidative metabolism and consequently quiescent cells (Hardie et al., 2012). Hardie et al., 1989 discovered that AMPK phosphorylates and inactivates the two key enzymes of fatty acid and cholesterol synthesis: ACC1 (Acetyl-CoA carboxylase-1) and 3-hydroxy-3-methylglutaryl-CoA reductase (HMGCR) respectively. The phosphorylation of ACC-1 is now a

widely used biomarker for AMPK activation. Phosphorylated AMPK inhibits the Mammalian Target of Rapamycin (mTOR) pathway; which is switched on by nutrient availability and promotes cell growth through anabolic pathways (Hardie et al., 2012; **Figure 4.1**). AMPK is also important for the promotion of autophagy, through the direct phosphorylation of autophagy proteins within the mTORC1, ULK1 and PIK3C3/VPS34 complexes (Li & Chen, 2019; **Chapter 1, Section 1.12**). Phosphorylated AMPK inhibits mTORC, which relieves phosphorylation of ULK1 at Ser757 residue; AMPK phosphorylates two other residues of ULK1, Ser555 and Ser317, in order to trigger autophagy (Bach et al., 2011; Kim et al., 2011; Tian et al., 2015). Therefore, mTOR is an important regulator of autophagy, as mTOR can prevent autophagy through the phosphorylation of Ser757 residue of ULK1.

mTOR is a nutrient sensor that regulates growth, proliferation and survival. mTOR is a serine/threonine protein kinase, which forms two structurally and functionally distinct multiprotein complexes; mTORC1 and mTORC2 (Kim et al., 2017). Both mTORC1 and mTORC2 contain the key components, mTOR, DEP domain-containing mTOR-interacting protein (DEPTOR), and mammalian lethal with sec-13 protein 8 (mLST8). The unique components of mTORC1 are regulatory-associated protein of mammalian target of rapamycin (RAPTOR) and proline-rich AKT substrate of 40 kDa (PRAS40, a negative regulator of mTORC1; **Figure 4.2**). The role of mTORC1 is to promote nucleotide synthesis and protein synthesis and also inhibit autophagy, as previously described in **Chapter 1 Section 1.12**. The two main substrates of mTORC1 are the ribosomal protein S6 kinase 1 (S6K; formally known as p70 ribosomal S6 kinase; P70S6K) and the eukaryotic initiation factor 4E binding protein 1 (4EBP1; Durán et al., 2012; **Figure 4.3**). The phosphorylation of S6K (p-p70S6K) is the most widely used biomarker for mTOR activation (Granville et al., 2007). Whereas, mTORC2 is defined by the rapamycin-insensitive companion of mTOR (RICTOR), protein observed with RICTOR (PROTOR) and stress-activated MAP kinase interacting protein 1 (mSIN1; **Figure 4.2**). The two main substrates of mTORC2 are AKT (also known as protein kinase B), protein kinase C (PKC; for cytoskeletal reorganisation) and

serum/glucocorticoid regulated kinase 1 (SGK1, important for iron transport; Jacinto et al., 2004; Durán et al., 2012; **Figure 4.3**). The role of mTORC2 is less understood but is known to activate AKT and therefore inhibits apoptosis (described in detail in **Chapter 1 Section 1.13**).

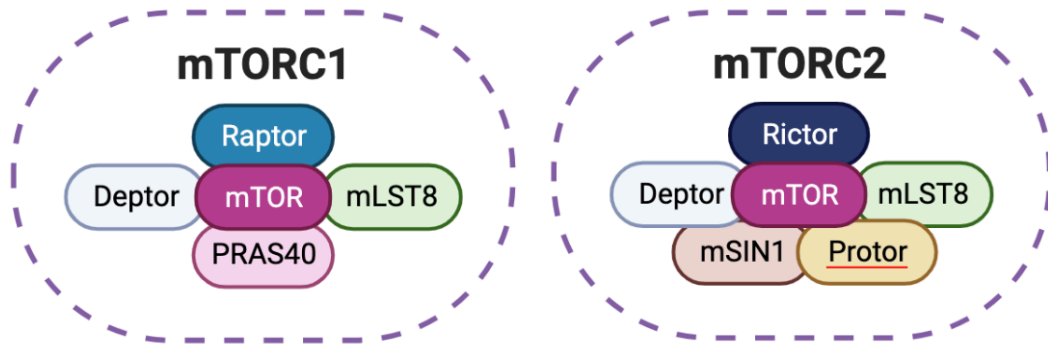


Figure 4.2: Schematic structure of mTORC1 and mTORC2. Both complexes contain mTOR, DEPTOR and mLST8. Unique to mTORC1 is RAPTOR and PRAS40, whereas mTORC2 contains RICTOR, mSIN1 and PROTOR (Adapted from BioRender.com).

The activity of mTORC1 is controlled by the small GTPase Ras-homologue enriched in brain (RHEB; Yang et al., 2013; Kim et al., 2017). The tuberous sclerosis complex 2 (TSC2) is primarily associated with the activation of the small GTPase RHEB. TSC is a complex that causes the formation of benign tumours within vital organs caused by mutations in *TSC1* (hamartin) and *TSC2* (Tuberin) genes. These tumours express continued activation of mTORC1 (Tee et al., 2003; Parkhitko et al., 2011). The activation of PI3K-AKT signalling results in the inhibition of TSC1-TSC2 and therefore the activation of mTORC1, AKT can also phosphorylate PRAS40, alleviating its inhibition on mTORC1.

Small GTPases are also responsible for regulating mTOR in response to amino acid availability (Takahara et al., 2020). These GTPases interact with RAPTOR and consequently RHEB, resulting in the activation of mTORC1. The amino acid glutamine in combination with leucine has been shown to activate mTORC1 by enhancing glutaminolysis and α -KG production (Durán et al., 2012). Durán et al., 2012 found that the inhibition of glutaminolysis resulted in

the activation of mTORC1, and therefore inhibits autophagy (Durán et al., 2012).

Naturally occurring compounds such as rapamycin (sirolimus) and its analogs are known to inhibit mTORC1 (Laplante & Sabatini, 2012; **Figure 4.3**). However, how rapamycin interacts with mTORC1 is unknown, but it has been proposed that rapamycin destabilises the mTOR-Raptor complex (Kim et al., 2002). Rapamycin has also been found to suppress mTORC2 when higher concentrations or chronic treatments are used (Foster & Toschi, 2009). Rapamycin is a naturally occurring substance that is produced by the bacterium *Streptomyces hygroscopicus* and was initially used as an antifungal agent (Ballou & Lin, 2008). Since then, rapamycin was found to be an effective immunosuppressant, and was therefore FDA approved for the prevention of renal allograft rejection (Ballou & Lin, 2008). Further studies have also shown promising anti-cancer effects of rapamycin in mouse models (Granville et al., 2007; Ehninger et al., 2014). Pharmaceutical compounds such as 1-[4-[4-(1-Oxopropyl)-1-piperazinyl]-3-(trifluoromethyl)phenyl]-9 (3-quinolinyl)-benzo[h]-1,6-naphthyridin-2(1H)-one (Torin-1) is known to inhibit both mTORC1 and mTORC2 (Thoreen et al., 2009; **Figure 4.3**). Torin-1 has been found to be a more potent inhibitor of mTOR in comparison to rapamycin (Thoreen et al., 2009). Torin-1 is a selective ATP-competitive mTOR inhibitor, therefore inhibiting both complexes: mTORC1 and mTORC2 (Leontieva et al., 2015).

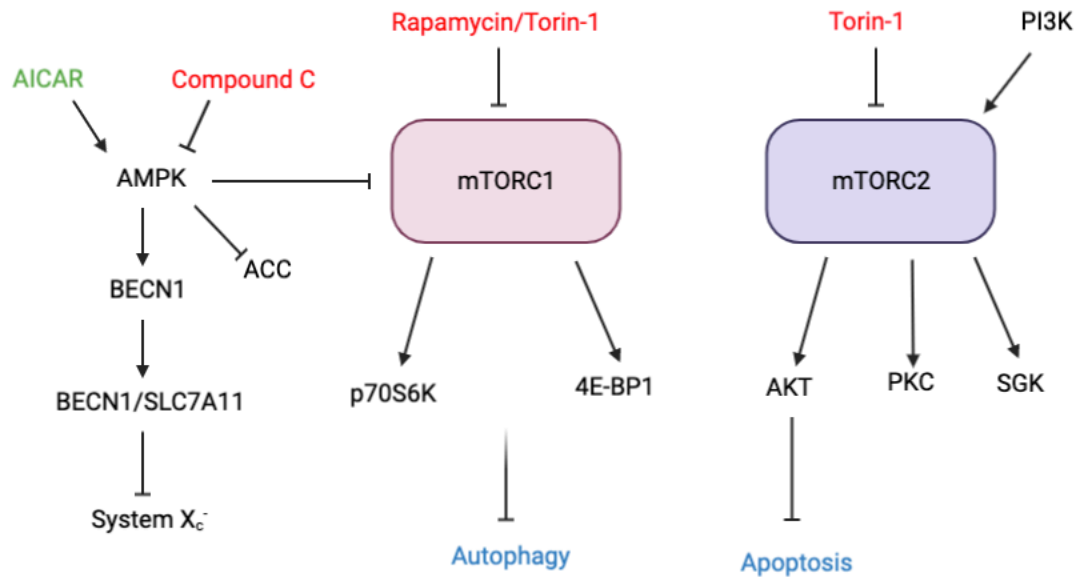


Figure 4.3: Schematic of cellular metabolism.

Recent studies have shown that ferroptosis can be inhibited through AMPK-dependent phosphorylation (Lee et al., 2020). Cancer cells with high basal AMPK activation have been found to be resistant to ferroptotic induction. The AMPK activator, AICAR has been shown to block ferroptosis and lipid peroxide production in mouse embryonic fibroblasts (MEFs; Li et al., 2020). Lee et al., 2020 showed that inhibition of AMPK by compound C sensitised a ferroptosis resistant cell line, ACHN, which has high basal AMPK, to ferroptotic induction by Erastin. Whereas, the ferroptosis sensitive cell line Caki-1, which has low basal AMPK, was partly protected against ferroptotic induction by Erastin due to increased ACC phosphorylation. The phosphorylation and inhibition of ACC by AMPK, inhibits ferroptosis due to the role ACC plays in the synthesis of PUFAs (Lee et al., 2020). This was also supported by Li et al., 2020, who found that ACC is required for ferroptotic induction in cells with deficient AMPK and LKB1. However, Lee et al., 2020 found that compound C inhibited ferroptosis in MEFs and also AMPK double knockout MEFs, indicating that compound C inhibition is independent of AMPK. However, the resistance to ferroptosis via AMPK is not likely due to the induction of autophagy as other studies have shown that autophagy promoted ferroptosis (Liu et al., 2020). LKB1 is the main

activator of AMPK, however the tumour suppressor is commonly mutated in tumour cells. Li et al., 2020 used non-small cell lung cancer cells, in which LKB1 is mutated to demonstrate that the loss of LKB1 enhances cancer cell susceptibility to ferroptosis.

The key regulator of autophagy, BECN1, has been found to promote ferroptosis, in an autophagy-independent manner through the direct inhibition of SLC7A11, the core component of system X_C⁻ (Song et al., 2018; **Figure 4.3**). AMPK phosphorylates BECN1 and as a result forms the BECN1-SLC7A11 complex to consequently induce ferroptosis. Song et al., 2018 found that Erastin, the system X_C⁻ inhibitor promoted BECN1 binding to SLC7A11 in order to initiate ferroptosis.

The glutaminolysis pathway also results in the formation of GSH and therefore plays a role in ferroptosis (Gorrini et al., 2013). The glutaminases GLS1 and GLS2 catalyse the conversion of glutamine to glutamate, which can then either enter the TCA cycle or react with cysteine for the production of GSH (Gao et al., 2015). Glutaminases have previously been shown to be regulated by oncogenes and consequently contribute to tumour cell growth (Wang et al., 2010). Gorrini et al., (2013) found that GLS2 is essential for the induction of ferroptosis. Accordingly, GLS1 is upregulated in cancers, whereas GLS2 is repressed (Hu et al., 2010). Before entering the TCA cycle, glutamate is converted into α -KG by the glutamate dehydrogenase enzyme. Inhibition of glutaminolysis directly suppresses ferroptosis, whereas supplementation with α -KG or downstream intermediates, results in ferroptotic cell death (Gao et al., 2015; Gao et al., 2019; **Figure 4.4**). The inhibition of α -KG dehydrogenase suppressed the induction of ferroptosis even after cystine starvation (Shin et al., 2020). The importance of the TCA cycle and α -KG in ferroptotic induction is poorly understood but could be related to the function in the electron transport chain and fatty acid biosynthesis (Gan, 2021).

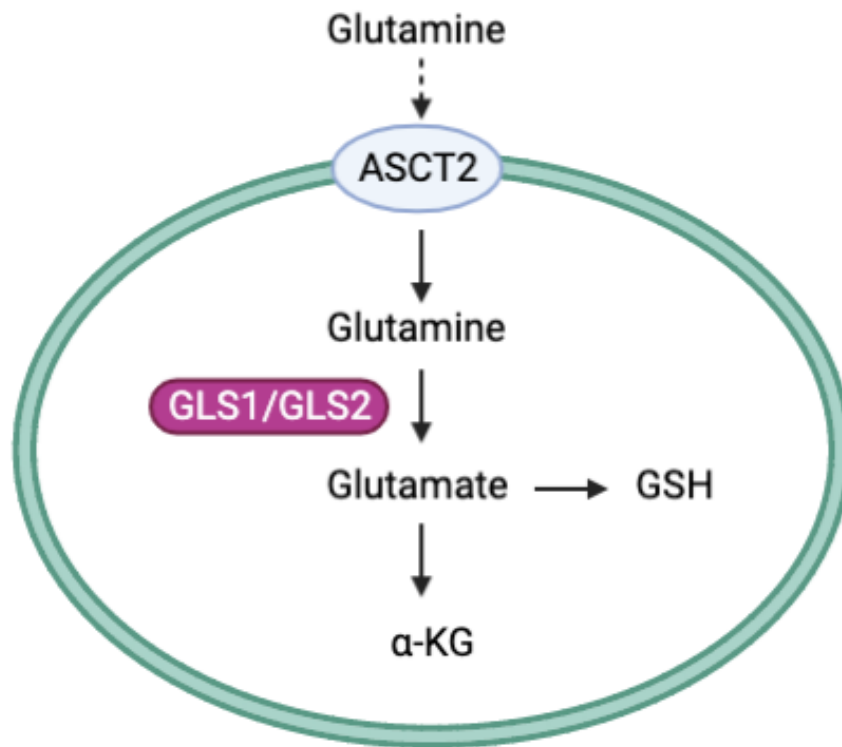


Figure 4.4: Schematic overview of the Glutaminolysis Pathway. The pathway results in the generation of glutathione (GSH) or α -ketoglutarate (α -KG). Glutamine is incorporated into the cell via the transporter ASCT2. Glutamine is converted to glutamate by the glutaminases, GLS1 and GLS2. Glutamate is either converted into α -KG to fuel the TCA cycle or used to biosynthesise GSH, the reducing substrate of GPX4 activity (Created in BioRender.com).

Glutathione is a thiol-containing tripeptide, requiring cysteine, glycine and glutamate for synthesis. Cysteine is a major rate restricting precursor, that is acquired by cancer cells through the system X_c⁻. Cancer cells are also able to biosynthesise cysteine, derived from methionine using the transsulfuration pathway. This pathway is responsible for controlling sulphur metabolism and involves the transfer of sulphur from homocysteine to cysteine using cystathionine (McBean, 2012; Sbodio et al., 2019; **Figure 4.5**).

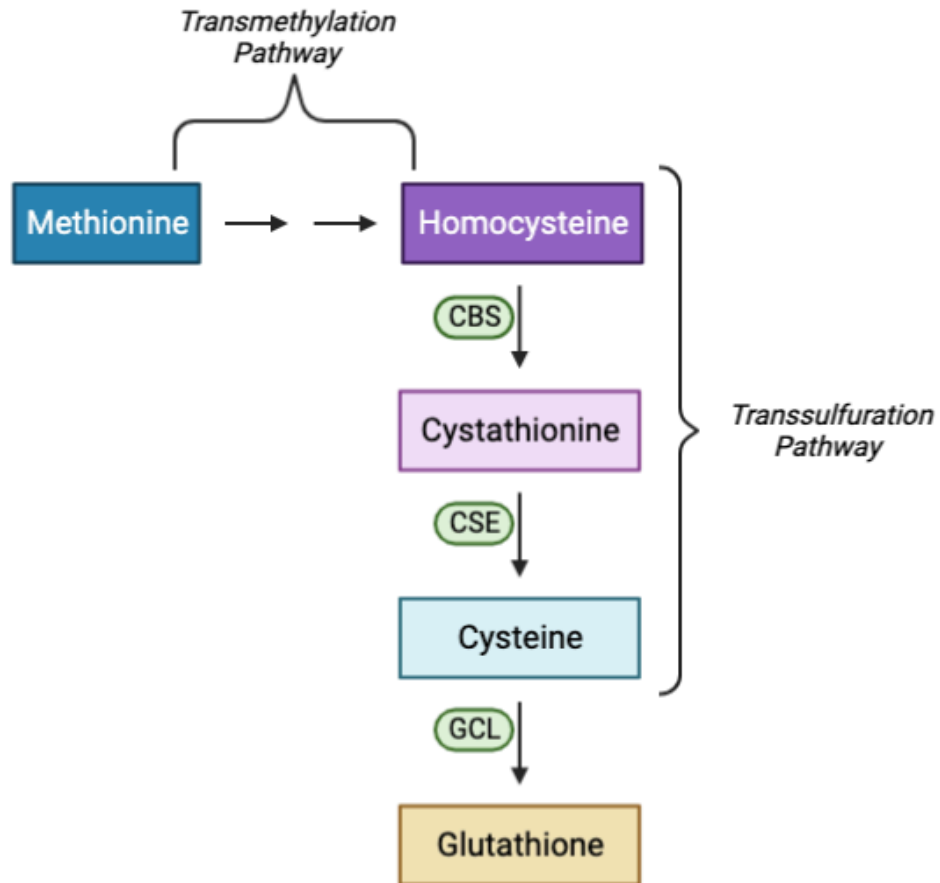


Figure 4.5: Schematic overview of the Transsulfuration Pathway. The pathway results in the generation of cysteine from methionine. Homocysteine is converted to cystathionine by cystathionine β -synthase (CBS) before generating cystine by cystathionine γ -lyase (CSE). Cysteine is then condensed to synthesis glutathione by glutamate-cysteine ligase enzyme (GCL; Created in BioRender.com).

4.2 Aims and Hypothesis

Hypothesis: The inhibition of AMPK or mTOR increases cancer cell susceptibility to ferroptotic induction.

Aims:

1. To investigate the role of mTORC1 and mTORC2 in Erastin or RSL3-induced ferroptotic cell death.
2. To investigate the role of AMPK in Erastin or RSL3-induced ferroptotic cell death.
3. To investigate the role of glutaminases in ferroptotic induction.
4. To determine a link between ferroptosis and other forms of programmed cell death.

4.3 Materials and Methods

4.3.1 MTT ((3-(4, 5-dimethylthiazol-2-yl)-2, 5- diphenyltetrazolium bromide)) assay

Cells were seeded at the required density, 2.5×10^3 (OVCAR8 ovarian), 5.0×10^3 (4T1 breast and MC-38 colon), 7.5×10^3 (LC-2 lung, PEO1 ovarian and PEO4 ovarian) cells/well in a 96-well plate (Helena Biosciences Cat#92096) 24 h prior to treatment. Cells were treated in triplicate with AMPK and mTOR inhibitors and inducers (compound C (10 μ M; Calbiochem, Cat#171260), AICAR (1mM; Merk, Cat#A9978), torin-1 (50 nM; Bio-Techne, Cat#4247) and rapamycin (500 nM; Bio-Techne, Cat#1292)) diluted in 50 μ l of complete media for 30 mins, 37°C, 5% CO₂ in air. Cells were then treated with Erastin (2.5 μ M) or RSL3 (0.625 μ M) diluted in 50 μ l of complete media before further incubation for 24 h, 37°C, 5% CO₂ in air. Alternatively, cells were treated for 30 mins with Compound 968 (10 μ M; Sigma, Cat#SML1327) prior to treatment with Erastin (2.5 μ M) or RSL3 (0.625 μ M), diluted in 100 μ l of complete media before further incubation for 24 h, 37°C, 5% CO₂ in air. At the end of the incubation time an MTT assay was performed (**Chapter 2; Section 2.7**). Briefly, cells were incubated with 10 mg/ml MTT for 2 h at 37°C, formazan crystals were dissolved in DMSO and absorbance was measured at 570 m using a microplate reader (POLARstar Omega; BMG).

4.3.2 Western Blot

Cells were seeded at the required density, 5.0×10^4 (4T1 breast, MC-38 colon and LC-2 lung) cells/well in a 6-well plate (Greiner Cat#657160) 24 h prior to treatment. Cells were then treated with AMPK and mTOR inhibitors and inducers (compound C (10 μ M), AICAR (1mM)) diluted in 500 μ l of complete media for 30 mins, 37°C, 5% CO₂ in air. Cells were then treated with Erastin (2.5 μ M) or RSL3 (0.625 μ M), for a further 24 h, 37°C, 5% CO₂ in air. Cells then underwent protein extraction and quantification using the DC assay, followed by western blot (**Chapter 2; Section 2.8**). Briefly 10 μ g/lane of protein was probed overnight to quantify the abundance of phospho-P70S6K,

P70S6K, LC3B, phospho-AMPK, AMPK, Beclin-1, GPX4, ULK1, SER757, SER555 and β -actin (**Table 3**).

4.3.3 Statistics

GraphPad prism 7.0 was used for statistical analysis. Normally distributed data were subjected to a one-way or two-way ANOVA with Brown-Forsythe or Dunnett's or Bonferroni post-hoc test; comparing the treatment in relation to the vehicle for $n \geq 3$. Significance was assumed when $P < 0.05$.

4.4 Results

Currently little is known about the link between ferroptosis and the AMPK/mTOR pathway, although recent studies have shown a link between ferroptosis and metabolism (Shimada et al., 2016). Initially, the panel of cancer cells were treated with known activators and inhibitors of AMPK and mTOR in order to link these pathways with ferroptosis.

4.4.1 Investigating mTOR and ferroptosis in a panel of cancer cell lines

Crosstalk between energy stress and ferroptosis was explored in a panel of cancer cells. The cells were treated with the mTOR inhibitors Torin-1 (50 nM; inhibits mTORC1 and mTORC2) and Rapamycin (500 nM; inhibits mTORC1). The cells were also co-treated with the ferroptosis inducers Erastin (2.5 μ M; **Figure 4.6**) or RSL3 (0.625 μ M; **Figure 4.7**).

The treatment of rapamycin (500 nM) or torin-1 (50 nM) alone resulted in a significant reduction in cell viability in breast cancer cells (**Figure 4.6 a**). There was a significant decrease in colon cancer (**Figure 4.6 b**) cell viability after cotreatment of torin-1 (50 nM) and Erastin (2.5 μ M), but also an observed insignificant decrease with rapamycin (500 nM) and Erastin (2.5 μ M;

P=0.0514). These results indicate that the mTOR pathway may not affect ferroptosis in the majority of cancers.

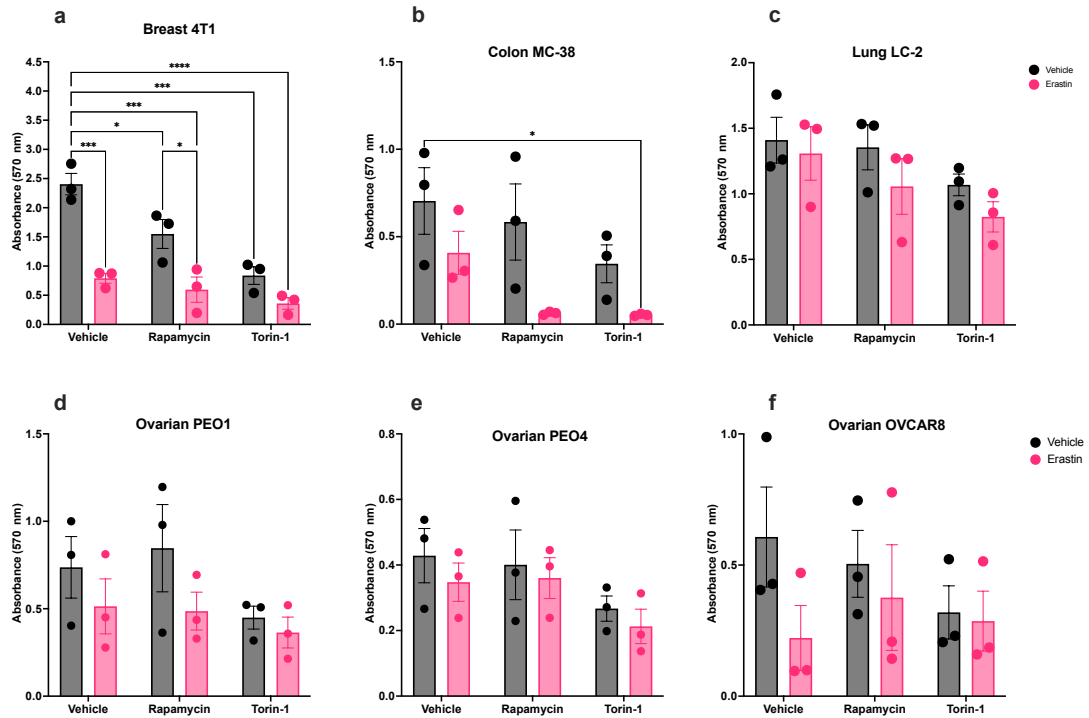


Figure 4.6: Synergistic effect of mTOR inhibitors Rapamycin and Torin-1 with the ferroptosis inducer Erastin. The panel of cancer cell lines (a) 4T1, (b) MC-38, (c) LC-2, (d) PEO1, (e) PEO4, (f) OVCAR8 were cultured in media containing vehicle or Rapamycin or Torin-1 or Erastin. Cells were treated with Rapamycin or Torin-1 30 min prior to treatment with Erastin for 24 h. Cell viability was evaluated using MTT assay after 24 h. Data was presented as mean (SEM) from three independent experiments and analysed using 2-way ANOVA; *p<0.05, **p<0.001, ***<0.001.

The treatment of rapamycin (500 nM) and torin-1 (50 nM) alone resulted in a significant reduction in cell viability in breast cancer cells (**Figure 4.7 a**). There was a significant decrease in cell viability in breast (**Figure 4.7 a**), colon (**Figure 4.7 b**), lung (**Figure 4.7 c**) and ovarian PEO1 (**Figure 4.7 d**) cancer cell lines after cotreatment with rapamycin (500 nM) or torin-1 (50 nM) with RSL3 (0.625 μ M); however, this was the same effect as RSL3 (0.625 μ M) treatment alone. These results further indicate that the mTOR pathway may not affect ferroptosis in the majority of cancers.

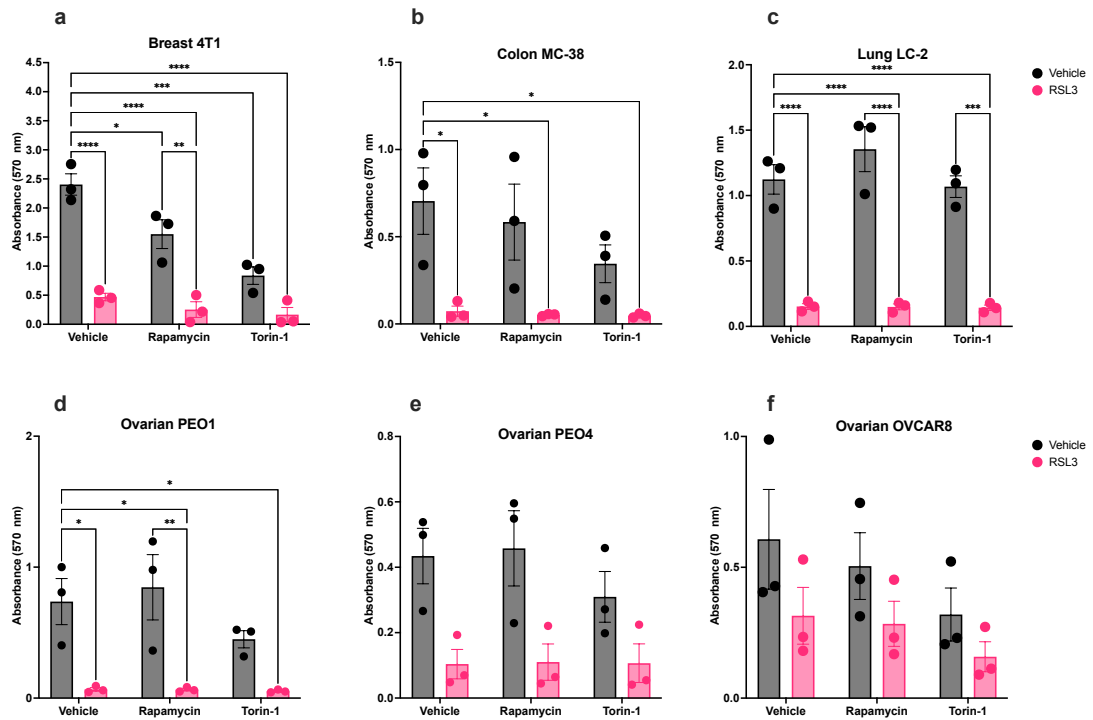


Figure 4.7: Synergistic effect of mTOR inhibitors Rapamycin and Torin-1 with the ferroptosis inducer RSL3. The panel of cancer cell lines (a) 4T1, (b) MC-38, (c) LC-2, (d) PEO1, (e) PEO4, (f) OVCAR8 were cultured in media containing vehicle or Rapamycin or Torin-1 or RSL3. Cells were treated with Rapamycin or Torin-1 30 min prior to treatment with RSL3 for 24 h. Cell viability was evaluated using MTT assay after 24 h. Data was presented as mean (SEM) from three independent experiments and analysed using 2-way ANOVA; * $p < 0.05$, ** $p < 0.001$, *** $p < 0.001$.

4.4.2 Investigating AMPK and ferroptosis in a panel of cancer cell lines

The panel of cancer cells were treated with the AMPK inhibitor, compound C (10 μ M) and the AMPK activator, 5-aminoinidazole-4-carboxamide-ribose-5-phosphate (AICAR; 1mM). The cells were also co-treated with Erastin (2.5 μ M; **Figure 4.8**) or RSL3 (0.625 μ M; **Figure 4.9**) in order to help determine the link between ferroptosis and the AMPK pathway.

The treatment of Compound C (10 μ M) and AICAR (1mM) alone resulted in a significant reduction in cell viability in breast (**Figure 4.8 a**) cancer cells. There was a significant reduction in lung (**Figure 4.8 c**) cancer cell viability after treatment with AICAR (1mM) and Erastin (2.5 μ M), in comparison to Erastin (2.5 μ M) treatment alone. There was a trend of decreased cell viability in colon

cancer cells cotreated with AICAR (1 mM) and Erastin (2.5 μ M; $P=0.0560$), although this did not reach significance (**Figure 4.8 b**).

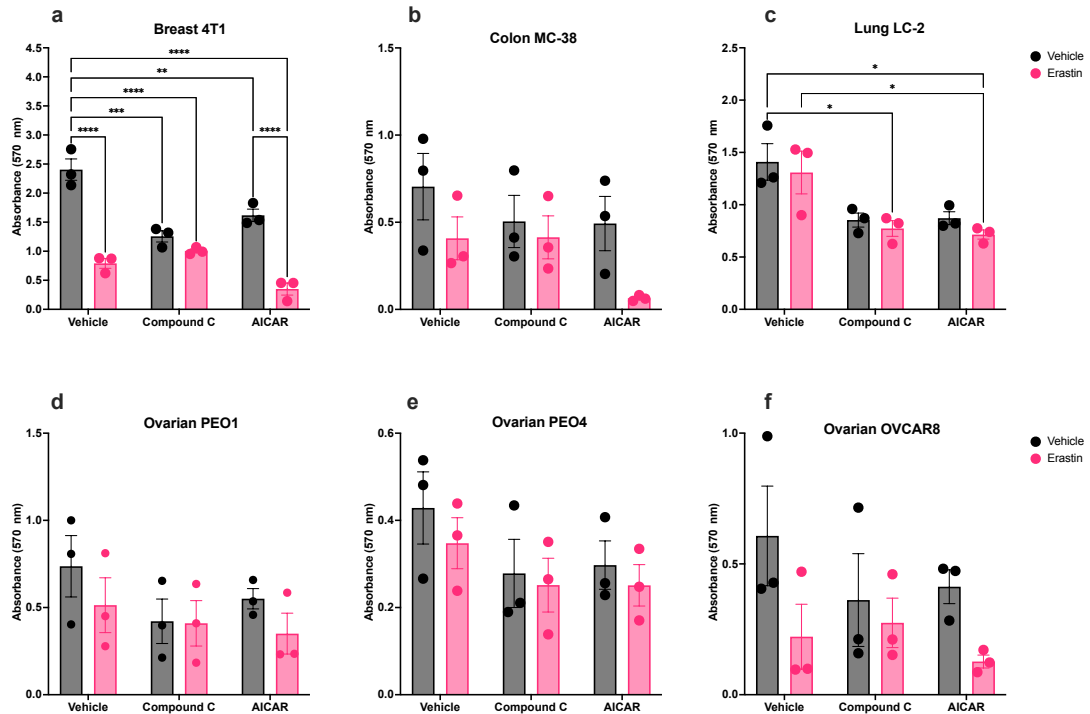


Figure 4.8: Synergistic effect of AMPK inhibitor Compound C and AMPK activator AICAR with the ferroptosis inducer Erastin. The panel of cancer cell lines (a) 4T1, (b) MC-38, (c) LC-2, (d) PEO1, (e) PEO4, (f) OVCAR8 were cultured in media containing vehicle or compound C or AICAR or Erastin. Cells were treated with Compound C or AICAR 30 min prior to treatment with Erastin for 24 h. Cell viability was evaluated using MTT assay after 24 h. Data was presented as mean (SEM) from three independent experiments and analysed using 2-way ANOVA; * $p<0.05$, ** $p<0.001$, *** $p<0.001$.

The treatment of Compound C (10 μ M) alone resulted in a significant reduction in cell viability in breast cancer cells (**Figure 4.9 a**). There was a significant increase in cell viability with the cotreatment of Compound C (10 μ M) and RSL3 (0.625 μ M) in breast (**Figure 4.9 a**) and lung cancer MC cells (**Figure 4.9 c**), indicating that Compound C is able to rescue against RSL3 induced ferroptotic cell death. There was also an observed insignificant increase in cell viability under the cotreatment of compound C (10 μ M) and RSL3 (0.625 μ M) in the colon ($P=0.2880$, **Figure 4.9 b**), ovarian PEO1 ($P=0.3360$; **Figure 4.9 d**) and ovarian PEO4 ($P=0.7375$; **Figure 4.9 e**) cells, in comparison to RSL3 (0.625

μM) treatment alone. The cotreatment of AICAR (1 mM) and RSL3 (0.625 μM) resulted in a significant increase in cell viability in breast cancer cells (**Figure 4.9 a**).

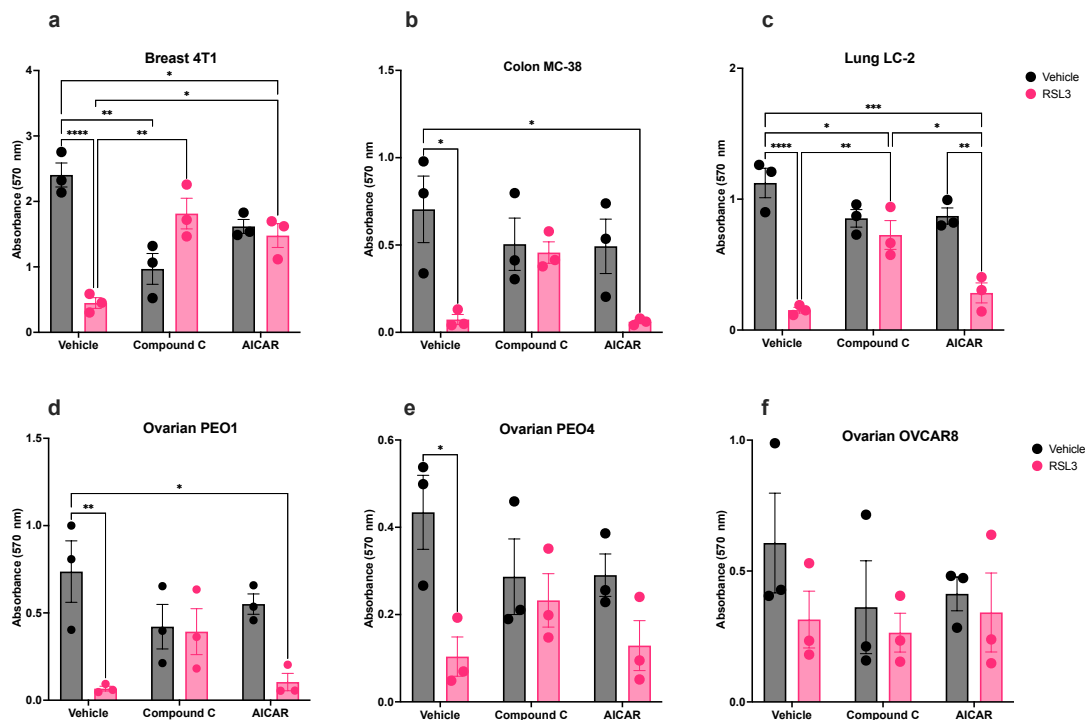


Figure 4.9: Synergistic effect of AMPK inhibitor Compound C and AMPK activator AICAR with the ferroptosis inducer RLS3. The panel of cancer cell lines (a) 4T1, (b) MC-38, (c) LC-2, (d) PEO1, (e) PEO4, (f) OVCAR8 were cultured in media containing vehicle or compound C or AICAR or RSL3. Cells were treated with Compound C or AICAR 30 min prior to treatment with RSL3 for 24 h. Cell viability was evaluated using MTT assay after 24 h. Data was presented as mean (SEM) from three independent experiments and analysed using 2-way ANOVA; * $p < 0.05$, ** $p < 0.001$, *** $p < 0.001$.

Due to the effects compound C and AICAR had on the panel of cancer cells, they were used for more in depth investigations. Moving forward, the breast, colon and lung cancer cells were focused on to assess the contribution of mTOR/AMPK pathways to ferroptosis. Initially the key ferroptosis enzyme, GPX4 was looked at to determine the increased rescue compound C had against RSL3 and also the increased cell death AICAR had with Erastin.

Previously, the breast cancer cell line displayed a significant increase in cell viability after the cotreatment of RSL3 with compound C or AICAR, in comparison to RSL3 treatment alone (**Figure 4.9 a**). However, the breast

cancer cells showed no significant changes in GPX4 protein after treatment with Erastin, RSL3 or combination with compound C and AICAR (**Figure 4.10**).

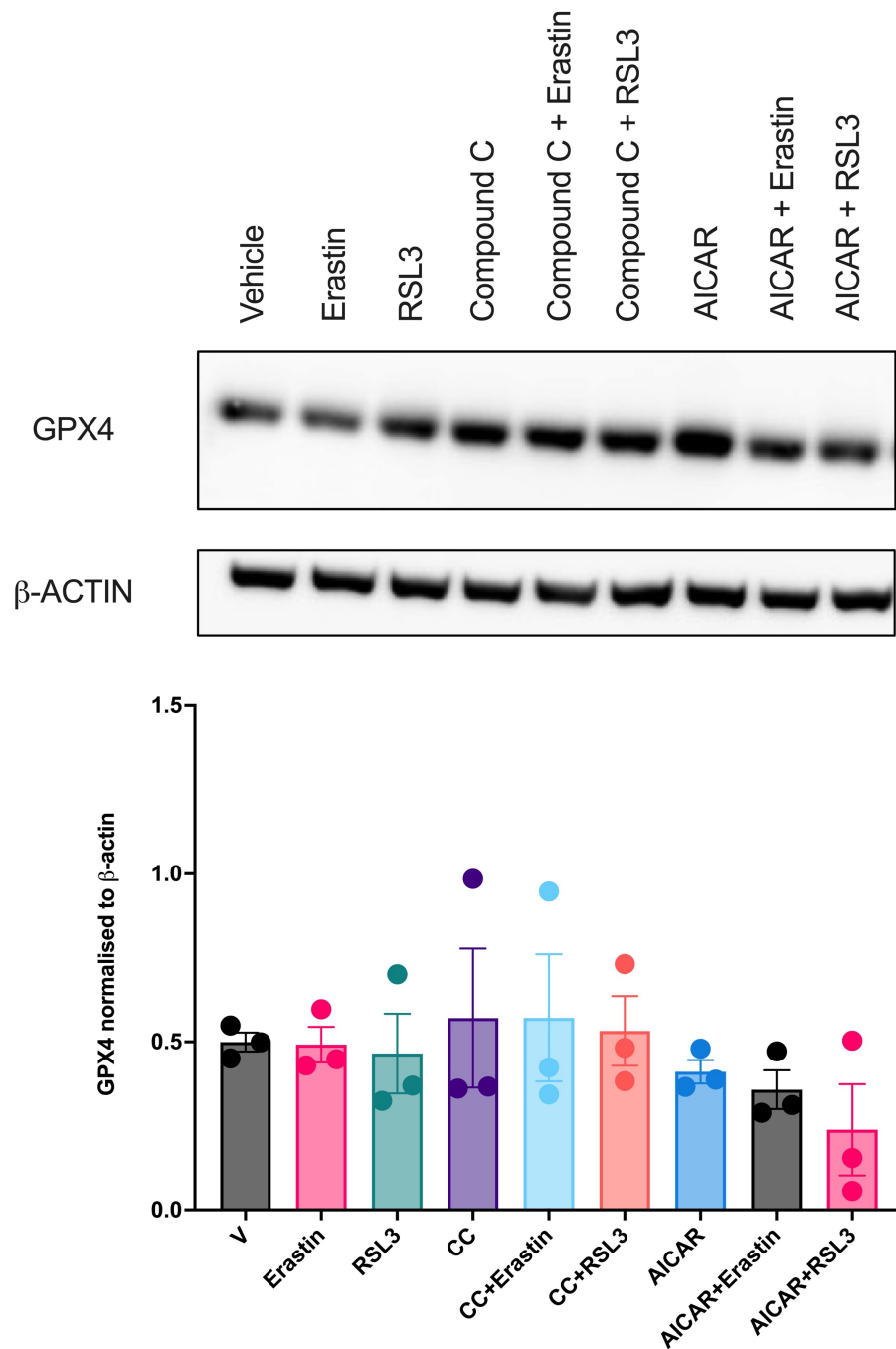


Figure 4.10: GPX4 western blot for 4T1 breast cancer cells. The breast cancer cells were treated with vehicle or compound C or AICAR for 30 min prior to treatment with Erastin or RSL3 for 4 h, and GPX4 analysed by western blot. Representative western blot for GPX4 and β -actin are shown. Data are presented as mean (SEM) of three independent experiments and analysed using 1-way ANOVA; * $p < 0.05$, ** $p < 0.001$, **** $p < 0.0001$.

The colon cancer cells initially showed an increase in cell death after cotreatment of Erastin and AICAR (**Figure 4.8**), and increased cell viability after cotreatment of RSL3 and compound C (**Figure 4.9**). The western blots for GPX4 showed no changes in GPX4 expression across all treatments, except for RSL3 alone and in combination with AICAR (**Figure 4.11**). However, this is probably correlating with the instability of the house-keeping protein, which could be caused by cell death from RSL3 treatment.

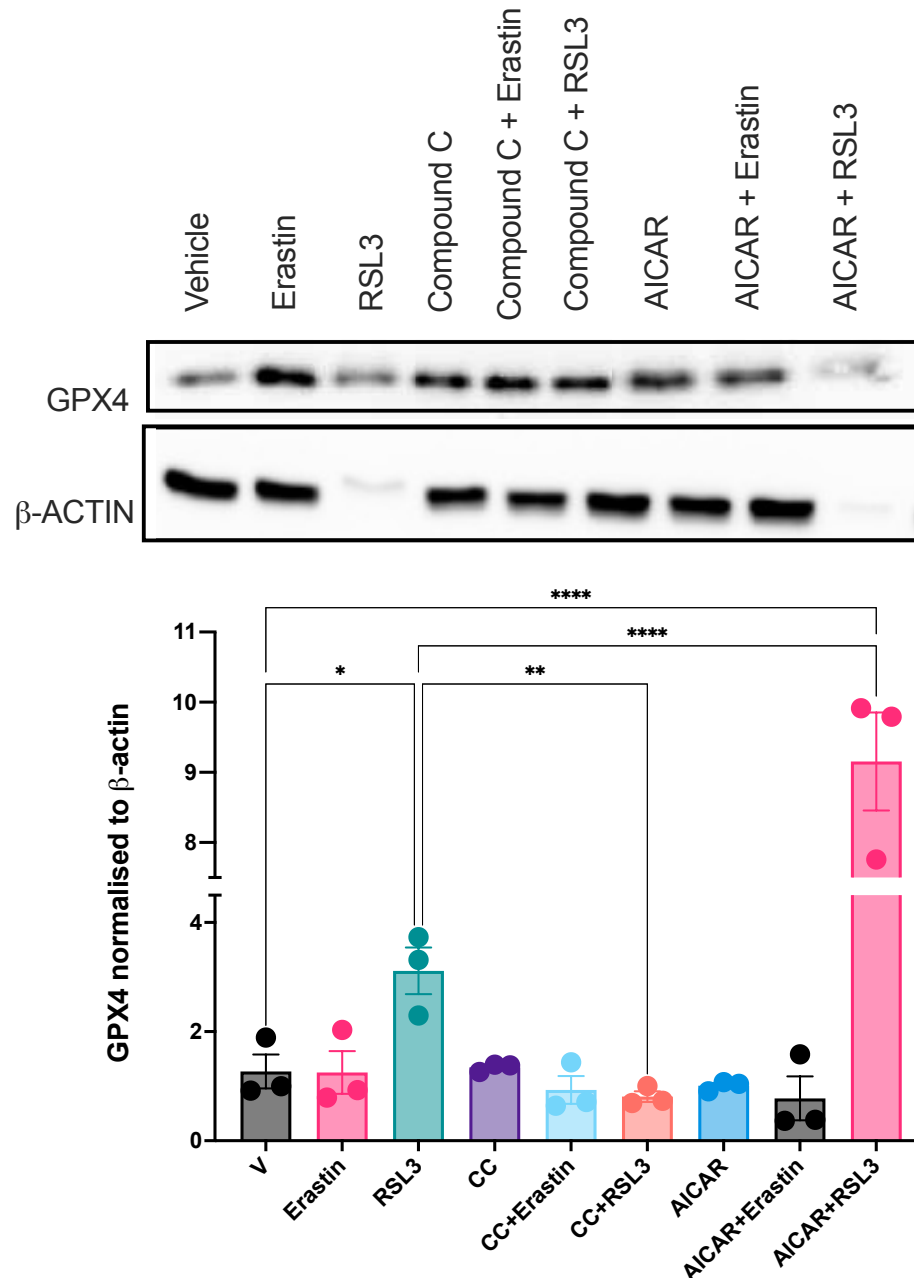


Figure 4.11: GPX4 western blot for MC38 colon cancer cells. The colon cancer cells were treated with vehicle or compound C or AICAR for 30 min prior to treatment with Erastin or RSL3 for 4 h, and GPX4 analysed by western blot. Representative western blot for GPX4 and β -actin are shown. Data are presented as mean (SEM) of three independent experiments and analysed using 1-way ANOVA; * $p < 0.05$, ** $p < 0.001$, **** $p < 0.0001$

Previously, the lung cancer cell line showed a significant reduction in cell viability with the cotreatment of Erastin and AICAR (**Figure 4.8 c**) and a significant rescue in cell viability after the cotreatment of compound C and RSL3 (**Figure 4.9 c**). There was a trend towards decreased GPX4 expression after RSL3 treatment (**Figure 4.12**). However, there was some instability in the house-keeping protein.

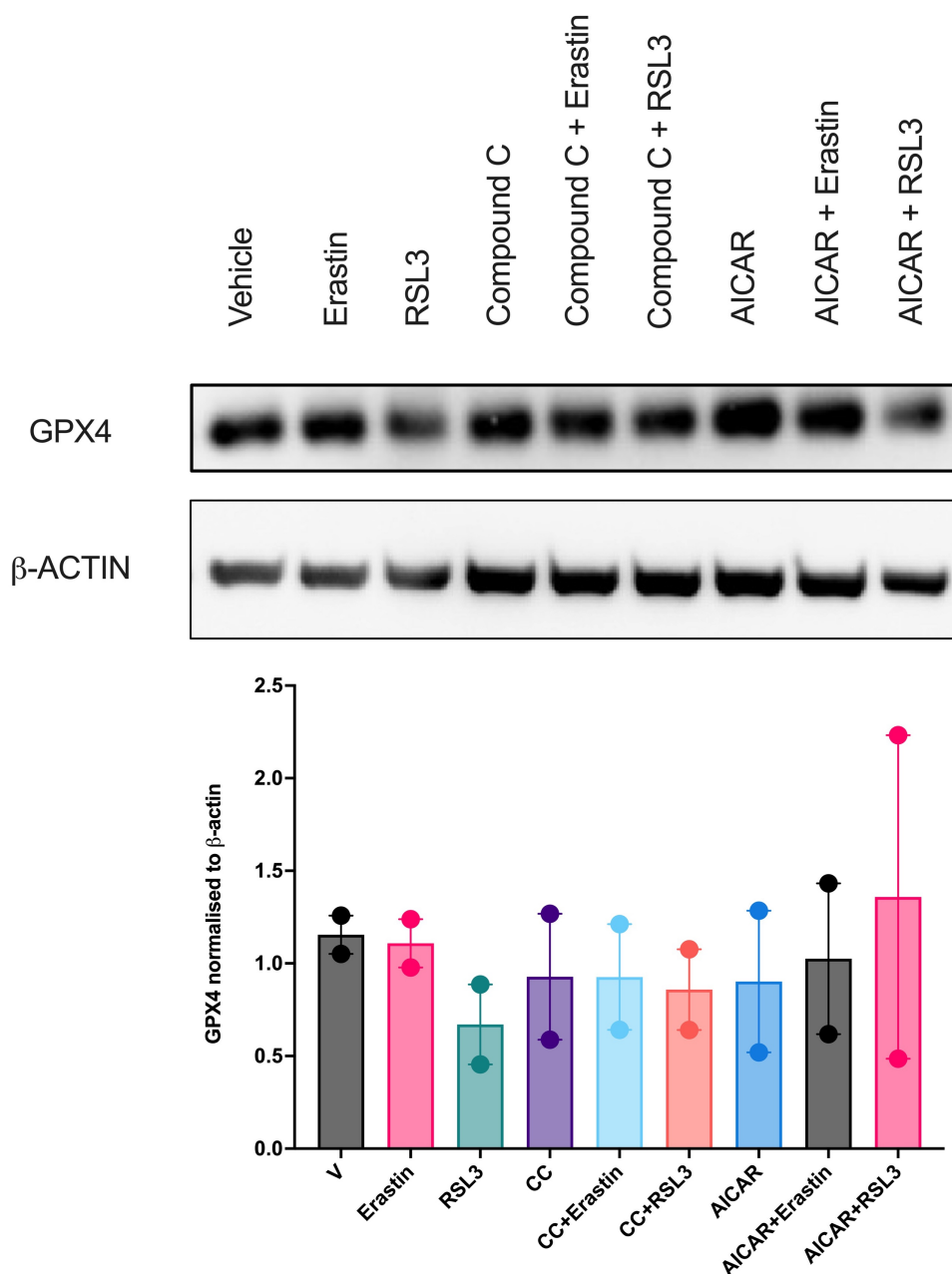


Figure 4.12: GPX4 western blot for LC2 lung cancer cells. The colon cancer cells were treated with vehicle or compound C or AICAR for 30 min prior to treatment with Erastin or RSL3 for 4 h, and GPX4 analysed by western blot. Representative western blot for GPX4 and β -actin are shown. Data are presented as mean (SEM) of two independent experiments.

The mTOR pathway was then investigated, looking at one of the main substrates of mTORC1; P70-S6K. Although the mTORC1 inhibitor rapamycin and mTORC1 and mTORC2 inhibitor torin-1 had no effect on the cancer cell lines (apart from breast cancer cells), the mTOR substrate P70-S6K was investigated with the AMPK inhibitor (compound C) and inducer (AICAR). In the breast cancer cell line, there was a trend towards decreased phosphorylated-P70-S6K after treatment with Erastin, RSL3 and compound C alone (Figure 4.13). There was also a trend towards increased total-P70-S6K after treatment with AICAR alone, and compound C in combination with Erastin or RSL3 (**Figure 4.13**).

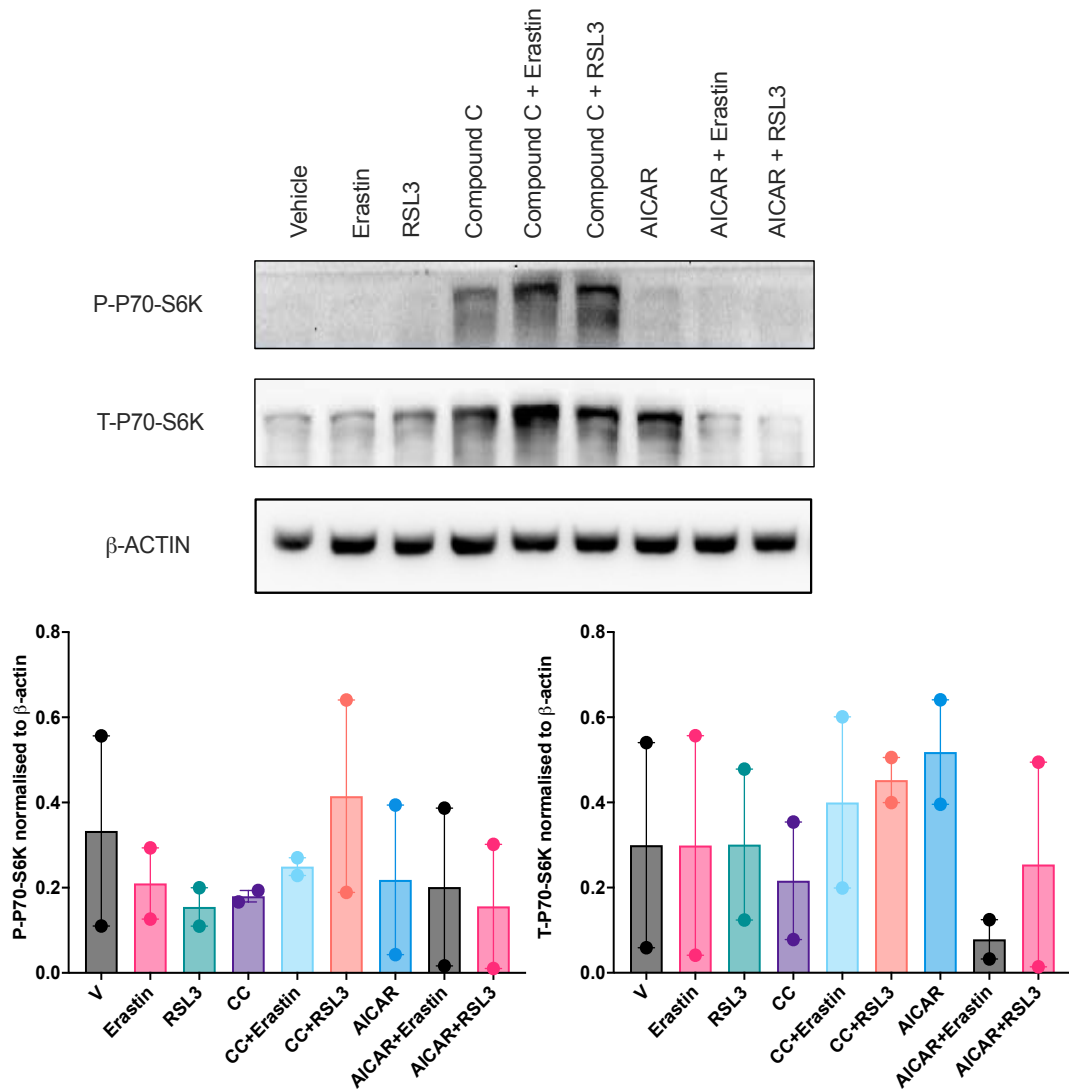


Figure 4.13: P70S6K western blot for 4T1 breast cancer cells. The breast cancer cells were treated with vehicle or compound C or AICAR for 30 min prior to treatment with Erastin or RSL3 for 4 h, and the phosphorylation of ribosomal protein S6 kinase 1 (P-P70-S6K) and total ribosomal protein S6 kinase (T-P70-S6K), were analysed by western blot. Representative western blot for P-P70-S6K, T-P70-S6K and β -actin are shown. Data was presented as mean (SEM) from two independent experiments and analysed using 1-way ANOVA; * $p < 0.05$, ** $p < 0.001$, **** $p < 0.0001$.

The colon cancer cell line showed an increase in total-P70-S6K after treatment with AICAR and in cotreatment of AICAR with Erastin or RSL3 (**Figure 4.14**). There was also a trend towards increased phosphorylated-P70-S6K after cotreatment of AICAR with RSL3 (**Figure 4.14**). However, there was instability in the house-keeping protein after RSL3 treatment.

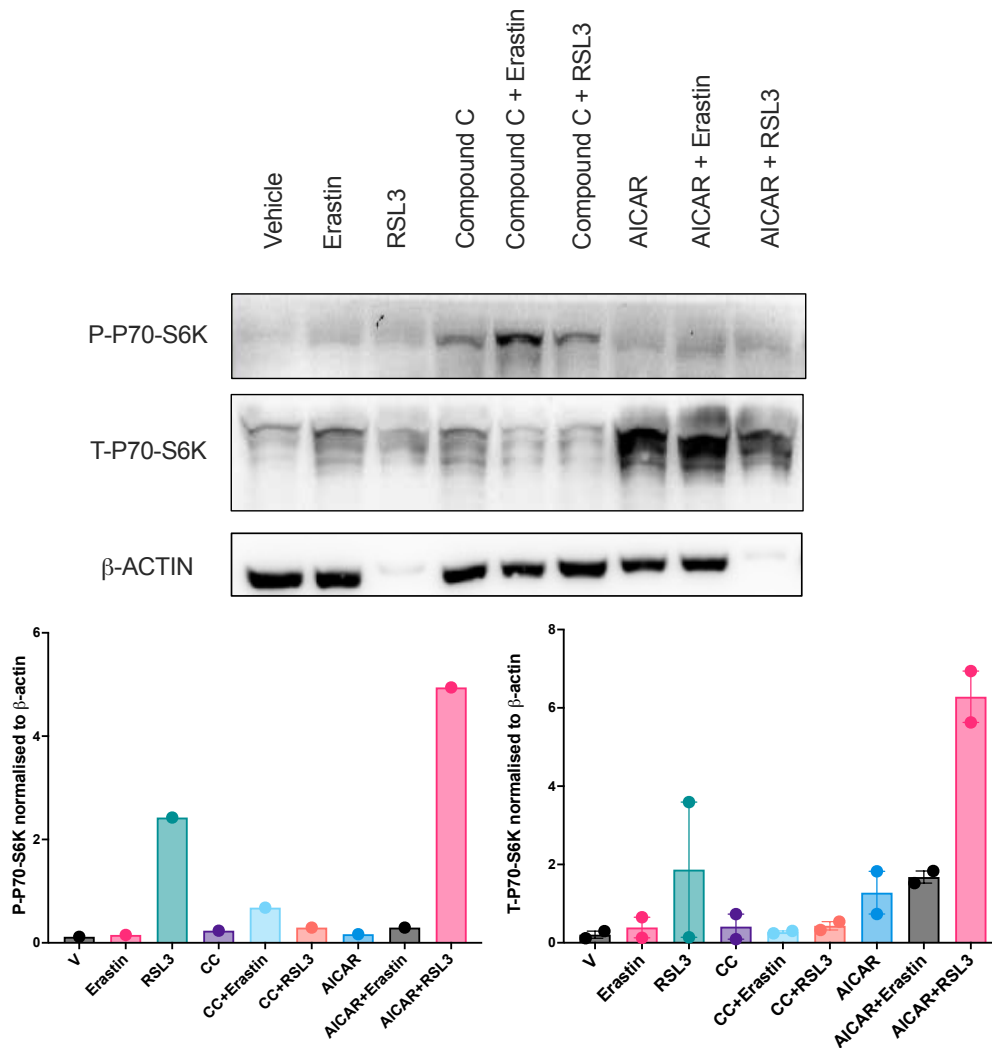


Figure 4.14: P70S6K western blot for MC38 colon cancer cells. The colon cancer cells were treated with vehicle or compound C or AICAR for 30 min prior to treatment with Erastin or RSL3 for 4 h, and the phosphorylation of ribosomal protein S6 kinase 1 (P-P70-S6K) and total ribosomal protein S6 kinase (T-P70-S6K), were analysed by western blot. Representative western blot for P-P70-S6K, T-P70-S6K and β -actin are shown. Data was presented as mean (SEM) from one independent experiment for P-P70-S6K and two independent experiments for T-P70-S6K.

The lung cancer cell line showed an increase in phosphorylated-P70-S6K after treatment with compound C and cotreatment of compound C with Erastin or RSL3 (**Figure 4.15**).

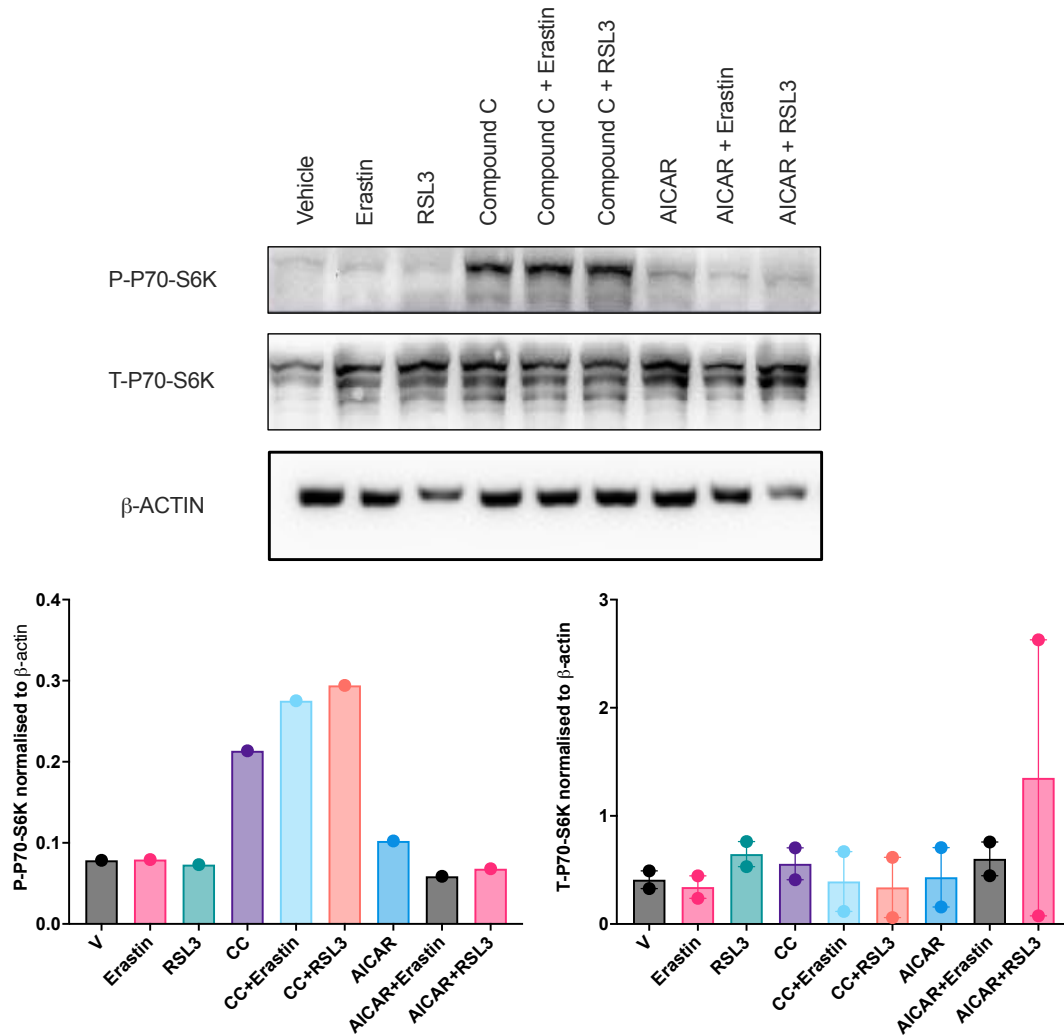


Figure 4.15: P70S6K western blot for LC2 lung cancer cells. The lung cancer cells were treated with vehicle or compound C or AICAR for 30 min prior to treatment with Erastin or RSL3 for 4 h, and the phosphorylation of ribosomal protein S6 kinase 1 (P-P70-S6K) and total ribosomal protein S6 kinase (T-P70-S6K), were analysed by western blot. Representative western blot for P-P70-S6K, T-P70-S6K and β-actin are shown. Data was presented as mean (SEM) from one independent experiment for P-P70-S6K and two independent experiments for T-P70-S6K and analysed using 1-way ANOVA; * $p < 0.05$, ** $p < 0.001$, **** $p < 0.0001$.

During autophagy, AMPK phosphorylates the Ser555 residue of ULK1 and mTOR can prevent autophagy through the phosphorylation of Ser757 residue of ULK1 (Bach et al., 2011; Kim et al., 2014; Tian et al., 2015). Therefore Ser555, Ser757 and ULK1 were investigated by western blot.

The breast cancer cell line showed a trend towards decreased SER757 expression after all treatments in comparison to the vehicle but increased SER555 expression after cotreatment of AICAR with RSL3 (**Figure 4.16**). However, repeats are required to make any conclusions.

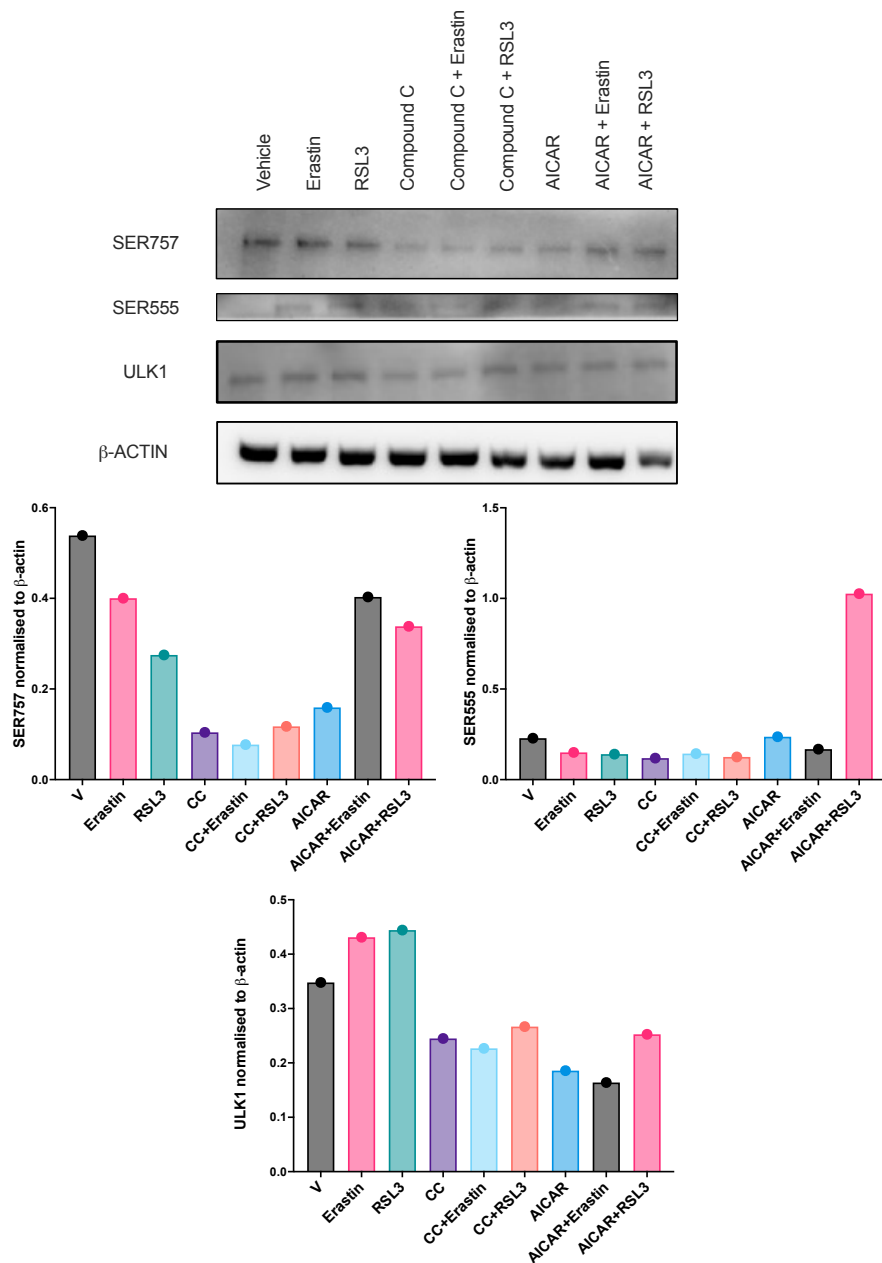


Figure 4.16: ULK1 western blot for 4T1 breast cancer cells. The breast cancer cells were treated with vehicle or compound C or AICAR for 30 min prior to treatment with Erastin or RSL3 for 4 h, and the expression of SER555, SER757 and ULK1, were analysed by western blot. Representative western blot for SER555, SER757, ULK1 and β -actin are shown. Data was presented as mean (SEM) from one independent experiment.

The colon cancer cells showed a low expression of Ser757, with no detection of expression after treatment with RSL3 and cotreatment of AICAR and RSL3, however the house keeper is erratic for these treatments, presumably due to cell death as a result of RSL3 treatment, therefore it is difficult to interpret the data and should therefore be treated with caution (**Figure 4.17**). There was a trend towards increased ULK1 expression after cotreatment with AICAR and RSL3, again the house keeper is erratic and therefore the data should be treated with caution (**Figure 4.17**).

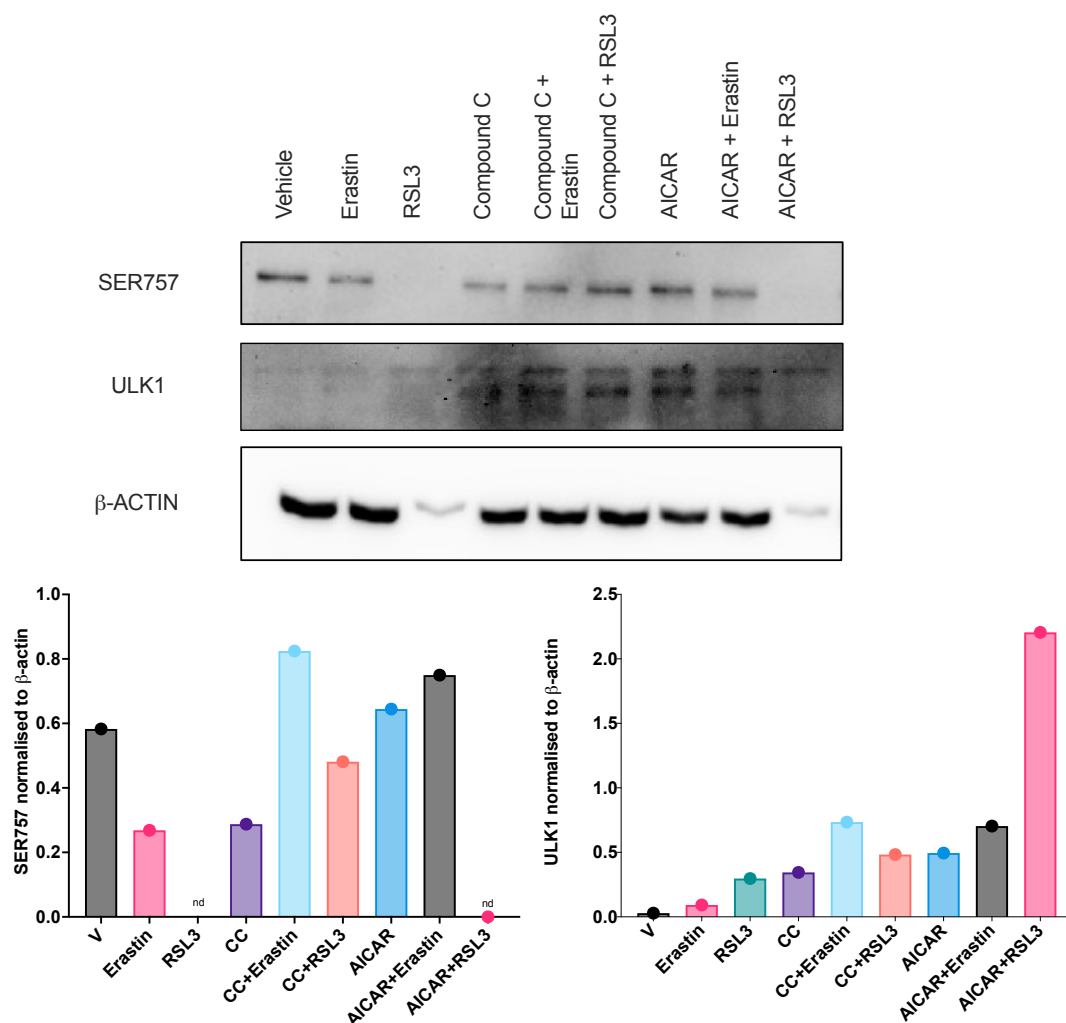


Figure 4.17: ULK1 western blot for MC38 colon cancer cells. The colon cancer cells were treated with vehicle or compound C or AICAR for 30 min prior to treatment with Erastin or RSL3 for 4 h, and the expression of SER757 and ULK1, were analysed by western blot. Representative western blot for SER757, ULK1 and β -actin are shown. Data was presented as mean (SEM) from one independent experiment.

The activation of AMPK was also investigated in the three cancer cell lines after treatment with the inhibitor (compound C) and activator (AICAR) of AMPK.

Previously, the breast cancer cell line displayed a significant increase in cell viability after the cotreatment of RSL3 with compound C or AICAR, in comparison to RSL3 treatment alone (**Figure 4.9 a**). The western blot showed an increase in phosphorylated AMPK after treatment with AICAR and cotreatment of AICAR with either Erastin or RSL3. As expected, there was an opposite effect (decrease) in phosphorylated AMPK after treatment with compound C, but an increase in total AMPK (**Figure 4.18**).

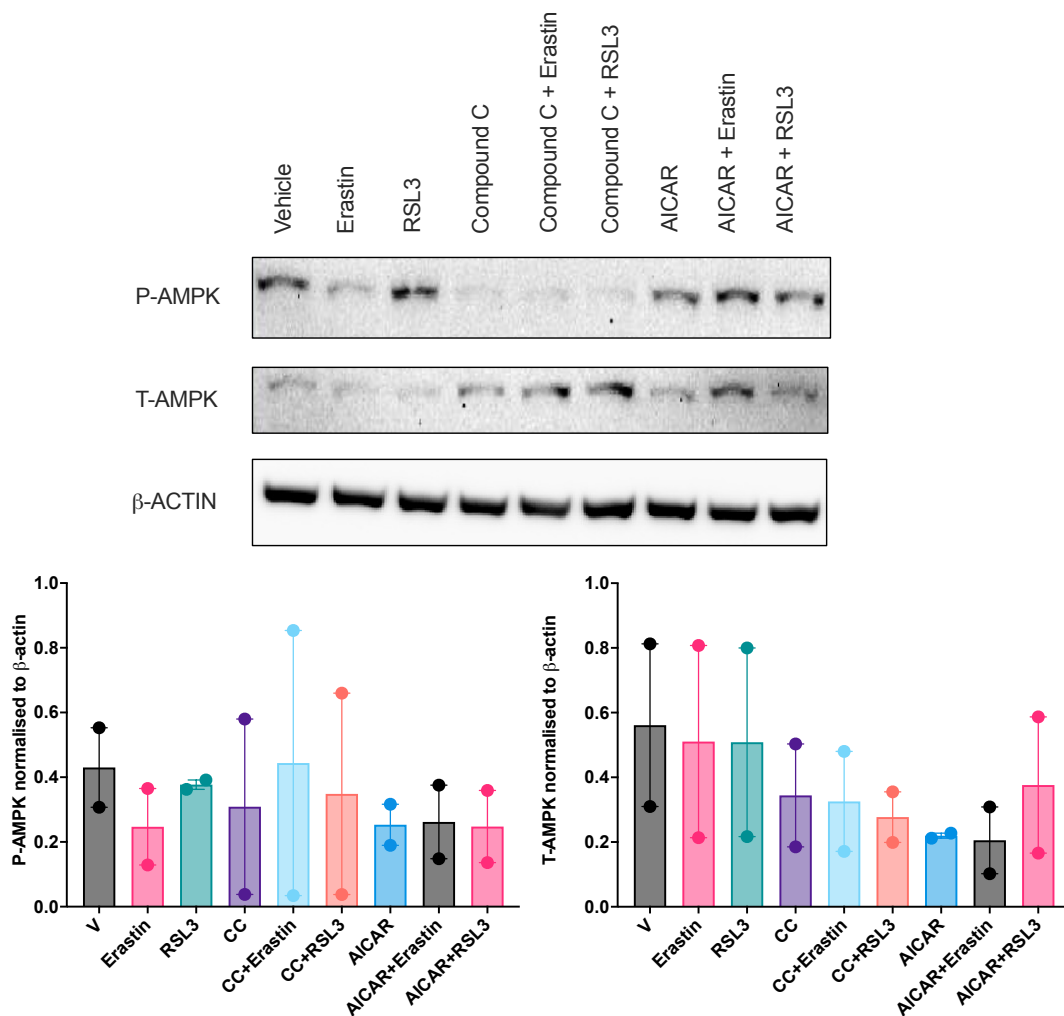


Figure 4.18: AMPK western blot for 4T1 breast cancer cells. The breast cancer cells were treated with vehicle or compound C or AICAR for 30 min prior to treatment with Erastin or RSL3 for 4 h, and the phosphorylation of AMPK (P-AMPK) and total AMPK (T-AMPK), were analysed by western blot. Representative western blot for P-AMPK, T-AMPK and β -actin are shown. Data was presented as mean (SEM) from two independent experiments.

Initially the colon cancer cells showed an increase in cell death after cotreatment of Erastin and AICAR (**Figure 4.8**), and increased cell viability after cotreatment of RSL3 and compound C (**Figure 4.9**). The western blot showed an increase in phosphorylated AMPK after treatment with AICAR and co treatment with Erastin. There was instability in the house-keeping to determine the effect of RSL3 or the cotreatment of AICAR and RSL3 had on AMPK expression, which also resulted in no detection for one of the western blots. There was decreased phosphorylated AMPK after treatment with

compound C and cotreatment of compound C with Erastin or RSL3 (**Figure 4.19**).

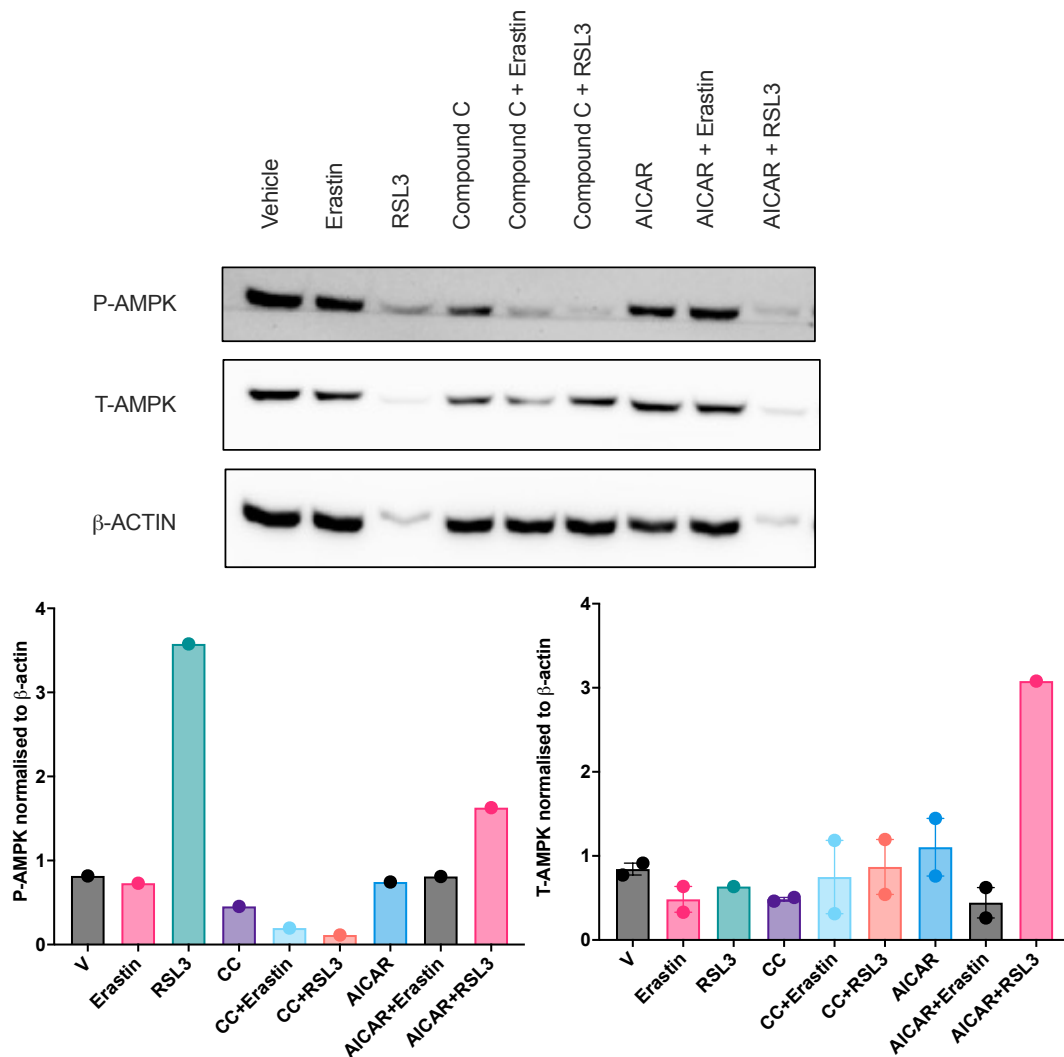


Figure 4.19: AMPK western blot for MC38 colon cancer cells. The colon cancer cells were treated with vehicle or compound C or AICAR for 30 min prior to treatment with Erastin or RSL3 for 4 h, and the phosphorylation of AMPK (P-AMPK) and total AMPK (T-AMPK), were analysed by western blot. Representative western blot for P-AMPK, T-AMPK and β -actin are shown. Data was presented as mean (SEM) from one independent experiment for P-AMPK and two independent experiments for T-AMPK.

Previously, the lung cancer cell line showed a significant reduction in cell viability with the cotreatment of Erastin and AICAR (**Figure 4.8 c**) and a significant rescue in cell viability after the cotreatment of compound C and RSL3 (**Figure 4.9 c**). The western blot showed an increase in phosphorylated

AMPK (P-AMPK) after treatment with RSL3, cotreatment of AICAR and Erastin, and AICAR and RSL3. There was trend towards decreased total AMPK (T-AMPK) after treatment with RSL3, cotreatment of compound C and RSL3, AICAR and Erastin and AICAR and RSL3, in comparison to the vehicle (**Figure 4.20**).

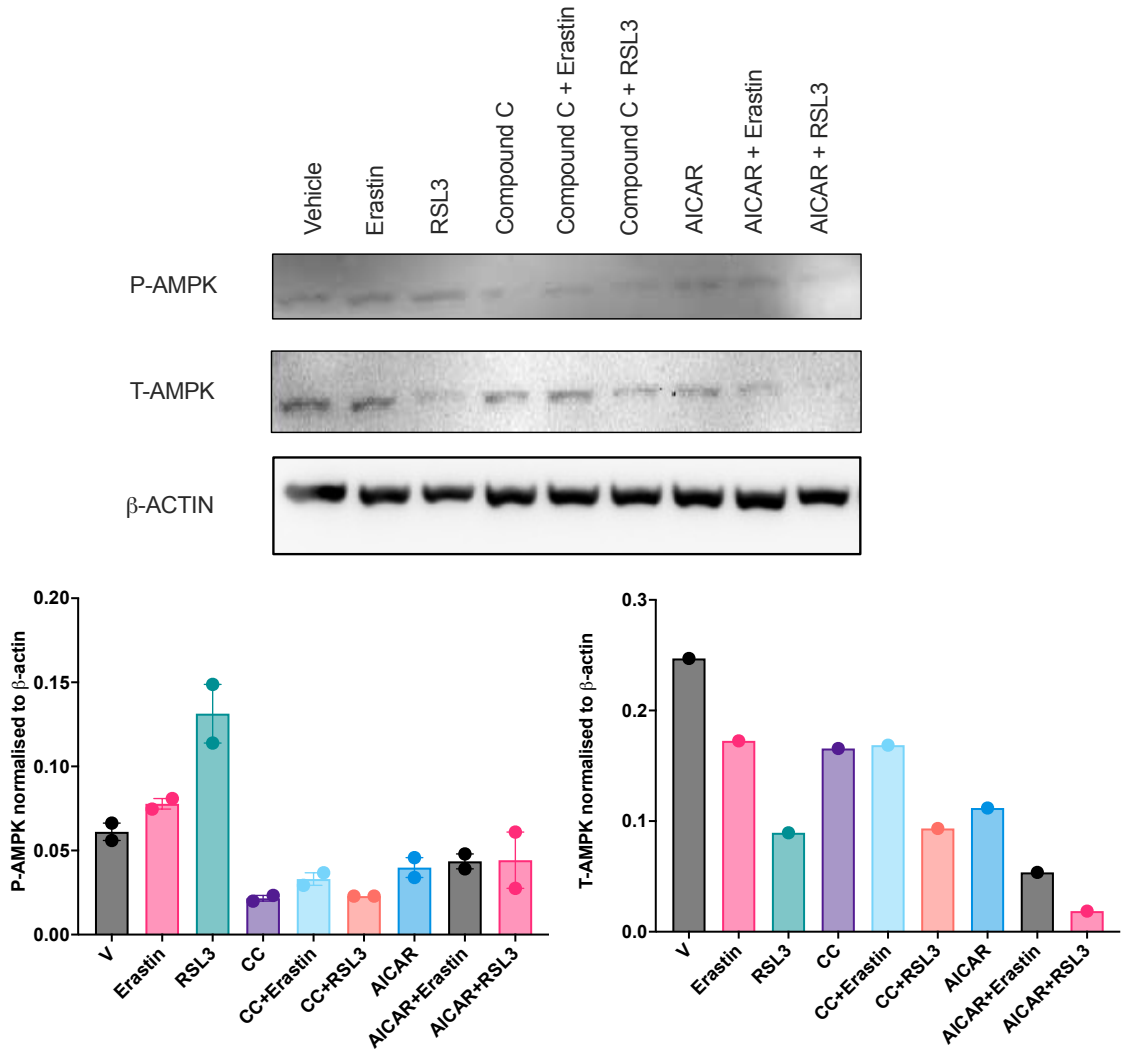


Figure 4.20: AMPK western blot for LC2 lung cancer cells. The lung cancer cells were treated with vehicle or compound C or AICAR for 30 min prior to treatment with Erastin or RSL3 for 4 h, and the phosphorylation of AMPK (P-AMPK) and total AMPK (T-AMPK) were analysed by western blot. Representative western blot for P-AMPK, T-AMPK and β -actin are shown. Data was presented as mean (SEM) from one independent experiment for P-AMPK and two independent experiments for T-AMPK.

A key regulator of autophagy is BECN1, which has been found to promote ferroptosis (Song et al., 2018), therefore BECN1 was investigated. The breast cancer western blots showed variation in BECN1 expression after all treatments, there is a trend towards increased expression after treatment with AICAR and RSL3, although it did not lead to significance (**Figure 4.21**).

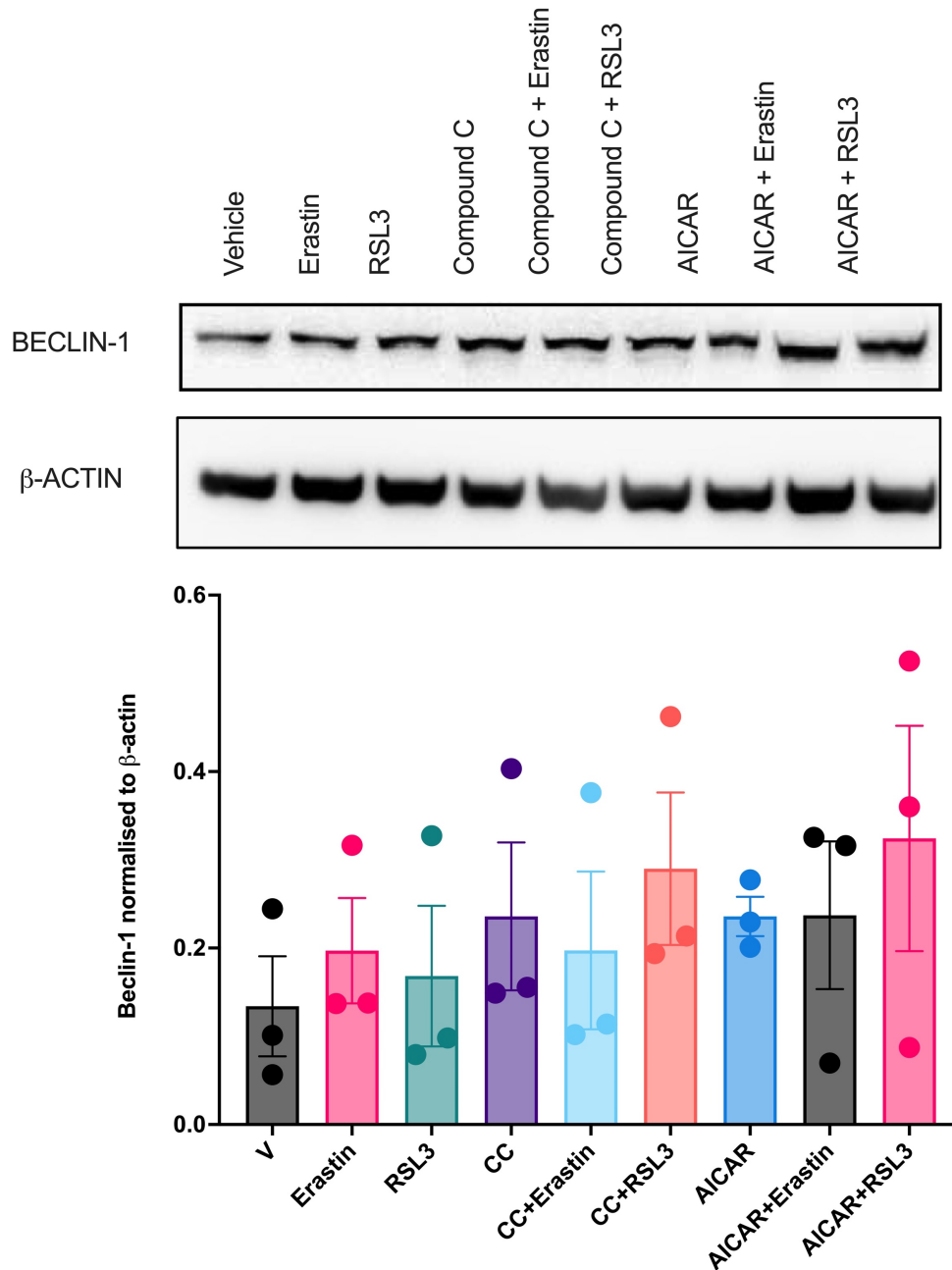


Figure 4.21: BECN1 western blots for 4T1 breast cancer cells. The breast cancer cells were treated with vehicle or compound C or AICAR for 30 min prior to treatment with Erastin or RSL3 or 4 h, and the BECN1 (Beclin-1) was analysed by western blot. Representative western blot for Beclin-1 and β-actin are shown. Data was presented as mean (SEM) from three independent experiments and analysed using 1-way ANOVA.

The colon cancer western blots for BECN1 showed an increase in expression after treatment with RSL3 and cotreatment of AICAR and RSL3, although it did not result in significance (Figure 4.22). However, there was some instability in the house-keeping protein for RSL3 treatment and cotreatment of AICAR and RSL3.

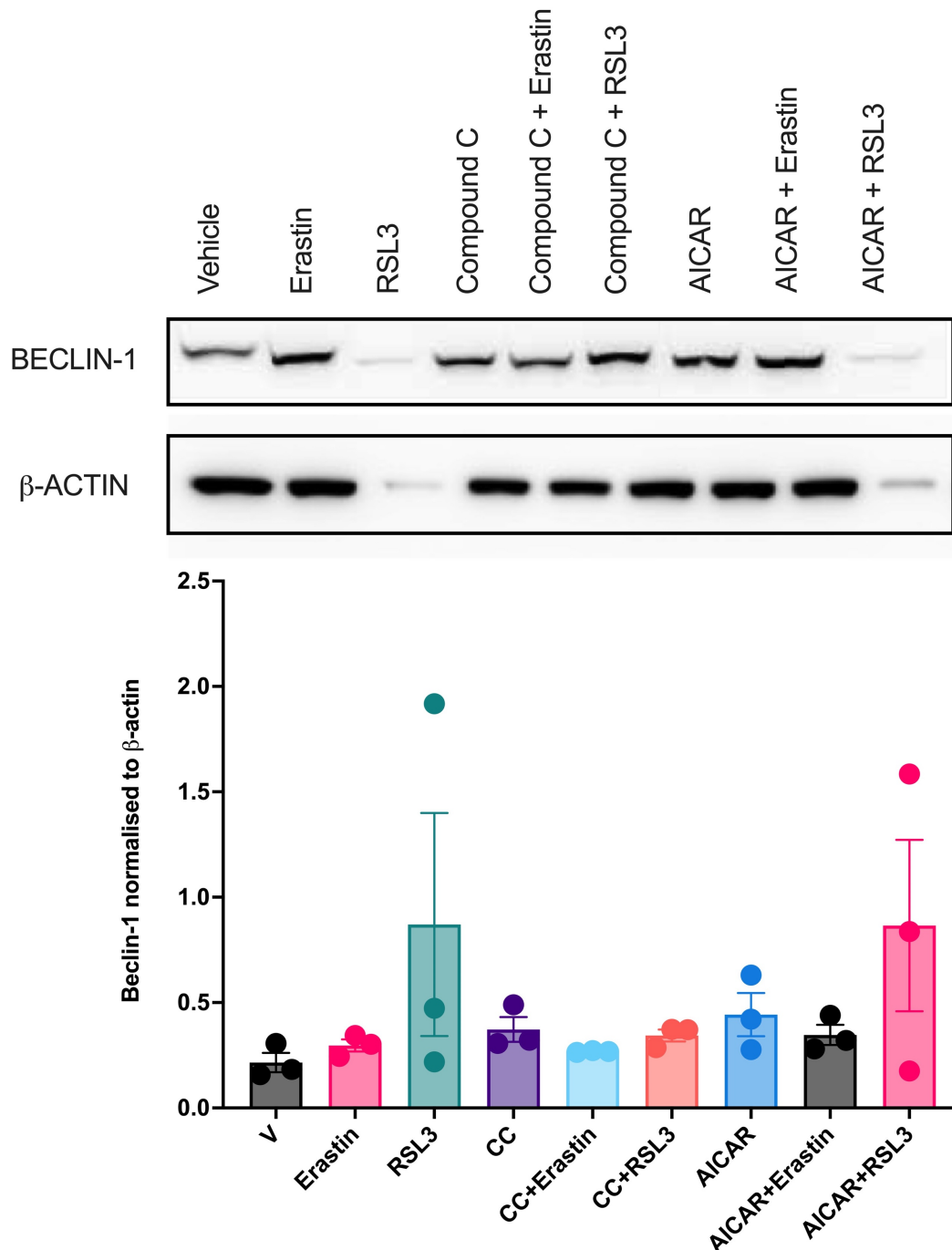


Figure 4.22: BECN1 western blots for mc38 colon cancer cells. The colon cancer cells were treated with vehicle or compound C or AICAR for 30 min prior to treatment with Erastin or RSL3 or 4 h, and the BECN1 (Beclin-1) was analysed by western blot. Representative western blot for Beclin-1 and β -actin are shown. Data was presented as mean (SEM) from three independent experiments and analysed using 1-way ANOVA.

The lung cancer western blots for BECN1 shoed a reduction in expression after treatment with AICAR and RSL3 (**Figure 4.23**). However, there was some instability in the house-keeping protein after cotreatment of AICAR and RSL3.

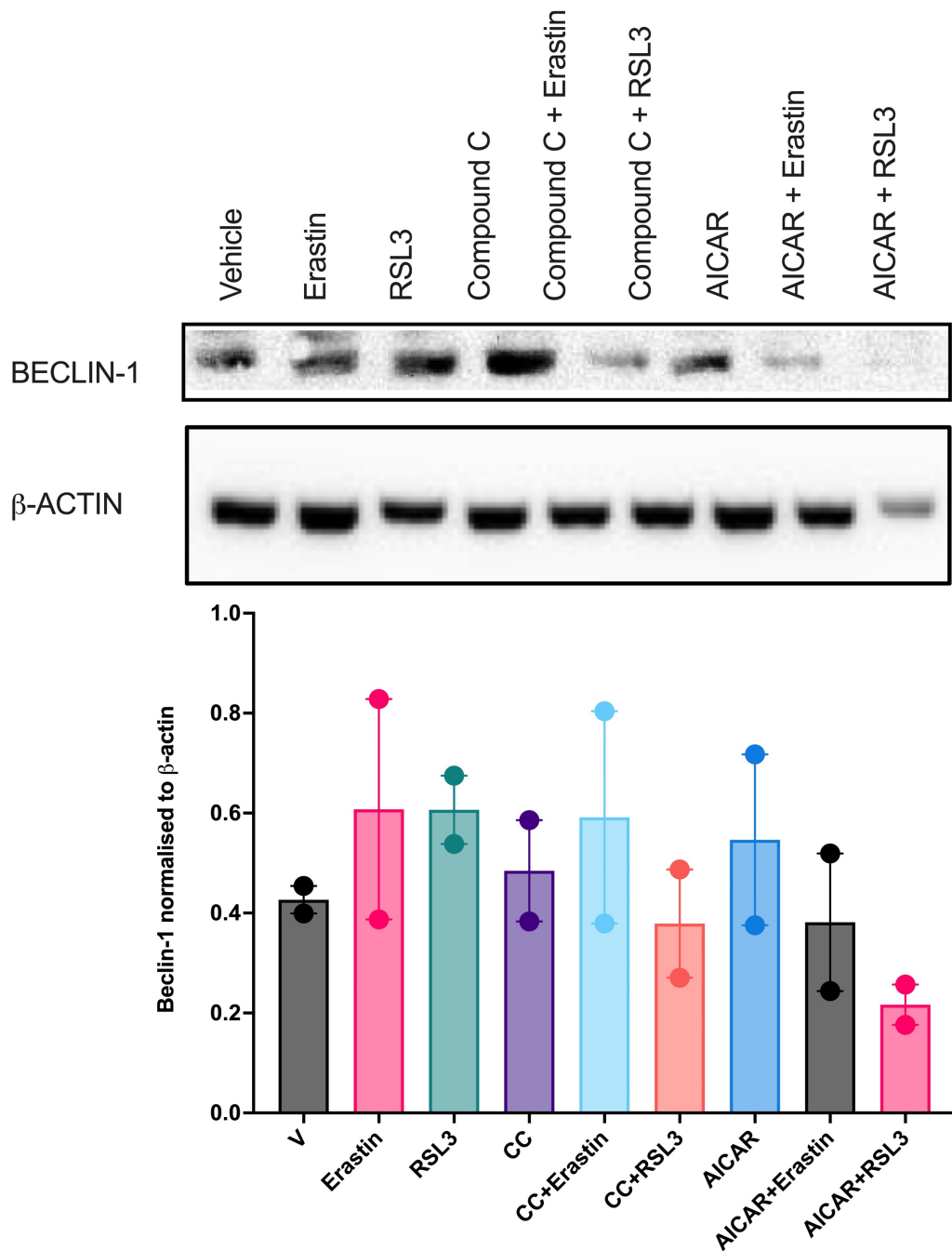


Figure 4.23: BECN1 western blot for LC2 lung cancer cells. The lung cancer cells were treated with vehicle or compound C or AICAR for 30 min prior to treatment with Erastin or RSL3 or 4 h, and the BECN1 (Beclin-1) was analysed by western blot. Representative western blot for Beclin-1 and β -actin are shown. Data was presented as mean (SEM) from two independent experiments.

The autophagic marker, LC3B, is widely used, due to the clear correlation between LC3B-II and the number of autophagosomes (Mizushima & Yoshimori, 2007). The expression of LC3B-I increased after treatment with RSL3, compound C, cotreatment of compound C with Erastin or RSL3 and AICAR. The expression of LC3B-II increased after treatment with compound C and the cotreatment of compound C with Erastin or RSL3 (**Figure 4.24**).

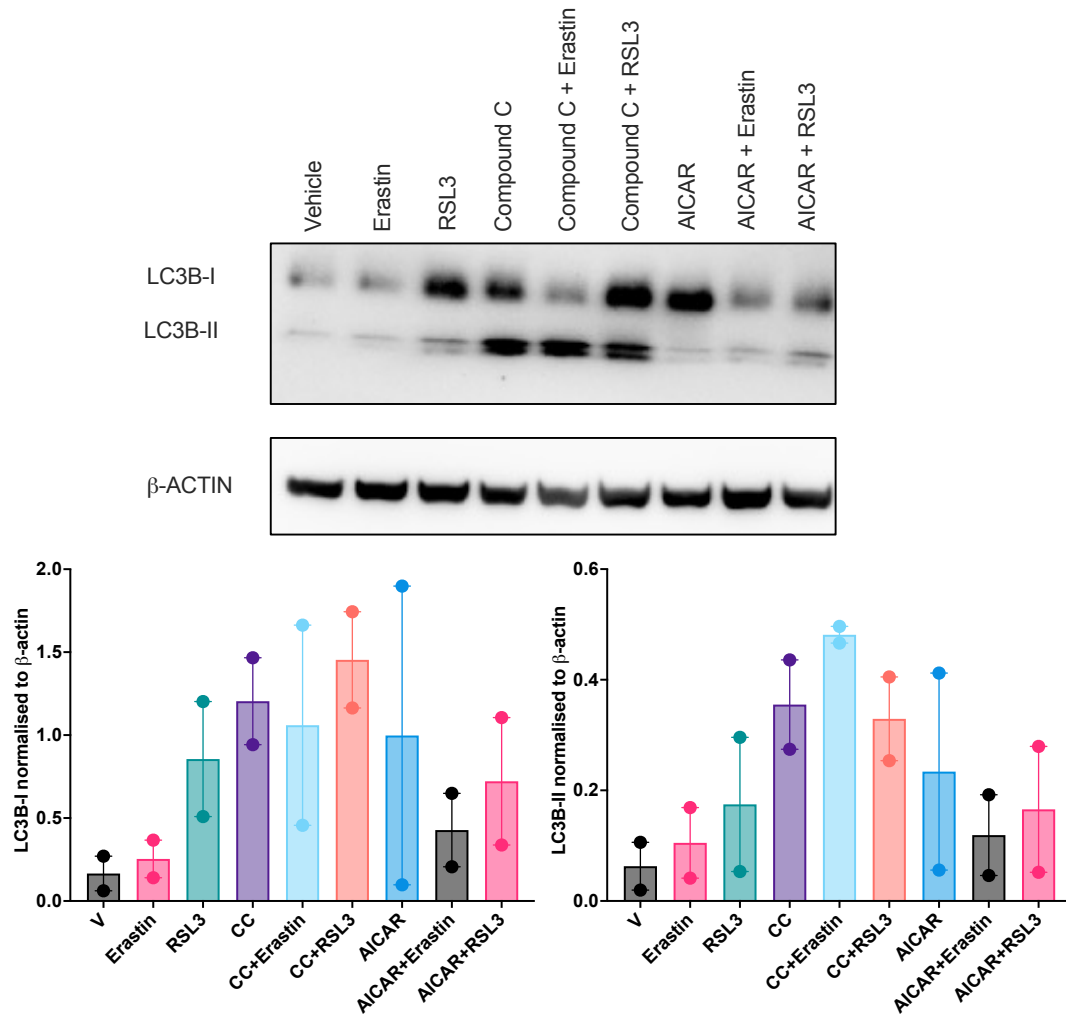


Figure 4.24: LC3B western blot for 4T1 breast cancer cells. The breast cancer cells were treated with vehicle or compound C or AICAR for 30 min prior to treatment with Erastin or RSL3 or 4 h, and LC3B-I and LC3B-II were analysed by western blot. Representative western blot for LC3B-I, LC3B-II and β-actin are shown. Data was presented as mean (SEM) from two independent experiments.

In the colon cancer cells the LC3B-1 remained similarly expressed throughout all treatments, the decrease in expression of LC3B-I after treatment with RSL3 and cotreatment of AICAR and RSL3 is correlating with the instability of the house-keeping protein for these treatments. The expression of LC3B-II increased after treatment with compound C, and the cotreatment of compound C with Erastin or RSL3 (**Figure 4.25**). The expression of LC3B-II was not detected in one of the western blots after treatment with RSL3 and cotreatment of AICAR and RSL3, probably correlating with the instability of the house-keeping protein.

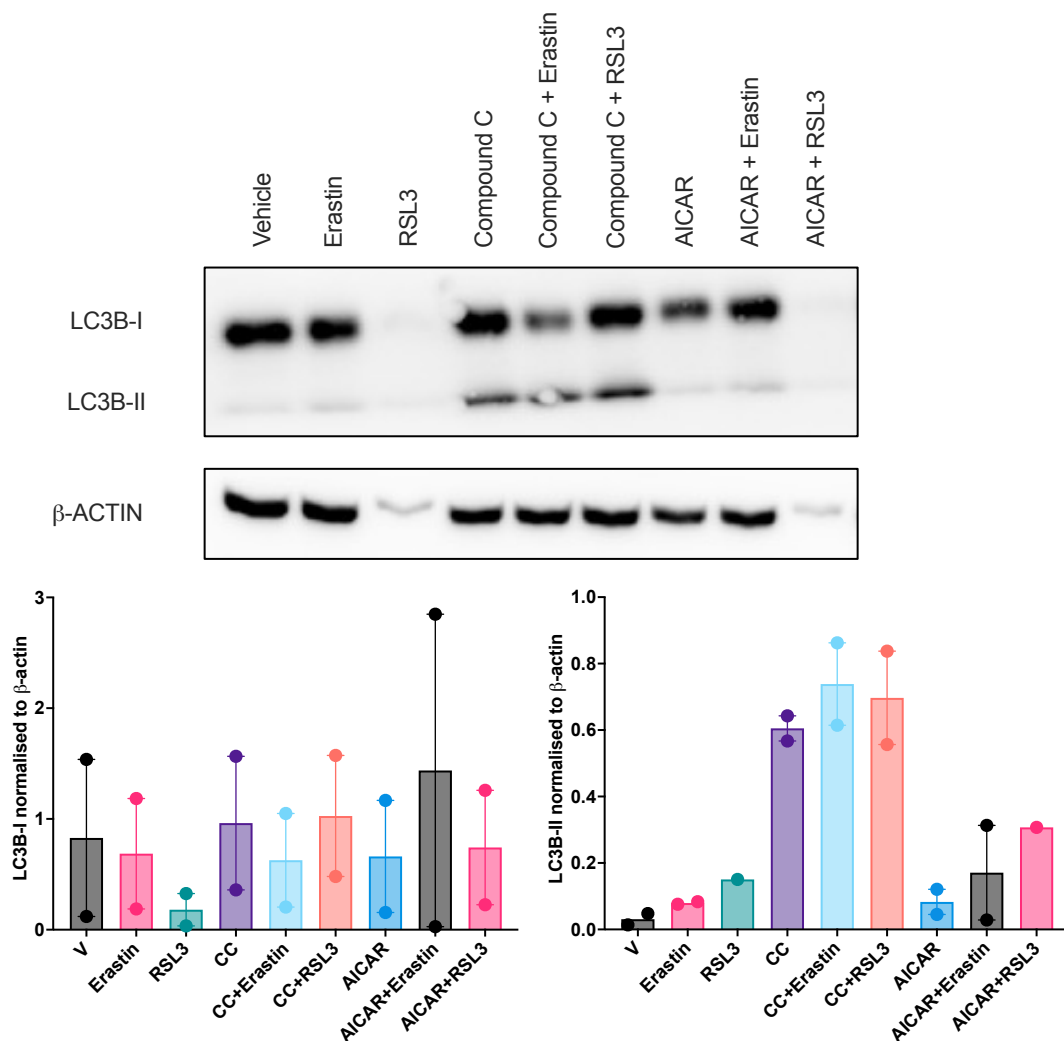


Figure 4.25: LC3B western blot for MC38 colon cancer cells. The colon cancer cells were treated with vehicle or compound C or AICAR for 30 min prior to treatment with Erastin or RSL3 or 4 h, and LC3B-I and LC3B-II were analysed by western blot. Representative western blot for LC3B-I, LC3B-II and β -actin are shown. Data was presented as mean (SEM) from two independent experiments.

The lung cancer cells the expression of LC3B-II increased after treatment with compound C and cotreatment of compound C with Erastin or RSL3 (**Figure 4.26**). However for one of the western blots the expression of LC3B-II could not be detected for the vehicle and treatment with RSL3.

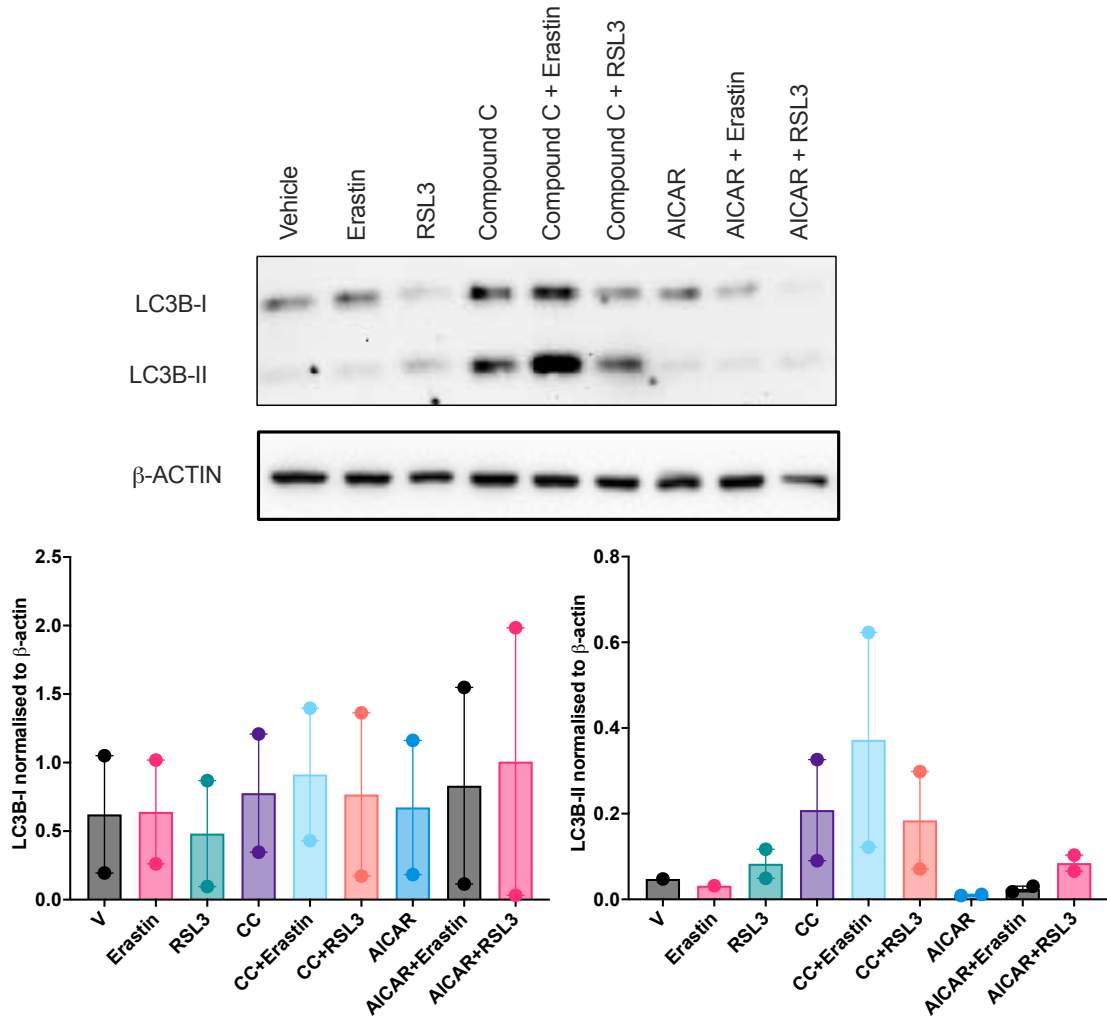


Figure 4.26: LC3B western blot for LC2 lung cancer cells. The lung cancer cells were treated with vehicle or compound C or AICAR for 30 min prior to treatment with Erastin or RSL3 or 4 h, and LC3B-I and LC3B-II were analysed by western blot. Representative western blot for LC3B-I, LC3B-II and β -actin are shown. Data was presented as mean (SEM) from two independent experiments.

The glutaminase GLS2 is known to be involved in the induction of ferroptosis (Gorrini et al., 2013); this a glutaminase inhibitor Compound 968 (C968; 10 μ M) in conjunction with the ferroptosis inducer Erastin was investigated in the panel of cancer cell lines. The 4T1 breast cancer and LC2 lung cancer cell lines showed a significant reduction in cell viability with treatment of C968 (Figure 4.27 a and c). The cotreatment of C968 (10 μ M) and Erastin (2.5 μ M) had the same significant reduction in cell viability in the 4T1 breast cancer cell line as Erastin (2.5 μ M) treatment alone (Figure 4.27 a). Whereas the cotreatment of C968 (10 μ M) and Erastin (2.5 μ M) resulted in a significant reduction in cell viability in the LC2 lung cancer cell line (Figure 4.27 c).

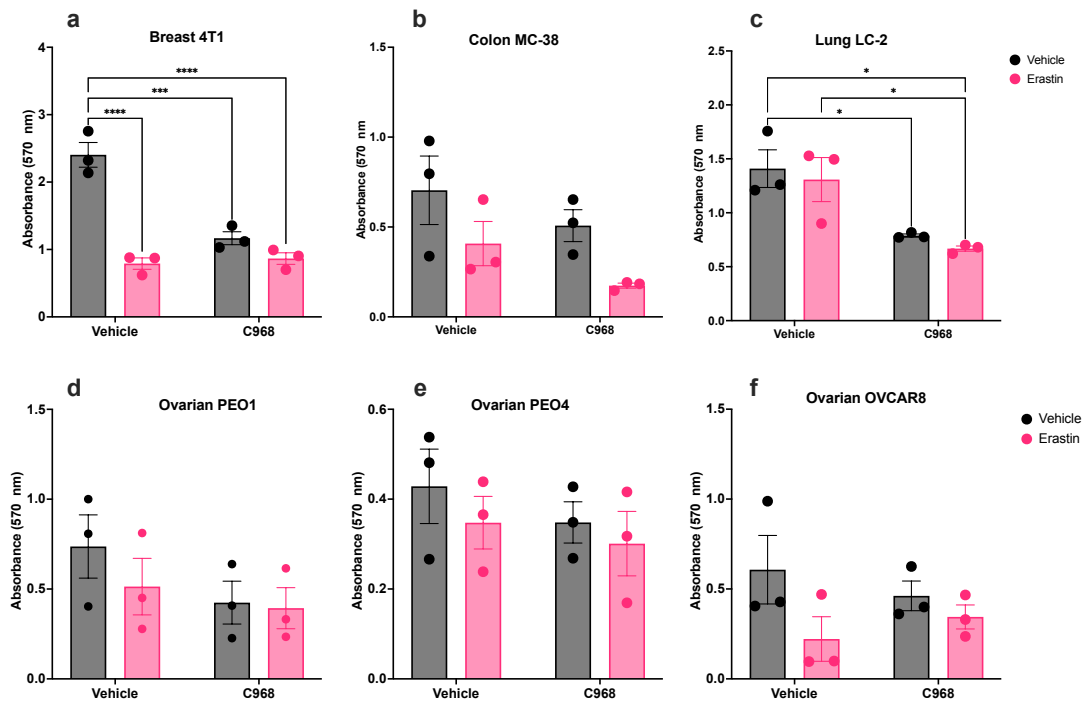


Figure 4.27: The effect of glutaminase inhibitor, compound 968 and Erastin. The panel of cancer cell lines (a) 4T1; (b) MC-38; (c) LC-2; (d) PEO1; (e) PEO4; (f) OVCAR8 were cultured in media containing vehicle (v) or C968 (10 μ M) or Erastin (2.5 μ M). Cells were treated with C968 for 30 min prior to treatment with Erastin for 24 h. Cell viability was evaluated using MTT assay after 24 h. Data was presented as mean (SEM) from three independent cell passage experiments and analysed using 2-way ANOVA, * p <0.05, ** p <0.001, *** p <0.0001.

Cells were also treated with the system GPX4 inhibitor RSL3 (0.625 μM) in order to determine the effect on cell viability after cotreatment with C968 (10 μM ; **Figure 4.28**). Again, the 4T1 breast cancer cell line showed a significant decrease in cell viability with the treatment of C968 (10 μM ; **Figure 4.28 a**). However, the cotreatment of C968 (10 μM) and RSL3 (0.625 μM) resulted in a significant rescue in cell viability in the 4T1 breast cancer cell line in comparison to RSL3 (0.625 μM) treatment alone. There was also an observed rescue effect of the cotreatment (C968 and RSL3) in the MC38 colon, LC2 lung, PEO1 ovarian and PEO4 ovarian, although it did not result in significance ($P=0.4970$, $P=0.1855$, $P=0.4130$ and $P=0.4553$ respectively; **Figure 4.28 b, c, d, and e**), suggesting glutaminase may play a role in ferroptosis induction, potentially via GSH (Gao et al., 2015).

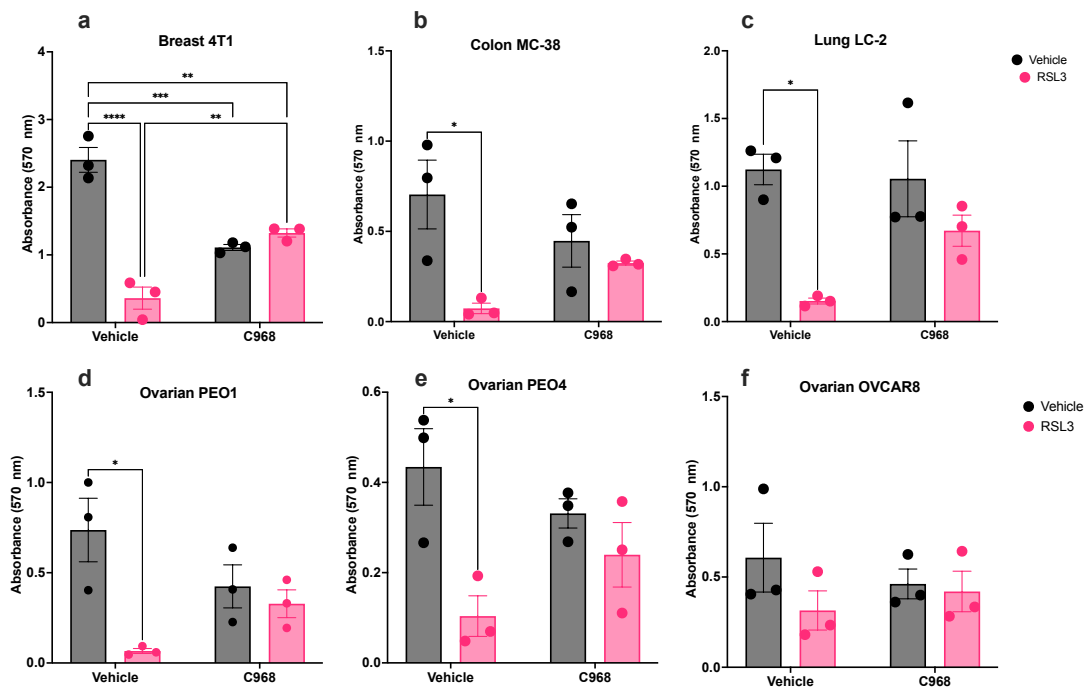


Figure 4.28: The effect of glutaminolysis inhibitor, compound 968 and RSL3. The panel of cancer cell lines (a) 4T1; (b) MC-38; (c) LC-2; (d) PEO1; (e) PEO4; (f) OVCAR8 were cultured in media containing vehicle (v) or C968 (10 μM) or RSL3 (0.625 μM). Cells were treated with c968 for 30 min prior to treatment with RSL3 for 24 h. Cell viability was evaluated using MTT assay after 24 h. Data was presented as mean (SEM) from three independent cell passage experiments and analysed using 2-way ANOVA; * $p<0.05$, ** $p<0.001$, *** $p<0.001$, **** $p<0.0001$.

The key regulator of ferroptosis, GPX4 was investigated by western blot for the treatment of C968 and cotreatment of C968 with Erastin or RSL3. Along

with the key regulator of autophagy BECN1, which has also been found to induce ferroptosis (Song et al., 2018), therefore BECN1 was investigated (Figure 4.29). The breast cancer cells showed a trend towards increased GPX4 expression after treatment with C968 and cotreatment of C968 with Erastin, although this did not reach significance ($P=0.8824$, $P=0.3065$ respectively; **Figure 4.29**). The breast cancer cells also showed a trend towards increased expression of BECN1 after treatment with C968 and cotreatment of C968 with Erastin or RSL3, although this did not reach significance ($P=0.5813$, $P=0.3883$ and $P=0.1292$ respectively (**Figure 4.29**).

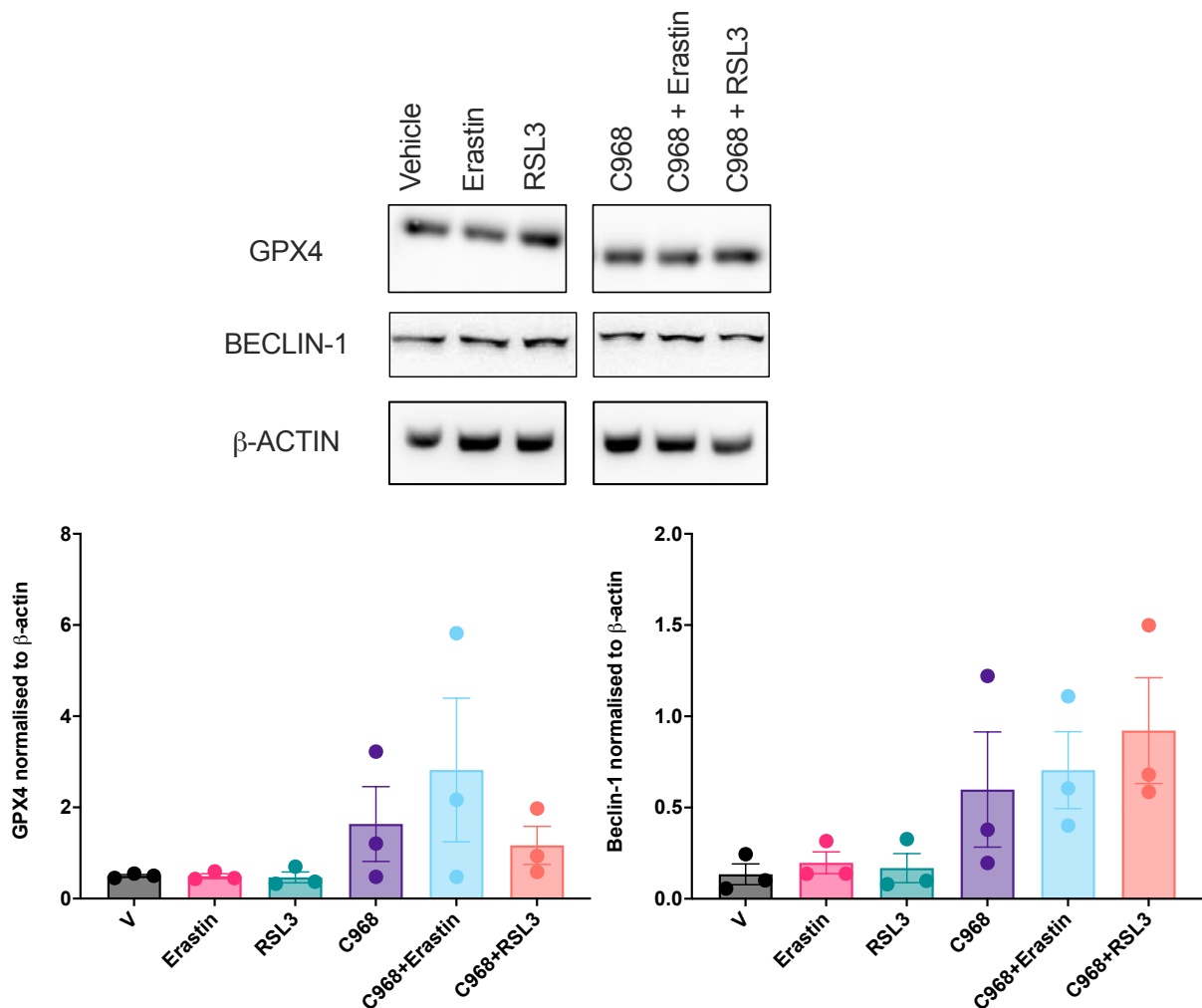


Figure 4.29: GPX4 and BECN1 western blots for 4T1 breast cancer cells. The breast cancer cells were treated with vehicle or C968 for 30 min prior to treatment with Erastin or RSL3 or 4 h, and GPX4 and BECN1 were analysed by western blot. Representative western blot for GPX4, BECN1 and β -actin are shown. Data was presented as mean (SEM) from three independent experiments and data was analysed with a 1-way ANOVA.

The colon cancer cells densitometry showed a significant increase in GPX4 expression after treatment with RSL3 alone. However, the housekeeper was erratic, again presumably due to cell death after RSL3 treatment, and therefore this data should be treated with caution. There was also a trend towards increased GPX4 expression after treatment with C968 alone, although this did not result in significance ($P=0.2526$, **Figure 4.30**). The cotreatment of C968 with either Erastin or RSL3 significantly reduced GPX4 expression (**Figure 4.30**). The colon cancer cells also showed a trend towards increased expression of BECN1 after treatment with RSL3 alone, although this did not result in significance ($P=0.3606$, **Figure 4.30**).

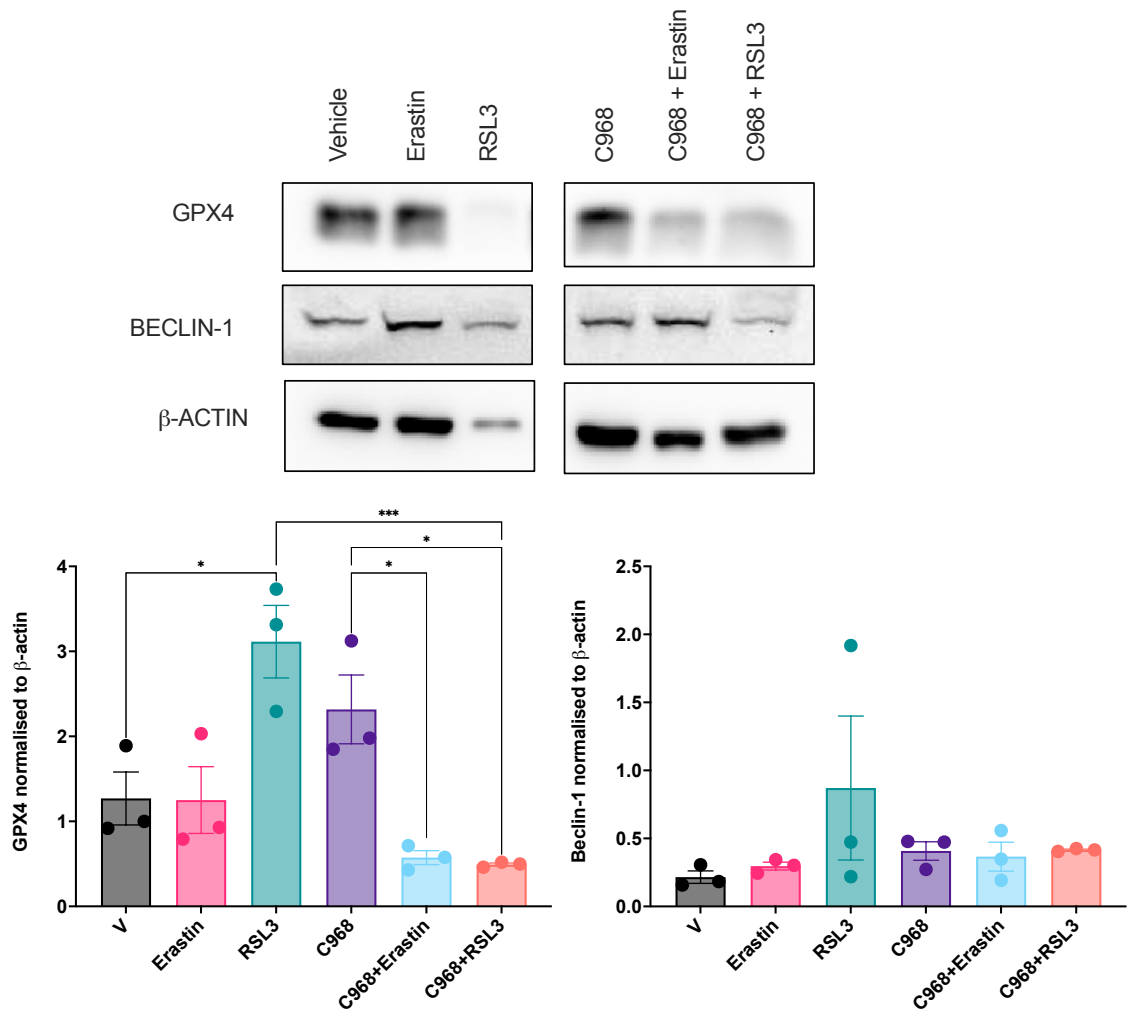


Figure 4.30: GPX4 and BECN1 western blots for MC38 colon cancer cells. The colon cancer cells were treated with vehicle or C968 for 30 min prior to treatment with Erastin or RSL3 or 4 h, and GPX4 and BECN1 were analysed by western blot. Representative western blot for GPX4, BECN1 and β -actin are shown. Data was presented as mean (SEM) from three independent experiments and data was analysed with a 1-way ANOVA; *p<0.05, ***<0.001.

In the lung cancer cells there was a trend towards increased GPX4 and BECN1 expression after treatment with C968 and cotreatment of C968 with Erastin or RSL3 (**Figure 4.31**).

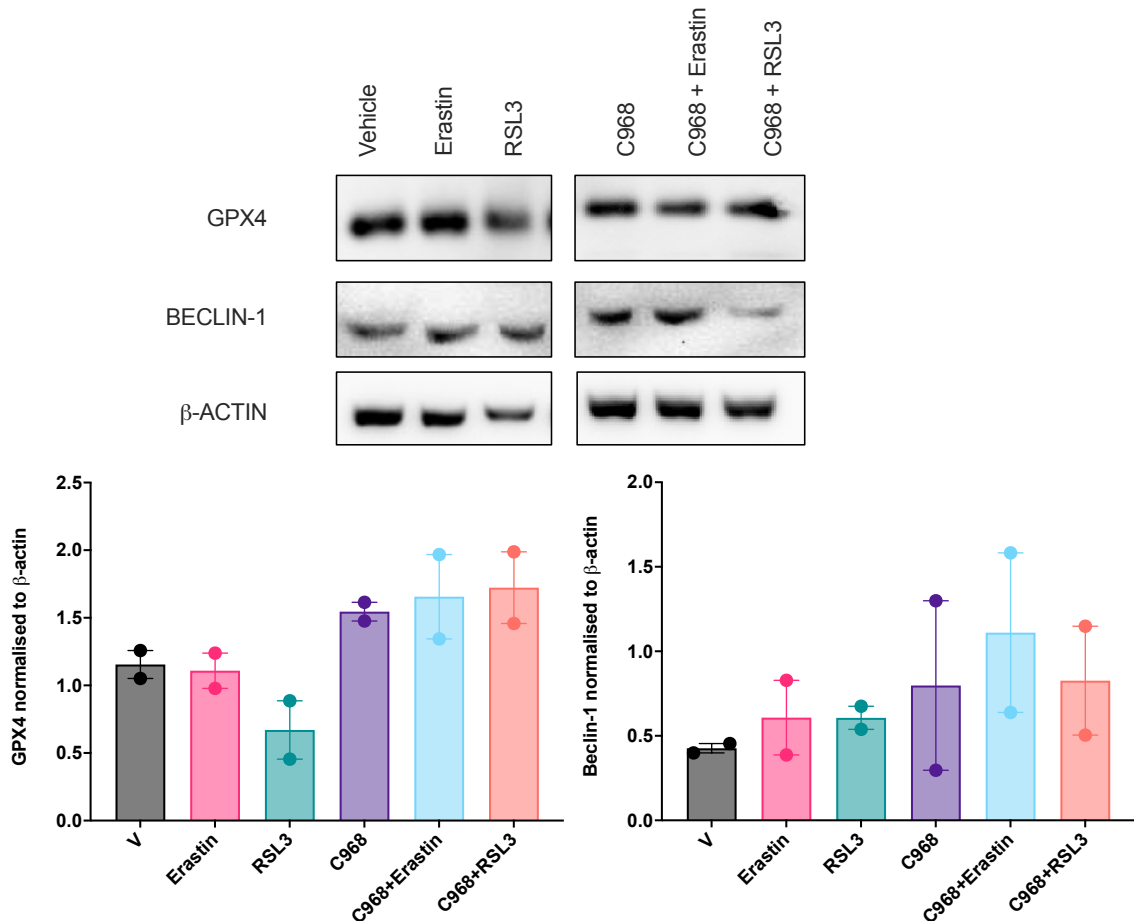


Figure 4.31:GPX4 and BECN1 western blots for LC2 lung cancer cells. The lung cancer cells were treated with vehicle or C968 for 30 min prior to treatment with Erastin or RSL3 or 4 h, and GPX4 and BECN1 were analysed by western blot. Representative western blot for GPX4, BECN1 and β-actin are shown. Data was presented as mean (SEM) from three independent experiments

The main substrate of the mTORC1 pathway is P70-S6K which was investigated by western blot for the treatment of C968 and cotreatment of C968 with Erastin or RSL3. mTOR can also prevent the induction of autophagy through the phosphorylation of Ser757 residue of ULK1(Bach et al., 2011; Kim et al., 2014; Tian et al., 2015). Whereas AMPK phosphorylates the Ser555 residue of ULK1 (Bach et al., 2011; Kim et al., 2014; Tian et al., 2015). Therefore Ser555, Ser757 and ULK1 were investigated by western blot.

The breast cancer cell line showed a decrease in the expression of phosphorylated-P70-S6K after all treatments in comparison to the vehicle, but an increase in total-P70-S6K after cotreatment of C968 with Erastin or RSL3 (**Figure 4.32**). There was a trend towards decreased expression of Ser757 after treatment with C968 and cotreatment of C968 with Erastin or RSL3. There was also a trend towards decreased expression of Ser55 after treatment with Erastin or RSL3 alone but increased expression after treatment with C968 alone. There was also a trend towards decreased ULK1 expression after treatment with C968 and cotreatment of C968 with Erastin (**Figure 4.32**).

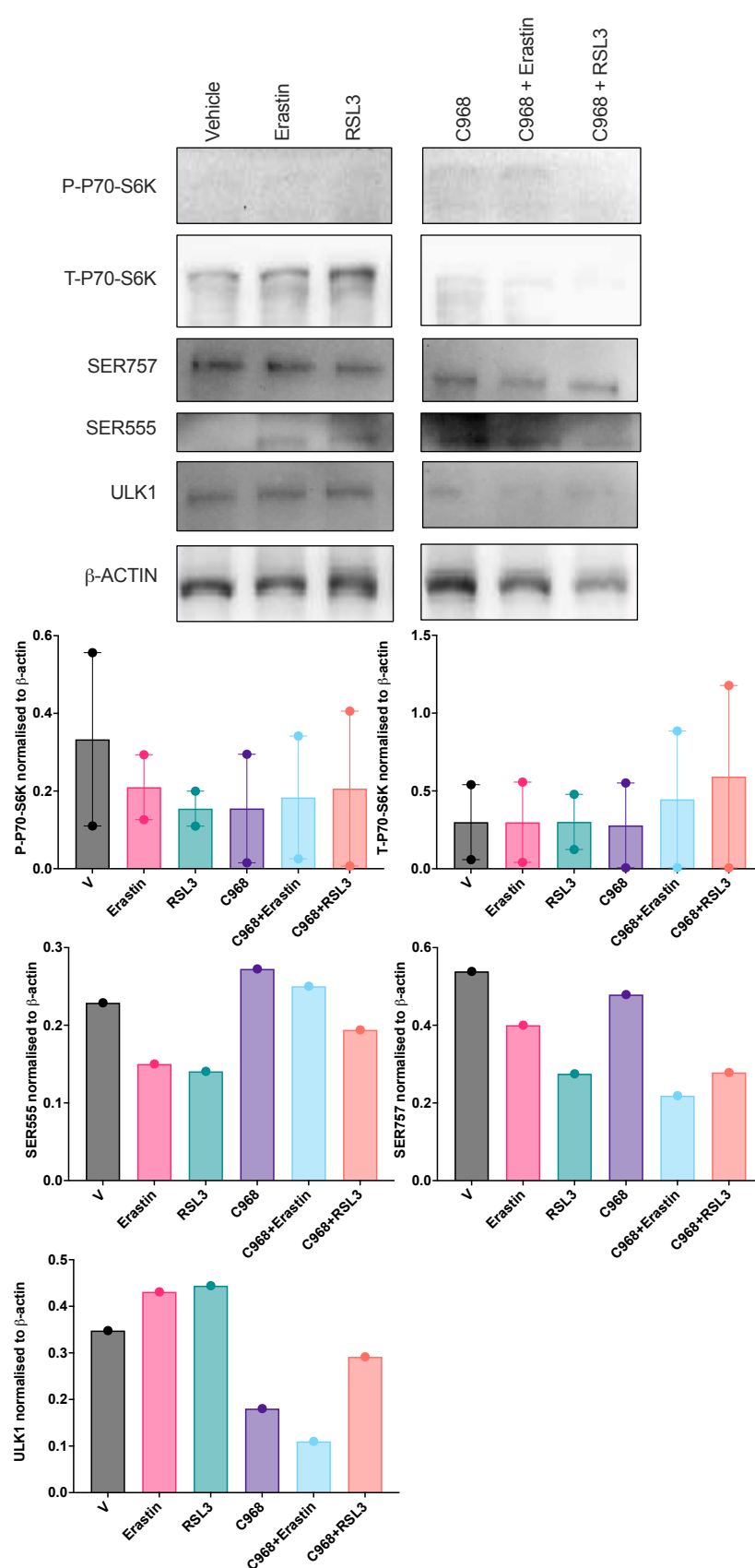


Figure 4.32: P70S6K and ULK1 western blots for 4T1 breast cancer cells. The breast cancer cells were treated with vehicle or C968 for 30 min prior to treatment with Erastin or RSL3 or 4 h, and phosphorylated P70S6K (P-P70-S6K), total P70S6K (T-P70-S6K), SER757, SER555 and ULK1 were analysed by western blot. Representative western blot for P-P70-S6K, T-P70-S6K, SER555, SER757, ULK1 and β -actin are shown. Data was presented as mean (SEM) from two independent experiments for P70S6K and one independent experiment for ULK1.

The colon cancer cells showed an increase in phosphorylated P70-S6K (P-P70-S6K) after treatment with RSL3, and a decrease in expression of P-P70-S6K after treatment with C968 and cotreatment of C968 with Erastin or RSL3. There was an observed increase in total P70-S6K (T-P70-S6K) after treatment with RSL3 alone, C68 and cotreatment with C968 and either Erastin or RSL3 (**Figure 4.33**). There was a reduced expression of Ser7575 after treatment with RSL3 alone. The total ULK1 showed an increased expression after all treatments, in comparison to the vehicle (**Figure 4.33**). However, the house-keeping protein was unstable, presumably due to cell death after treatment with RSL3, therefore this data should be treated with caution.

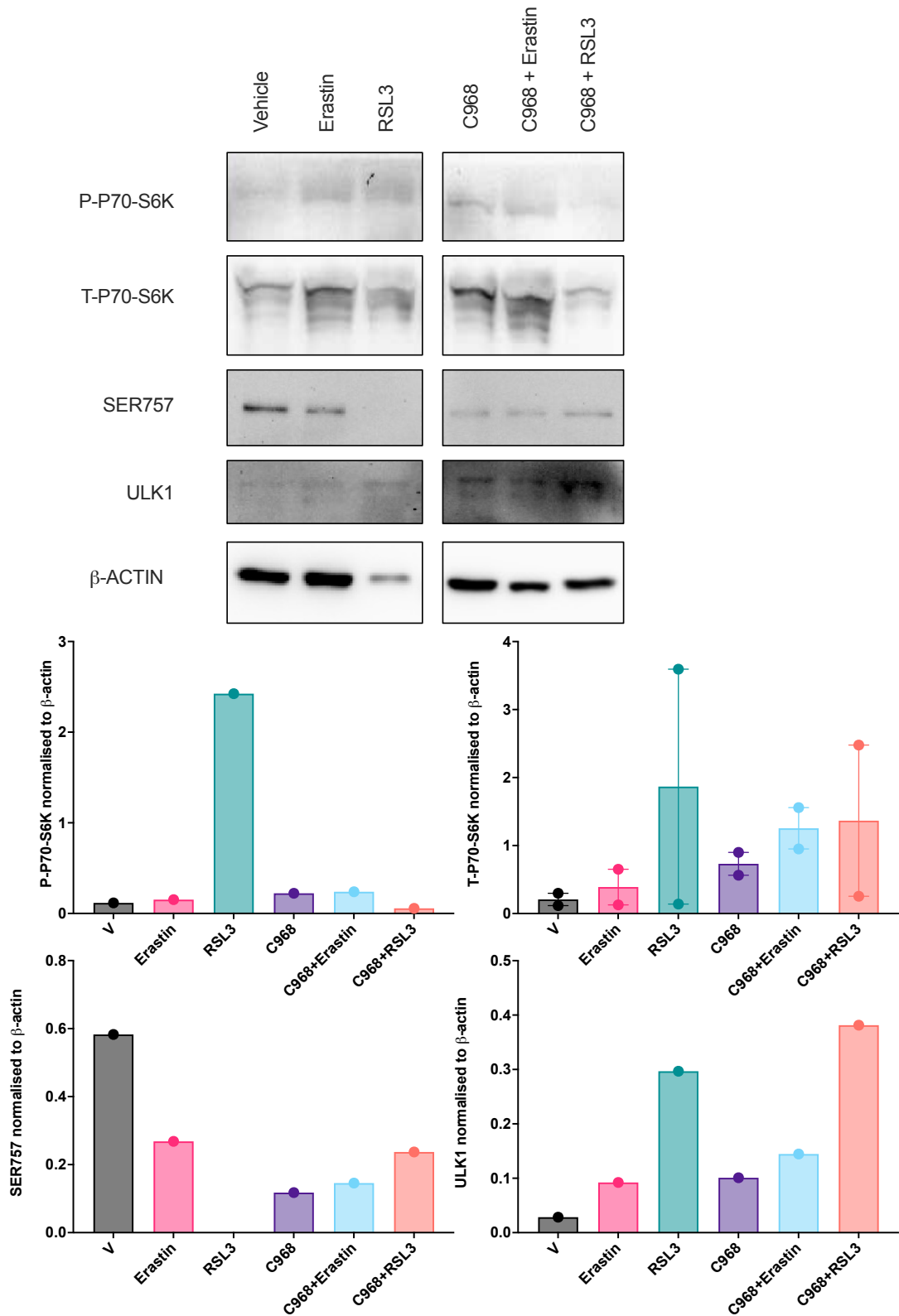


Figure 4.33: P70S6K and ULK1 western blots for MC38 colon cancer cells. The colon cancer cells were treated with vehicle or C968 for 30 min prior to treatment with Erastin or RSL3 or 4 h, and phosphorylated P70S6K (P-P70-S6K), total P70S6K (T-P70-S6K), SER757 and ULK1 were analysed by western blot. Representative western blot for P-P70-S6K, T-P70-S6K, SER757, ULK1 and β -actin are shown. Data was presented as mean (SEM) from two independent experiments for P70S6K and one independent experiment for ULK1.

The lung cancer cells showed an increase in phosphorylated P70-S6K (P-P70-S6K) expression after treatment with Erastin, and a decreased expression after cotreatment with C968 alone and cotreatment with Erastin or RSL3, in comparison to the vehicle (**Figure 4.34**). There was a trend towards increased expression of total P70S6K (T-P70-S6K) after treatment with RSL3 and C968 alone, and also cotreatment of C968 with RSL3 (**Figure 4.34**).

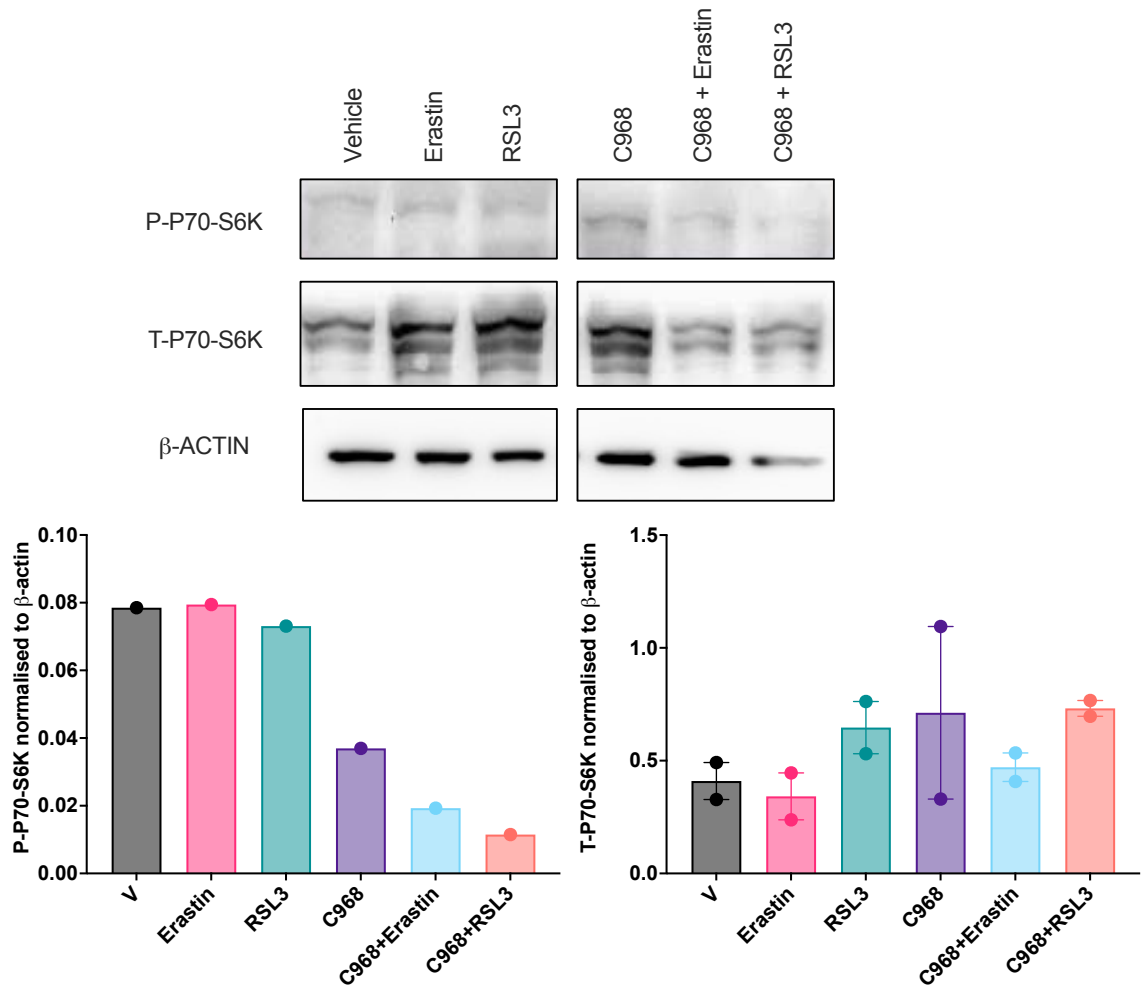


Figure 4.34: P70S6K western blots for LC2 lung cancer cells. The lung cancer cells were treated with vehicle or C968 for 30 min prior to treatment with Erastin or RSL3 or 4 h, and phosphorylated P70S6K (P-P70-S6K) and total P70S6K (T-P70-S6K) were analysed by western blot. Representative western blot for P-P70-S6K, T-P70-S6K, and β -actin are shown. Data was presented as mean (SEM) from one independent experiments for P-P70S6K and two independent experiment for T-P70S6K.

Finally, the autophagy promotor, AMPK and LC3B a widely used marker for autophagy were investigated. In the breast cancer cells, there was trend towards increased expression of P-AMPK after treatment with C968 alone and cotreatment of C968 with Erastin (**Figure 4.35**). Total AMPK (T-AMPK) increased after treatment with C968 alone. There was a trend towards increased expression of LC3B-I after treatment with RSL3 and C968 alone, whereas LC3B-II increased after cotreatment of C968 and Erastin (**Figure 4.35**).

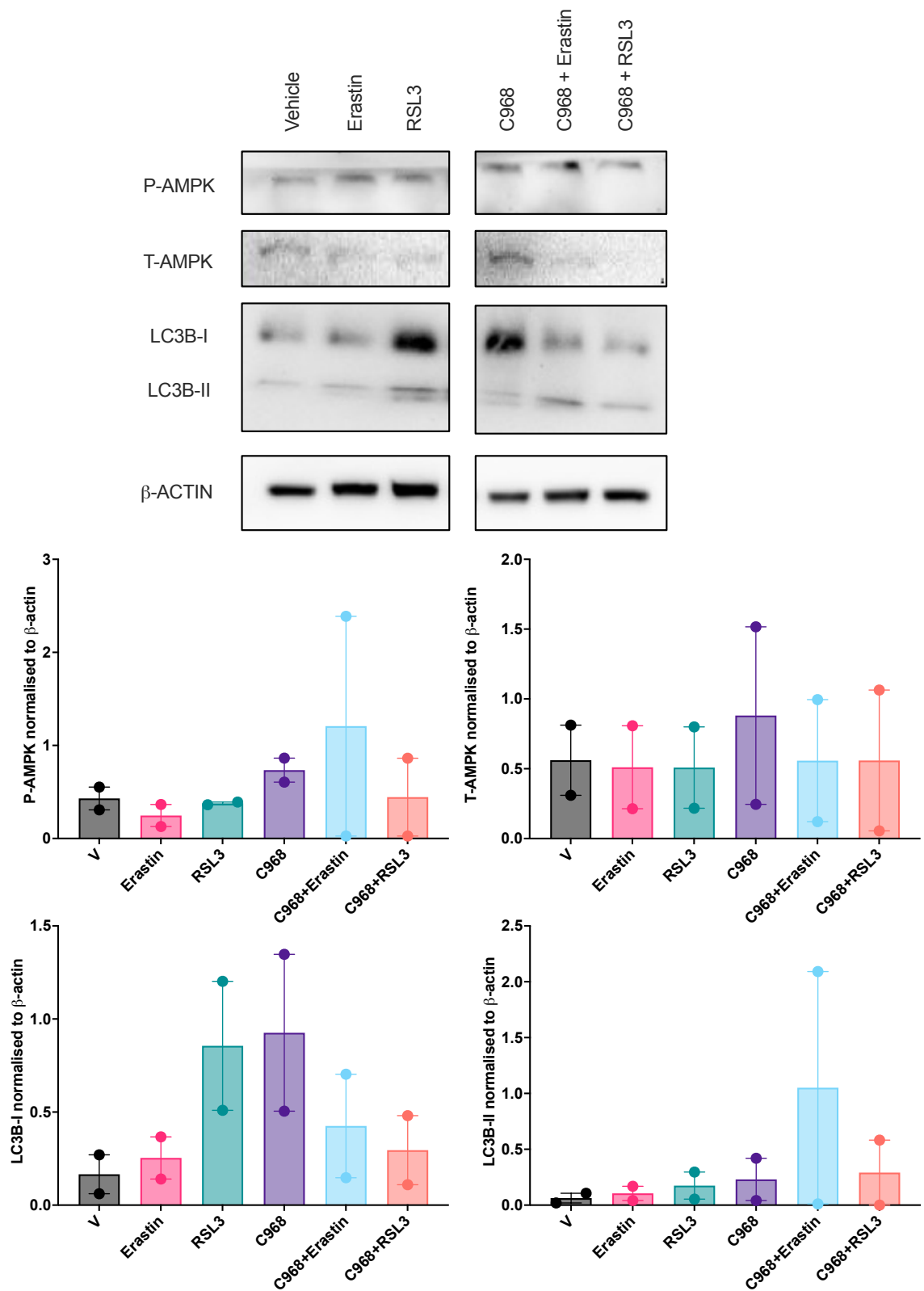


Figure 4.35: AMPK and LC3B western blots for 4T1 breast cancer cells. The breast cancer cells were treated with vehicle or C968 for 30 min prior to treatment with Erastin or RSL3 or 4 h, and phosphorylated AMPK (P-AMPK), total AMPK (T-AMPK), LC3B-I and LC3B-II were analysed by western blot. Representative western blot for P-AMPK, T-AMPK, LC3B-I, LC3B-II and β -actin are shown. Data was presented as mean (SEM) from two independent experiments.

The colon cancer cells showed an increased expression of phosphorylated AMPK (P-AMPK) after treatment with RSL3 alone (**Figure 4.36**). With a trend towards decreased expression of total AMPK (T-AMPK) after cotreatment with C968 with Erastin or RSL3 (**Figure 4.36**). The colon cancer cells showed a decrease in expression of LC3B-I after treatment with RSL3 alone, but an increase in LC3B-II. There was also a trend towards decreased expression of LC3B-I after cotreatment with C968 and either Erastin or RSL3 (**Figure 4.36**). There was a trend towards increased expression of LC3B-II after treatment with Erastin alone (**Figure 4.36**).

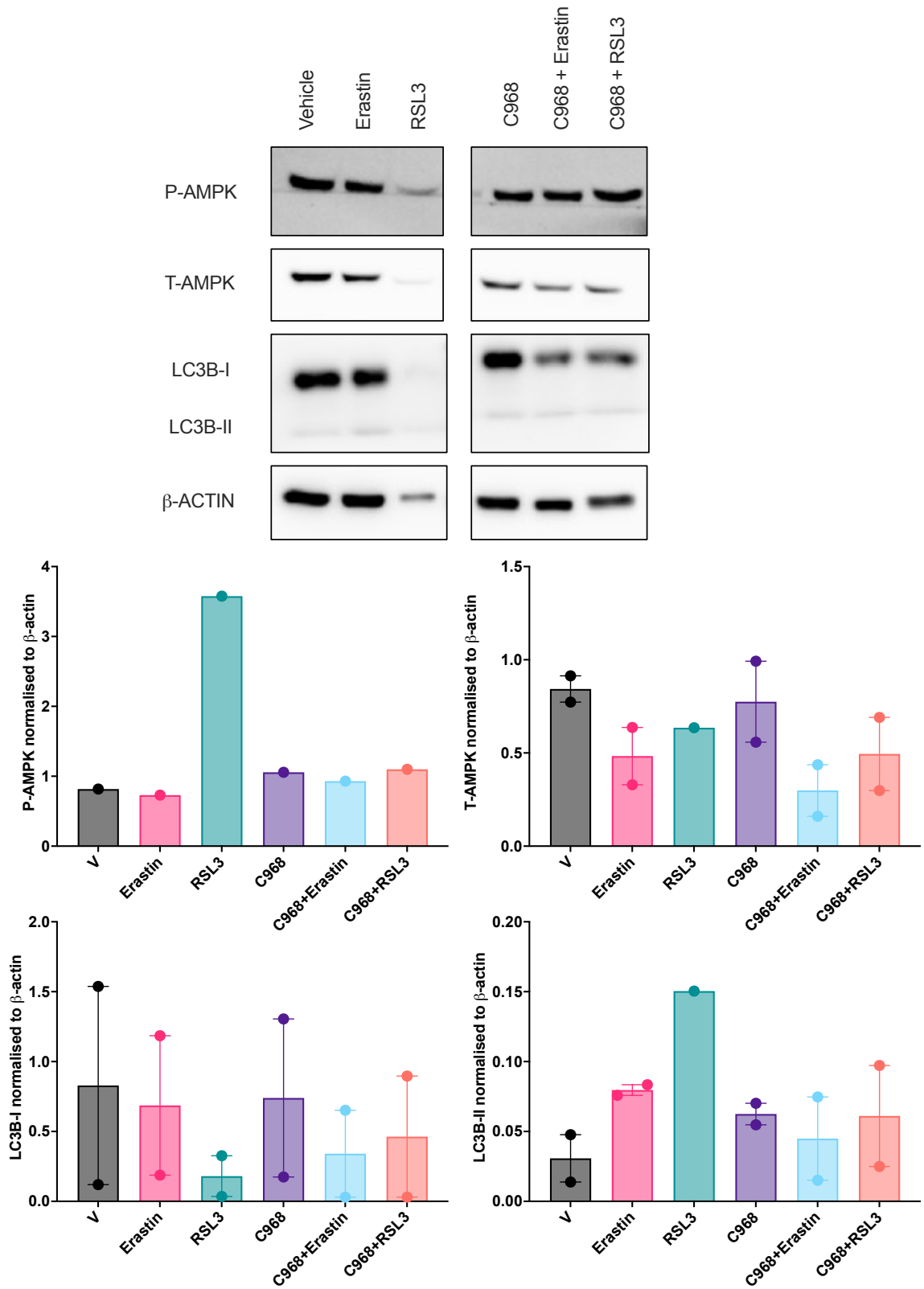


Figure 4.36: AMPK and LC3B western blots for MC38 colon cancer cells. The colon cancer cells were treated with vehicle or C968 for 30 min prior to treatment with Erastin or RSL3 or 4 h, and phosphorylated AMPK (P-AMPK), total AMPK (T-AMPK), LC3B-I and LC3B-II were analysed by western blot. Representative western blot for P-AMPK, T-AMPK, LC3B-I, LC3B-II and β -actin are shown. Data was presented as mean (SEM) from two independent experiments.

The lung cancer cells showed an increase in phosphorylated AMPK after treatment with RSL3 alone. There was a trend towards decreased expression of total AMPK for each treatment in comparison to the vehicle (**Figure 4.37**). There was an observed increase in LC3B-I after treatment with C968 alone and cotreatment of C968 with either Erastin or RSL3 (**Figure 4.37**). There was also an observed increase in LC3B-II after treatment with RSL3 alone, in comparison to the vehicle (**Figure 4.37**).

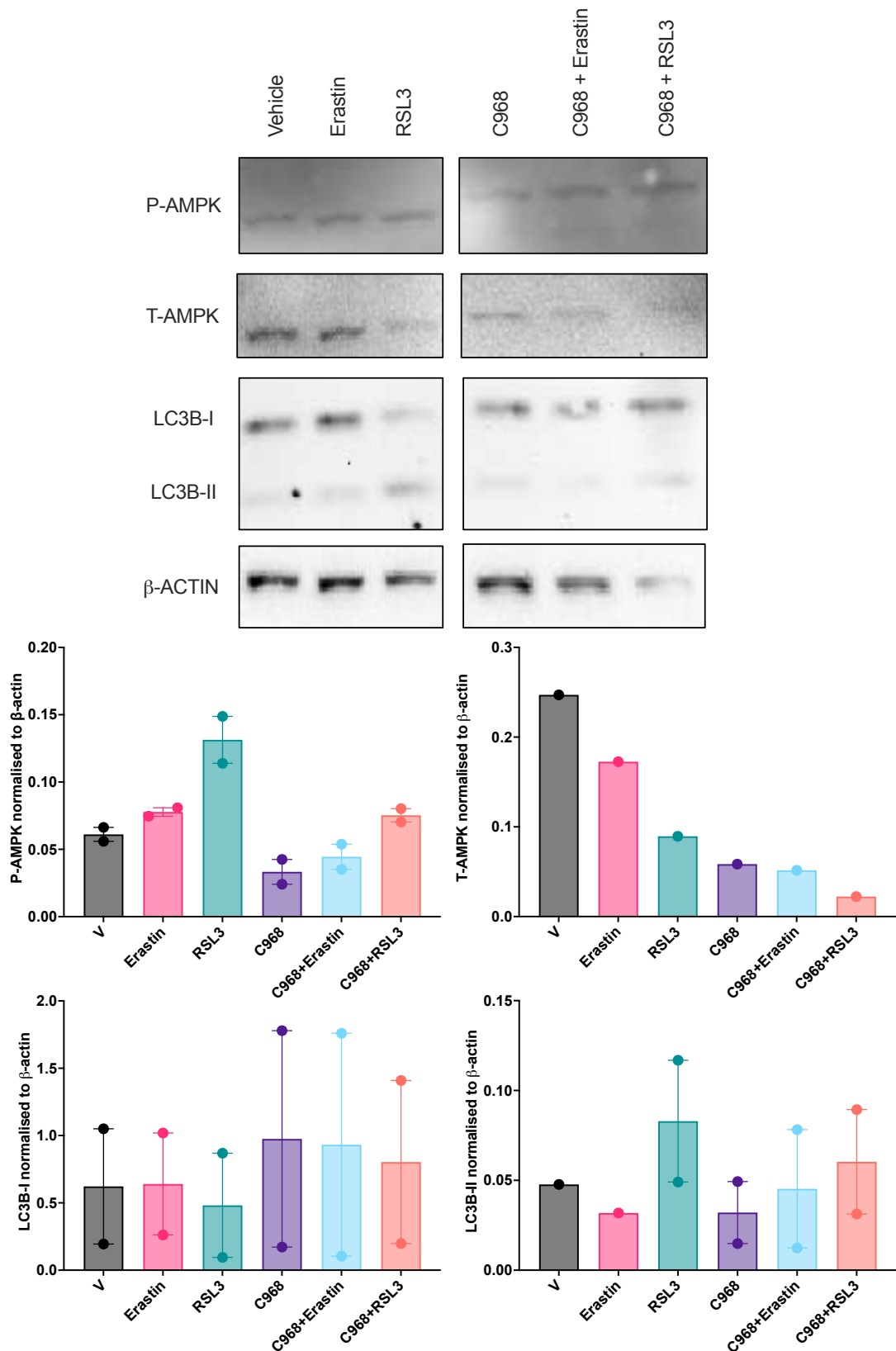


Figure 4.37: AMPK and LC3B western blots for LC2 lung cancer cells. The lung cancer cells were treated with vehicle or C968 for 30 min prior to treatment with Erastin or RSL3 or 4 h, and phosphorylated AMPK (P-AMPK), total AMPK (T-AMPK), LC3B-I and LC3B-II were analysed by western blot. Representative western blot for P-AMPK, T-AMPK, LC3B-I, LC3B-II and β -actin are shown. Data was presented as mean (SEM) from one independent experiment for AMPK and two independent experiments for LC3B.

4.5 Discussion

Cellular energy metabolism is regulated by AMPK and mTOR. mTOR is a nutrient sensor that regulates growth, proliferation and survival. mTOR is inhibited under nutrient deplete conditions by AMPK but can also be inhibited by the pharmaceutical compound Torin-1 or the naturally occurring rapamycin (Thoreen et al., 2009; Laplante & Sabatini, 2012). In the present chapter, rapamycin resulted in decreased cell viability in the breast cancer cells only. TNBC has been found to be resistant to rapamycin treatment *in vivo*, but this was attributed to the hypoxic tumour microenvironment. Other research has shown that the sensitivity of TNBC to rapamycin is also dependent on the expression of Rictor (Watanabe et al., 2020), indicating that 4T1 breast cancer cells may have a low expression of Rictor. Torin-1 also resulted in decreased cell viability in the breast cancer cells only. Inhibition of TNBC tumour growth has previously been shown *in vivo* after consecutive treatment with Torin-1 (Dai et al., 2021).

Energy stress activates AMPK, which works to counteract decreased energy by switching on catabolic pathways such as glycolysis and turning off anabolic pathways and inhibiting mTORC (Mihaylova & Shaw, 2011; Hardie et al., 2016). AMPK can also be activated by pharmaceutical compounds such as AICAR (Corton et al., 1995), but also inhibited by compound C (Liu et al., 2014). Compound C has previously been shown to suppress ferroptosis induced by Erastin (Song et al., 2018), surprisingly we found no changes in cell viability after the cotreatment of compound C and Erastin, in comparison to Erastin treatment alone, in the panel of cancer cell lines. However, we did show a rescue effect against RSL3 induced ferroptosis by compound C in the majority of cancer cell lines, currently no research has shown this correlation. Previous work undertaken in MEFs showed the inhibition of Erastin and RSL3 induced ferroptosis by cotreatment with AICAR, through the reduction in lipid hydroperoxides (Li et al., 2020). This current chapter showed a rescue of RSL3 induced ferroptosis by AICAR in the breast cancer cell line; however there was

a further reduction in cell viability with the cotreatment of AICAR with Erastin in the breast, colon and lung cancer cell lines.

The protein level of GPX4 has previously been shown to decrease after treatment with AICAR. The activation of AMPK by AICAR was concluded to regulate ferroptosis through the regulation of GPX4 (Li et al., 2022). This present chapter showed no changes in the protein level of GPX4 after the treatment with AICAR or compound C. Initially the colon cancer cells showed a significant reduction in cell viability after treatment with RSL3 and cotreatment of AICAR and RSL3. There was an observed increase in GPX4 protein levels for these two treatments, however, there was instability in the house-keeping protein, β -actin. The breast cancer cells initially showed a rescue in cell viability after cotreatment of AICAR and RSL3, the protein levels for GPX4 decreased after the cotreatment. Therefore, changes in GPX4 expression could be a coping mechanism in order to evade ferroptotic cell death.

The phosphorylation of P70-S6K (p-p70-S6K) is the most widely used biomarker for mTOR activation and autophagy inhibition (Granville et al., 2007). Previous studies have shown that compound C sustains high levels of p-p70-S6K and decreases p-ULK1 at residue Ser757 (Zhao et al., 2018). This current chapter showed that the inhibition of AMPK by compound C resulted in increased protein levels of P-P70-S6K in breast, colon and lung cancer cells. However, there was some variability in the data, therefore further experiments need to be undertaken in order to make a full conclusion. Compound C showed a rescue against RSL3 induced ferroptosis in breast, colon and lung cancer, indicating that the activation of mTOR rescues against ferroptotic induction.

As expected, the total-P70-S6K (T-P70-S6K) was increased after compound C treatment and cotreatment of compound C with either Erastin or RSL3. The activation of AMPK by AICAR also resulted in increased T-P70-S6K in breast and colon cancer cells. Previous studies have shown that P70-S6K is overexpressed in some cancer cells due to the role the PI3K/mTOR pathway

plays in cell growth and survival (Heinonen et al., 2008). Therefore, the increase in P70-S6K in breast and colon cancer cells could be a coping mechanism in order to prevent cell death (Segatto et al., 2014).

The activation of mTOR prevents ULK1 activation through the phosphorylation of the Ser757 residue (Kim et al., 2011). However, in this chapter the ULK1 Ser757 residue showed a reduction in protein levels in the breast and colon cancer cells, indicating that mTOR is not activated. The breast cancer cells showed an increase in the ULK1 Ser555 residue indicating P-AMPK activation. However, further investigation into ULK1, Ser757 and Ser555 residues is required, in order to get a better understanding of ULK1's role in ferroptosis.

There were high basal levels of P-AMPK in breast and lung cancer cells. The breast and cancer cell lines displayed increased P-AMPK after AICAR treatment and decreased P-AMPK after compound C treatment as expected. The breast and lung cancer cells initially showed a rescue in cell viability after cotreatment of AICAR and RSL3, indicating that P-AMPK activation rescues against RSL3-induced ferroptosis. Whereas, the colon cancer cell line did not show any changes from basal P-AMPK levels, which could indicate why no changes were observed in cell viability for cotreatment of AICAR and RSL3.

A key regulator of autophagy is BECN1, which has been found to promote ferroptosis (Song et al., 2018). However, in this chapter no changes in BECN1 expression were observed in the cancer cell lines tested. Finally, the autophagic marker LC3B-II was increased in all three cancer cell lines after treatment with compound C and cotreatment of compound C with either Erastin or RSL3, indicating the induction of autophagy, through the production of autophagosomes. However, studies have shown that the activation of LC3B-I to LC3B-II does not always result in complete autophagy (Gimenez-Xavier et al., 2008). The induction of autophagy may involve signalling pathways that bypass mTORC (Ajoalabady et al., 2021), due to the observed increase in P-P70-S6K and downregulation of ULK1 Ser757.

Compound 986 is known to inhibit the glutaminases, subsequently inhibiting the glutaminolysis pathway, which is essential for ferroptosis (Gao et al., 2015; Yuan et al., 2016). There was a significant reduction in breast cancer cell viability after treatment with compound 968, which is supported by et al., 2010, who also showed reduced growth of breast tumours after treatment with 10 μ M compound 968. Previous work undertaken by Gao et al., 2015 showed that compound 968 inhibited Erastin induced ferroptotic cell death. However, in this chapter, there was no significant rescue of cell viability after the cotreatment of compound 968 and Erastin. Although, Gao et al., 2015 used double the concentration of compound 968 at 20 μ M and a lower dose of Erastin at 1 μ M.

Compound 968 did rescue the panel of cancer cells from RSL3-induced ferroptosis, which could be a result of the increased expression of GPX4 protein levels in the breast and lung cancer cell lines. The cotreatment also showed increased levels of BECN1 in breast and lung cancer cells, indicating that autophagy was induced in order to evade RSL3-induced ferroptosis. The cotreatment of compound 968 and Erastin, further resulted in reduced cell viability, but also increased levels of BECN1, indicating that BECN1 promoted Erastin-induced ferroptosis. It has previously been shown that BECN1 promotes ferroptosis, in an autophagy-independent manner through the direct inhibition of SLC7A11 (Song et al., 2018).

All cancer cell lines showed a reduction in phosphorylated P70-S6K indicating that mTOR was not activated. There was an observed increase in P-AMPK after cotreatment of compound 968 and RSL3, along with an increase in LC3B-II, further indicating that autophagy was activated in order to evade RSL3-induced ferroptosis. There was observed increase in P-AMPK after cotreatment of compound 968 and Erastin in the colon cancer cells, indicating that autophagy was induced, which further promoted Erastin-induced ferroptosis. AMPK has also been shown to phosphorylate BECN1 which

consequently forms the BECN1-SLC7A11 complex and results in ferroptotic cell death (Song et al., 2018).

4.6 Conclusion

The AMPK inhibitor, compound C, rescued cell viability from RSL3-induced ferroptosis. The increase in the mTOR activation biomarker, phosphorylated P70-S6K, indicates that mTOR activation protects against RSL3-induced ferroptotic cell death. However, the increase in the autophagy marker, LC3B-II shows that autophagy was induced, therefore autophagy may involve signalling pathways that bypass mTORC.

The AMPK activator, AICAR, also rescued cell viability from RSL3-induced ferroptosis. The increase in P-AMPK and LC3B-II indicates that autophagy was induced in order to evade RSL3-induced ferroptotic cell death.

The glutaminolysis inhibitor, compound 968, rescued cell viability from RSL3-induced ferroptosis, which could be due to the increase in GPX4. Compound 968 further reduced cell viability with Erastin, the increase in BECN1 expression indicates that the BECN1-SLC7A11 complex was formed, further promoting ferroptotic cell death.

Chapter 5: Nanoparticle Development

5.1 Introduction

Malignant tumour cells exhibit different metabolic requirements compared to most normal differentiated cells necessitating the ability to reprogramme metabolic pathways. Iron is essential throughout the development of tumours; primarily for survival and proliferation of tumour cells but also promotion of the metastatic cascade (Torti & Torti, 2013). Therefore, cancer cells display deregulated iron homeostasis, which is achieved via upregulation of the transferrin receptor protein 1 (TFR1). Increased expression of iron-regulated genes, such as *TFR1*, ferritin light chain (*FTL*) and iron regulatory protein-2 (*IRP2*) are correlated with poor prognosis and the development of a higher tumour grade and increased chemoresistance (Basuli et al., 2017). However, excess intracellular iron may generate ROS, which can subsequently attack membrane lipids, inducing ferroptosis: an iron-dependent form of programmed cell death (Stockwell et al., 2017). Therapies that interfere with key regulators of iron metabolism and cellular iron trafficking represent a promising new class of therapeutic agents (Crielaard et al., 2017). As iron overload is essential for ferroptotic induction, nanoparticles that may increase cellular levels of iron to toxic levels are promising for cancer therapy.

Over the past few decades, nanotechnology has become an emerging new therapy for cancer treatment (Dadwal et al., 2018). Nanoparticle delivery systems are a form of precision medicine that can be personalised to the patient, as the surface of the nanoparticles can be manipulated with tumour-specific targeting moieties, which further increases accumulation at the tumour site and decrease off-target effects (Shah & Dobrovolskaia, 2018; Mundekkad & Cho, 2022). During tumour progression angiogenesis is induced and new vasculature is developed in order to provide the tumour with nutrients required for further progression. During vasculature development, gaps form between the endothelial cells, resulting in a leaky structure through which nanoparticles can penetrate, this is known as the enhanced permeability and retention effect (EPR effect). The EPR effect was first described in 1986 by Matsumura and Maeda, who observed the prolonged accumulation of macromolecules in the

tumour, due to the hyper-vasculature, enhanced permeability and lack of recovery by the blood and lymphatic vessels (Matsumura & Maeda, 1986). The EPR effect results in favourable accumulation of nanoparticles at the tumour site rather than accumulation in normal tissues (Maeda & Islam, 2020). However, this passive application of nanoparticles cannot discriminate between cancer cells and healthy cells (Golombek et al., 2018). Also some solid tumours display a low-EPR effect which limits the efficacy of passive targeting. Active targeting nanoparticles can overcome the low-EPR by taking advantage of overexpressed receptors on the tumour cell surface; such as EGFR, folate receptor or transferrin receptor (Soetaert et al., 2020). This targeted approach aims to improve the selectivity of nanoparticle delivery to cancer cells while minimising exposure to healthy tissue.

Superparamagnetic iron oxide nanoparticles (SPIONs) are at the forefront of nanomaterials in cancer therapy. The SPION core is either magnetite (Fe_3O_4) or maghemite ($\gamma\text{Fe}_2\text{O}_3$), both of which occur naturally within the environment as nano-sized crystals (Singh et al., 2010). SPIONs are divided into three categories based on their hydrodynamic diameter: oral SPION (300 nm-3.5 μm), standard SPION (50-150 nm) and ultra-small SPION (<50 nm: Jin et al., 2014). Intravenous injection is the most common administration of SPIONs and accounts for 1.25-5% of the total body iron stores (Elias & Tsourkas, 2009).

Iron oxide is biodegradable and excess iron is free to enter the bodies iron stores, protecting against the onset of anaemia, which is frequently observed in patients undergoing chemotherapy (Knight et al., 2004; Sun et al., 2010). The available iron is metabolised within the liver before either being excreted by the kidneys or used in the formation of red blood cells (Anzai et al., 2003). The initial principle behind SPION development was the aim to use of an external magnetic field to guide nanoparticles directly to the tumour sites. This application is known as superparamagnetism, meaning that SPIONs exhibit saturation magnetisation when a magnetic field is present, but upon removal

of a magnetic field the SPIONs do not exhibit any residual magnetic interactions (Arora, 2012). More recently, due to their magnetic properties and biodegradability, SPIONs are primarily used in cancer theragnostic applications, such as magnetic resonance imaging (MRI). Within this application SPIONs have enabled the early detection of progressive diseases (Amstad et al., 2009). The magnetic field guides SPIONs to the target area in order to maximise the therapeutic treatment; however, this results in the accumulation of iron in a localised area, causing iron overload, which can result in toxic effects (Singh et al., 2010). Irons ability to cause oxidative stress through the Fenton reaction can result in cytotoxic effects, this study aims to use iron overload to an advantage for cancer treatment.

The toxicity and biocompatibility of SPIONs for biomedical purposes still pose some concern, with research still ongoing (Vakili-Ghartavol et al., 2020). The physio-chemical properties of SPIONs enable them to cross the complex biological barriers and interact with all cell types, consequently resulting in SPION-induced genotoxicity (DNA damage, oxidative stress, micronuclei formation and chromosome condensation; Fubini et al., 2010; Ghosh et al., 2020), Insulin-coated gold nanoparticles of 20 nm have been found to pass the blood-brain barrier and accumulate within the brain, even after being injected into the tail vein of mice (Betzer et al., 2017). The surfaces of SPIONs are coated with surfactants or capping agents in order to maintain SPION size and shape and prevent agglomeration (Zook et al., 2011). Ghosh et al., 2020 found that encapsulating SPIONs with either α -tocopheryl-polyethelene glycol-succinate (TPGS) or didodecyl-dimethyl-ammonium-bromide (DMAB) reduced cytotoxicity, genotoxicity and ROS generation in comparison to the uncoated SPION. Encapsulating the SPION core is an important characteristic to consider during synthesis and is also essential for their use as a drug delivery vehicle (Vangijzegem et al., 2023), for example, they can be conjoined with chemotherapeutics in order to produce effective cancer treatments. The encapsulating material also has an effect on the nanoparticle size, zeta potential and blood half-life (1-36 h) which contribute to the biodistribution and retention of the nanoparticles and therefore affects

clearance rate and toxicity (Poller et al., 2017). For *in vivo* and clinical applications nanoparticles must be non-toxic and compatible with bodily fluids (Malhortra et al., 2020). These particles have a tendency to undergo degradation within the body, emphasising the importance of understanding the toxicity associated with both the particles in their entirety and the by-products. Iron oxide nanoparticles have displayed adverse effects, including inflammation, hypersensitivity and even anaphylactic shock (Geppert & Himly, 2021). The toxicity of iron oxide nanoparticles is linked to their physiochemical characteristics (size, shape, coating and surface charge; Feng et al., 2018).

The biodistribution of iron oxide nanoparticles in the body is dependent on the concentration administered intravenously, initially the nanoparticles circulate in the blood before depositing in different organs. Gaharwar et al (2019) demonstrated that elevated doses of iron oxide nanoparticles (30mg/kg), led to substantial accumulation in the liver, spleen and kidneys of rats. The liver serves as a primary line of defence against nanoparticles, and the deposition of these particles in the liver is attributed to the role of Kupffer cells in the organ. Larger nanoparticles are effectively eliminated from circulation and deposited in the spleen by macrophages and internalisation of red blood cells. Accumulated nanoparticles in the kidney indicates that the nanoparticles were unable to be excreted through urine (Gaharwar et al., 2019). Therefore understanding the intricate biodistribution patterns of iron oxide nanoparticles is vital for assessing their safety and potential impacts on physiological functions.

Within this study one SPION was used; Ferumoxytol[®], which is coated with a polyglucose carboxymethylether, which form branches of polysaccharides. Ferumoxytol was approved in the European union (EU) for iron replacement therapy in patients who have chronic kidney disease (CKD). Ferumoxytol was found to cause serious hypersensitivity reactions including fatal anaphylaxis which resulted in its removal from the UK in 2015 but still has FDA approval in America. Ferumoxytol is the only FDA approved product after other products (Resovist and Feridex) were removed due to safety issues. Ferumoxytol has

numerous properties that would lend themselves to repurposing within biomedical applications. The use of intravenous ferumoxytol (Feraheme™) was more effective than oral iron therapy to increase haemoglobin levels, transferrin saturation and ferritin production in patients with CKD (Schwenk, 2010; Pai & Garba, 2012). The mean diameter of ferumoxytol is 30 nm with a molecular weight of 750 KDa, their large size results in the nanoparticles becoming trapped within the intravascular space (Lehrman et al., 2018). The coating protects the bioactive iron from dissociation, caused by plasma components, until it enters reticuloendothelial system (RES) macrophages (Balakrishnan et al., 2009). RES macrophages break down the nanoparticles so that the iron is free to enter the body's iron stores, whilst the carbohydrate coating is excreted (Lehrman et al., 2018). However, the dextran coating has been shown to bond poorly with the iron oxide core, resulting in detachment, aggregation and precipitation of the nanoparticles (Jung, 1995).

A study undertaken by Zanganeh et al., 2016 showed that ferumoxytol nanoparticles significantly suppressed adenocarcinoma cells when co-cubated with macrophages. They showed that tumour suppression was associated with pro-inflammatory macrophages, with an increase in M1 macrophages within the tumour tissue (Zanganeh et al., 2016).

Polymers are the most widely used coating agents for nanoparticles, improving colloidal stability through steric stabilisation (Boyer et al., 2010). Synthetic polymers such as polyethylene glycol (PEG), polyvinyl alcohol (PVA) and polyvinyl pyrrolidone (PVP) are among the most commonly used coatings for nanoparticle stabilisation (Vangijzegem et al., 2023). Within this study PEG was used for the stabilisation of iron oxide nanoparticles.

Coating the surface of nanoparticles with PEG can help improve the efficiency and stability of drug delivery. The FDA have classified PEG as Generally Regarded as Safe (GRAS); therefore, PEG is the most widely used polymer coating in the drug delivery field. In 1995 the FDA approved the first PEGylated nanoparticle, Doxil; since then, PEGylation has become the central component

of nanoparticle formulation (Barenholz, 2012). This polymer coating provides a barrier and prevents the uptake of nanoparticles by RES macrophages. The PEG chains create a hydrophilic protective layer around the nanoparticle core, which repels the absorption of opsonins. Overall, PEG increases plasma half-life and tumour-specific targeting (Weissleder et al., 1995; Zhang et al., 2002; Dulinska-Litewka et al., 2019; Amatya et al., 2021). PEGylated iron oxide nanoparticles have been shown to have no obvious cytotoxic effects in macrophages and cancer cells, even at higher doses (30 nm; Feng et al., 2018). Lower doses (10 nm) of PEGylated iron oxide nanoparticles have been shown to increase cellular uptake and tumour accumulation (Feng et al., 2018).

Iron oxide nanoparticles have been shown to induce ferroptosis in glioblastoma cells (Wen et al., 2021). The findings from Wen et al., 2021, showed an increase in ferroptosis markers, which were reported to be regulated by Beclin1/ATG5-dependent autophagy pathways. Iron oxide nanoparticles have also been shown to induce ferroptosis in macrophages through the upregulation of p53, the transcription factor responsible for tumour suppression (Wu et al., 2022). Recently, a novel iron oxide nanoparticle coated with gallic acid and polyacrylic acid was shown to induce ferroptosis in glioblastoma, neuroblastoma and fibrosarcoma cells (Fernandez-Acosta et al., 2022).

This chapter focuses on using iron oxide nanoparticles as a possible novel therapy for melanoma. Metastatic melanoma is the most aggressive form of skin cancer, with asymptomatic metastasis, and poor prognosis, there are currently limited treatment options (Huang & Zappasodi, 2022). The main treatment for melanoma was dacarbazine, a chemotherapy drug, which is used against advanced stages of cancer. However, melanoma cancer patients treated with dacarbazine showed poor response rates of 7.5% (Agarwala, 2009; Mundra et al., 2015). Chemotherapy and nanomedicines, still remain extremely ineffective due to therapy resistance (Gogas et al., 2007; Bilbao-

Asensio et al., 2022), therefore new therapy strategies are required in order to enhance therapy delivery.

The majority of cancers metastasise through the blood, although this process is highly inefficient and results in cancer cell death (Alitalo & Detmar, 2012). Epithelial cancers and melanoma are also able to metastasise through the lymphatic system (Alitalo & Detmar, 2012). Lymphangiogenesis is known to be induced during cancer progression, resulting in increased lymphatic density and ultimately promoting metastasis of cancer cells to lymph nodes (Christiansen & Detmar, 2011). Studies have shown that B16F10 melanoma tumours metastasise through draining lymph nodes prior to secondary invasion of the lungs (Harrell et al., 2007). Harrell et al., 2007 demonstrated that lymphangiogenesis is initiated prior to initial metastasis of the melanoma cells, indicating that tumour cells release lymphangiogenic growth factors.

Melanomas and other cancer cells are able to evade ferroptosis by metastasising through the lymph rather than through the blood. The lymphatic environment provides protection against ferroptosis due to increased levels of GSH and oleic acid, a monounsaturated fatty acid (MUFA), and less free iron (Ubellacker et al., 2020). This environment also enables cancer cells to metastasise further due to the incorporation of oleic acids into the cells, protecting them from ferroptosis during dissemination through the blood (Ubellacker et al., 2020). Lipids are important regulators of cell death and are responsible for the induction of apoptosis, necroptosis and ferroptosis. Specifically, lipid peroxidation is a pivotal trigger in the final stages of ferroptosis. However, a recent study undertaken by Magtanong et al., 2019 found that MUFAs have the potential to inhibit the induction of ferroptosis. Activation of MUFAs by acyl-coenzyme A (CoA) synthetase long-chain family member 3 (ACSL3), promotes the displacement of polyunsaturated fatty acids (PUFAs) within the plasma membrane. Overall, MUFAs and ACSL3 activity specifically promote a ferroptosis-resistant cell state (Magtanong et al., 2019). Whereas acyl-coenzyme A (CoA) synthetase long-chain family member 4

(ACSL4) has been found to be an essential component for ferroptotic cell death (Doll et al., 2016).

Ferroptosis induction is exacerbated in the presence of longer and more unsaturated fatty acids. Yang et al., 2016, found that PUFAs are highly susceptible to lipid peroxidation due to the presence of bis-allylic carbon (electrons incorporated into surrounding double bonds, resulting in a weakened hydrogen bond), the protons are vulnerable to free hydrogen ions, which are essential for the implementation of ferroptosis. The interaction between the two results in alkyl-radicals, which are available to further react with oxygen to result in peroxy-radicals, which are then free to react with PUFAs causing a continual chain reaction of lipid peroxidation (Yang et al., 2016).

A recent Swansea University study (Bilbao-Asensio et al., 2022) showed *in vivo* suppression of B16F10 melanoma tumours through the induction of ferroptosis using phospholipid-modified Pt(IV) prodrug-loaded iron oxide nanoparticle (IONP)-filled micelles (mIONP-PL-Pt(IV)). The mIONP-PL-Pt(IV) enabled effective lymphatic delivery of cisplatin, without the need for direct intratumoral injection. The use of ⁶⁷Ga-radiolabeled mIONP-PL-Pt(IV) injected at distant subcutaneous sites showed mIONP-PL-Pt(IV) trafficking at draining lymph nodes and tumour site. Redox-triggered release of cisplatin and iron resulted in an increase in ROS production by the Fenton reaction. The presence of H₂O₂ and ascorbic acid enhanced the cytotoxic effects of the mIONP-PL-Pt(IV) on melanoma cells *in vivo*. The lymphatic system has previously been shown to provide resistance and protection against cancer therapies and ferroptosis, and enables cancer metastasis (Ubellacker et al., 2020). However the use of mIONP-PL-Pt(IV) overcomes this problem, whilst also reducing the treatment dose by 10-100 fold in comparison to other intravenous treatments (Bilbao-Asensio et al., 2022).

Overall therapy-resistant cancer cells have been shown to be vulnerable to ferroptosis (Viswanathan et al., 2017). Iron addiction may be cancers' 'Achilles heel' and a novel therapeutic target.

5.2 Aims and Hypothesis

Hypothesis: Therapy-resistant cancer cells are vulnerable to iron oxide nanoparticle-induced ferroptotic programmed cell death.

Aims:

1. Characterise B16F10 melanoma cells for ferroptotic cell death, based on *Chapter 3* and *Chapter 4*.
2. To synthesise an iron oxide nanoparticle with PUFA chains in order to increase cancer cell susceptibility to ferroptosis.
3. To assay the effect of surface modified iron oxide nanoparticles on cell viability and the synergistic effect of combining iron oxide nanoparticles with either Erastin or RSL3.
4. To confirm any loss in viability is due to ferroptotic induction and not another form of programmed cell death.

5.3 Materials and Methods

5.3.1 Synthesis of mIONP-DLin

The mIONP-DLin particles were produced by self-assembly using a dry-film hydration method. In total 4 mg of IONP (Swansea University Chemistry Department) were dissolved in chloroform (300 μ l) with 16:0 PEG2000 PE (8 mg; Avanti polar lipids, Cat#880160P) and D-Lin-MC3-DMA (4 mg; Insight Biotechnology, Cat#HY-112251). The solvent was left to evaporate overnight at room temperature, leaving a dried film behind in universal. The film was then placed under vacuum for 1 hr to remove any remaining solvent. The film was then heated in a water bath at 70°C for 30 s, followed by hydration with 1 ml of nanopure water for 30 min. The suspension was purified by centrifugation (1 cycle, 9000 x g for 5 min) after which the pellet was discarded and the supernatant underwent ultracentrifugation (3 cycles, 200,000 xg for 45 min) and the supernatant was discarded.

5.3.2 MTT ((3-(4, 5-dimethylthiazol-2-yl)-2, 5- diphenyltetrazolium bromide)) assay

Cell viability was determined by the MTT assay (Wu et al., 2018). Cells were seeded at the required density, 2.5×10^3 (OVCAR8 ovarian), 5.0×10^3 (4T1 breast and MC-38 colon), 7.5×10^3 (LC-2 lung, PEO1 ovarian and PEO4 ovarian) cells/well in a 96-well plate (Helena Biosciences Cat#92096) 24 h prior to treatment. Cells were then treated in triplicate with increasing concentrations of Erastin (0, 0.15625, 0.3125, 0.625, 1.25 and 2.5 μ M) or RSL3 (0.0390625, 0.078125, 0.15625, 0.3125 and 0.625 μ M) diluted in 100 μ l of complete media before further incubation for 24 h, 37°C, 5% CO₂ in air. Alternatively, cells were treated with IFN γ (10 ng/ml; R&D Systems, Cat#DY285B) or vehicle for 30 mins prior to addition of Erastin (2.5 μ M) or RSL3 (0.625 μ M), diluted in 100 μ l of complete media before further incubation for 24 h, 37°C, 5% CO₂ in air. Alternatively, cells were treated for 30 mins with Compound 968 (10 μ M; Sigma, Cat#1327) prior to treatment with Erastin (2.5 μ M) or RSL3 (0.625 μ M), diluted in 100 μ l of complete media before further

incubation for 24 h, 37°C, 5% CO₂ in air. Alternatively, Cells were treated in triplicate with AMPK and mTOR inhibitors and inducers (compound C (10 µM; Calbiochem, Cat#171260), AICAR (1mM; Merk, Cat#A9978), torin-1 (50 nM; Bio-Techne, Cat#4247) and rapamycin (500 nM; Bio-Techne, Cat#1292)) diluted in 50 µl of complete media for 30 mins, 37°C, 5% CO₂ in air. Cells were then treated with Erastin (2.5 µM) or RSL3 (0.625 µM) diluted in 50 µl of complete media before further incubation for 24 h, 37°C, 5% CO₂ in air. Alternatively, cells were treated in triplicate with increasing concentrations of Erastin (0, 0.625, 1.25, 2.5 µM) diluted in 100 µl of complete media before further incubation for 24 h, 37°C, 5% CO₂ in air. All media was removed before the cells were further treated with nanoparticles (mIONP-COOH, Ferumoxytol, IONP-Cit and mIONP-DLin) in 100 µl of complete medium. Controls were treated with 100 µl of complete medium only. Cells were exposed to the nanoparticle treatment for 24 h and incubated at 37°C, 5% CO₂ in air. At the end of the incubation time an MTT assay was performed (**Chapter 2; Section 2.7**). Briefly, cells were incubated with 10 mg/ml MTT for 2 h at 37°C, formazan crystals were dissolved in DMSO and absorbance was measured at 570 m using a microplate reader (POLARstar Omega; BMG).

5.3.1 Flow cytometric analysis of cell viability by Deep Red Anthraquinone 7 – DRAQ7

B16F10 cells were seeded in 1 ml of complete media at the required density 4.5×10^4 cells/well in a 24-well plate (Helena Biosciences, Cat#92024) 24 h prior to treatment. Media was replaced with vehicle control or Erastin (0.625 µM, 1.25 µM and 2.5 µM) or RSL3 (0.15625 µM, 0.3125 µM and 0.625 µM), cells were then further incubated for 24 hrs at 37°C, 5% CO₂ in air. Cells were then washed with 1 ml PBS (Gibco, Cat#10010-015), and detached by 100 µl of Accutase (Sigma, Cat#A6964) before being centrifuged at 500 xg for 5 min. The supernatant was discarded, and the cells were resuspended in 100 µl of FACs buffer. Then 5 µl of a 1 in 15 dilution of DRAQ7 (Biostatus, Cat#DR71000) was added to each sample before incubation for 15 min at room temperature in the dark. Then, 500 µl of FACS buffer was added to each

sample before being centrifuged at 500 xg for 5 min. The supernatant was discarded and the cell were resuspended in 100 μ l FACs buffer. Using a NovoCyte Flow Cytometer (ACEA Biosciences), cell populations were gated based on the forward and side scatter parameters and the non-single events excluded based on forward area and height scatter parameters (FlowJo, LCC software; **Figure 5.1**).

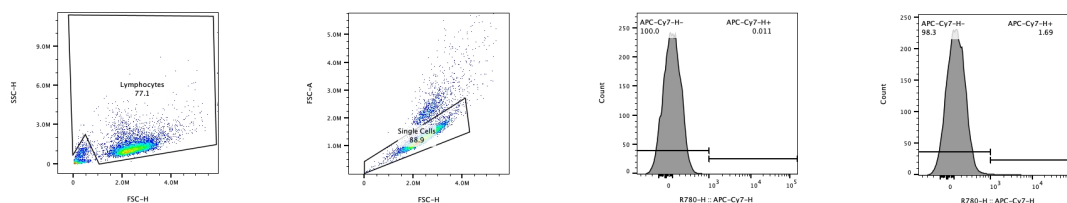


Figure 5.1: Gating strategy to determine cell viability using DRAQ7. The total population was first selected, gating out the debris such as dead cells. The singlets were selected using a FSC-H vs FSC-A dot plot. A histogram visualising the percentage positive cells was used to determine cell viability (% dead). Left histogram shows the unstained sample results and the right histogram shows the vehicle sample results.

5.3.2 Western Blot

Cells were seeded at the required density, 5.0×10^4 cells/well in a 6-well plate (Greiner Cat#657160) 24 h prior to treatment. Cells were then treated with AMPK and mTOR inhibitors and inducers (compound C (10 μ M), AICAR (1mM)) diluted in 500 μ l of complete media for 30 mins, 37°C, 5% CO₂ in air. Cells were then treated with Erastin (2.5 μ M) or RSL3 (0.625 μ M), for a further 24 h, 37°C, 5% CO₂ in air. Cells then underwent protein extraction and quantification using the DC assay, followed by western blot (**Chapter 2; Section 2.8**). Briefly 10 μ g/lane of protein was probed overnight to quantify the abundance of SLC7A11, Lamin-B1, phospho-P70S6K, P70S6K, LC3B, phospho-AMPK, AMPK, Beclin-1, GPX4, and β -actin (**Table 3**).

5.3.3 Flow cytometric analysis of intracellular staining

Cells were seeded at the required density 2.5×10^4 (OVCAR8 ovarian), 5.0×10^4 (B16F10 melanoma, 4T1 breast and MC-38 colon), 7.5×10^4 (LC-2 lung, PEO1 ovarian and PEO4 ovarian) cells/well in a 12-well plate (Greiner Cat#665180) 24 h prior to treatment. Media was replaced with water (1% in complete media; Sigma, Cat#SHBH9957) vehicle control or nanoparticles at a concentration of 500 μM of iron oxide in 1 ml complete media, cells were then further incubated for 24 hrs at 37°C, 5% CO₂ in air. Cells were then washed with 1 ml PBS (Gibco, Cat#10010-015), and detached by 100 μl of Accutase (Sigma, Cat#A6964) before being centrifuged at 290 xg for 5 min. Cells were then fixed with 100 μl of 4% paraformaldehyde solution for 20 min at 4°C and then washed two times in staining buffer (PBS (Gibco, Cat#10010-015) and 1% FBS (BIOSERA, Cat#FB-1550/500)) before centrifugation at 350 xg for 5 min. Cells were then resuspended in 1 ml perm/wash (BD Biosciences, Cat#555028) for 15 min at room temperature, before centrifugation at 350 xg for 5 min. Then, 100 μl of a 1/400 dilution of primary antibody/staining buffer (GPX4; ABCAM, Cat#ab125066) was added to the cells for 1 h at room temperature. Cells were centrifuged at 350 xg for 5 min and washed in staining buffer before 100 μl off a 1/500 dilution of secondary antibody/staining buffer (Anti-rabbit IgG Fab2 Alexa Fluor® 488 molecular probes; Cell signaling technology, Cat#4412S) was added for 30 min at room temperature in the dark. Cells were centrifuged at 350 xg for 5 min and washed in staining buffer before resuspension in 200 μl FACS buffer. Using a NovoCyte Flow Cytometer (ACEA Biosciences), cell populations were gated based on the forward and side scatter parameters and the non-single events excluded based on forward area and height scatter parameters (FlowJo, LCC software, **Figure 5.2**).

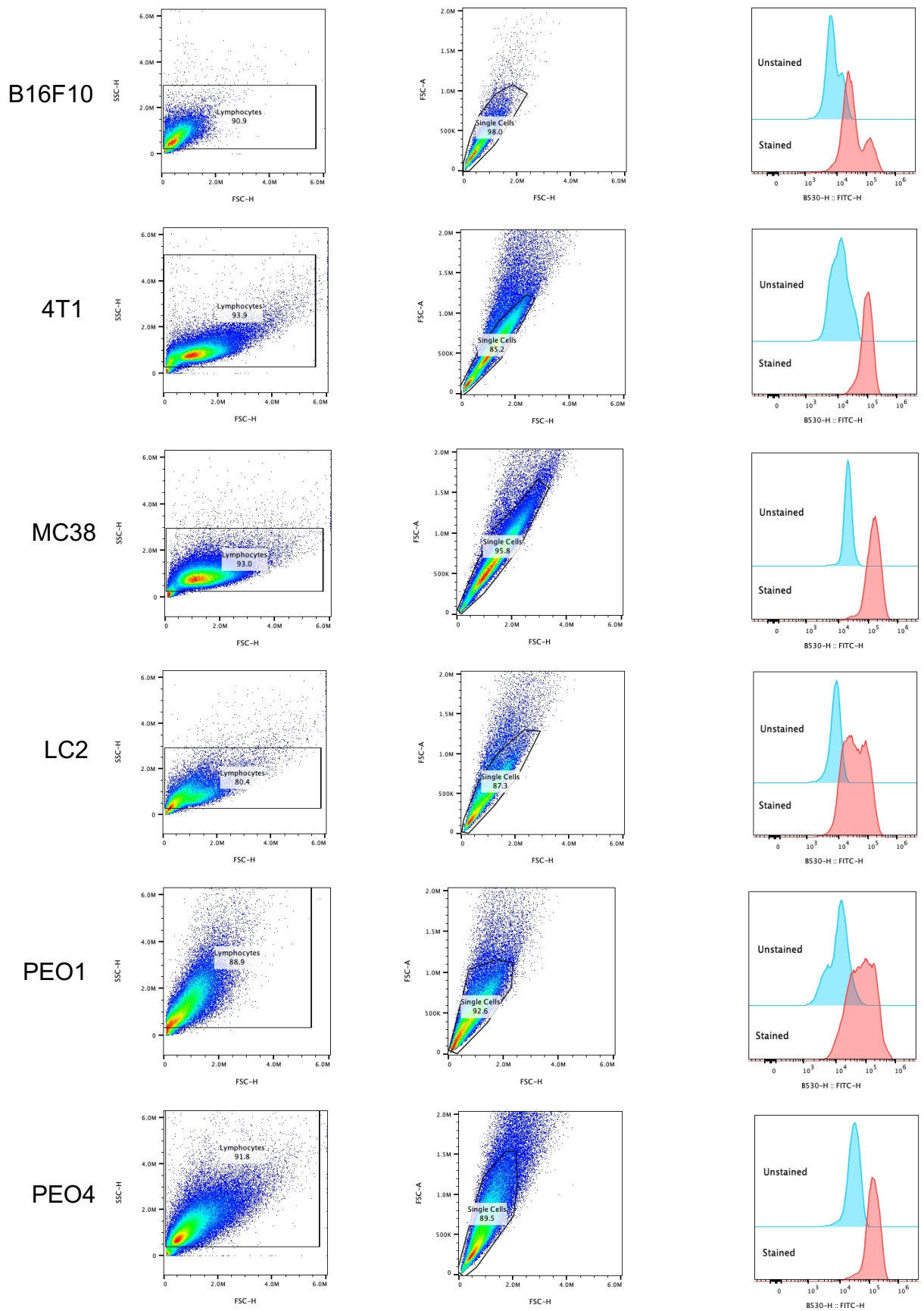


Figure 5.2: Gating strategy to determine intracellular GPX4 levels by MFI of Alexa Fluor 488. The total population was first selected, gating out the debris such as dead cells. The singlets were selected using a FSC-H vs FSC-A dot plot. A histogram visualising the MFI for Alexa Fluor 488 was then created. An unstained sample (blue histogram) shows the background of the sample. The stained sample (red histogram), demonstrates the presence of GPX4 with Alexa Fluor 488 signals.

5.3.4 Statistics

GraphPad prism 7.0 was used for statistical analysis. Normally distributed data were subjected to a two-way ANOVA with Dunnett's or Bonferroni post-hoc test; comparing the treatment in relation to the vehicle for $n \geq 3$. Significance was assumed when $P < 0.05$.

5.4 Results

The group has previously published the effects of PEGylated MUFA (oleic acid) coated iron oxide nanoparticles on cell viability of B16-F10(OVA) hereafter known as B16-F10, after preconditioning with increasing concentrations of Erastin *in vitro* and in an *in vivo* mouse model (Ruiz-de-Angulo et al., 2020).

Here, in order to develop a ferroptosis inducing iron oxide nanoparticle that used the PUFA linoleic acid, preliminary experiments were carried out in the previously established B16-F10 mouse melanoma cell line. The development of these nanoparticles was broken down into four main stages, the first stage was characterising ferroptosis in the melanoma cancer cell line, the second stage was to characterise well established iron oxide nanoparticles from the group (Ruiz-de-Angulo et al., 2020) and the effect they had on B16-F10(OVA). This was then compared to preliminary linoleic acid nanoparticles in order to determine developmental progression. The fourth stage of development was the use of finalised linoleic acid nanoparticles on a panel of cancer cell lines.

5.4.1 Characterising the B16F10 melanoma cell line

Treating melanoma cancer cells with Erastin or RSL3 induces ferroptosis to reduce cell viability.

In order to determine cancer cell susceptibility to ferroptotic induction, initially the mouse melanoma B16-F10 cells were treated with varying concentrations of ferroptosis inducers: Erastin (system X_c^- inhibitor; 0.625 μ M – 2.5 μ M; **Figure 5.3 a**) and RSL3 (GPX4 inhibitor; 0.15625 μ M - 0.625 μ M; **Figure 5.3 b**). Both Erastin (IC₅₀ 0.8617 μ M) and RSL3 (IC₅₀ 0.2985 μ M) treatment resulted in a significant reduction in cell viability at all concentrations, indicating that melanoma cells are susceptible to ferroptotic induction.

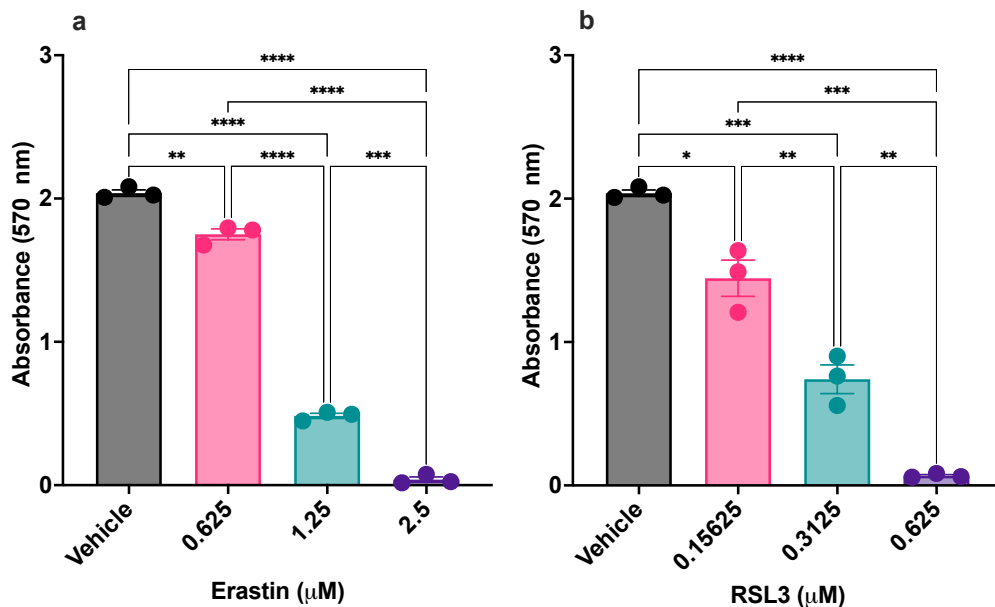


Figure 5.3: Effect of (a) Erastin and (b) RSL3 on mouse melanoma cell viability. The B16-F10 skin melanoma cell line was cultured in media containing vehicle, (a) Erastin or (b) RSL3 for 24 h. Cell viability was evaluated using MTT assay after 24 h. Data was presented as mean (\pm SEM) from three independent cell passages and analysed using 2-way ANOVA, *p<0.05, **p<0.01, ***<0.001, ****<0.0001.

The cell viability was also assessed using a cell death stain, DRAQ7. The B16-F10 cancer cells showed a significant increase in cell death at 1.25 μ M Erastin (**Figure 5.4 a**, IC₅₀ 0.8096 μ M) within 24 h treatment. Treatment with RSL3 (**Figure 5.4 b**, IC₅₀ 0.2016 μ M) showed a significant increase in cell death at 0.15625 μ M in the B16-F10 cancer cell line.

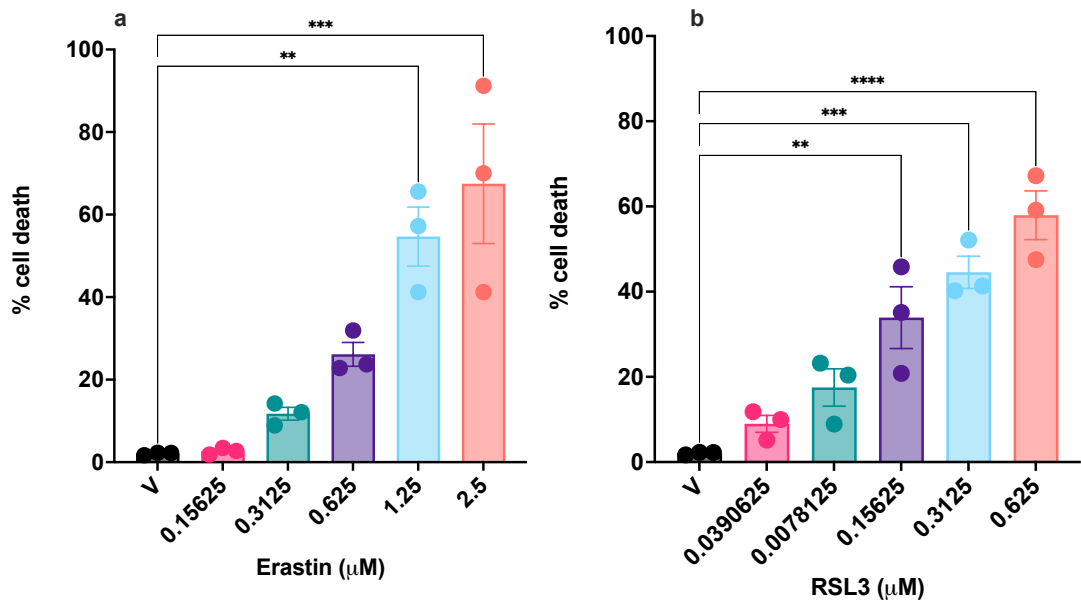


Figure 5.4: Effect of Erastin and RSL3 on cell viability, determined by DRAQ7. The B16-F10 skin melanoma cell line was cultured in media containing vehicle, (a) Erastin or (b) RSL3 for 24 h. Cell death was assessed by flow cytometry using DRAQ7 after 24 h. Data was presented as mean (SEM) from three independent cell passage experiments and analysed using 1-way ANOVA; ** $p < 0.01$, *** $p < 0.001$, **** $p < 0.0001$.

From the DRAQ7 data, the size of the cancer cells was determined, in order to understand how the cancer cells respond to ferroptotic treatment. The shrinking of cells is a key signature of ferroptosis (Yu et al., 2016). There were no significant changes in the size of the melanoma cells after treatment with all concentrations of Erastin or RSL3 (**Figure 5.5 a-b**).

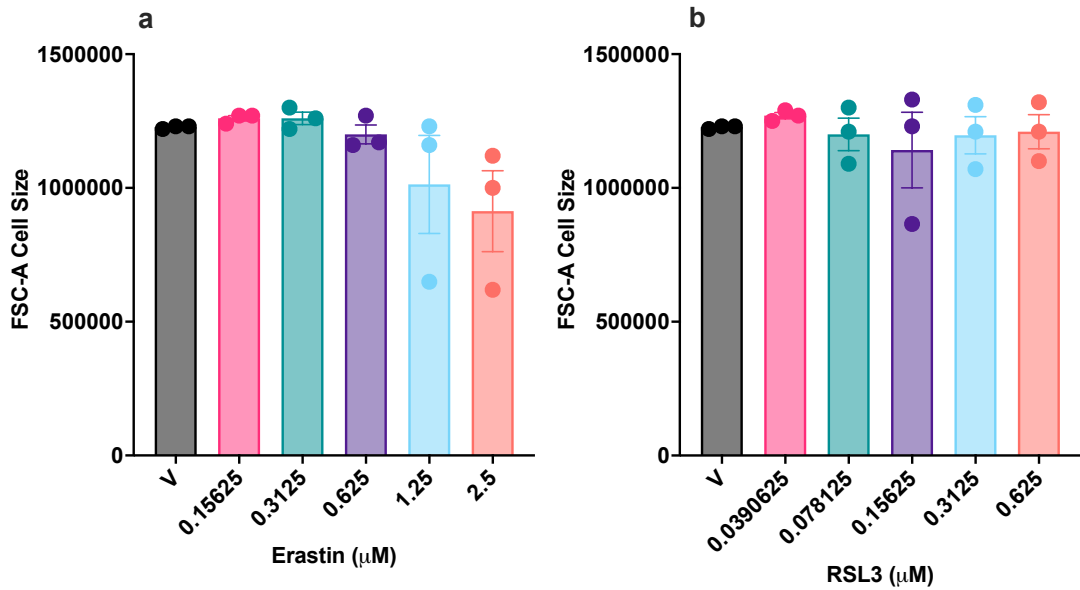


Figure 5.5: Effect of Erastin and RSL3 on cell size (FSC-A). The panel of cancer cell lines (a) 4T1; (b) MC-38; (c) LC-2; (d) PEO1; (e) PEO4; (f) OVCAR8 were cultured in media containing vehicle (v) or the individual concentrations of Erastin. Cell size was determined from the DRAQ7 data. Data was presented as mean (SEM) from three independent cell passage experiments and analysed using 1-way ANOVA; ** $p < 0.01$, **** $p < 0.0001$.

Erastin inhibits the SLC7A11 light chain component of system Xc⁻, therefore the SLC7A11 protein was next assessed for each cancer cell line by western immunoblotting (**Figure 5.6**). The quantity of SLC7A11 present in each cell line could provide an understanding for the cells' susceptibility to ferroptotic induction by Erastin. RSL3 inhibits the GPX4 enzyme, which is essential for ferroptotic induction (Yang et al., 2014), therefore the GPX4 protein was next assessed for each cancer cell line by western immunoblotting. The quantity of GPX4 present in each cell line could provide an understanding for the cells' susceptibility to ferroptotic induction by RSL3. Both GPX4 and SLC7A11 were expressed in the B16F10 cell line, however a better housekeeping gene should have been used, although Lamin-B1 was chosen in this case due to the size of the SLC7A11 protein.

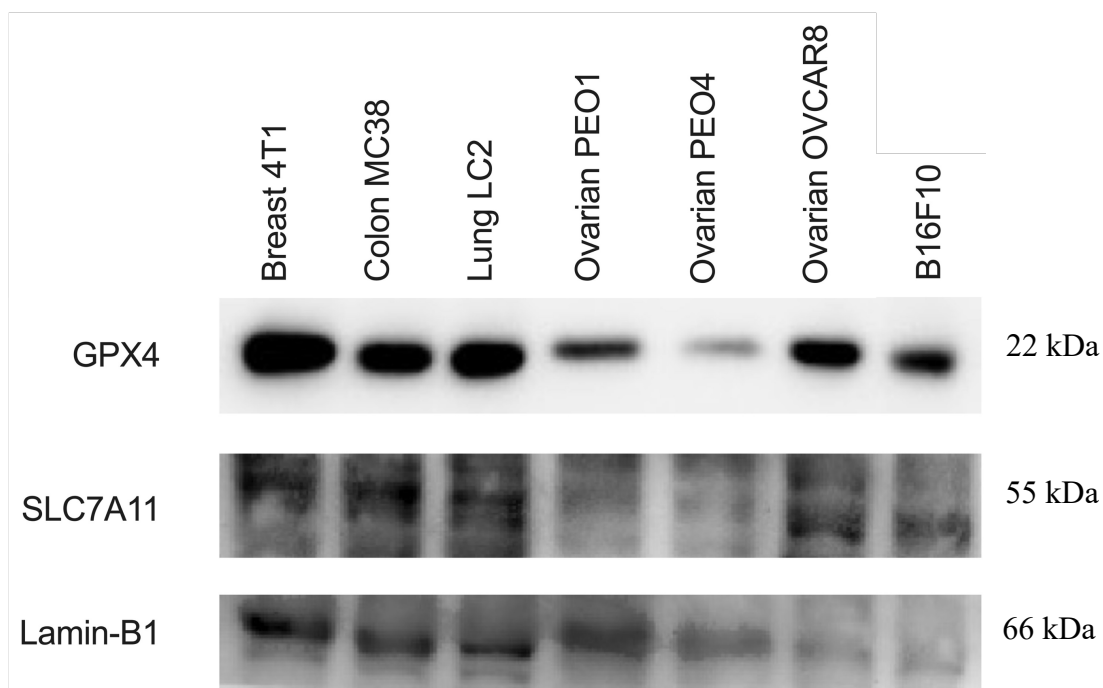


Figure 5.6: GPX4 and SLC7A11 western blots for B16F10 cancer cells. GPX4 was observed at 22 kDa, SLC7A11 was observed at 55 kDa and the housekeeping protein Lamin-B1 was observed at 66 kDa

Liproxstatin rescues against Erastin and RSL3 induced ferroptotic cell death.

The lipid peroxide scavenger Liproxstatin (Lip) was also used to determine if there was a rescue effect on viability of cells treated with Erastin (2.5 μ M) or RSL3 (0.625 μ M). Initially cells were treated with a concentration range from 25 nM to 1000 nM of LIP and 2.5 μ M Erastin (**Appendix, Figure 1**), it was determined that 100nM was sufficient to rescue against ferroptotic induction. Treatment with Lip (100 nM) alone had no effect on cancer cell viability. However, there was a significant rescue effect of the cotreatment of Lip with Erastin or RSL3 (**Figure 5.7**).

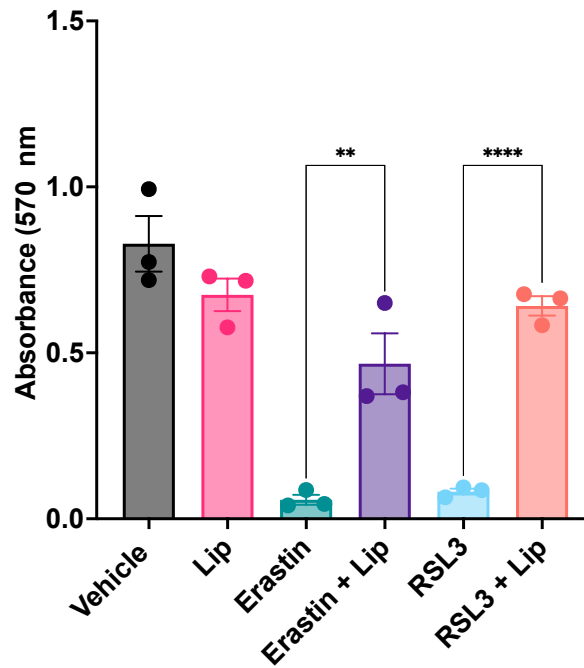


Figure 5.7: The rescue effect of Liproxstatin-1 treatment against the ferroptosis inducers, Erastin and RSL3. The mouse melanoma cells were cultured in media containing vehicle (v) or liproxstatin-1 (100 nM) or Erastin (2.5 μ M) or RSL3 (0.625 μ M). Cells were treated with liproxstatin-1 for 30 min prior to treatment with Erastin or RSL3 for 24 h. Cell viability was evaluated using MTT assay after 24 h. Data was presented as mean (SEM) from three independent cell passage experiments and analysed using 2-way ANOVA, ** $p < 0.001$, **** $p < 0.0001$.

IFN γ does not affect mouse melanoma cell viability

As discussed previously in *Chapter 3*, IFN γ is believed to downregulate *SLC7A11* and *SLC3A2*, the two components of system X $_C^-$, resulting in the induction of ferroptosis (Wang et al., 2019). Therefore, to characterise the role of IFN γ (10 ng/ml), the mouse melanoma cell line was treated concurrently with Erastin (2.5 μ M; **Figure 5.8**) or RSL3 (0.625 μ M; **Figure 5.8**), and IFN γ (10 ng/ml). The IFN γ (10 ng/ml) alone had no significant effect on cell viability, whereas Erastin (2.5 μ M) and RSL3 (0.625 μ M) alone significantly reduced cell viability. The cotreatment of IFN γ (10 ng/ml) with Erastin (2.5 μ M) or RSL3 (0.625 μ M) was similar to that of Erastin (2.5 μ M) or RSL3 (0.625 μ M) treatment alone.

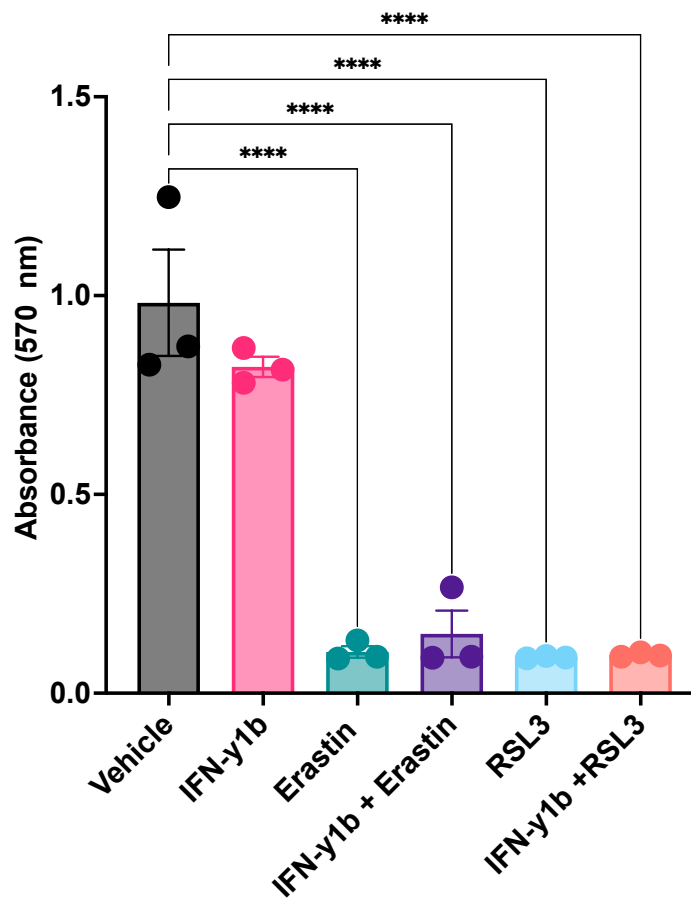


Figure 5.8: The effect of cotreatment with IFN γ and Erastin or RSL3. The mouse melanoma cells were cultured in media containing vehicle (v) or IFN γ (10ng/ml) or Erastin (2.5 μ M) or RSL3 (0.625 μ M) or IFN γ plus Erastin or IFN γ plus RLS3. Cells were treated with IFN γ for 30 min prior to treatment with Erastin or RSL3 for 24 h. Cell viability was evaluated using MTT assay after 24 h. Data was presented as mean (SEM) from three independent cell passage experiments and analysed using 2-way ANOVA, ****p<0.0001.

AMPK inhibition rescues cell viability against RSL3 induced cell death.

As discussed previously in *Chapter 4*, the mouse melanoma cells were treated with the mTOR inhibitors Torin-1 (50 nM; inhibits mTORC1 and mTORC2) and Rapamycin (500 nM; inhibits mTORC1). The cells were also co-treated with the ferroptosis inducers Erastin (2.5 μ M; **Figure 5.9 a**) or RSL3 (0.625 μ M; **Figure 5.9 b**). The mouse melanoma cells were also treated with the AMPK inhibitor, compound C (10 μ M) and the AMPK activator, 5-aminoinidazole-4-carboxamide-ribose-5-phosphate (AICAR; 1mM). The cells were also co-treated with Erastin (2.5 μ M; **Figure 5.9 a**) or RSL3 (0.625 μ M; **Figure 5.9 b**) in order to help determine the link between ferroptosis and the AMPK pathway.

The treatment of Rapamycin (500 nM) and Torin-1 (50 nM) alone resulted in a significant reduction in cell viability in melanoma cells (**Figure 5.9 a**). These results indicate that the mTOR pathway does not affect ferroptosis in melanoma cancer. The treatment of compound C (10 μ M) alone resulted in a significant reduction in cell viability in melanoma cells. There was an observed significant increase in cell viability with the cotreatment of compound C (10 μ M) with RSL3 (0.625 μ M; **Figure 5.9 b**)

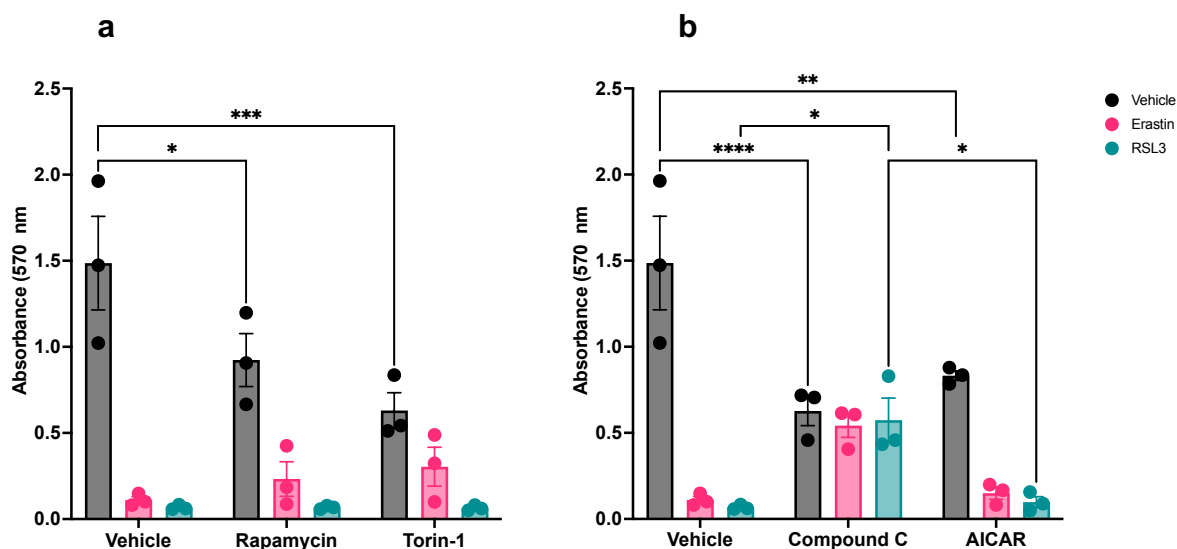


Figure 5.9: Synergistic effect of (a) mTOR inhibitors Rapamycin and Torin-1, (b) AMPK inhibitor Compound C and AMPK activator AICAR, with the ferroptosis inducers Erastin and RSL3.

- (a) The melanoma cells were cultured in media containing vehicle or Rapamycin or Torin-1 or Erastin or RSL3. Cells were treated with Rapamycin (500 nM) or Torin-1 (50 nM) 30 min prior to treatment with Erastin (2.5 μ M) or RSL3 (0.625 μ M) for 24 h. Cell viability was evaluated using MTT assay after 24 h. Data was resented as mean (SEM) form three independent experiments and analysed using 2-way ANOVA; * $p < 0.05$, *** < 0.001 .
- (b) The melanoma cells were cultured in media containing vehicle or compound C or AICAR or Erastin or RSL3. Cells were treated with Compound C (10 μ M) or AICAR (1mM) 30 min prior to treatment with Erastin (2.5 μ M) or RSL3 (0.625 μ M) for 24 h. Cell viability was evaluated using MTT assay after 24 h. Data was resented as mean (SEM) form three independent experiments and analysed using 2-way ANOVA; * $p < 0.05$, ** $p < 0.001$, **** < 0.0001 .

As in *Chapter 4*, the key regulator of ferroptosis, GPX4 was investigated by western blot for the treatment of compound C or AICAR. Along with being a key regulator of autophagy BECN1, which has also been found to induce ferroptosis (Song et al., 2018), therefore BECN1 was investigated (Figure 4.29). The B16-F10 cells showed an increase in GPX4 protein levels after treatment with RSL3, although it did not lead to significance (**Figure 5.10**). There was also an observed increase in BECN1 protein levels after treatment with AICAR (**Figure 5.10**).

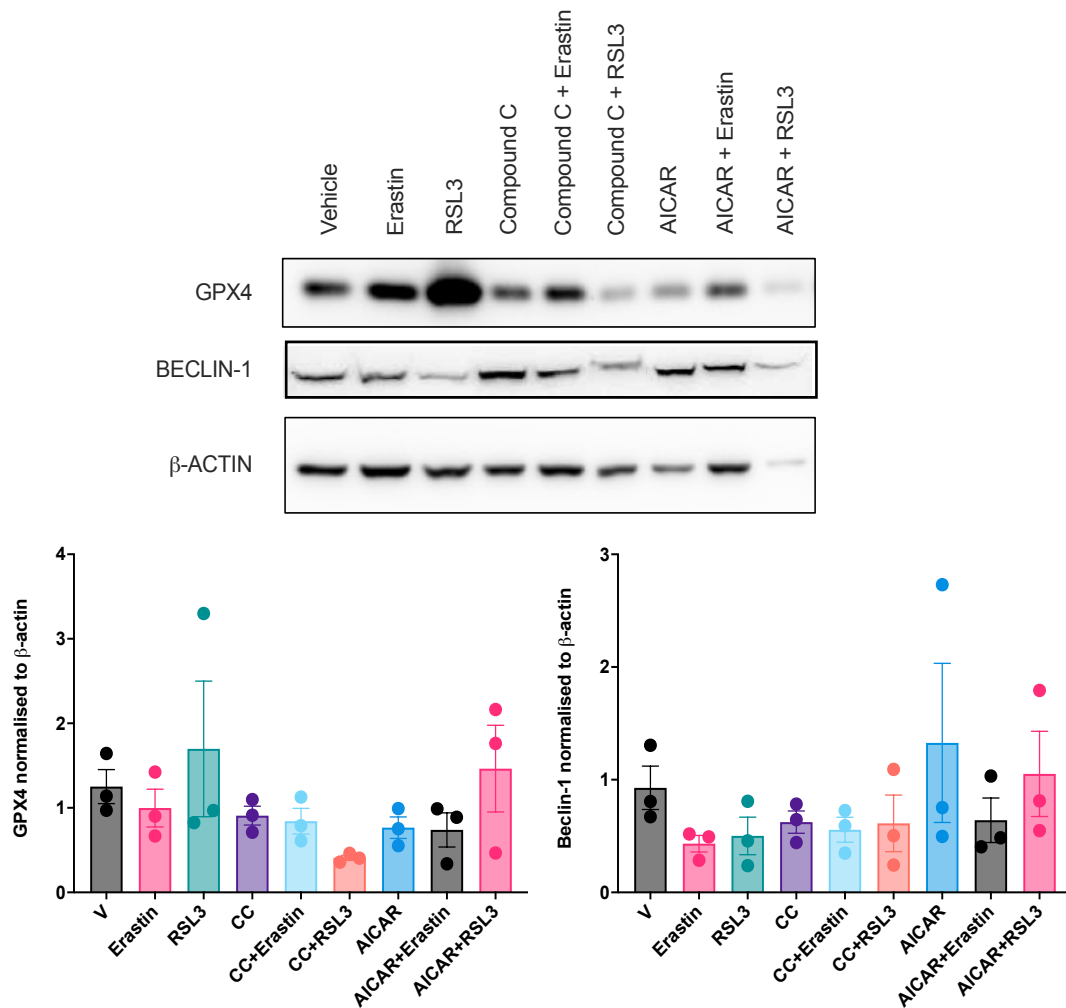


Figure 5.10: GPX4 and BECN1 western blots for B16-F10 melanoma cells. The melanoma cells were treated with vehicle or compound C or AICAR for 30 min prior to treatment with Erastin or RSL3 or 4 h, and GPX4 and BECN1 were analysed by western blot. Representative western blot for GPX4, BECN1 and β -actin are shown. Data was presented as mean (SEM) from three independent experiments and data was analysed with a 1-way ANOVA.

The main substrate of the mTORC1 pathway is P70-S6K which was investigated by western blot for the treatment of compound C and AICAR. mTOR can also prevent the induction of autophagy through the phosphorylation of Ser757 residue of ULK1 (Bach et al., 2011; Kim et al., 2014; Tian et al., 2015), whereas AMPK phosphorylates the Ser555 residue of ULK1 (Bach et al., 2011; Kim et al., 2014; Tian et al., 2015). Therefore, Ser555, Ser757 and ULK1 were investigated by western blot. There was an observed

increase in phosphorylated P70-S6K after treatment with compound C and cotreatment of compound C with either Erastin or RSL3 (**Figure 5.11**). The cotreatment also resulted in decreased ULK1 and ULK1 residues Ser7575 and Ser555. The AICAR treatment and cotreatment with Erastin or RSL3 resulted in increased total P70-S6K and decreased ULK1 and ULK1 residues Ser757 and Ser555 (**Figure 5.11**).

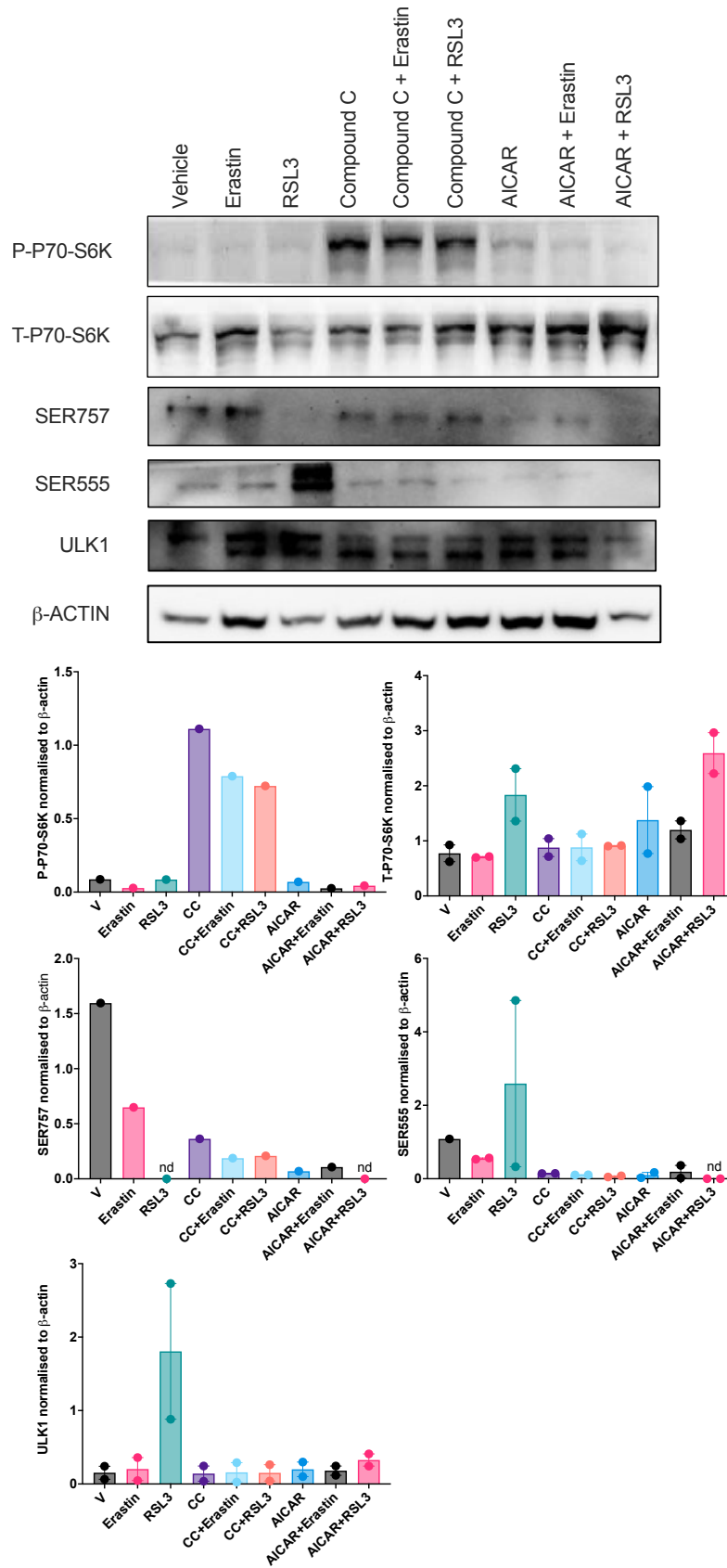


Figure 5.11: P70S6K and ULK1 western blots for B16-F10 melanoma cells. The melanoma cells were treated with vehicle or compound C or AICAR for 30 min prior to treatment with Erastin or RSL3 for 4 h, and phosphorylated P70S6K (P-P70-S6K), total P70S6K (T-P70-S6K), SER757, SER555 and ULK1 were analysed by western blot. Representative western blot for P-P70-S6K, T-P70-S6K, SER555, SER757, ULK1 and β -actin are shown. Data was presented as mean (SEM) from one or two independent experiments.

Finally, the autophagy promotor, AMPK and LC3B a widely used marker for autophagy were investigated. There was an observed increase in P-AMPK after treatment with RSL3 and AICAR alone (**Figure 5.12**). There were high levels of total AMPK in the vehicle and after treatment with compound C. There was increased LC3B-II protein levels after treatment with RSL3, compound C and cotreatment of compound C with either Erastin or RSL3 (**Figure 5.12**).

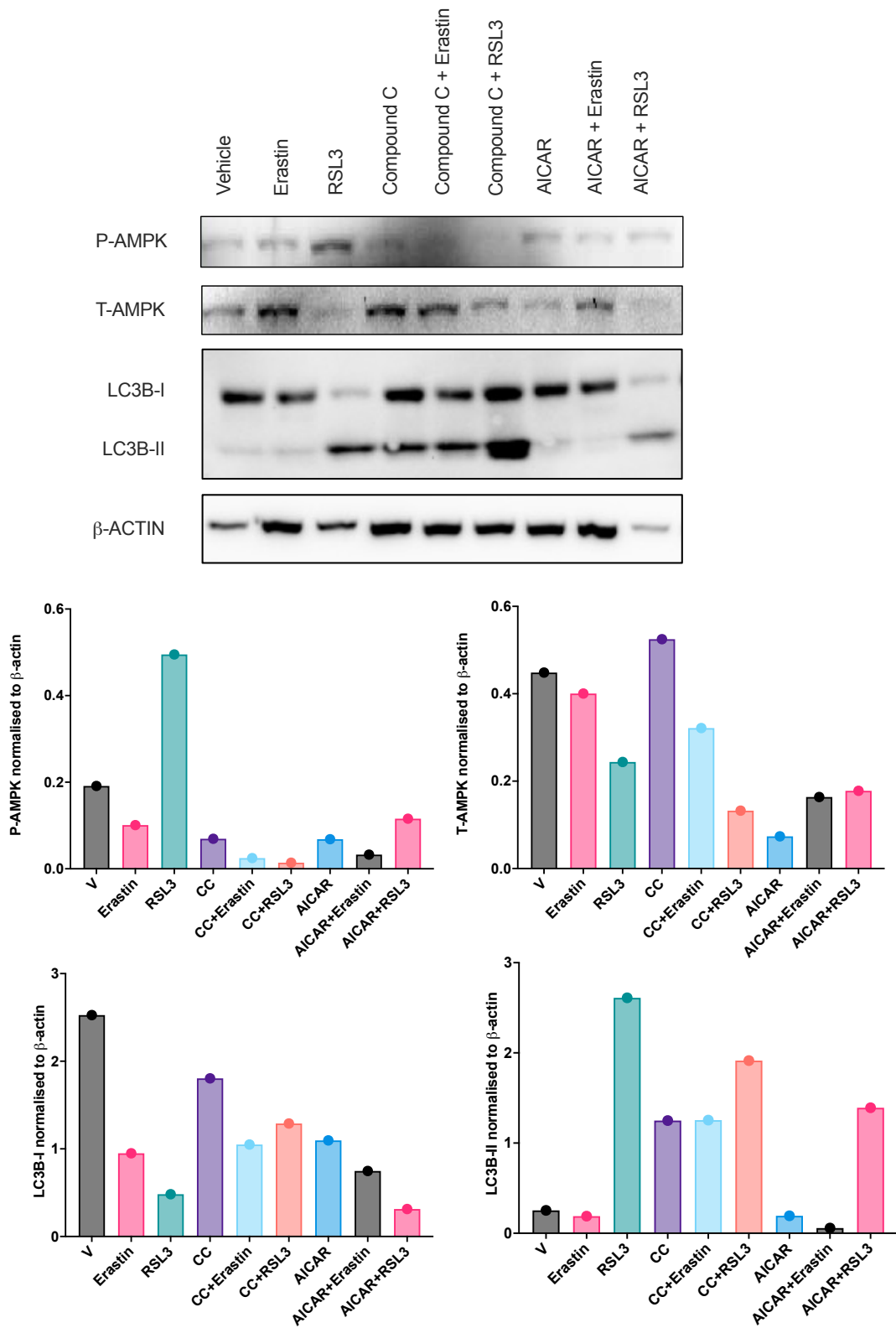


Figure 5.12: AMPK and LC3B western blots for B16-F10 melanoma cells. The melanoma cells were treated with vehicle or compound C or AICAR for 30 min prior to treatment with Erastin or RSL3 or 4 h, and phosphorylated AMPK (P-AMPK), total AMPK (T-AMPK), LC3B-I and LC3B-II were analysed by western blot. Representative western blot for P-AMPK, T-AMPK, LC3B-I, LC3B-II and β -actin are shown. Data was presented from one independent experiment.

Glutaminase inhibitor reduces melanoma cell viability.

As discussed previously in *Chapter 4*, the glutaminase isozyme GLS2 is known to be involved in the induction of ferroptosis (Gorrini et al., 2013). Therefore, to similarly characterise the B16-F10 melanoma cell line, a glutaminase inhibitor C968 (10 μM) in conjunction with the ferroptosis inducers Erastin (2.5 μM) or RSL3 (0.625 μM) was investigated. The melanoma cells showed a significant reduction in cell viability with treatment of C968 (**Figure 5.13**), indicating a dependency on glutaminase for cell viability. However, there was a trend towards a rescue in cells cotreated with C968 and Erastin (2.5 μM ; $P=0.2118$) or RSL3 (0.625 μM ; $P=0.7885$), although this did not reach significance (**Figure 5.13**).

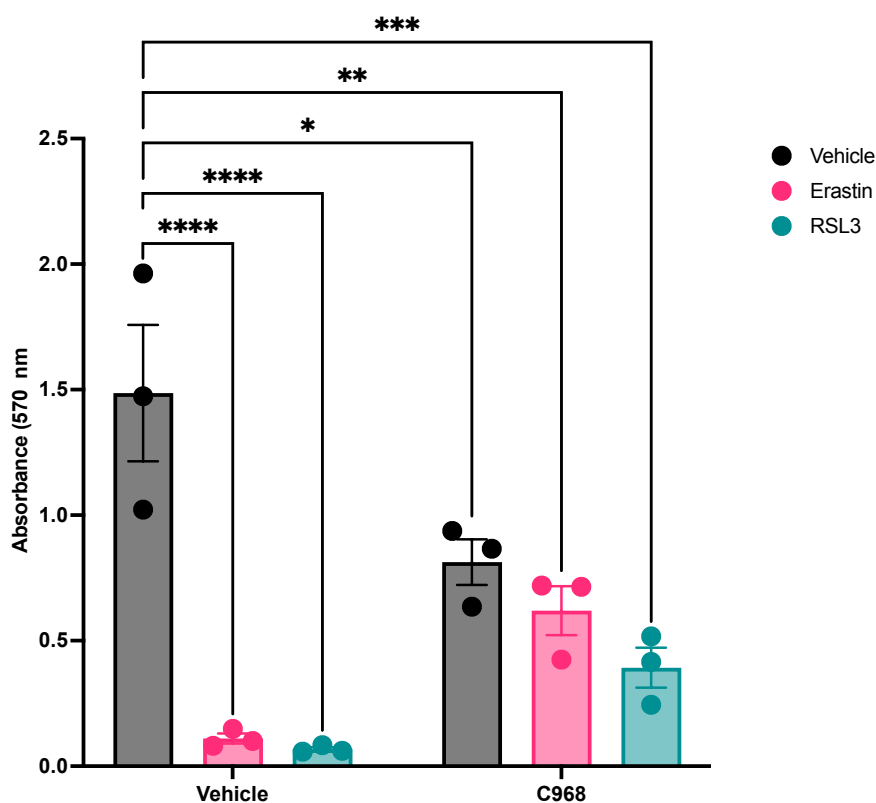


Figure 5.13: The effect of glutaminase inhibitor, compound 968 and the ferroptosis inducers, Erastin and RSL3. The mouse melanoma cells were cultured in media containing vehicle (v) or Compound 968 (10 μM) or Erastin (2.5 μM) or RSL3 (0.625 μM). Cells were treated with Compound 968 for 30 min prior to treatment with Erastin or RSL3 for 24 h. Cell viability was evaluated using MTT assay after 24 h. Data was presented as mean (SEM) from three independent cell passage experiments and analysed using 2-way ANOVA, * $p < 0.05$, ** $p < 0.01$, *** $p < 0.001$, **** $p < 0.0001$.

The protein levels of GPX4 and BECN1 were then investigated for treatment with C968 and cotreatment of C968 with either Erastin or RSL3. There was no significant changes in GPX4 expression after treatment, but an observed increase in BECN1 after cotreatment of C968 and RSL3 (**Figure 5.14**).

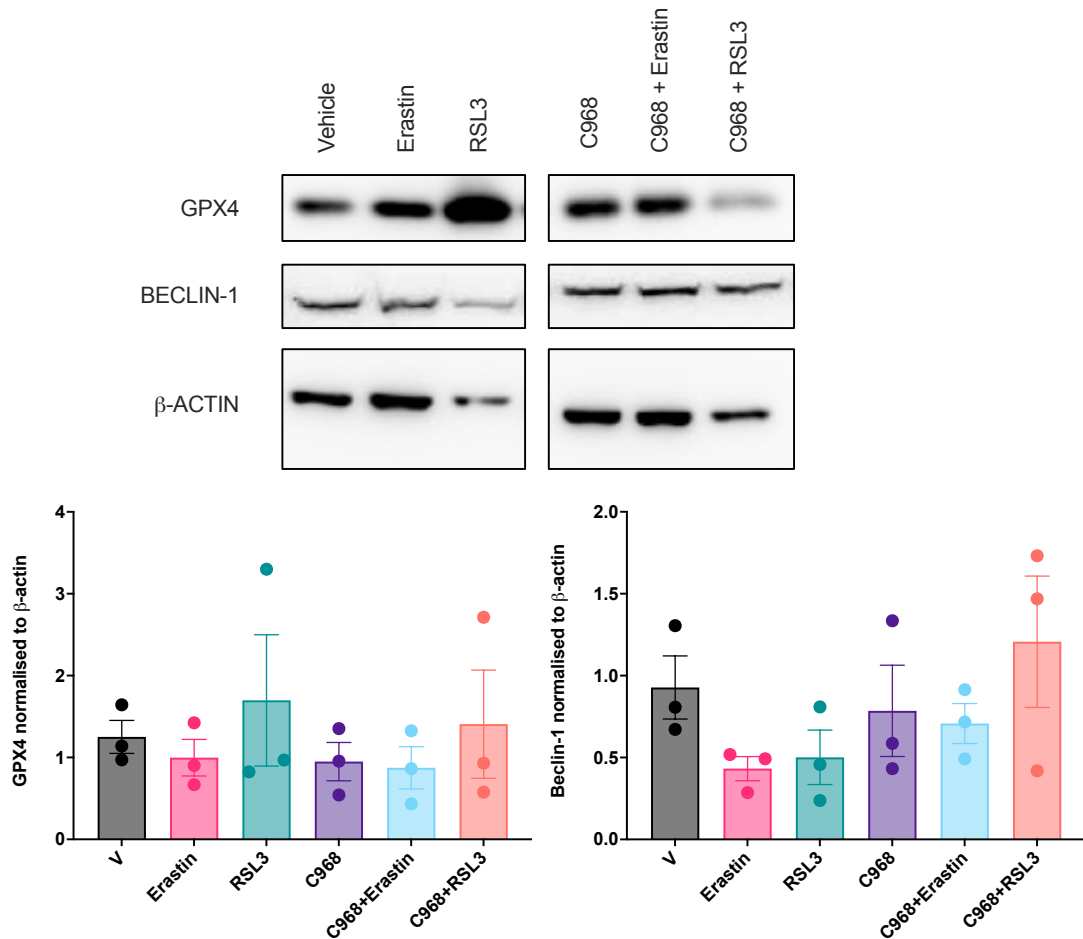


Figure 5.14: GPX4 and BECN1 western blots for B6-F10 melanoma cells. The melanoma cells were treated with vehicle or C968 for 30 min prior to treatment with Erastin or RSL3 or 4 h, and GPX4 and BECN1 were analysed by western blot. Representative western blot for GPX4, BECN1 and β -actin are shown. Data was presented as mean (SEM) from three independent experiments and data was analysed with a 1-way ANOVA.

The B16-F10 cells showed no changes in phosphorylated P70-S6K but an increase in total P70-S6K after treatment with C968 and cotreatment with Erastin and RSL3 (**Figure 5.15**). There was an observed decrease in ULK1 and ULK1 residues Ser7575 and Ser555 (**Figure 5.15**).

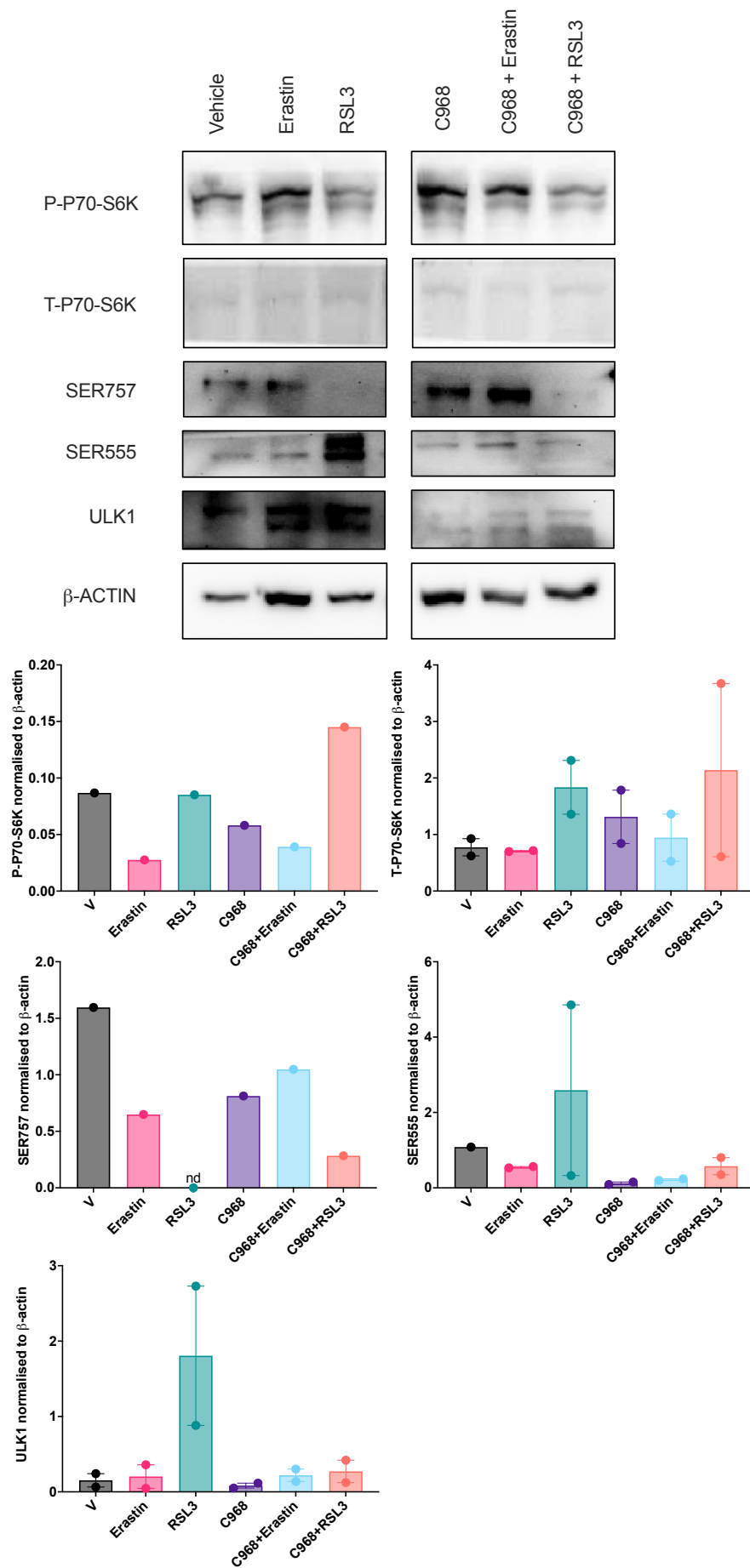


Figure 5.15: P70S6K and ULK1 western blots for B16-F10 melanoma cells. The melanoma cells were treated with vehicle or C968 for 30 min prior to treatment with Erastin or RSL3 or 4 h, and phosphorylated P70S6K (P-P70-S6K), total P70S6K (T-P70-S6K), SER757, SER555 and ULK1 were analysed by western blot. Representative western blot for P-P70-S6K, T-P70-S6K, SER555, SER757, ULK1 and β -actin are shown. Data was presented as mean (SEM) from one or two independent experiments.

Finally, the autophagy promotor, AMPK and LC3B a widely used marker for autophagy were investigated. There was an observed increase in P-AMPK after treatment with RSL3 and cotreatment of C968 and RSL3 (**Figure 5.16**). LC3B-II was increased after treatment with RSL3 and cotreatment of C968 and RSL3 (**Figure 5.16**).

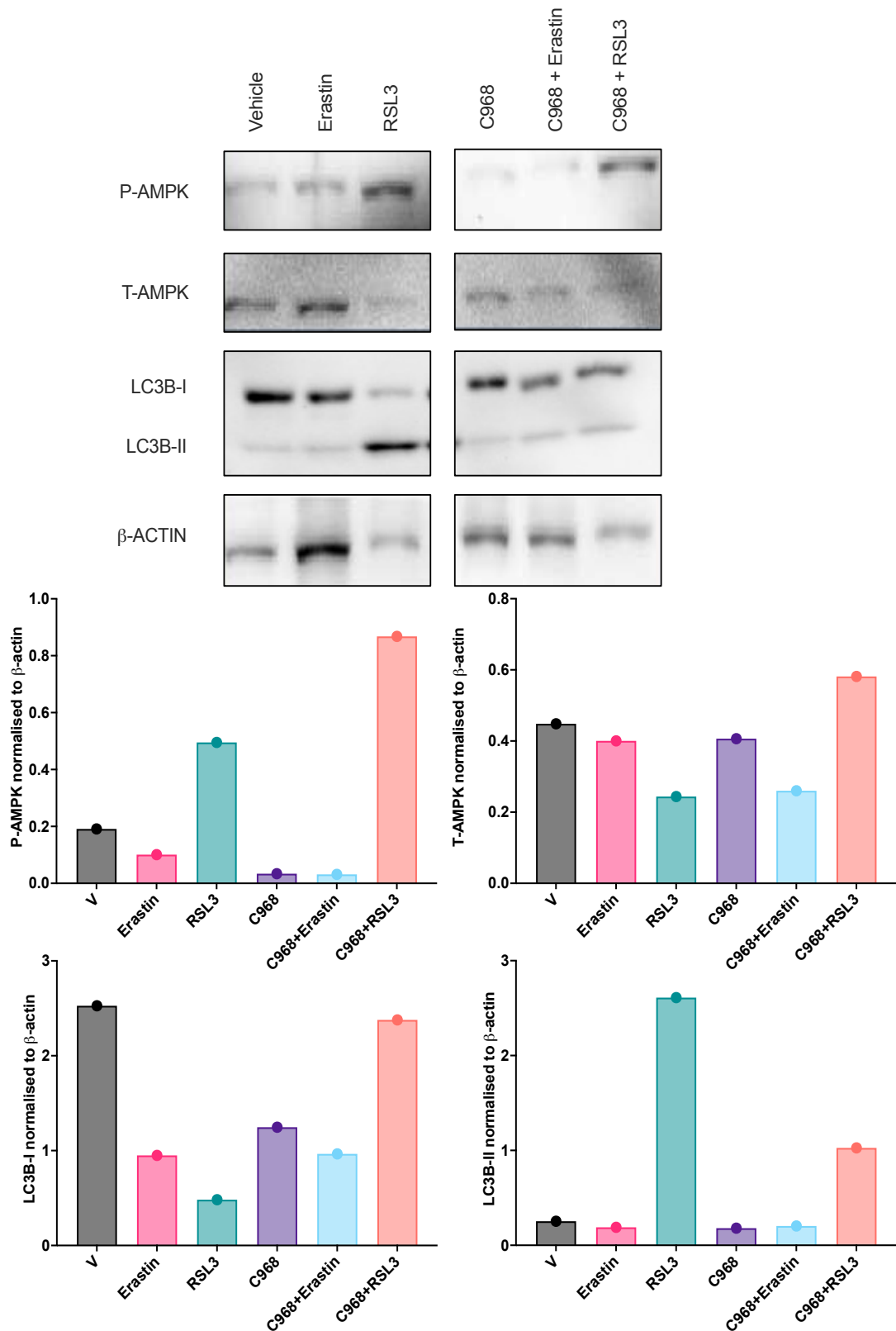


Figure 5.16: AMPK and LC3B western blots for B16-F10 melanoma cells. The melanoma cells were treated with vehicle or C968 for 30 min prior to treatment with Erastin or RSL3 or 4 h, and phosphorylated AMPK (P-AMPK), total AMPK (T-AMPK), LC3B-I and LC3B-II were analysed by western blot. Representative western blot for P-AMPK, T-AMPK, LC3B-I, LC3B-II and β -actin are shown. Data was presented from one independent experiment.

5.4.2 Development of Iron oxide nanoparticles: Phase one

Phase one nanoparticles included the previously established Ferumoxytol (Figure 5.17). Ferumoxytol is a very small superparamagnetic iron oxide (SPION) with a carboxymethyl dextran coating.

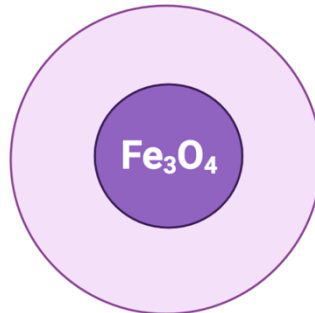


Figure 5.17: Illustration of Ferumoxytol. With an iron oxide core (dark purple) and a dextrose coating (light purple).

Phase one nanoparticles included the SPION with FDA approved PEGylation (Figure 5.18). The MUFA oleic acid was used as a surfactant to stabilize the magnetic nanoparticle. All preliminary experiments used Erastin as a basis for ferroptotic induction until the nanoparticle model was developed, and then experiments also included RSL3 as a treatment.

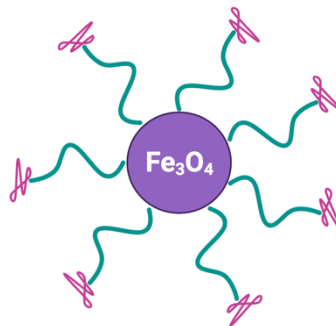


Figure 5.18: Illustration of the PEGylated SPION. With an iron oxide core (dark purple), oleic acid (green) and PEG (pink).

Erastin but not iron oxide nanoparticles induced ferroptosis in mouse melanoma cells

Phase one nanoparticle treatments were carried out on the B16-F10-OVA mouse melanoma cell line. This cell line is a stable transfectant derived from the B16-F10 melanoma that express chicken ovalbumin (OVA). The expression of OVA stimulates cellular and humoral immune responses *in vivo*; therefore, this cell line is widely used for screening the efficacy of immunoncology therapeutics.

The system X_C^- inhibitor Erastin significantly reduced mouse melanoma cell (B16-F10-OVA) viability. Ferumoxytol (**Figure 5.19 a**) or PEGylated (**Figure 5.19 b**) iron oxide nanoparticles alone or in combination with Erastin did not result in further reductions in cell viability. Indicating that these two SPIONs may not induce ferroptosis (or other forms of cell death) in mouse melanoma cells. Although, there was a trend of reduced cell viability when Ferumoxytol (**Figure 5.19 a**) or PEGylated (**Figure 5.19 b**) iron oxide nanoparticles were cotreated with 2.5 μ M Erastin (Ferumoxytol 125nM, P=0.9885, 250 nM, P=0.9994, 500 nM, P=0.9530 and 1000 nM, P=0.5285; PEGylated 125 nM, P=0.7283, 250 nM, P=0.7485, 500 nM, P=0.7485 and 1000 nM, P=0.7342).

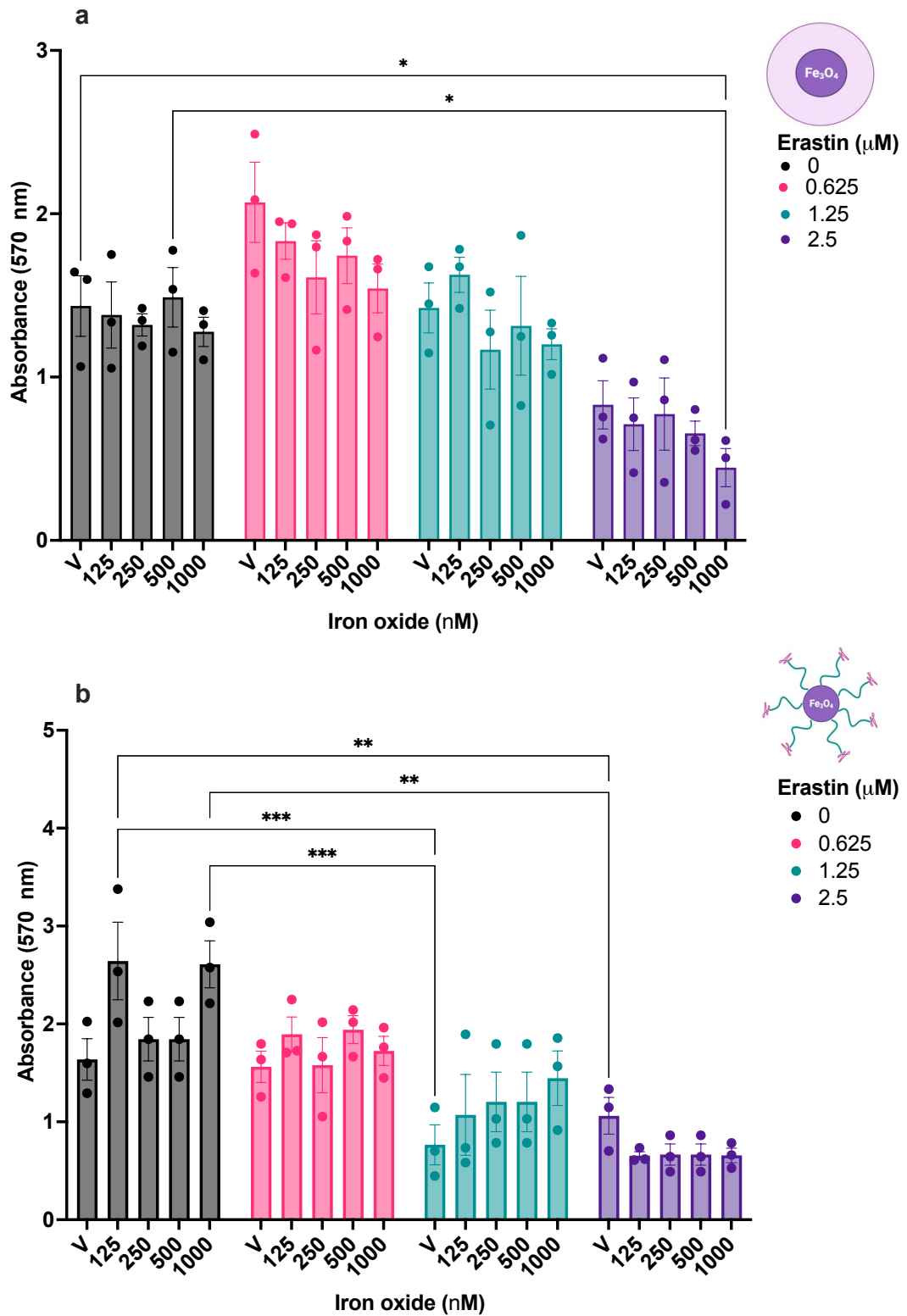


Figure 5.19: Effect of Erastin in combination with (a) Ferumoxytol or (b) PEGylated iron oxide nanoparticles on cell viability (absorbance at 570 nm) in mouse melanoma cells. Mouse melanoma cells were cultured in media containing vehicle (v) or the individual concentrations of Erastin for 24 h followed by 24 h treatment of iron oxide nanoparticles. Cell viability was evaluated using MTT assay. Data was presented as mean (\pm SEM) from three independent cell passages and analysed using 2-way ANOVA, * $p < 0.05$, ** $p < 0.01$, *** $p < 0.001$.

Unstable linoleic acid nanoparticles eradicated mouse melanoma cells

Linoleic acid provides structural support within membrane phospholipids (Whelan & Fritsche, 2013). Linoleic acid is the most common PUFA and is highly susceptible to lipid peroxidation, the main characteristic for ferroptotic induction. Therefore, we hypothesised the addition of a linoleic acid coating to an iron oxide core would potentially create a ferroptosis inducing nanoparticle (**Figure 5.20**).



Figure 5.20: Illustration of stage one Linoleic acid nanoparticles. With an iron oxide core (dark purple), hydrophobic linoleic acid (blue) and oleic acid (green).

Treating the melanoma cells with linoleic acid iron oxide nanoparticles resulted in cancer cell eradication at the higher concentrations of iron oxide (25 μM and 50 μM). The combination of linoleic nanoparticles with Erastin showed a significant reduction in cell viability at the lower concentrations of iron oxide (**Figure 5.21**). However, these linoleic nanoparticles were tested by colleagues in the Swansea University Chemistry department and were found to be unstable and had a tendency to aggregate; therefore, further development was required in order to create a stable ferroptosis inducing nanoparticle.

5.4.1 Development of Iron oxide nanoparticles: Phase two

A new generation of linoleic acid coated iron oxide nanoparticles needed to be synthesised in order to overcome the difficulties of stability and aggregation exhibited by the first phase linoleic acid nanoparticles (**Figure 5.22**). The new linoleic acid nanoparticles needed to address the issues with stability and aggregation, which could be achieved using a polyethylene glycol (PEG) coating (**Figure 5.22**). The new nanoparticles were synthesised by self-assembly using a dry-film hydration method with 16:0 PEG2000 PE ($C_{129}H_{259}N_2O_{55}P$, FW: 2749.42). The covalent binding of PEG has been shown to improve the pharmacokinetic behaviour of nanoparticles. The amphiphilic polymer improves solubility, stability and reduces aggregation (Veronese & Mero, 2008; Suk et al., 2016).

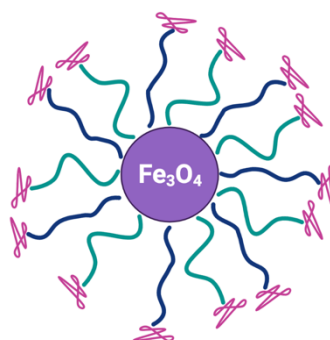


Figure 5.22: Illustration of next generation stabilised Linoleic acid nanoparticles. With an iron oxide core (dark purple), hydrophobic linoleic acid (blue), oleic acid (green) and PEG (pink).

A working ratio of PEG to Linoleic acid within the coating of the iron oxide nanoparticle needed to be established, therefore five different nanoparticles were synthesised (**Table 4**) and tested on the mouse melanoma cells.

Table 8: The five particles synthesised for different ratios of PEG to linoleic acid (LA).

PARTICLE	%PEG	%LA
1	100	0
2	75	25
3	60	40
4	50	50
5	40	60

Next generation PEGylated linoleic acid nanoparticles reduced cell viability.

Next generation PEGylated linoleic acid iron oxide nanoparticles (500 nm) significantly reduced mouse melanoma cell viability over 24 h, in comparison to the vehicle (**Figure 5.23**). These results indicated that the addition of linoleic acid to the iron oxide core created a potentially ferroptosis inducing nanoparticle that could be stabilised by PEGylation.

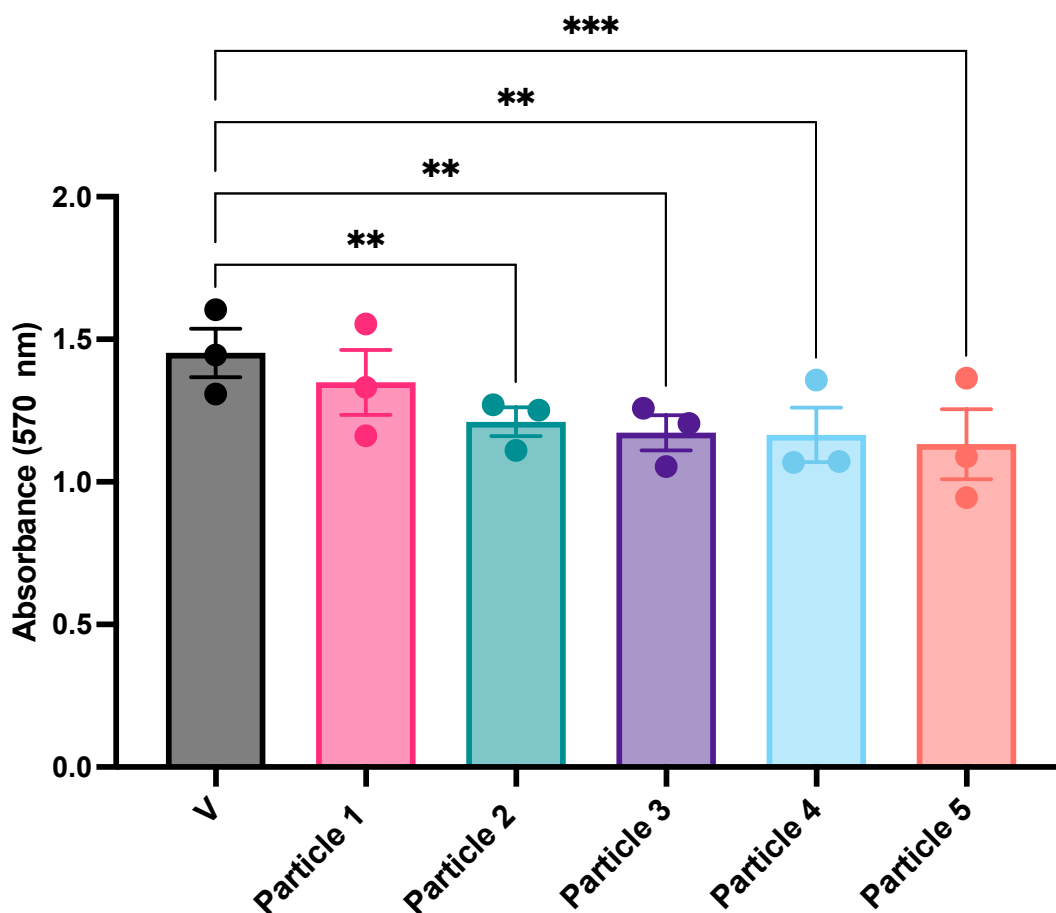


Figure 5.23: Effect of PEGylated linoleic acid iron oxide nanoparticles on cell viability (absorbance at 570 nm) of mouse melanoma cells. Particle 1 to Particle 5 show increasing concentration of linoleic acid. Particle 1; 100:0 (PEG:LA), Particle 2; 75:25, Particle 3; 60:40, Particle 4; 50:50 and Particle 5 40:60. Mouse melanoma cells were cultured in media containing vehicle (v) or complete media for 24 h followed by 24 h treatment of PEGylated linoleic acid iron oxide nanoparticles (500 nM). Cell viability was evaluated using MTT assay. Data was presented as mean (\pm SEM) from three independent cell passages and analysed using 2-way ANOVA, * $p < 0.05$, ** $p < 0.01$, *** $p < 0.001$.

The next generation PEGylated linoleic acid nanoparticles (500 nm) were then used in combination with the system X_c^- inhibitor, Erastin, where a concentration of 1.25 μ M was chosen based on the data collected during phase one of the nanoparticle treatments (**Figure 5.3**). Here, there was a significant reduction in cell viability of the mouse melanoma cells with the cotreatment of each nanoparticle and Erastin. Nanoparticles 4 (50% PEG: 50% LA) and 5 (40% PEG: 60% LA) in combination with Erastin had greatest significant reduction in cell viability (**Figure 5.24**). These results indicate that Erastin increases cancer cell susceptibility to ferroptotic induction by the PEGylated linoleic acid iron oxide nanoparticles.

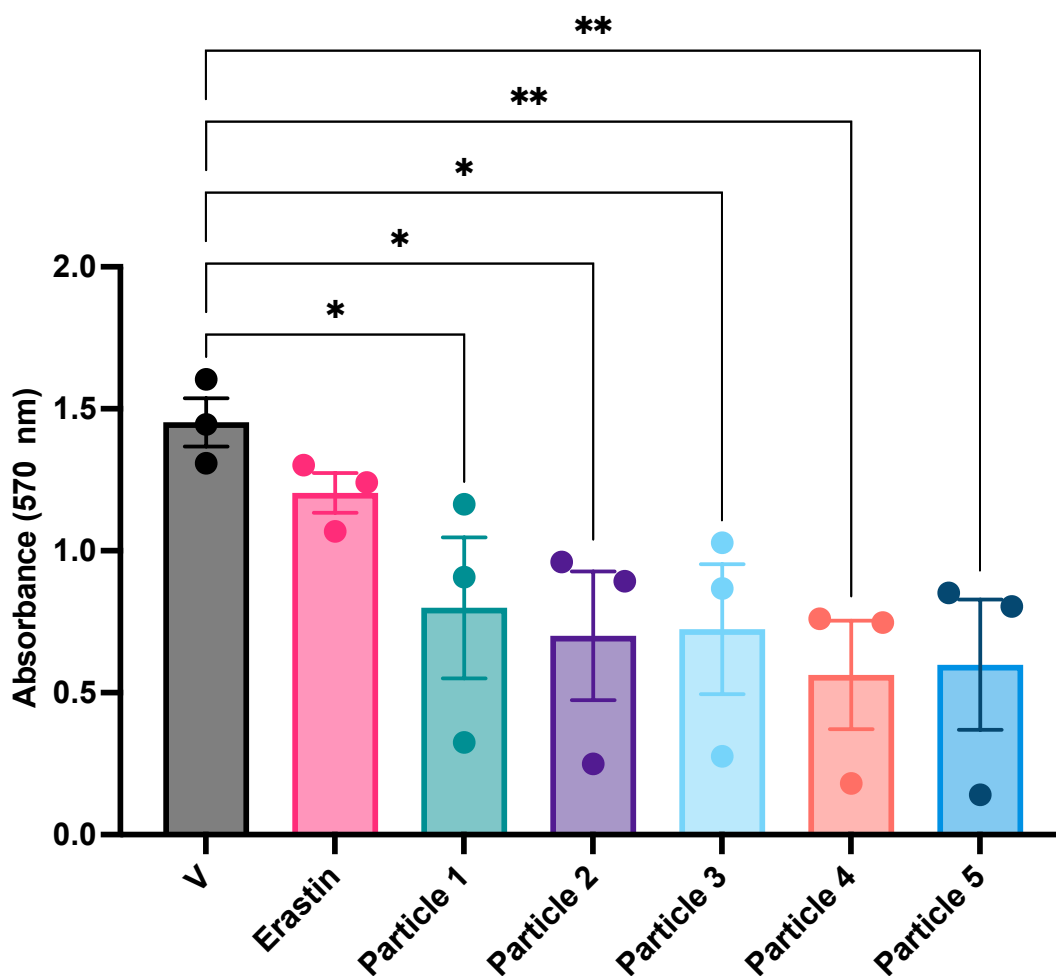


Figure 5.24: Effect PEGylated linoleic acid iron oxide nanoparticles in combination with Erastin at 1.25 μ M on cell viability of mouse melanoma cells. Particle 1 to Particle 5 show increasing concentration of linoleic acid. Particle 1; 100:0 (PEG:LA), Particle 2; 75:25, Particle 3; 60:40, Particle 4; 50:50 and Particle 5; 40:60. Cell viability was evaluated using MTT assay after 24 h treatment of Erastin followed by 24 h treatment of PEGylated linoleic acid iron oxide nanoparticle (500 nM). Data was presented as mean (\pm SEM) from three independent cell passages and analysed using 2-way ANOVA, * $p < 0.05$, ** $p < 0.01$.

Moving forward, two next generation nanoparticles were chosen for further testing. Particle 1 (100% PEG: 0% LA) was chosen as a control nanoparticle as it did not contain linoleic acid (LA) and therefore provides a control for the addition of PEG. Particle 4 (50% PEG: 50% LA) was also chosen as this nanoparticle worked best in combination with the system X_C^- inhibitor, Erastin.

Ovarian cancer cells are vulnerable to PEGylated Linoleic acid iron oxide nanoparticles in combination with Erastin

After determining the effect of the next generation PEGylated linoleic acid nanoparticles on the mouse melanoma cell line, the effect was then determined on other cancer cell lines. The ovarian cancer cell lines chosen were PEO1s, which were used to model chemotherapy sensitivity and PEO4s to model chemotherapy resistance disease. Previous work (**Figure 3.8**) showed that these cell lines were less vulnerable to the induction of ferroptosis, therefore the concentration of 2.5 μ M of Erastin was used.

Interestingly, treating the PEO1 cell line with the control nanoparticle (Particle 1, 100% PEG: 0% LA; 500 nm) resulted in a significant increase in cell proliferation in comparison to the vehicle. Whereas the combination of Particle 1 (100% PEG: 0% LA; 500 nm) and the system X_c^- inhibitor, Erastin (2.5 μ M) reduced cell viability ($P=0.4445$, **Figure 5.25 a**). Suggesting that the PEGylated iron oxide nanoparticle increased Erastin induced ferroptosis in the chemotherapy sensitive ovarian cancer cell line.

However, the PEO4 cell line showed no effect with Particle 1 alone (100% PEG: 0% LA; 500 nm), but a significant reduction in cell viability with treatment of Particle 1 (100% PEG: 0% LA; 500 nm) in combination Erastin (2.5 μ M; **Figure 5.25 b**). The PEO4 cell line showed a significant reduction in cell viability after treatment with Particle 4 alone (50% PEG: 50% LA; 500 nm; **Figure 5.25 b**). The combination of Particle 4 (500 nm) and Erastin (2.5 μ M) resulted in a significant reduction in cell viability (**Figure 5.25 b**). Suggesting that the PEGylated iron oxide nanoparticle increased Erastin induced ferroptosis in the chemotherapy resistant ovarian cancer cell line.

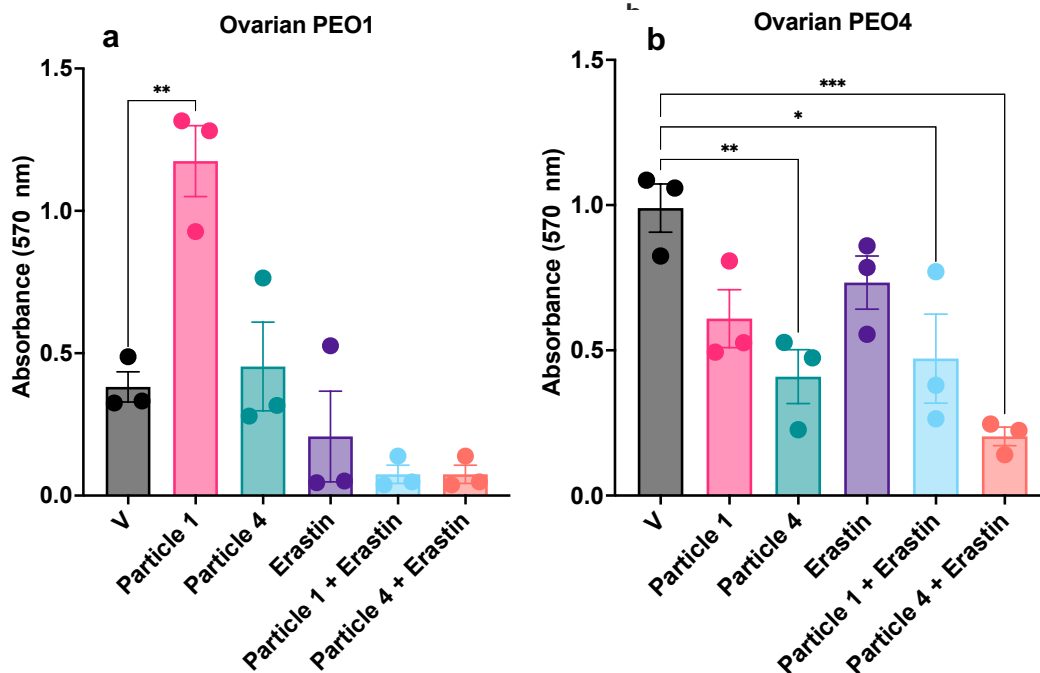


Figure 5.25: Effect of PEGylated Linoleic acid nanoparticles in combination with Erastin (2,5 μ M) on cell viability on (a) chemo-sensitive (PEO1) and (b) chemo-resistant (PEO4) ovarian cancer cells. Cell viability was evaluated using MTT assay after 24 h treatment of Erastin (2.5 μ M) followed by 24 h treatment of nanoparticle (500 nm). Data was presented as mean (\pm SEM) from three independent cell passages and analysed using 2-way ANOVA, * $p < 0.05$, ** $p < 0.01$, *** $p < 0.001$.

5.4.1 Development of Iron oxide nanoparticles: Phase three

During the final phase of nanoparticle development, a panel of cancer cell lines were introduced. At this stage three nanoparticles were used; Particle 1 (mIONP-COOH, 100:0, PEG:LA), Particle 4 (mIONP-DLin, 50:50, PEG:LA) and a citric acid coated iron oxide nanoparticle (IONP-Cit). Citric acid is a widely accepted coating material for nanoparticle synthesis, and extensive research has been undertaken on the use of citric acid in the preparation of aqueous stable iron oxide nanoparticles (Li et al., 2013; Omelyanchik et al., 2021). The surface modifications that occur to SPIONS as a result of citric acid coating are also well understood (Trincu et al., 2015).

The IONP-Cit nanoparticles have a simple structure (**Figure 5.26**). Citric acid is a biocompatible short-chained tricarboxylic acid, which is adsorbed onto the surface of the iron oxide nanoparticle. This is achieved through the exposure of a carboxylic acid group.

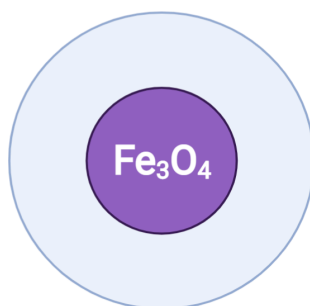


Figure 5.26: Illustration of citric acid coated iron oxide nanoparticle. With an iron oxide core (dark purple) and citric acid (blue).

GPX4 is a key regulator of ferroptosis, therefore the enzymes inactivation or depletion can readily induce ferroptosis. The effect the different coated iron oxide nanoparticles (mIONP-COOH, IONP-Cit and mIONP-DLin; 500 nm) had on GPX4 expression was determined by intracellular staining for the protein and flow cytometry. The GPX4 expression was significantly reduced after treatment with IONP-Cit nanoparticles (500 nm) and reduced after treatment with mIONP-DLin ($P=0.0597$; 500 nm; **Figure 5.27**).

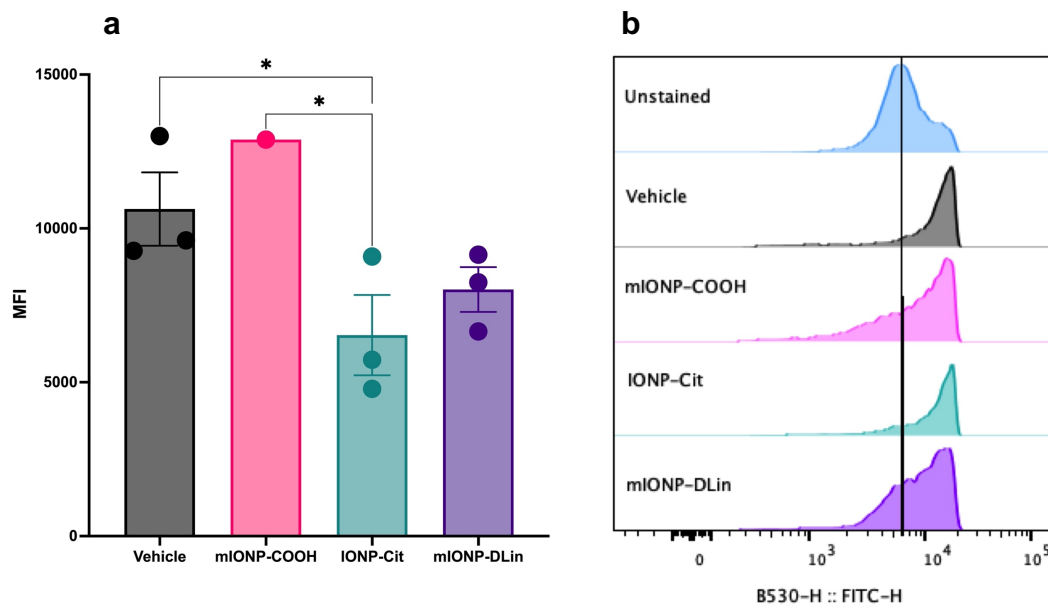


Figure 5.27: Effect of iron oxide nanoparticles on GPX4 expression in mouse melanoma cells. (a) Mouse melanoma cells were cultured in media containing vehicle or iron oxide nanoparticle (500 nm): mIONP-COOH (PEGylated), IONP-Cit (Citric acid coated) or mIONP-DLin (Linoleic acid coated) for 24 h. GPX4 expression was determined by flow cytometry. Data was presented as mean (\pm SEM) from three independent cell passages and analysed using 2-way ANOVA, * $p < 0.05$, ** $p < 0.001$, *** $p < 0.001$. (b) B16F10 incubated with vehicle or iron oxide nanoparticle (500 nm): mIONP-COOH, IONP-Cit or mIONP-DLin for 24 h, Representative flow cytometric profiles for intracellular GPX4 with Alexa Fluor 488 signals.

A panel of cancer cell lines were treated with the three different iron oxide nanoparticles (**Figure 5.28**). The PEGylated (mIONP-COOH; 500 nm) nanoparticles alone resulted in a significant reduction in cell viability in colon, lung and ovarian (PEO4, OVCAR8) cell lines (**Figure 5.28 b, c, e and f**). The cell viability was further reduced with the co-treatment of mIONP-COOH nanoparticles and Erastin in breast and ovarian (PEO4, OVCAR8) cell lines (**Figure 5.28 e and f**). Furthermore, co-treatment with RSL3 also significantly reduced cell viability in lung and ovarian OVCAR8 cell lines (**Figure 5.28 c and f**).

The IONP-Cit (500 nm) nanoparticles alone significantly reduced cell viability in all cell lines. The addition of Erastin further reduced cell viability in the colon and ovarian PEO4 cell line (**Figure 5.28 b and e**), whereas RSL3 further reduced cell viability in only the ovarian OVCAR8 ovarian cell lines (**Figure 5.28 f**)

The mIONP-DLin (500 nm) nanoparticles alone significantly reduced cell viability of all the cancer cell lines (**Figure 5.28 a-f**). The addition of Erastin did not further reduce cell viability, and the addition of RSL3 further reduced cell viability in just the lung cancer cell line (**Figure 5.28 a**).

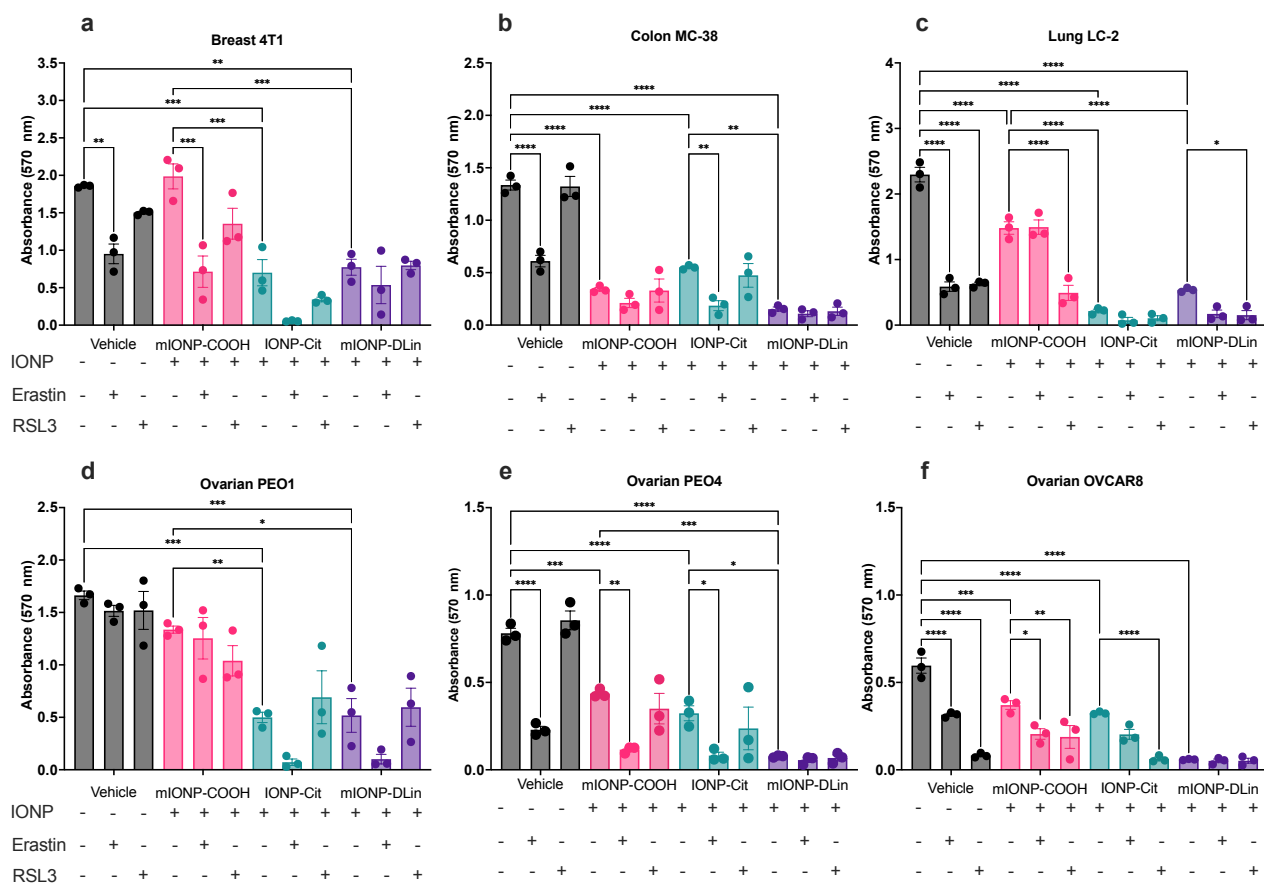


Figure 5.28: Effect of iron oxide nanoparticles on cell viability in a panel of cancer cell lines. The panel of cancer cell lines (a) 4T1, (b) MC-38, (c) LC-2, (d) PEO1, (e) PEO4, (f) OVCAR8 were cultured in media containing vehicle or Erastin or RSL3 for 24 h prior to treatment with iron oxide nanoparticle (500 nm): mIONP-COOH (PEGylated), IONP-Cit (Citric acid coated) or mIONP-DLin (Linoleic acid coated). Cell viability was evaluated using MTT assay after a further 24 h. Data was presented as mean (\pm SEM) from three independent cell passages and analysed using 2-way ANOVA, * $p < 0.05$, ** $p < 0.001$, *** $p < 0.001$.

The GPX4 expression for each nanoparticle treatment was determined for each cancer cell line by intracellular staining. The MC-38 colon cancer cells when treated with IONP-Cit (50 nm) nanoparticles showed a significant reduction in GPX4 expression (**Figure 5.29 b**). The other cancer cell lines showed no significant changes in GPX4 expression under the three different treatments.

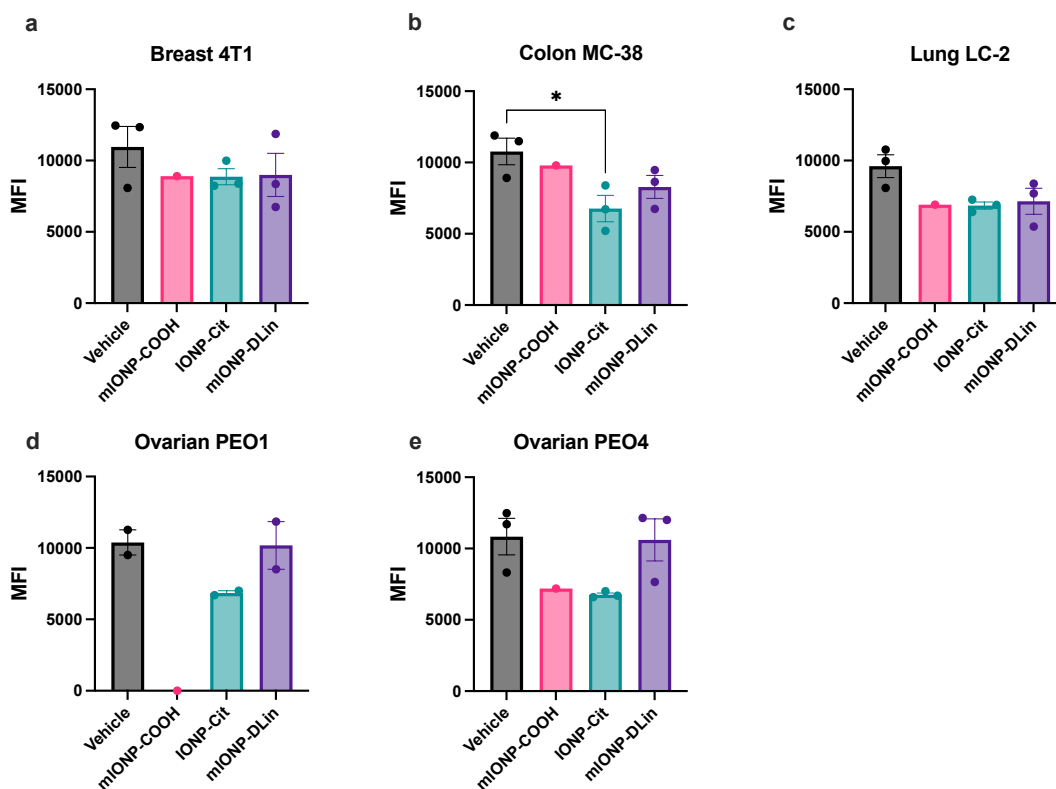


Figure 5.29: Effect of iron oxide nanoparticles on GPX4 expression in a panel of cancer cell lines. The panel of cancer cell lines (a) 4T1, (b) MC-38, (c) LC-2, (d) PEO1, and (e) PEO4, were cultured in media containing vehicle or iron oxide nanoparticle (500 nm): mIONP-COOH (PEGylated), IONP-Cit (Citric acid coated) or mIONP-DLin (Linoleic acid coated) for 24 h. GPX4 expression was determined by flow cytometry. Data was presented as mean (\pm SEM) from two or three independent cell passages and analysed using 2-way ANOVA, * $p < 0.05$, ** $p < 0.001$, *** $p < 0.001$.

Ferroptosis is dependent on the accumulation of lipid peroxides. The formation of reactive oxygen species superoxides, are a result of the Fenton reaction and oxidative stress (Orino et al., 2001; Grivennikova & Vinogradov, 2006). Superoxide dismutase converts superoxides back to hydrogen peroxide in order to be broken down into oxygen and water (Younus 2018). Otherwise, superoxides are free to attack membrane lipids, producing toxic lipid peroxides: a key characteristic of ferroptotic induction (Dixon & Stockwell, 2019). The concentration of hydrogen peroxide is difficult to measure; therefore, the mitochondrial superoxide levels for the three nanoparticles treatments in all cancer cell lines were quantified by MitoSOX, which assays mitochondrial derived superoxide O_2^- . The presence of superoxides results in the oxidation of MitoSOX, resulting in a red fluorescence, which can be quantified using flow cytometry. The mIONP-COOH (500 nm) nanoparticle

displayed no observable effect on superoxide levels in all cancer cell lines. Whereas the IONP-Cit (500 nm) nanoparticle significantly increased mitochondrial superoxide levels in the colon MC-38, Ovarian (PEO1, OVCAR8) cell lines (**Figure 5.30 b, d and f**). Finally, the mIONP-DLin (500 nm) nanoparticle significantly increased mitochondrial superoxide levels in the Breast 4T1 and Colon MC38 cell lines (**Figure 5.30 a and b**).

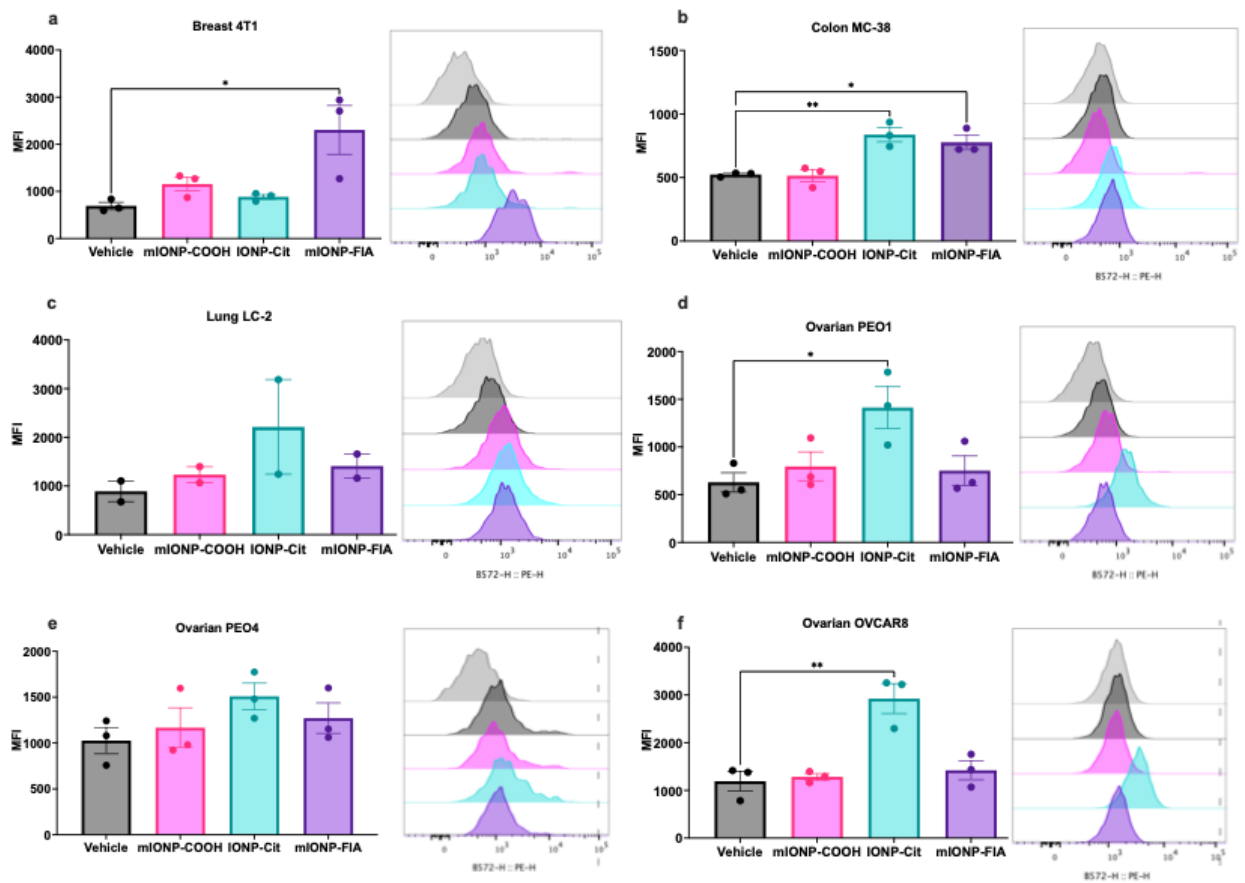


Figure 5.30: Effect of iron oxide nanoparticles on mitochondrial superoxide levels in a panel of cancer cell lines. The panel of cancer cell lines (a) 4T1, (b) MC-38, (c) LC-2, (d) PEO1, (e) PEO4, (f) OVCAR8 were cultured in media containing vehicle or iron oxide nanoparticles (500 nm): mIONP-COOH (PEGylated), IONP-Cit (Citric acid coated) or mIONP-DLin (Linoleic acid coated) for 24 h. Mitochondrial superoxide quantity was determined via flow cytometry using MitoSOX. Data was presented as mean (\pm SEM) from three independent cell passages and analysed using 2-way ANOVA, * $p < 0.05$, ** $p < 0.001$, *** $p < 0.001$.

5.5 Discussion

The melanoma cells were prone to ferroptotic induction by both Erastin and RSL3. There were observed differences in cancer cell sensitivity to Erastin-induced ferroptosis between the MTT cell viability assay and DRAQ7 cell death stain. This further indicates that Erastin may also be binding to VDAC, as in *Chapter 3*. The ability of liproxtstain-1 to rescue cell viability of the melanoma cells from ferroptosis induced by Erastin or RSL3 indicates that ferroptosis was induced.

Compound C has previously been shown to suppress ferroptosis induced by Erastin (Song et al., 2018). In this chapter, there was a rescue in cell viability after the cotreatment of compound C and either Erastin or RSL3. There was an observed increase in the phosphorylation of P70-S6K (p-p70-S6K), indicating that the activation of mTOR rescues against ferroptotic induction in the melanoma cells. However, the increase in LC3B-II expression after these treatments, indicates the induction of autophagy (also observed in *Chapter 4*), the induction of autophagy may involve signalling pathways that bypass mTORC (Ajoalabady et al., 2021). Therefore either the activation of mTORC or autophagy rescues against Erastin or RSL3-induced ferroptosis. There was also an observed rescue in Erastin and RSL3-induced ferroptosis by compound 968, however, further investigation into the mechanism of rescue is required.

Nanoparticles are at the forefront of cancer therapy, including their synergistic use with chemotherapy. However there has been little progress in this area, with poor clinical outcomes (Hare et al., 2017). The murine B16-F10 melanoma model is widely used for preclinical assessment of immunotherapies and therefore provided a key starting point for nanoparticle development. Iron oxide nanoparticles have FDA-approval for diagnosis and some cancer therapies (Soetaert et al., 2020). Iron is necessary for numerous physiological processes but could also be an important in triggering of oxidative stress and therefore lipid peroxidation. Therefore, iron could be used for anticancer treatment, by

targeting ferroptosis. However, the PEGylated iron oxide nanoparticles themselves did not further induce ferroptosis in the melanoma cells, even with pre-treatment of Erastin in the melanoma cells. Although, there was increased cell growth of the ovarian PEO1 cell line, indicating that the iron was used for cancer cell proliferation. The previous FDA-approved iron oxide nanoparticle, ferumoxytol has been shown to reduce tumour size through the activation and repolarisation of macrophages using Fenton chemistry (Zanganeh et al., 2016). However, we have shown that linoleic acid micelles filled with iron oxide nanoparticles can significantly surpass the antitumour effects of ferumoxytol.

Ferroptosis is dependent on iron and characterised by the toxic accumulation of lipid peroxides (Stockwell et al., 2017). Linoleic acid is a PUFA and therefore highly susceptible to lipid peroxidation, coating iron oxide nanoparticles with this PUFA provides a way to specifically target ferroptosis. The pre-treatment with Erastin, sensitised all cancer cell lines to particle-induced ferroptosis, suggesting that the inhibition of glutathione production is a rate limiting step for particle-induced cell death. Glutathione is the main cofactor for GPX4, therefore its depletion results in the build-up of ROS and consequently leads to ferroptotic cell death (Guan et al., 2021).

PEGylated (mIONP-COOH) and citric acid (IONP-Cit) coated iron oxide nanoparticles were used within the study as control particles, due to the extensive research that has been undertaken on their properties. The mIONP-COOH nanoparticles significantly reduced cell viability in the colon, lung, ovarian PEO4 and OVCAR8 cell lines, indicating the overload of iron resulted in cancer cell death. Whereas, the breast and ovarian PEO1 cancer cells showed no changes in cell viability, indicating that these cells were able to utilise the iron and maintain proliferation. The IONP-Cit nanoparticles were more potent and significantly reduced cell viability in all cell lines. Citric acid has previously been shown to release total iron from ferritin stores, consequently inducing ferroptosis (Zhu et al., 2022). The PUFA (IONP-DLin) coated iron oxide nanoparticles showed a further reduction in cell viability in the colon, ovarian PEO4 and OVCAR8 cancer cell lines in comparison to the

IONP-Cit nanoparticles. Indicating that the combination of a PUFA and iron induced ferroptotic cell death, which corresponds with an observed increase in mitochondrial ROS. The pre-treatment of Erastin and RSL3 prior to IONP-DLin, further induced cancer cell death, however, further investigation is required determine ferroptotic induction. However, pre-treatment with RSL3 in the breast and ovarian PEO1 did not increase cell death induced by IONP-DLin.

The majority of cancers show tightly regulated but elevated levels of ROS in order to promote tumour growth and development (Liou & Storz, 2014). Lipid ROS plays a central role in the induction of ferroptosis (Su et al., 2019). Cancer cells are known to upregulate the enzyme GPX4 in order to eliminate the toxic accumulation of ROS and therefore prevent the induction of ferroptosis. The significant reduction in GPX4 expression in the colon cancer cells after treatment with citric acid coated iron oxide nanoparticles, is mirrored by an increase in lipid ROS accumulation. This relationship was the same when GPX4 expression was not altered in chemotherapy sensitive and resistant ovarian cancer cell lines. There was no increase in ROS levels after these treatments. However, GPX4 expression was reduced in other cancer cell lines but this was not mirrored in the MitoSOX results. Therefore indicating that some cancers are more prone to lipid ROS, whereas others may be able to regulate ROS levels more effectively.

However, this study did not investigate nanoparticle internalisation into the cancer cells or nanoparticle agglomeration. As the dose of nanoparticles increases so does agglomeration, and the agglomeration state is an important factor influencing cell internalisation. Therefore no concrete conclusions can be made for the negative results observed for PEGylated and Ferumoxitol nanoparticles until agglomeration and internalisation are investigated, Therefore future work should evaluate agglomeration across the applied dose range by centrifugal liquid sedimentation (CLS) and TEM microscopy should be undertaken to ensure nanoparticle uptake and determine uptake rate.

5.6 Conclusion

This chapter presents evidence suggesting the induction of ferroptosis in cancer cells by novel iron oxide nanoparticles. The novel iron oxide nanoparticles induce a cell death mechanism that presents several hallmarks of ferroptosis. Even though more experimentation is required to establish the precise mechanism for the ferroptosis induction, and to define better applications of these nanoparticles for cancer therapy. In the future *in vivo* experimentation needs to be carried out in order to exploit the therapeutic effects of the novel iron oxide nanoparticle. Tumours *in vivo* may be more prone to ferroptotic induction due to nanoparticle selectivity and the EPR effect, which will result in increased accumulation of nanoparticles at the tumour site.

Chapter 6: General discussion and conclusions

6.1 Discussion

Although cancer patients are highly responsive to initial treatment, acquired resistance leads to a relapse in the disease (Cancer Research UK, 2020). The plasticity of cancer cell metabolism impedes on the progress of chemotherapy treatment, therefore new targets are required that take advantage of cancer metabolic vulnerabilities. Ferroptosis is considered to be an emerging target for tumour therapy.

Ferroptosis was first discovered in 2012 as a novel form of programmed cell death, dependent on iron and characterised by the toxic accumulation of lipid peroxides (Dixon et al., 2012). However, cancer cells are able to evade ferroptotic induction by the upregulation of the regulating enzyme GPX4, which converts lipid peroxides into their equivalent alcohols (Stockwell et al., 2017). Targeting ferroptosis through iron accumulation, lipid peroxidation and inhibition of GPX4 could provide a new cancer therapy.

Targeting GPX4 can be achieved directly by using RSL3, which covalently and irreversibly binds to the enzyme (Dixon et al., 2012). Erastin can indirectly inhibit GPX4 by binding to the SLC7A11 subunit of system X_C^- and consequently reduces the synthesis of GSH, which is required for the conversion of lipid peroxides to alcohol (Cao & Dixon, 2016; Stockwell et al., 2017; Sato et al., 2018). The results obtained within this study found that ferroptosis could be induced in a panel of cancer cell lines by both Erastin and RSL3. As expected the cancer cells were more susceptible to ferroptotic cell death through the direct inhibition of GPX4. Although there is no definitive marker for ferroptotic induction there were observed changes in GPX4 expression, increased production of lipid peroxides and the addition of a lipid peroxide scavenger reversed cancer cell death, concluding ferroptosis was induced. However, iron and GSH levels were not measured, which could have further concluded ferroptotic induction.

Further research into the mechanism of Erastin-induced ferroptosis is required. Although previous studies have shown the inhibition of System X_C^- by Erastin,

the MTT assay and DRAQ7 stain showed different sensitivities of Erastin-induced cell death. The MTT assay looks at the viability of the mitochondria, the assay showed an increased sensitivity of the cells to Erastin, even at lower doses. A characteristic morphological change during ferroptotic induction is the mitochondrial membrane, therefore the MTT assay could show that ferroptosis was induced or the assay is not suitable for ferroptotic investigation. Erastin did increase the production of lipid peroxides, which could be rescued with the addition of a lipid peroxide scavenger, indicated the induction of ferroptosis.

Further research into the immune system and ferroptosis is required. The addition of IFN γ with the ferroptosis-inducers was surprising, as IFN γ has been shown to downregulate SLC7A11 and SLC3A2 (system X $_c^-$ components; Wang et al., 2019), it was expected that IFN γ would enhance Erastin-induced ferroptosis. However, there was observed rescue against Erastin in lung and ovarian OVCAR8 and also a rescue against RSL3 in breast, ovarian PEO4 and ovarian OVCAR8. Previous studies have shown that IFN γ induced ferroptotic cancer cell death is dependent on ACSL4 (Liao et al., 2022). Future research should determine the expression of ACSL4 in the cancer cell lines.

The AMPK/mTOR metabolism pathways were investigated to determine how they could interact with ferroptosis. However, future research is required to further breakdown these complicated interactions. The inhibition of mTORC1 and mTORC2 by rapamycin and Torin-1 did not further induce or rescue against Erastin or RSL3-induced ferroptosis. Concluding that ferroptosis works independently to mTOR. The inhibition of AMPK by compound C actually rescued against RSL3-induced ferroptosis, indicating that AMPK activation is required for ferroptosis. The increased phosphorylated P70-S6K indicates that AMPK was inhibited and mTOR was activated, which also indicates that mTOR activation rescues against ferroptosis. There was increased expression of LC3B-II indicating that AMPK was not inhibited due to the induction of autophagy, however, LC3B-II is also required for the induction of ferritinophagy, a form of autophagy. This indicates that a form of autophagy is

required to rescue against ferroptosis. Therefore further research is required to determine which autophagy pathway is undertaken during RSL3-induced ferroptotic cell death. However, the activation of P-AMPK by AICAR, also showed a rescue against RSL3-induced ferroptosis, which indicates that ferroptosis induction is independent of autophagy. Overall, how ferroptosis was rescued has not been fully determined, therefore further research is required.

Nanoparticles are at the forefront of cancer therapy, including their synergistic use with chemotherapy. However there has been little progress in this area, with poor clinical outcomes (Hare et al., 2017). This study presents evidence suggesting the induction of ferroptosis in cancer cells by novel iron oxide nanoparticles. Ferroptosis is dependent on iron and characterised by the toxic accumulation of lipid peroxides (Stockwell et al., 2017). Linoleic acid is a PUFA and therefore highly susceptible to lipid peroxidation, coating iron oxide nanoparticles with this PUFA provides a way to specifically target ferroptosis. The uptake of iron oxide nanoparticles by the cells would result in iron accumulation and consequently cause an iron overload, which is essential for ferroptotic induction. The novel PUFA coated iron oxide nanoparticles synthesised during this study, showed increased cell death and increased lipid peroxidation in all cell lines in comparison to ferroptosis treatment alone. Indicating that the addition of iron and linoleic acid induced ferroptosis. Therefore, synthesising a ferroptosis inducing nanoparticle could provide a new therapy treatment for cancer patients. The next stage would be to carry out *in vivo* experimentation to further exploit the therapeutic effects of the novel iron oxide nanoparticles.

There are only characteristic markers for the induction of ferroptosis, there is no definitive marker. This study did show increased lipid peroxidation, changes in GPX4 expression and a rescue against ferroptosis by a lipid peroxidation scavenger. Further investigation into other ferroptosis characteristics is required to further conclude ferroptotic induction. This study did not identify if another form of programmed cell death was induced, although markers for

autophagy were looked at, further investigation into other programmed cell death markers should be carried out. This study did not determine nanoparticle uptake by the cells, therefore it could not be concluded how the nanoparticles interacted with the cancer cells or how ferroptosis was induced. It would have also been beneficial to look at the LIP of the cells before and after the addition of nanoparticles. This study also did not determine how ferroptosis inducers such as RSL3 and Erastin, or how the nanoparticles would react with healthy cells. Although a recent study has shown that linoleic acid protects CD8+ T cells in order to promote antitumour responses (Lauson et al., 2023).

The critical drawback in this study is the absence of testing on 'normal', non-cancerous cells, which is critical to determining if there are any off target effects or toxicity. Therefore it is vital that all ferroptosis experiments are carried out on a suitable non-cancerous cell line before advancing further.

The future work of this study is to involve *in vivo* experiments, therefore the utilisation of both mouse and human secondary cell lines was required to establish a relevant foundation for subsequent investigations. In the proposed *in vivo* study, mice will receive subcutaneous injections of cancer cells, and regular measurements will be conducted to monitor tumour size. Subsequently, tumour-bearing mice will be subcutaneously administered with IONP-DLin, with the specific dosage, frequency and duration determined based on additional *in vitro* experiments. The efficacy of the treatment will be assessed through imaging techniques (MRI, CT or caliper measurements) to determine any reduction in tumour size. Criteria for humane endpoint would include tumours greater than 1.5 cm diameter or ulceration.

Overall, this study aimed to characterise the induction of ferroptosis in a diverse range of cancer cell lines. The research successfully synthesised a novel iron oxide nanoparticle designed to induce ferroptosis, demonstrating a significant reduction in cancer cell viability. Importantly, the susceptibility to ferroptotic induction varied among different cancer types, suggesting the potential for personalised treatment approaches.

This research contributes to the growing understanding of ferroptosis as a potential avenue for cancer treatment, showcasing the potential of engineered nanoparticles to induce this form of cell death selectively. *In vivo* studies are crucial to validate these findings and explore the translational potential of ferroptosis-targeted nano-therapies for cancer patients.

References

Abbaspour, N., Hurrell, R. and Kelishadi, R., (2014). Review on iron and its importance for human health. *Journal of research in medical sciences: the official journal of Isfahan University of Medical Sciences*, 19.

Adams, S., Loi, S., Toppmeyer, D., Cescon, D.W., De Laurentiis, M., Nanda, R., Winer, E.P., Mukai, H., Tamura, K., Armstrong, A. and Liu, M.C., (2019). Pembrolizumab monotherapy for previously untreated, PD-L1-positive, metastatic triple-negative breast cancer: cohort B of the phase II KEYNOTE-086 study. *Annals of Oncology*, 30.

Agarwala, S.S., (2009). Current systemic therapy for metastatic melanoma. *Expert review of anticancer therapy*, 9.

Ajoolabady, A., Aslkhodapasandhokmabad, H., Libby, P., Tuomilehto, J., Lip, G.Y., Penninger, J.M., Richardson, D.R., Tang, D., Zhou, H., Wang, S. and Klionsky, D.J., (2021). Ferritinophagy and ferroptosis in the management of metabolic diseases. *Trends in Endocrinology & Metabolism*, 32.

Alberg, A.J. and Samet, J.M., (2003). Epidemiology of lung cancer. *Chest*, 123.

Alexandrov, L.B., Nik-Zainal, S., Wedge, D.C., Aparicio, S.A., Behjati, S., Biankin, A.V., Bignell, G.R., Bolli, N., Borg, A., Børresen-Dale, A.L. and Boyault, S., (2013). Signatures of mutational processes in human cancer. *Nature*, 500.

Alitalo, A. and Detmar, M., (2012). Interaction of tumor cells and lymphatic vessels in cancer progression. *Oncogene*, 31.

Amatya, R., Hwang, S., Park, T., Min, K.A. and Shin, M.C., (2021). In vitro and in vivo evaluation of pegylated starch-coated iron oxide nanoparticles for enhanced photothermal cancer therapy. *Pharmaceutics*, 13.

Amstad, E., Zurcher, S., Mashaghi, A., Wong, J.Y., Textor, M. and Reimhult, E., (2009). Surface functionalization of single superparamagnetic iron oxide nanoparticles for targeted magnetic resonance imaging. *small*, 5.

Anzai, Y., Piccoli, C.W., Outwater, E.K., Stanford, W., Bluemke, D.A., Nurenberg, P., Saini, S., Maravilla, K.R., Feldman, D.E., Schmiedl, U.P. and Brunberg, J.A., (2003). Evaluation of neck and body metastases to nodes with ferumoxtran 10-enhanced MR imaging: phase III safety and efficacy study. *Radiology*, 228.

Arora, S., (2012). Superparamagnetic iron oxide nanoparticles: magnetic nanoplatforms as drug carriers. *International journal of nanomedicine*, 7.

Ascierto, P.A., Long, G.V., Robert, C., Brady, B., Dutriaux, C., Di Giacomo, A.M., Mortier, L., Hassel, J.C., Rutkowski, P., McNeil, C. and Kalinka-Warzocha, E., (2019). Survival outcomes in patients with previously untreated BRAF wild-type advanced melanoma treated with nivolumab therapy: three-year follow-up of a randomized phase 3 trial. *JAMA oncology*, 5.

Ayhan, A., Kurman, R.J., Vang, R., Logani, S., Seidman, J.D. and Shih, I.M., (2009). Defining the cut-point between low-and high-grade ovarian serous carcinomas: a clinicopathologic and molecular genetic analysis. *The American Journal of Surgical Pathology*, 33.

Bach, M., Larance, M., James, D.E. and Ramm, G., (2011). The serine/threonine kinase ULK1 is a target of multiple phosphorylation events. *Biochemical Journal*, 440.

Balakrishnan, V.S., Rao, M., Kausz, A.T., Brenner, L., Pereira, B.J.G., Frigo, T.B. and Lewis, J.M., (2009). Physicochemical properties of ferumoxytol, a new intravenous iron preparation. *European journal of clinical investigation*, 39.

Ballou, L.M. and Lin, R.Z., (2008). Rapamycin and mTOR kinase inhibitors. *Journal of chemical biology*, 1.

Barenholz, Y.C., (2012). Doxil®—the first FDA-approved nano-drug: lessons learned. *Journal of controlled release*, 160.

Basilion, J.P., Rouault, T.A., Massinople, C.M., Klausner, R.D. and Burgess, W.H., (1994). The iron-responsive element-binding protein: localization of the RNA-binding site to the aconitase active-site cleft. *Proceedings of the National Academy of Sciences*, 91.

Baulida, J., Díaz, V.M. and García de Herreros, A., (2019). Snail1: a transcriptional factor controlled at multiple levels. *Journal of clinical medicine*, 8.

Bersuker, K., Hendricks, J.M., Li, Z., Magtanong, L., Ford, B., Tang, P.H., Roberts, M.A., Tong, B., Maimone, T.J., Zoncu, R. and Bassik, M.C., (2019). The CoQ oxidoreductase FSP1 acts parallel to GPX4 to inhibit ferroptosis. *Nature*, 575.

Betzer, O., Shilo, M., OPOCHINSKY, R., Barnoy, E., Motiei, M., Okun, E., Yadid, G. and Popovtzer, R., (2017). The effect of nanoparticle size on the ability to cross the blood–brain barrier: an in vivo study. *Nanomedicine*, 12.

Bilbao-Asensio, M., Ruiz-de-Angulo, A., Arguinzoniz, A.G., Cronin, J., Llop, J., Zabaleta, A., Michue-Seijas, S., Sosnowska, D., Arnold, J.N. and Mareque-

Rivas, J.C., (2022). Redox-Triggered Nanomedicine via Lymphatic Delivery: Inhibition of Melanoma Growth by Ferroptosis Enhancement and a Pt (IV)-Prodrug Chemoimmunotherapy Approach. *Advanced Therapeutics*.

Bowen, N.J., Logani, S., Dickerson, E.B., Kapa, L.B., Akhtar, M., Benigno, B.B. and McDonald, J.F., (2007). Emerging roles for PAX8 in ovarian cancer and endosalpingeal development. *Gynecologic Oncology*, 104.

Bowtell, D.D., Böhm, S., Ahmed, A.A., Aspuria, P.J., Bast Jr, R.C., Beral, V., Berek, J.S., Birrer, M.J., Blagden, S., Bookman, M.A. and Brenton, J., (2015). Rethinking ovarian cancer II: reducing mortality from high-grade serous ovarian cancer. *Nature Reviews. Cancer*, 15.

Boyer, C., Whittaker, M.R., Bulmus, V., Liu, J. and Davis, T.P., (2010). The design and utility of polymer-stabilized iron-oxide nanoparticles for nanomedicine applications. *NPG Asia Materials*, 2.

Brahmer, J.R., Drake, C.G., Wollner, I., Powderly, J.D., Picus, J., Sharfman, W.H., Stankevich, E., Pons, A., Salay, T.M., McMiller, T.L. and Gilson, M.M., (2010). Phase I study of single-agent anti-programmed death-1 (MDX-1106) in refractory solid tumors: safety, clinical activity, pharmacodynamics, and immunologic correlates. *Journal of clinical oncology*, 28.

Brand, K.A. and Hermfisse, U., (1997). Aerobic glycolysis by proliferating cells: a protective strategy against reactive oxygen species 1. *The FASEB journal*, 11.

Cairns, R.A. and Mak, T.W., (2016). The current state of cancer metabolism. *Nat. Rev. Cancer*, 16.

Cao, Y., Li, Y., He, C., Yan, F., Li, J.R., Xu, H.Z., Zhuang, J.F., Zhou, H., Peng, Y.C., Fu, X.J. and Lu, X.Y., (2021). Selective ferroptosis inhibitor liproxstatin-1 attenuates neurological deficits and neuroinflammation after subarachnoid hemorrhage. *Neuroscience Bulletin*, 37.

Chen, X., Kang, R., Kroemer, G. and Tang, D., (2021). Broadening horizons: the role of ferroptosis in cancer. *Nature reviews Clinical oncology*, 18.

Christiansen, A. and Detmar, M., (2011). Lymphangiogenesis and cancer. *Genes & cancer*, 2.

Ciriello, G., Miller, M.L., Aksoy, B.A., Senbabaoglu, Y., Schultz, N. and Sander, C., (2013). Emerging landscape of oncogenic signatures across human cancers. *Nature Genetics*, 45.

Cleator, S., Heller, W. and Coombes, R.C., (2007). Triple-negative breast cancer: therapeutic options. *The lancet oncology*, 8.

Condé, J. ed., (2018). *Handbook of Nanomaterials for Cancer Theranostics*. Elsevier.

Conrad, M.E. and Schade, S.G., (1968). Ascorbic acid chelates in iron absorption: a role for hydrochloric acid and bile. *Gastroenterology*, 55.

Cooke, S.L. and Brenton, J.D., (2011). Evolution of platinum resistance in high-grade serous ovarian cancer. *The Lancet Oncology*, 12.

Cortes, J. and Saura, C., (2010). Nanoparticle albumin-bound (nabTM)-paclitaxel: improving efficacy and tolerability by targeted drug delivery in metastatic breast cancer. *European Journal of Cancer Supplements*, 8.

Cortés, M., Sanchez-Moral, L., de Barrios, O., Fernández-Aceñero, M.J., Martínez-Campanario, M.C., Esteve-Codina, A., Darling, D.S., Györffy, B., Lawrence, T., Dean, D.C. and Postigo, A., (2017). Tumor-associated macrophages (TAMs) depend on ZEB1 for their cancer-promoting roles. *The EMBO Journal*, 36.

Cortez-Retamozo, V., Etzrodt, M., Newton, A., Rauch, P.J., Chudnovskiy, A., Berger, C., Ryan, R.J., Iwamoto, Y., Marinelli, B., Gorbатов, R. and Forghani, R., (2012). Origins of tumor-associated macrophages and neutrophils. *Proceedings of the National Academy of Sciences*, 109.

Corton, J.M., Gillespie, J.G., Hawley, S.A. and Hardie, D.G., (1995). 5-Aminoimidazole-4-carboxamide ribonucleoside: a specific method for activating AMP-activated protein kinase in intact cells?. *European journal of biochemistry*, 229.

Corvino, A., Corvino, F., Radice, L. and Catalano, O., (2015). Synchronous mucinous colonic adenocarcinoma and multiple small intestinal adenocarcinomas: report of a case and review of literature. *Clinical imaging*, 39.

Coussens, L.M., Fingleton, B. and Matrisian, L.M., (2002). Matrix metalloproteinase inhibitors and cancer—trials and tribulations. *Science*, 295.

Couto, D., Freitas, M., Carvalho, F. and Fernandes, E., (2015). Iron oxide nanoparticles: An insight into their biomedical applications. *Current Medicinal Chemistry*, 22.

Czerski, L. and Nuñez, G., (2004). Apoptosome formation and caspase activation: is it different in the heart?. *Journal of Molecular and Cellular Cardiology*, 37.

Dadwal, A., Baldi, A. and Kumar Narang, R., (2018). Nanoparticles as carriers for drug delivery in cancer. *Artificial cells, nanomedicine, and biotechnology*, 46.

Dai, M., Yan, G., Wang, N., Daliah, G., Edick, A.M., Poulet, S., Boudreault, J., Ali, S., Burgos, S.A. and Lebrun, J.J., (2021). In vivo genome-wide CRISPR screen reveals breast cancer vulnerabilities and synergistic mTOR/Hippo targeted combination therapy. *Nature Communications*, 12.

D'Andrea, A.D., (2018). Mechanisms of PARP inhibitor sensitivity and resistance. *DNA repair*, 71.

Dean, M., Davis, D.A. and Burdette, J.E., (2017). Activin A stimulates migration of the fallopian tube epithelium, an origin of high-grade serous ovarian cancer, through non-canonical signaling. *Cancer letters*, 391.

DeBerardinis, R.J. and Chandel, N.S., (2016). Fundamentals of cancer metabolism. *Science advances*, 2.

Dixon, S.J. and Stockwell, B.R., (2019). The hallmarks of ferroptosis. *Annual Review of Cancer Biology*, 3.

Dixon, S.J., Lemberg, K.M., Lamprecht, M.R., Skouta, R., Zaitsev, E.M., Gleason, C.E., Patel, D.N., Bauer, A.J., Cantley, A.M., Yang, W.S. and Morrison, B., (2012). Ferroptosis: an iron-dependent form of nonapoptotic cell death. *cell*, 149.

Dixon, S.J., Winter, G.E., Musavi, L.S., Lee, E.D., Snijder, B., Rebsamen, M., Superti-Furga, G. and Stockwell, B.R., (2015). Human haploid cell genetics reveals roles for lipid metabolism genes in nonapoptotic cell death. *ACS chemical biology*, 10.

Doll, S., Freitas, F.P., Shah, R., Aldrovandi, M., da Silva, M.C., Ingold, I., Goya Grocin, A., Xavier da Silva, T.N., Panzilius, E., Scheel, C.H. and Mourão, A., (2019). FSP1 is a glutathione-independent ferroptosis suppressor. *Nature*, 575.

Doll, S., Proneth, B., Tyurina, Y.Y., Panzilius, E., Kobayashi, S., Ingold, I., Irmeler, M., Beckers, J., Aichler, M., Walch, A. and Prokisch, H., (2017). ACSL4 dictates ferroptosis sensitivity by shaping cellular lipid composition. *Nature chemical biology*, 13.

Dolle, J.M., Daling, J.R., White, E., Brinton, L.A., Doody, D.R., Porter, P.L. and Malone, K.E., (2009). Risk factors for triple-negative breast cancer in women under the age of 45 years. *Cancer Epidemiology Biomarkers & Prevention*, 18.

Duan, J., Cui, L., Zhao, X., Bai, H., Cai, S., Wang, G., Zhao, Z., Zhao, J., Chen, S., Song, J. and Qi, C., (2020). Use of immunotherapy with programmed cell death 1 vs programmed cell death ligand 1 inhibitors in patients with cancer: a systematic review and meta-analysis. *JAMA oncology*, 6.

Dulińska-Litewka, J., Łazarczyk, A., Hałubiec, P., Szafranski, O., Karnas, K. and Karewicz, A., (2019). Superparamagnetic iron oxide nanoparticles—Current and prospective medical applications. *Materials*, 12

Durán, R.V., Oppliger, W., Robitaille, A.M., Heiserich, L., Skendaj, R., Gottlieb, E. and Hall, M.N., (2012). Glutaminolysis activates Rag-mTORC1 signaling. *Molecular cell*, 47.

Eagle, H., (1955). Nutrition needs of mammalian cells in tissue culture. *Science*, 122.

Efimova, I., Catanzaro, E., Van der Meeren, L., Turubanova, V.D., Hammad, H., Mishchenko, T.A., Vedunova, M.V., Fimognari, C., Bachert, C., Coppieters, F. and Lefever, S., (2020). Vaccination with early ferroptotic cancer cells induces efficient antitumor immunity. *Journal for immunotherapy of cancer*, 8.

Ehninger, D., Neff, F. and Xie, K., (2014). Longevity, aging and rapamycin. *Cellular and molecular life sciences*, 71.

Elias, A. and Tsourkas, A., (2009). Imaging circulating cells and lymphoid tissues with iron oxide nanoparticles. *ASH Education Program Book*, 2009.

Elmore, S., (2007). Apoptosis: a review of programmed cell death. *Toxicologic pathology*, 35.

Emens, L.A., Braiteh, F.S., Cassier, P., Delord, J.P., Eder, J.P., Fasso, M., Xiao, Y., Wang, Y., Molinero, L., Chen, D.S. and Krop, I., (2015). Inhibition of PD-L1 by MPDL3280A leads to clinical activity in patients with metastatic triple-negative breast cancer (TNBC). *Cancer Research*, 75.

Erekat, N.S., (2018). Apoptosis and its Role in Parkinson's Disease. *Exon Publications*.

Estrella, V., Chen, T., Lloyd, M., Wojtkowiak, J., Cornell, H.H., Ibrahim-Hashim, A., Bailey, K., Balagurunathan, Y., Rothberg, J.M., Sloane, B.F. and Johnson, J., (2013). Acidity Generated by the Tumor Microenvironment Drives Local Invasion Acid-Mediated Invasion. *Cancer research*, 73.

Feng, H. and Stockwell, B.R., (2018). Unsolved mysteries: How does lipid peroxidation cause ferroptosis?. *PLoS Biology*, 16.

Feng, Q., Lui, Y., Huang, J., Chen, K., Huang, J. and Xiao, K., (2018). Uptake, distribution, clearance, and toxicity of iron oxide nanoparticles with different sizes and coatings. *Scientific Reports*, 8.

Feng, Y., He, D., Yao, Z. and Klionsky, D.J., (2014). The machinery of macroautophagy. *Cell research*, 24.

Feng, Y., Madungwe, N.B., Aliagan, A.D.I., Tombo, N. and Bopassa, J.C., (2019). Ferroptosis inhibitor, liproxstatin-1, protects the myocardium against ischemia/reperfusion injury by decreasing VDAC1 levels and rescuing GPX4 levels. *Biochemical and biophysical research communications*, 520.

Fernández-Acosta, R., Iriarte-Mesa, C., Alvarez-Alminaque, D., Hassannia, B., Wiernicki, B., Díaz-García, A.M., Vandenabeele, P., Vanden Berghe, T. and Pardo Andreu, G.L., (2022). Novel iron oxide nanoparticles induce ferroptosis in a panel of cancer cell lines. *Molecules*, 27.

Fong, P.C., Boss, D.S., Yap, T.A., Tutt, A., Wu, P., Mergui-Roelvink, M., Mortimer, P., Swaisland, H., Lau, A., O'connor, M.J. and Ashworth, A., (2009). Inhibition of poly (ADP-ribose) polymerase in tumors from BRCA mutation carriers. *New England Journal of Medicine*, 361.

Foster, D.A. and Toschi, A., (2009). Targeting mTOR with rapamycin: one dose does not fit all. *Cell Cycle*, 8.

Franklin, R.A. and Li, M.O., (2016). Ontogeny of tumor-associated macrophages and its implication in cancer regulation. *Trends in Cancer*, 2.

Franzese, E., Centonze, S., Diana, A., Carlino, F., Guerrera, L.P., Di Napoli, M., De Vita, F., Pignata, S., Ciardiello, F. and Orditura, M., (2019). PARP inhibitors in ovarian cancer. *Cancer Treatment Reviews*, 73.

Freed-Pastor, W. and Prives, C., (2016). Targeting mutant p53 through the mevalonate pathway. *Nature Cell Biology*, 18.

Frisch, S.M. and Francis, H., (1994). Disruption of epithelial cell-matrix interactions induces apoptosis. *The Journal of cell biology*, 124.

Fubini, B., Ghiazza, M. and Fenoglio, I., (2010). Physico-chemical features of engineered nanoparticles relevant to their toxicity. *Nanotoxicology*, 4.

Gaharwar, U.S., Meena, R. and Rajamani, P., (2019). Biodistribution, clearance and morphological alterations of intravenously administered iron oxide nanoparticles in male wistar rats. *International Journal of Nanomedicine*, pp.9677-9692.

Galadari, S., Rahman, A., Pallichankandy, S. and Thayyullathil, F., (2017). Reactive oxygen species and cancer paradox: to promote or to suppress?. *Free Radical Biology and Medicine*, 104.

Galon, J. and Bruni, D., (2019). Approaches to treat immune hot, altered and cold tumours with combination immunotherapies. *Nature reviews Drug discovery*, 18.

Gan, B., (2021). Mitochondrial regulation of ferroptosis. *Journal of Cell Biology*, 220.

Gao, M., Monian, P., Quadri, N., Ramasamy, R. and Jiang, X., (2015). Glutaminolysis and transferrin regulate ferroptosis. *Molecular cell*, 59.

Gao, M., Yi, J., Zhu, J., Minikes, A.M., Monian, P., Thompson, C.B. and Jiang, X., (2019). Role of mitochondria in ferroptosis. *Molecular cell*, 73.

Gao, X., Zacharek, A., Salkowski, A., Grignon, D.J., Sakr, W., Porter, A.T. and Honn, K.V., (1995). Loss of heterozygosity of the BRCA1 and other loci on chromosome 17q in human prostate cancer. *Cancer research*, 55.

García-Cañaveras, J.C., Chen, L. and Rabinowitz, J.D., (2019). The Tumor Metabolic Microenvironment: Lessons from Lactate. *Cancer research*, 79.

Geppert, M. and Himly, M., (2021). Iron oxide nanoparticles in bioimaging-an immune perspective. *Frontiers in Immunology*, 12.

Ghosh, S., Ghosh, I., Chakrabarti, M. and Mukherjee, A., (2020). Genotoxicity and biocompatibility of superparamagnetic iron oxide nanoparticles: Influence of surface modification on biodistribution, retention, DNA damage and oxidative stress. *Food and Chemical Toxicology*, 136.

Giardina, P.J. and Grady, R.W., (1995). Chelation therapy in beta-thalassemia: the benefits and limitations of desferrioxamine. In *Seminars in hematology*, 32.

Giardina, P.J. and Grady, R.W., (2001). Chelation therapy in β -thalassemia: an optimistic update. In *Seminars in hematology*, 38.

Giménez-Xavier, P., Francisco, R., Platini, F., Pérez, R. and Ambrosio, S., (2008). LC3-I conversion to LC3-II does not necessarily result in complete autophagy. *International journal of molecular medicine*, 22.

Glick, D., Barth, S. and Macleod, K.F., (2010). Autophagy: cellular and molecular mechanisms. *The Journal of pathology*, 221.

Gogas, H.J., Kirkwood, J.M. and Sondak, V.K., (2007). Chemotherapy for metastatic melanoma: time for a change?. *Cancer: Interdisciplinary International Journal of the American Cancer Society*, 109.

Golombek, S.K., May, J.N., Theek, B., Appold, L., Drude, N., Kiessling, F. and Lammers, T., (2018). Tumor targeting via EPR: Strategies to enhance patient responses. *Advanced drug delivery reviews*, 130.

Gorrini, C., Harris, I.S. and Mak, T.W., (2013). Modulation of oxidative stress as an anticancer strategy. *Nature reviews Drug discovery*, 12.

Granville, C.A., Warfel, N., Tsurutani, J., Hollander, M.C., Robertson, M., Fox, S.D., Veenstra, T.D., Issaq, H.J., Linnoila, R.I. and Dennis, P.A., (2007). Identification of a highly effective rapamycin schedule that markedly reduces the size, multiplicity, and phenotypic progression of tobacco carcinogen-induced murine lung tumors. *Clinical cancer research*, 13.

Gray, D.C., Mahrus, S. and Wells, J.A., (2010). Activation of specific apoptotic caspases with an engineered small-molecule-activated protease. *Cell*, 142.

Grivennikova, V.G. and Vinogradov, A.D., (2006). Generation of superoxide by the mitochondrial Complex I. *Biochimica et Biophysica Acta (BBA)-Bioenergetics*, 1757.

Grossmann, J., (2002). Molecular mechanisms of “detachment-induced apoptosis—Anoikis”. *Apoptosis*, 7.

Guan, Q., Zhou, L.L. and Dong, Y.B., (2021). Ferroptosis in cancer therapeutics: a materials chemistry perspective. *Journal of Materials Chemistry B*, 9.

Gupta, A.K. and Gupta, M., (2005). Synthesis and surface engineering of iron oxide nanoparticles for biomedical applications. *biomaterials*, 26.

Haass, N.K., Smalley, K.S., Li, L. and Herlyn, M., (2005). Adhesion, migration and communication in melanocytes and melanoma. *Pigment cell research*, 18.

Hallberg, L., Brune, M. and Rossander, L., (1989). Iron absorption in man: ascorbic acid and dose-dependent inhibition by phytate. *The American journal of clinical nutrition*, 49.

Hamanishi, J., Mandai, M., Ikeda, T., Minami, M., Kawaguchi, A., Matsumura, N., Abiko, K., Baba, T., Yamaguchi, K., Ueda, A. and Hosoe, Y., (2015). Durable tumor remission in patients with platinum-resistant ovarian cancer receiving nivolumab.

Han, C.Y., Patten, D.A., Richardson, R.B., Harper, M.E. and Tsang, B.K., (2018). Tumor metabolism regulating chemosensitivity in ovarian cancer. *Genes & cancer*, 9.

Hanahan, D. and Weinberg, R.A., (2011). Hallmarks of cancer: the next generation. *cell*, 144.

Hardie, D.G., Ross, F.A. and Hawley, S.A., (2012). AMPK: a nutrient and energy sensor that maintains energy homeostasis. *Nature reviews Molecular cell biology*, 13.

Hardie, D.G., Schaffer, B.E. and Brunet, A., (2016). AMPK: an energy-sensing pathway with multiple inputs and outputs. *Trends in cell biology*, 26.

Hare, J.I., Lammers, T., Ashford, M.B., Puri, S., Storm, G. and Barry, S.T., (2017). Challenges and strategies in anti-cancer nanomedicine development: An industry perspective. *Advanced drug delivery reviews*, 108.

Harrell, M.I., Iritani, B.M. and Ruddell, A., (2007). Tumor-induced sentinel lymph node lymphangiogenesis and increased lymph flow precede melanoma metastasis. *The American journal of pathology*, 170.

Heinonen, H., Nieminen, A., Saarela, M., Kallioniemi, A., Klefström, J., Hautaniemi, S. and Monni, O., (2008). Deciphering downstream gene targets of PI3K/mTOR/p70S6K pathway in breast cancer. *BMC genomics*, 9.

Helissey, C., Vicier, C. and Champiat, S., (2016). The development of immunotherapy in older adults: new treatments, new toxicities?. *Journal of geriatric oncology*, 7.

Holmes, D., (2015). The problem with platinum. *Nature*, 527.

Hou, J., Jiang, C., Wen, X., Li, C., Xiong, S., Yue, T., Long, P., Shi, J. and Zhang, Z., (2022). ACSL4 as a potential target and biomarker for anticancer: From molecular mechanisms to clinical therapeutics. *Frontiers in Pharmacology*, 13.

Hsueh, A.J.W., McGee, E.A., Hayashi, M. and Hsu, S.Y., (2000). Hormonal regulation of early follicle development in the rat ovary. *Molecular and cellular endocrinology*, 163.

- Hu, J., Fu, S., Peng, Q., Han, Y., Xie, J., Zan, N., Chen, Y. and Fan, J., (2017). Paclitaxel-loaded polymeric nanoparticles combined with chronomodulated chemotherapy on lung cancer: In vitro and in vivo evaluation. *International journal of pharmaceuticals*, 516.
- Hu, W., Zhang, C., Wu, R., Sun, Y., Levine, A. and Feng, Z., (2010). Glutaminase 2, a novel p53 target gene regulating energy metabolism and antioxidant function. *Proceedings of the National Academy of Sciences*, 107.
- Huang, A.C. and Zappasodi, R., (2022). A decade of checkpoint blockade immunotherapy in melanoma: understanding the molecular basis for immune sensitivity and resistance. *Nature immunology*, 23.
- Huang, C., Park, C.C., Hilsenbeck, S.G., Ward, R., Rimawi, M.F., Wang, Y.C., Shou, J., Bissell, M.J., Osborne, C.K. and Schiff, R., (2011). β 1 integrin mediates an alternative survival pathway in breast cancer cells resistant to lapatinib. *Breast cancer research*, 13.
- Huang, K.J., Wei, Y.H., Chiu, Y.C., Wu, S.R. and Shieh, D.B., (2019). Assessment of zero-valent iron-based nanotherapeutics for ferroptosis induction and resensitization strategy in cancer cells. *Biomaterials science*, 7.
- Hudson, E.R., Pan, D.A., James, J., Lucocq, J.M., Hawley, S.A., Green, K.A., Baba, O., Terashima, T. and Hardie, D.G., (2003). A novel domain in AMP-activated protein kinase causes glycogen storage bodies similar to those seen in hereditary cardiac arrhythmias. *Current biology*, 13.
- Hunt, J.R., Zito, C.A. and Johnson, L.K., (2009). Body iron excretion by healthy men and women. *The American journal of clinical nutrition*, 89.
- Hurley, R.L., Anderson, K.A., Franzone, J.M., Kemp, B.E., Means, A.R. and Witters, L.A., (2005). The Ca²⁺/calmodulin-dependent protein kinase kinases are AMP-activated protein kinase kinases. *Journal of Biological Chemistry*, 280.
- Hüsemann, Y., Geigl, J.B., Schubert, F., Musiani, P., Meyer, M., Burghart, E., Forni, G., Eils, R., Fehm, T., Riethmüller, G. and Klein, C.A., (2008). Systemic spread is an early step in breast cancer. *Cancer cell*, 13.
- Igelmann, S., Neubauer, H.A. and Ferbeyre, G., (2019). STAT3 and STAT5 activation in solid cancers. *Cancers*, 11.
- Inoki, K., Kim, J. and Guan, K.L., (2012). AMPK and mTOR in cellular energy homeostasis and drug targets. *Annual review of pharmacology and toxicology*, 52.

Iqbal, T.H., Lewis, K.O. and Cooper, B.T., (1994). Phytase activity in the human and rat small intestine. *Gut*, 35.

Jacinto, E., Loewith, R., Schmidt, A., Lin, S., Rüegg, M.A., Hall, A. and Hall, M.N., (2004). Mammalian TOR complex 2 controls the actin cytoskeleton and is rapamycin insensitive. *Nature cell biology*, 6.

Jerant, A.F., Johnson, J.T., Sheridan, C.D. and Caffrey, T.J., (2000). Early detection and treatment of skin cancer. *American family physician*, 62.

Jin, R., Lin, B., Li, D. and Ai, H., (2014). Superparamagnetic iron oxide nanoparticles for MR imaging and therapy: design considerations and clinical applications. *Current opinion in pharmacology*, 18.

Jossé, L., Xie, J., Proud, C.G. and Smales, C.M., (2016). mTORC1 signalling and eIF4E/4E-BP1 translation initiation factor stoichiometry influence recombinant protein productivity from GS-CHOK1 cells. *Biochemical Journal*, 473.

Jung, C.W., (1995). Surface properties of superparamagnetic iron oxide MR contrast agents: ferumoxides, ferumoxtran, ferumoxsil. *Magnetic resonance imaging*, 13.

Kerr, J.F., Wyllie, A.H. and Currie, A.R., (1972). Apoptosis: a basic biological phenomenon with wideranging implications in tissue kinetics. *British journal of cancer*, 26.

Kievit, F.M. and Zhang, M., (2011). Surface engineering of iron oxide nanoparticles for targeted cancer therapy. *Accounts of chemical research*, 44.

Kim, J., Kundu, M., Viollet, B. and Guan, K.L., (2011). AMPK and mTOR regulate autophagy through direct phosphorylation of Ulk1. *Nature cell biology*, 13.

Kim, L.C., Cook, R.S. and Chen, J., (2017). mTORC1 and mTORC2 in cancer and the tumor microenvironment. *Oncogene*, 36.

Kim, Y.N., Koo, K.H., Sung, J.Y., Yun, U.J. and Kim, H., (2012). Anoikis resistance: an essential prerequisite for tumor metastasis. *International journal of cell biology*, 2012.

Kipps, E., Tan, D.S. and Kaye, S.B., (2013). Meeting the challenge of ascites in ovarian cancer: new avenues for therapy and research. *Nature Reviews. Cancer*, 13.

Knight, K., Wade, S. and Balducci, L., (2004). Prevalence and outcomes of anemia in cancer: a systematic review of the literature. *The American journal of medicine*, 116.

Koneri, K., Goi, T., Hirono, Y., Katayama, K. and Yamaguchi, A., (2007). Beclin 1 gene inhibits tumor growth in colon cancer cell lines. *Anticancer research*, 27.

Koppenol, W.H., Bounds, P.L. and Dang, C.V., (2011). Otto Warburg's contributions to current concepts of cancer metabolism. *Nature Reviews Cancer*, 11.

Koppula, P., Zhang, Y., Zhuang, L. and Gan, B., (2018). Amino acid transporter SLC7A11/xCT at the crossroads of regulating redox homeostasis and nutrient dependency of cancer. *Cancer Communications*, 38.

Kruiswijk, F., Labuschagne, C.F. and Vousden, K.H., (2015). p53 in survival, death and metabolic health: a lifeguard with a licence to kill. *Nature reviews Molecular cell biology*, 16.

Kuma, A. and Mizushima, N., (2010), September. Physiological role of autophagy as an intracellular recycling system: with an emphasis on nutrient metabolism. In *Seminars in cell & developmental biology*, 21.

Kurman, R.J. and Shih, I.M., (2010). The Origin and pathogenesis of epithelial ovarian cancer-a proposed unifying theory. *The American Journal of Surgical Pathology*, 34.

Labidi-Galy, S.I., Papp, E., Hallberg, D., Niknafs, N., Adleff, V., Noe, M., Bhattacharya, R., Novak, M., Jones, S., Phallen, J. and Hruban, C.A., (2017). High grade serous ovarian carcinomas originate in the fallopian tube. *Nature Communications*, 8.

Lacey Jr, J.V., Mink, P.J., Lubin, J.H., Sherman, M.E., Troisi, R., Hartge, P., Schatzkin, A. and Schairer, C., (2002). Menopausal hormone replacement therapy and risk of ovarian cancer. *The Journal of the American Medical Association*, 288.

Lane, J.D., Korolchuk, V.I., Murray, J.T., Zachari, M. and Ganley, I.G., (2017). The mammalian ULK1 complex and autophagy initiation. *Essays in biochemistry*, 61.

Lane, J.D., Slobodkin, M.R. and Elazar, Z., (2013). The Atg8 family: multifunctional ubiquitin-like key regulators of autophagy. *Essays in biochemistry*, 55.

Lang, X., Green, M.D., Wang, W., Yu, J., Choi, J.E., Jiang, L., Liao, P., Zhou, J., Zhang, Q., Dow, A. and Saripalli, A.L., (2019). Radiotherapy and Immunotherapy Promote Tumoral Lipid Oxidation and Ferroptosis via Synergistic Repression of SLC7A11. *Cancer discovery*, 9.

Laplante, M. and Sabatini, D.M., (2012). mTOR signaling in growth control and disease. *cell*, 149.

Lauson, C.B.N., Tiberti, S., Corsetto, P.A., Conte, F., Tyagi, P., Machwirth, M., Ebert, S., Loffreda, A., Scheller, L., Sheta, D. and Mokhtari, Z., (2023). Linoleic acid potentiates CD8⁺ T cell metabolic fitness and antitumor immunity. *Cell Metabolism*.

Le, D.T., Uram, J.N., Wang, H., Bartlett, B.R., Kemberling, H., Eyring, A.D., Skora, A.D., Lubber, B.S., Azad, N.S., Laheru, D. and Biedrzycki, B., (2015). PD-1 blockade in tumors with mismatch-repair deficiency. *New England Journal of Medicine*, 372.

Lehrman, E.D., Plotnik, A.N., Hope, T. and Saloner, D., (2019). Ferumoxytol-enhanced MRI in the peripheral vasculature. *Clinical radiology*, 74.

Leontieva, O.V., Demidenko, Z.N. and Blagosklonny, M.V., (2015). Dual mTORC1/C2 inhibitors suppress cellular geroconversion (a senescence program). *Oncotarget*, 6.

Lesniak, A., Fenaroli, F., Monopoli, M.P., Åberg, C., Dawson, K.A. and Salvati, A., (2012). Effects of the presence or absence of a protein corona on silica nanoparticle uptake and impact on cells. *ACS nano*, 6.

Li, C., Dong, X., Du, W., Shi, X., Chen, K., Zhang, W. and Gao, M., (2020). LKB1-AMPK axis negatively regulates ferroptosis by inhibiting fatty acid synthesis. *Signal Transduction and Targeted Therapy*, 5.

Li, G., Satyamoorthy, K. and Herlyn, M., (2001). N-cadherin-mediated intercellular interactions promote survival and migration of melanoma cells. *Cancer research*, 61.

Li, L., Mak, K.Y., Leung, C.W., Chan, K.Y., Chan, W.K., Zhong, W. and Pong, P.W.T., (2013). Effect of synthesis conditions on the properties of citric-acid coated iron oxide nanoparticles. *Microelectronic Engineering*, 110.

Li, S., He, Y., Chen, K., Sun, J., Zhang, L., He, Y., Yu, H. and Li, Q., (2021). RSL3 drives ferroptosis through NF- κ B pathway activation and GPX4 depletion in glioblastoma. *Oxidative Medicine and Cellular Longevity*, 2021.

Li, Y. and Chen, Y., (2019). AMPK and autophagy. *Autophagy: Biology and Diseases: Basic Science*.

Liang, J.Y., Wang, D.S., Lin, H.C., Chen, X.X., Yang, H., Zheng, Y. and Li, Y.H., (2020). A novel ferroptosis-related gene signature for overall survival prediction in patients with hepatocellular carcinoma. *International journal of biological sciences*, 16.

Liao, P., Wang, W., Wang, W., Kryczek, I., Li, X., Bian, Y., Sell, A., Wei, S., Grove, S., Johnson, J.K. and Kennedy, P.D., (2022). CD8+ T cells and fatty acids orchestrate tumor ferroptosis and immunity via ACSL4. *Cancer cell*, 40.

Licciardi, M., Scialabba, C., Puleio, R., Cassata, G., Cicero, L., Cavallaro, G. and Giammona, G., (2019). Smart copolymer coated SPIONs for colon cancer chemotherapy. *International Journal of Pharmaceutics*, 556.

Lin, H., Cheng, J., Mu, W., Zhou, J. and Zhu, L., (2021). Advances in universal CAR-T cell therapy. *Frontiers in immunology*, 12.

Linher-Melville, K., Haftchenary, S., Gunning, P. and Singh, G., (2015). Signal transducer and activator of transcription 3 and 5 regulate system Xc- and redox balance in human breast cancer cells. *Molecular and cellular biochemistry*, 405.

Liou, G.Y. and Storz, P., (2010). Reactive oxygen species in cancer. *Free radical research*, 44.

Liu, J., Kuang, F., Kroemer, G., Klionsky, D.J., Kang, R. and Tang, D., (2020). Autophagy-dependent ferroptosis: machinery and regulation. *Cell chemical biology*, 27.

Liu, R., Li, X. and Zhao, G., (2019). Beclin1-mediated ferroptosis activation is associated with isoflurane-induced toxicity in SH-SY5Y neuroblastoma cells. *Acta biochimica et biophysica Sinica*, 51.

Liu, S., Yan, S., Zhu, J., Lu, R., Kang, C., Tang, K., Zeng, J., Ding, M., Guo, Z., Lai, X. and Jiang, Y., (2022). Combination RSL3 treatment sensitizes ferroptosis- and EGFR-inhibition-resistant HNSCCs to cetuximab. *International journal of molecular sciences*, 23.

Liu, X., Chhipa, R.R., Nakano, I. and Dasgupta, B., (2014). The AMPK Inhibitor Compound C Is a Potent AMPK-Independent Antiglioma Agent. *Antiglioma Actions of Compound C. Molecular cancer therapeutics*, 13.

Loret, N., Denys, H., Tummers, P. and Berx, G., (2019). The Role of Epithelial-to-Mesenchymal Plasticity in Ovarian Cancer Progression and Therapy Resistance. *Cancers*, 11.

Lu, B., Chen, X.B., Ying, M.D., He, Q.J., Cao, J. and Yang, B., (2018). The role of ferroptosis in cancer development and treatment response. *Frontiers in pharmacology*, 8.

Lu, Y.C., Weng, W.C. and Lee, H., (2015). Functional roles of calreticulin in cancer biology. *BioMed research international*, 2015.

Lukanova, A. and Kaaks, R., (2005). Endogenous hormones and ovarian cancer: epidemiology and current hypotheses. *Cancer Epidemiology and Prevention Biomarkers*, 14.

Luo, X., Budihardjo, I., Zou, H., Slaughter, C. and Wang, X., (1998). Bid, a Bcl2 interacting protein, mediates cytochrome c release from mitochondria in response to activation of cell surface death receptors. *Cell*, 94.

Maeda, H. and Islam, W., (2020). Overcoming barriers for tumor-targeted drug delivery: The power of macromolecular anticancer drugs with the EPR effect and the modulation of vascular physiology. In *Polymer-Protein Conjugates*, Elsevier.

Malhotra, N., Lee, J.S., Liman, R.A.D., Ruallo, J.M.S., Villaflores, O.B., Ger, T.R. and Hsiao, C.D., (2020). Potential toxicity of iron oxide magnetic nanoparticles: a review. *Molecules*, 25.

Matsumura, Y. and Maeda, H., (1986). A new concept for macromolecular therapeutics in cancer chemotherapy: mechanism of tumoritropic accumulation of proteins and the antitumor agent smancs. *Cancer research*, 46.

Matte, I., Bessette, P. and Piché, A., (2017). Ascites in Ovarian Cancer Progression: Opportunities for Biomarker Discovery and New Avenues for Targeted Therapies. In *Ascites-Physiopathology, Treatment, Complications and Prognosis*.

McBean, G.J., (2012). The transsulfuration pathway: a source of cysteine for glutathione in astrocytes. *Amino acids*, 42.

McCawley, L.J. and Matrisian, L.M., (2000). Matrix metalloproteinases: multifunctional contributors to tumor progression. *Molecular medicine today*, 6.

McLaughlin, J.R., Risch, H.A., Lubinski, J., Moller, P., Ghadirian, P., Lynch, H., Karlan, B., Fishman, D., Rosen, B., Neuhausen, S.L. and Offit, K., (2007). Reproductive risk factors for ovarian cancer in carriers of BRCA1 or BRCA2 mutations: a case-control study. *The Lancet Oncology*, 8.

Mihaylova, M.M. and Shaw, R.J., (2011). The AMPK signalling pathway coordinates cell growth, autophagy and metabolism. *Nature cell biology*, 13.

Mizushima, N. and Yoshimori, T., (2007). How to interpret LC3 immunoblotting. *Autophagy*, 3.

Mosmann, T., (1983). Rapid colorimetric assay for cellular growth and survival: application to proliferation and cytotoxicity assays. *Journal of immunological methods*, 65.

Mundekkad, D. and Cho, W.C., (2022). Nanoparticles in clinical translation for cancer therapy. *International Journal of Molecular Sciences*, 23.

Mundra, V., Li, W. and Mahato, R.I., (2015). Nanoparticle-mediated drug delivery for treating melanoma. *Nanomedicine*, 10.

Murphy, M.P., (2009). How mitochondria produce reactive oxygen species. *Biochemical journal*, 417.

Narod, S., (2016). Can advanced-stage ovarian cancer be cured?. *Nature Reviews Clinical Oncology*, 13.

Natarajan, V.T., Ganju, P., Singh, A., Vijayan, V., Kirty, K., Yadav, S., Puntambekar, S., Bajaj, S., Dani, P.P., Kar, H.K. and Gadgil, C.J., (2014). IFN- γ signaling maintains skin pigmentation homeostasis through regulation of melanosome maturation. *Proceedings of the National Academy of Sciences*, 111.

Nedeljković, M. and Damjanović, A., (2019). Mechanisms of chemotherapy resistance in triple-negative breast cancer—how we can rise to the challenge. *Cells*, 8.

Nicklin, P., Bergman, P., Zhang, B., Triantafellow, E., Wang, H., Nyfeler, B., Yang, H., Hild, M., Kung, C., Wilson, C. and Myer, V.E., (2009). Bidirectional transport of amino acids regulates mTOR and autophagy. *Cell*, 136.

Nie, S., (2010). Understanding and overcoming major barriers in cancer nanomedicine. *Nanomedicine*, 5.

Nieman, K.M., Kenny, H.A., Penicka, C.V., Ladanyi, A., Buell-Gutbrod, R., Zillhardt, M.R., Romero, I.L., Carey, M.S., Mills, G.B., Hotamisligil, G.S. and Yamada, S.D., (2011). Adipocytes promote ovarian cancer metastasis and provide energy for rapid tumor growth. *Nature Medicine*, 17.

Oku, M. and Sakai, Y., (2018). Three distinct types of microautophagy based on membrane dynamics and molecular machineries. *Bioessays*, 40.

Omelyanchik, A., da Silva, F.G., Gomide, G., Kozenkov, I., Depeyrot, J., Aquino, R., Campos, A.F.C., Fiorani, D., Peddis, D., Rodionova, V. and Jovanović, S., (2021). Effect of citric acid on the morpho-structural and

magnetic properties of ultrasmall iron oxide nanoparticles. *Journal of Alloys and Compounds*, 883.

Onozuka, H., Tsuchihara, K. and Esumi, H., (2011). Hypoglycemic/hypoxic condition in vitro mimicking the tumor microenvironment markedly reduced the efficacy of anticancer drugs. *Cancer science*, 102.

Pai, A.B. and Garba, A.O., (2012). Ferumoxytol: a silver lining in the treatment of anemia of chronic kidney disease or another dark cloud?. *Journal of blood medicine*, 3.

Pantopoulos, K., (2004). Iron metabolism and the IRE/IRP regulatory system: an update. *Annals of the New York Academy of Sciences*, 1012.

Paoli, P., Giannoni, E. and Chiarugi, P., (2013). Anoikis molecular pathways and its role in cancer progression. *Biochimica et Biophysica Acta (BBA)-Molecular Cell Research*, 1833.

Park, C.C., Zhang, H.J., Yao, E.S., Park, C.J. and Bissell, M.J., (2008). β 1 integrin inhibition dramatically enhances radiotherapy efficacy in human breast cancer xenografts. *Cancer research*, 68.

Peto, R., Darby, S., Deo, H., Silcocks, P., Whitley, E. and Doll, R., (2000). Smoking, smoking cessation, and lung cancer in the UK since 1950: combination of national statistics with two case-control studies. *Bmj*, 321.

Petrova, V., Annicchiarico-Petruzzelli, M., Melino, G. and Amelio, I., (2018). The hypoxic tumour microenvironment. *Oncogenesis*, 7.

Poller, J.M., Zaloga, J., Schreiber, E., Unterweger, H., Janko, C., Radon, P., Eberbeck, D., Trahms, L., Alexiou, C. and Friedrich, R.P., (2017). Selection of potential iron oxide nanoparticles for breast cancer treatment based on in vitro cytotoxicity and cellular uptake. *International journal of nanomedicine*, pp.3207-3220.

Polson, H.E., de Lartigue, J., Rigden, D.J., Reedijk, M., Urbé, S., Clague, M.J. and Tooze, S.A., (2010). Mammalian Atg18 (WIPI2) localizes to omegasome-anchored phagophores and positively regulates LC3 lipidation. *Autophagy*, 6.

Qu, X., Yu, J., Bhagat, G., Furuya, N., Hibshoosh, H., Troxel, A., Rosen, J., Eskelinen, E.L., Mizushima, N., Ohsumi, Y. and Cattoretti, G., (2003). Promotion of tumorigenesis by heterozygous disruption of the beclin 1 autophagy gene. *The Journal of clinical investigation*, 112.

Rabinowitz, J.D. and White, E., (2010). Autophagy and metabolism. *Science*, 330.

Rampal, G., Khanna, N., Thind, T.S., Arora, S. and Vig, A.P., (2012). Role of isothiocyanates as anticancer agents and their contributing molecular and cellular mechanisms. *Med. Chem. Drug Discovery*, 3.

Robert, C., Ribas, A., Schachter, J., Arance, A., Grob, J.J., Mortier, L., Daud, A., Carlino, M.S., McNeil, C.M., Lotem, M. and Larkin, J.M., (2019). Pembrolizumab versus ipilimumab in advanced melanoma (KEYNOTE-006): post-hoc 5-year results from an open-label, multicentre, randomised, controlled, phase 3 study. *The Lancet Oncology*, 20.

Robert, C., Thomas, L., Bondarenko, I., O'Day, S., Weber, J., Garbe, C., Lebbe, C., Baurain, J.F., Testori, A., Grob, J.J. and Davidson, N., (2011). Ipilimumab plus dacarbazine for previously untreated metastatic melanoma. *New England Journal of Medicine*, 364.

Rodriguez-Bigas, M.A., Hoff, P. and Crane, C.H., (2006). Carcinoma of the colon and rectum. *Hollan-Frei Cancer Medicine*, 1369.

Rosenfeldt, M.T. and Ryan, K.M., (2011). The multiple roles of autophagy in cancer. *Carcinogenesis*, 32.

Ross, F.A., MacKintosh, C. and Hardie, D.G., (2016). AMP-activated protein kinase: a cellular energy sensor that comes in 12 flavours. *The FEBS journal*, 283.

Ruiz-de-Angulo, A., Bilbao-Asensio, M., Cronin, J., Evans, S.J., Clift, M.J., Llop, J., Feiner, I.V., Beadman, R., Bascarán, K.Z. and Mareque-Rivas, J.C., (2020). Chemically programmed vaccines: iron catalysis in nanoparticles enhances combination immunotherapy and immunotherapy-promoted tumor ferroptosis. *Iscience*, 23.

Russell, S.E., Hickey, G.I., Lowry, W.S., White, P. and Atkinson, R.J., (1990). Allele loss from chromosome 17 in ovarian cancer. *Oncogene*, 5.

Saito, H., Inazawa, J., Saito, S., Kasumi, F., Koi, S., Sagae, S., Kudo, R., Saito, J., Noda, K. and Nakamura, Y., (1993). Detailed deletion mapping of chromosome 17q in ovarian and breast cancers: 2-cM region on 17q21. 3 often and commonly deleted in tumors. *Cancer research*, 53.

Salvesen, G.S., (1999). Caspase 8: igniting the death machine. *Structure*, 7.

Sánchez-Tilló, E., Liu, Y., de Barrios, O., Siles, L., Fanlo, L., Cuatrecasas, M., Darling, D.S., Dean, D.C., Castells, A. and Postigo, A., (2012). EMT-activating transcription factors in cancer: beyond EMT and tumor invasiveness. *Cellular and Molecular Life Sciences*, 69.

Santana-Codina, N. and Mancias, J.D., (2018). The role of NCOA4-mediated ferritinophagy in health and disease. *Pharmaceuticals*, 11.

Santoro, M.M., (2020). The antioxidant role of non-mitochondrial CoQ10: mystery solved!. *Cell metabolism*, 31.

Sbodio, J.I., Snyder, S.H. and Paul, B.D., (2019). Regulators of the transsulfuration pathway. *British journal of pharmacology*, 176.

Scheff, R.J. and Schneider, B.J., (2013), June. Non–Small-Cell Lung Cancer: Treatment of Late Stage Disease: Chemotherapeutics and New Frontiers. In *Seminars in interventional radiology*, 30.

Schindelin, J., Arganda-Carreras, I., Frise, E., Kaynig, V., Longair, M., Pietzsch, T., Preibisch, S., Rueden, C., Saalfeld, S., Schmid, B. and Tinevez, J.Y., (2012). Fiji: an open-source platform for biological-image analysis. *Nature methods*, 9.

Schwartz, M.A., McRoberts, K., Coyner, M., Andarawewa, K.L., Frierson Jr, H.F., Sanders, J.M., Swenson, S., Markland, F., Conaway, M.R. and Theodorescu, D., (2008). Integrin agonists as adjuvants in chemotherapy for melanoma. *Clinical Cancer Research*, 14.

Schwenk, M.H., (2010). Ferumoxytol: a new intravenous iron preparation for the treatment of iron deficiency anemia in patients with chronic kidney disease. *Pharmacotherapy: The Journal of Human Pharmacology and Drug Therapy*, 30.

Segatto, I., Berton, S., Sonogo, M., Massarut, S., Fabris, L., Armenia, J., Mileto, M., Colombatti, A., Vecchione, A., Baldassarre, G. and Belletti, B., (2014). p70S6 kinase mediates breast cancer cell survival in response to surgical wound fluid stimulation. *Molecular oncology*, 8.

Shackelford, D.B. and Shaw, R.J., (2009). The LKB1–AMPK pathway: metabolism and growth control in tumour suppression. *Nature Reviews Cancer*, 9.

Shah, A. and Dobrovolskaia, M.A., (2018). Immunological effects of iron oxide nanoparticles and iron-based complex drug formulations: therapeutic benefits, toxicity, mechanistic insights, and translational considerations. *Nanomedicine: Nanotechnology, Biology and Medicine*, 14.

Sherman-Baust, C.A., Kuhn, E., Valle, B.L., Shih, I.M., Kurman, R.J., Wang, T.L., Amano, T., Ko, M.S., Miyoshi, I., Araki, Y. and Lehrmann, E., (2014). A genetically engineered ovarian cancer mouse model based on fallopian tube transformation mimics human high-grade serous carcinoma development. *The Journal of Pathology*, 233.

Shih, I.M. and Kurman, R.J., (2004). Ovarian tumorigenesis: a proposed model based on morphological and molecular genetic analysis. *The American Journal of Pathology*, 164.

Shimada, K., Skouta, R., Kaplan, A., Yang, W.S., Hayano, M., Dixon, S.J., Brown, L.M., Valenzuela, C.A., Wolpaw, A.J. and Stockwell, B.R., (2016). Global survey of cell death mechanisms reveals metabolic regulation of ferroptosis. *Nature chemical biology*, 12.

Shin, D., Lee, J., You, J.H., Kim, D. and Roh, J.L., (2020). Dihydrolipoamide dehydrogenase regulates cystine deprivation-induced ferroptosis in head and neck cancer. *Redox biology*, 30.

Shintoku, R., Takigawa, Y., Yamada, K., Kubota, C., Yoshimoto, Y., Takeuchi, T., Koshiishi, I. and Torii, S., (2017). Lipoygenase-mediated generation of lipid peroxides enhances ferroptosis induced by erastin and RSL3. *Cancer science*, 108.

Soetaert, F., Korangath, P., Serantes, D., Fiering, S. and Ivkov, R., (2020). Cancer therapy with iron oxide nanoparticles: Agents of thermal and immune therapies. *Advanced drug delivery reviews*, 163.

Son, J., Kim, M., Jou, I., Park, K.C. and Kang, H.Y., (2014). IFN- γ inhibits basal and α -MSH-induced melanogenesis. *Pigment cell & melanoma research*, 27.

Song, X., Zhu, S., Chen, P., Hou, W., Wen, Q., Liu, J., Xie, Y., Liu, J., Klionsky, D.J., Kroemer, G. and Lotze, M.T., (2018). AMPK-mediated BECN1 phosphorylation promotes ferroptosis by directly blocking system Xc- activity. *Current Biology*, 28.

Stine, Z.E., Walton, Z.E., Altman, B.J., Hsieh, A.L. and Dang, C.V., (2015). MYC, metabolism, and cancer. *Cancer discovery*, 5.

Stjepanovic, G., Baskaran, S., Lin, M.G. and Hurley, J.H., (2017). Vps34 kinase domain dynamics regulate the autophagic PI 3-kinase complex. *Molecular cell*, 67.

Strauss, S.J., Ng, T., Mendoza-Naranjo, A., Whelan, J. and Sorensen, P.H., (2010). Understanding micrometastatic disease and Anoikis resistance in ewing family of tumors and osteosarcoma. *The oncologist*, 15.

Su, L.J., Zhang, J.H., Gomez, H., Murugan, R., Hong, X., Xu, D., Jiang, F. and Peng, Z.Y., (2019). Reactive oxygen species-induced lipid peroxidation in apoptosis, autophagy, and ferroptosis. *Oxidative medicine and cellular longevity*, 2019.

Suk, J.S., Xu, Q., Kim, N., Hanes, J. and Ensign, L.M., (2016). PEGylation as a strategy for improving nanoparticle-based drug and gene delivery. *Advanced drug delivery reviews*, 99.

Sullivan, J.E., Brocklehurst, K.J., Marley, A.E., Carey, F., Carling, D. and Beri, R.K., (1994). Inhibition of lipolysis and lipogenesis in isolated rat adipocytes with AICAR, a cell-permeable activator of AMP-activated protein kinase. *FEBS letters*, 353.

Summers, H.D., Rees, P., Holton, M.D., Rowan Brown, M., Chappell, S.C., Smith, P.J. and Errington, R.J., (2011). Statistical analysis of nanoparticle dosing in a dynamic cellular system. *Nature nanotechnology*, 6.

Sun, C., Du, K., Fang, C., Bhattarai, N., Veiseh, O., Kievit, F., Stephen, Z., Lee, D., Ellenbogen, R.G., Ratner, B. and Zhang, M., (2010). PEG-mediated synthesis of highly dispersive multifunctional superparamagnetic nanoparticles: their physicochemical properties and function in vivo. *ACS nano*, 4.

Sun, Y., Chen, P., Zhai, B., Zhang, M., Xiang, Y., Fang, J., Xu, S., Gao, Y., Chen, X., Sui, X. and Li, G., (2020). The emerging role of ferroptosis in inflammation. *Biomedicine & Pharmacotherapy*, 127.

Takahara, T., Amemiya, Y., Sugiyama, R., Maki, M. and Shibata, H., (2020). Amino acid-dependent control of mTORC1 signaling: a variety of regulatory modes. *Journal of Biomedical Science*, 27.

Tee, A.R., Manning, B.D., Roux, P.P., Cantley, L.C. and Blenis, J., (2003). Tuberous sclerosis complex gene products, Tuberin and Hamartin, control mTOR signaling by acting as a GTPase-activating protein complex toward Rheb. *Current biology*, 13.

Tentori, L., Lacal, P.M. and Graziani, G., (2013). Challenging resistance mechanisms to therapies for metastatic melanoma. *Trends in pharmacological sciences*, 34.

Thoreen, C.C., Kang, S.A., Chang, J.W., Liu, Q., Zhang, J., Gao, Y., Reichling, L.J., Sim, T., Sabatini, D.M. and Gray, N.S., (2009). An ATP-competitive mammalian target of rapamycin inhibitor reveals rapamycin-resistant functions of mTORC1. *Journal of Biological Chemistry*, 284.

Tian, W., Li, W., Chen, Y., Yan, Z., Huang, X., Zhuang, H., Zhong, W., Chen, Y., Wu, W., Lin, C. and Chen, H., (2015). Phosphorylation of ULK1 by AMPK regulates translocation of ULK1 to mitochondria and mitophagy. *FEBS letters*, 589.

Tímár, J., Vizkeleti, L., Doma, V., Barbai, T. and Rásó, E., (2016). Genetic progression of malignant melanoma. *Cancer and Metastasis Reviews*, 35.

Tone, A.A., (2017). Taking the tube: from normal fallopian tube epithelium to ovarian high-grade serous carcinoma. *Clinical obstetrics and gynecology*, 60.

Trincu, N.F., Balșeanu, T.A., Ungureanu, B.S., Fifere, A., PIRICI, I., Săftoiu, A. and Neamțu, J., (2015). Blood clearance of citric acid-coated superparamagnetic iron oxide nanoparticles in rats-a pilot study. *Current Health Sciences Journal*, 41.

Trumbo, P., Yates, A.A., Schlicker, S. and Poos, M., (2001). Dietary reference intakes: vitamin A, vitamin K, arsenic, boron, chromium, copper, iodine, iron, manganese, molybdenum, nickel, silicon, vanadium, and zinc. *Journal of the Academy of Nutrition and Dietetics*, 101.

Vakili-Ghartavol, R., Momtazi-Borojeni, A.A., Vakili-Ghartavol, Z., Aiyelabegan, H.T., Jaafari, M.R., Rezayat, S.M. and Arbabi Bidgoli, S., (2020). Toxicity assessment of superparamagnetic iron oxide nanoparticles in different tissues. *Artificial Cells, Nanomedicine, and Biotechnology*, 48.

Vander Heiden, M.G., Cantley, L.C. and Thompson, C.B., (2009). Understanding the Warburg effect: the metabolic requirements of cell proliferation. *science*, 324.

Vangijzegem, T., Lecomte, V., Ternad, I., Van Leuven, L., Muller, R.N., Stanicki, D. and Laurent, S., (2023). Superparamagnetic Iron Oxide Nanoparticles (SPION): From Fundamentals to State-of-the-Art Innovative Applications for Cancer Therapy. *Pharmaceutics*, 15.

Vaughan, S., Coward, J.I., Bast Jr, R.C., Berchuck, A., Berek, J.S., Brenton, J.D., Coukos, G., Crum, C.C., Drapkin, R., Etemadmoghadam, D. and Friedlander, M., (2011). Rethinking ovarian cancer: recommendations for improving outcomes. *Nature reviews Cancer*, 11.

Veierød, M.B., Adami, H.O., Lund, E., Armstrong, B.K. and Weiderpass, E., (2010). Sun and solarium exposure and melanoma risk: effects of age, pigmentary characteristics, and nevi. *Cancer epidemiology, biomarkers & prevention*, 19.

Veronese, F.M. and Mero, A., (2008). The impact of PEGylation on biological therapies. *BioDrugs*, 22.

Visintin, I., Feng, Z., Longton, G., Ward, D.C., Alvero, A.B., Lai, Y., Tenthorey, J., Leiser, A., Flores-Saaib, R., Yu, H. and Azori, M., (2008). Diagnostic markers for early detection of ovarian cancer. *Clinical Cancer Research*, 14.

Vogt, J., Traynor, R. and Sapkota, G.P., (2011). The specificities of small molecule inhibitors of the TGF β s and BMP pathways. *Cellular signalling*, 23.

Wallace, D.F., (2016). The regulation of iron absorption and homeostasis. *The Clinical Biochemist Reviews*, 37.

Wang, H., Agarwal, P., Zhao, G., Ji, G., Jewell, C.M., Fisher, J.P., Lu, X. and He, X., (2018). Overcoming ovarian cancer drug resistance with a cold responsive nanomaterial. *ACS central science*, 4.

Wang, J.B., Erickson, J.W., Fuji, R., Ramachandran, S., Gao, P., Dinavahi, R., Wilson, K.F., Ambrosio, A.L., Dias, S.M., Dang, C.V. and Cerione, R.A., (2010). Targeting mitochondrial glutaminase activity inhibits oncogenic transformation. *Cancer cell*, 18.

Wang, L., Geng, H., Liu, Y., Liu, L., Chen, Y., Wu, F., Liu, Z., Ling, S., Wang, Y. and Zhou, L., (2023). Hot and cold tumors: Immunological features and the therapeutic strategies. *MedComm*, 4.

Wang, S.J., Li, D., Ou, Y., Jiang, L., Chen, Y., Zhao, Y. and Gu, W., (2016). Acetylation is crucial for p53-mediated ferroptosis and tumor suppression. *Cell reports*, 17.

Wang, W., Green, M., Choi, J.E., Gijón, M., Kennedy, P.D., Johnson, J.K., Liao, P., Lang, X., Kryczek, I., Sell, A. and Xia, H., (2019). CD8+ T cells regulate tumour ferroptosis during cancer immunotherapy. *Nature*, 569.

Wang, Z., Li, C., Ellenburg, M., Soistman, E., Ruble, J., Wright, B., Ho, J.X. and Carter, D.C., (2006). Structure of human ferritin L chain. *Acta Crystallographica Section D: Biological Crystallography*, 62.

Wang, Z., Wu, S., Zhu, C. and Shen, J., (2022). The role of ferroptosis in esophageal cancer. *Cancer Cell International*, 22.

Warburg, O., Wind, F. and Negelein, E., (1927). The metabolism of tumors in the body. *The Journal of general physiology*, 8.

Watanabe, R., Miyata, M. and Oneyama, C., (2020). Rictor promotes tumor progression of rapamycin-insensitive triple-negative breast cancer cells. *Biochemical and biophysical research communications*, 531.

Weil, M.K. and Chen, A., (2011). PARP inhibitor treatment in ovarian and breast cancer. *Current Problems in Cancer*, 35.

Weissleder, R., Bogdanov, A., Neuwelt, E.A. and Papisov, M., (1995). Long-circulating iron oxides for MR imaging. *Advanced Drug Delivery Reviews*, 16.

Wen, J., Chen, H., Ren, Z., Zhang, P., Chen, J. and Jiang, S., (2021). Ultrasmall iron oxide nanoparticles induced ferroptosis via Beclin1/ATG5-dependent autophagy pathway. *Nano Convergence*, 8.

Whelan, J. and Fritsche, K., (2013). Linoleic acid. *Advances in nutrition*, 4.

Wild, A.C., Moinova, H.R. and Mulcahy, R.T., (1999). Regulation of γ -glutamylcysteine synthetase subunit gene expression by the transcription factor Nrf2. *Journal of Biological Chemistry*, 274.

Wise, D.R. and Thompson, C.B., (2010). Glutamine addiction: a new therapeutic target in cancer. *Trends in biochemical sciences*, 35.

Wise, D.R., DeBerardinis, R.J., Mancuso, A., Sayed, N., Zhang, X.Y., Pfeiffer, H.K., Nissim, I., Daikhin, E., Yudkoff, M., McMahon, S.B. and Thompson, C.B., (2008). Myc regulates a transcriptional program that stimulates mitochondrial glutaminolysis and leads to glutamine addiction. *Proceedings of the National Academy of Sciences*, 105.

Wu, C., Shen, Z., Lu, Y., Sun, F. and Shi, H., (2022). p53 Promotes Ferroptosis in Macrophages Treated with Fe₃O₄ Nanoparticles. *ACS Applied Materials & Interfaces*, 14.

Wu, C., Zhao, W., Yu, J., Li, S., Lin, L. and Chen, X., (2018). Induction of ferroptosis and mitochondrial dysfunction by oxidative stress in PC12 cells. *Scientific reports*, 8.

Xiang, L. and Kong, B., (2013). PAX8 is a novel marker for differentiating between various types of tumor, particularly ovarian epithelial carcinomas. *Oncology Letters*, 5.

Xiang, L., Zheng, W. and Kong, B., (2012). Detection of PAX8 and p53 is beneficial in recognizing metastatic carcinomas in pelvic washings, especially in cases with suspicious cytology. *Gynecologic oncology*, 127.

Xiao, B., Heath, R., Saiu, P., Leiper, F.C., Leone, P., Jing, C., Walker, P.A., Haire, L., Eccleston, J.F., Davis, C.T. and Martin, S.R., (2007). Structural basis for AMP binding to mammalian AMP-activated protein kinase. *Nature*, 449.

Xing, Y., Zhao, S., Zhou, B.P. and Mi, J., (2015). Metabolic reprogramming of the tumour microenvironment. *The FEBS journal*, 282.

Yang, C., Zhang, Y., Xu, X. and Li, W., (2019). Molecular subtypes based on DNA methylation predict prognosis in colon adenocarcinoma patients. *Aging (Albany NY)*, 11.

Yang, H., Rudge, D.G., Koos, J.D., Vaidialingam, B., Yang, H.J. and Pavletich, N.P., (2013). mTOR kinase structure, mechanism and regulation. *Nature*, 497.

Yang, L., Venneti, S. and Nagrath, D., (2017). Glutaminolysis: a hallmark of cancer metabolism. *Annual review of biomedical engineering*, 19.

Yang, W.S., SriRamaratnam, R., Welsch, M.E., Shimada, K., Skouta, R., Viswanathan, V.S., Cheah, J.H., Clemons, P.A., Shamji, A.F., Clish, C.B. and Brown, L.M., (2014). Regulation of ferroptotic cancer cell death by GPX4. *Cell*, 156.

Yang, X. and Chasteen, N.D., (1999). Ferroxidase activity of ferritin: effects of pH, buffer and Fe (II) and Fe (III) concentrations on Fe (II) autoxidation and ferroxidation. *Biochemical Journal*, 338.

Yin, M., Li, X., Tan, S., Zhou, H.J., Ji, W., Bellone, S., Xu, X., Zhang, H., Santin, A.D., Lou, G. and Min, W., (2016). Tumor-associated macrophages drive spheroid formation during early transcoelomic metastasis of ovarian cancer. *The Journal of Clinical Investigation*, 126.

Yokota, J., (2000). Tumor progression and metastasis. *Carcinogenesis*, 21.

Yoshida, J., Horiuchi, A., Kikuchi, N., Hayashi, A., Osada, R., Ohira, S., Shiozawa, T. and Konishi, I., (2009). Changes in the expression of E-cadherin repressors, Snail, Slug, SIP1, and Twist, in the development and progression of ovarian carcinoma: the important role of Snail in ovarian tumorigenesis and progression. *Medical Molecular Morphology*, 42.

Younus, H., (2018). Therapeutic potentials of superoxide dismutase. *International journal of health sciences*, 12.

Yu, B., Choi, B., Li, W. and Kim, D.H., (2020). Magnetic field boosted ferroptosis-like cell death and responsive MRI using hybrid vesicles for cancer immunotherapy. *Nature communications*, 11.

Yuan, L., Sheng, X., Clark, L.H., Zhang, L., Guo, H., Jones, H.M., Willson, A.K., Gehrig, P.A., Zhou, C. and Bae-Jump, V.L., (2016). Glutaminase inhibitor compound 968 inhibits cell proliferation and sensitizes paclitaxel in ovarian cancer. *American journal of translational research*, 8.

Zanetta, G., Rota, S., Chiari, S., Bonazzi, C., Bratina, G., Torri, V. and Mangioni, C., (1998). The accuracy of staging: an important prognostic determinant in stage I ovarian carcinoma: a multivariate analysis. *Annals of Oncology*, 9.

Zanganeh, S., Hutter, G., Spitler, R., Lenkov, O., Mahmoudi, M., Shaw, A., Pajarinen, J.S., Nejadnik, H., Goodman, S., Moseley, M. and Coussens, L.M., (2016). Iron oxide nanoparticles inhibit tumour growth by inducing pro-inflammatory macrophage polarization in tumour tissues. *Nature nanotechnology*, 11.

Zeng, Q., Yang, Z., Gao, Y.J., Yuan, H., Cui, K., Shi, Y., Wang, H., Huang, X., Wong, S.T., Wang, Y. and Kesari, S., (2010). Treating triple-negative breast cancer by a combination of rapamycin and cyclophosphamide: an in vivo bioluminescence imaging study. *European Journal of Cancer*, 46.

Zhang, C., Liu, X., Jin, S., Chen, Y. and Guo, R., (2022). Ferroptosis in cancer therapy: a novel approach to reversing drug resistance. *Molecular cancer*, 21.

Zhang, J., Pavlova, N.N. and Thompson, C.B., (2017). Cancer cell metabolism: the essential role of the nonessential amino acid, glutamine. *The EMBO journal*, 36.

Zhang, Y., Kohler, N. and Zhang, M., (2002). Surface modification of superparamagnetic magnetite nanoparticles and their intracellular uptake. *Biomaterials*, 23.

Zhang, Y., Liu, L., Jin, L., Yi, X., Dang, E., Yang, Y., Li, C. and Gao, T., (2014). Oxidative stress-induced calreticulin expression and translocation: new insights into the destruction of melanocytes. *Journal of Investigative Dermatology*, 134.

Zhao, L., Zhou, X., Xie, F., Zhang, L., Yan, H., Huang, J., Zhang, C., Zhou, F., Chen, J. and Zhang, L., (2022). Ferroptosis in cancer and cancer immunotherapy. *Cancer Communications*, 42.

Zhao, X., Luo, G., Cheng, Y., Yu, W., Chen, R., Xiao, B., Xiang, Y., Feng, C., Fu, W., Duan, C. and Yao, F., (2018). Compound C induces protective autophagy in human cholangiocarcinoma cells via Akt/mTOR-independent pathway. *Journal of Cellular Biochemistry*, 119.

Zhou, B., Basu, J., Kazmi, H.R., Chitrala, K.N., Mo, X., Preston-Alp, S., Cai, K.Q., Kappes, D. and Zaidi, M.R., (2022). Interferon-gamma signaling promotes melanoma progression and metastasis. *Oncogene*.

Zhu, L., You, Y., Zhu, M., Song, Y., Zhang, J., Hu, J., Xu, X., Xu, X., Du, Y. and Ji, J., (2022). Ferritin-Hijacking Nanoparticles Spatiotemporally Directing Endogenous Ferroptosis for Synergistic Anticancer Therapy. *Advanced Materials*.

Zook, J.M., MacCuspie, R.I., Locascio, L.E., Halter, M.D. and Elliott, J.T., (2011). Stable nanoparticle aggregates/agglomerates of different sizes and the effect of their size on hemolytic cytotoxicity. *Nanotoxicology*, 5.

Bibliography

Cancer Research UK (2019) Overview Menopause. [ONLINE] Available at: <https://www.nhs.uk/conditions/menopause/treatment/>. [Accessed 26 December 2019].

Cancer Research UK (2019) Overview Periods. [ONLINE] Available at: <https://www.nhs.uk/conditions/periods/>. [Accessed 26 December 2019].

Cancer Research UK (2019) Bowel Cancer Survival Statistics . <https://www.cancerresearchuk.org/health-professional/cancer-statistics/statistics-by-cancer-type/bowel-cancer/survival#heading-Three> . [Accessed 2 August 2022].

Cancer Research UK (2021) What is breast cancer?. [ONLINE] Available at: <https://www.cancerresearchuk.org/about-cancer/breast-cancer/about>. [Accessed 21 September 2021].

Cancer Research UK (2021) Risk factors. [ONLINE] Available at: <https://www.cancerresearchuk.org/about-cancer/breast-cancer/risks-causes/risk-factors> [Accessed 21 September 2021].

Cancer Research UK (2021) Checkpoint Inhibitors [ONLINE] Available at: <https://www.cancerresearchuk.org/about-cancer/treatment/immunotherapy/types/checkpoint-inhibitors> [Accessed 6 February 2023].

Cancer Research UK (2020) Why some cancers come back. [ONLINE] Available at: <https://www.cancerresearchuk.org/about-cancer/what-is-cancer/why-some-cancers-come-back> [Accessed 7 February 2023]

Appendix

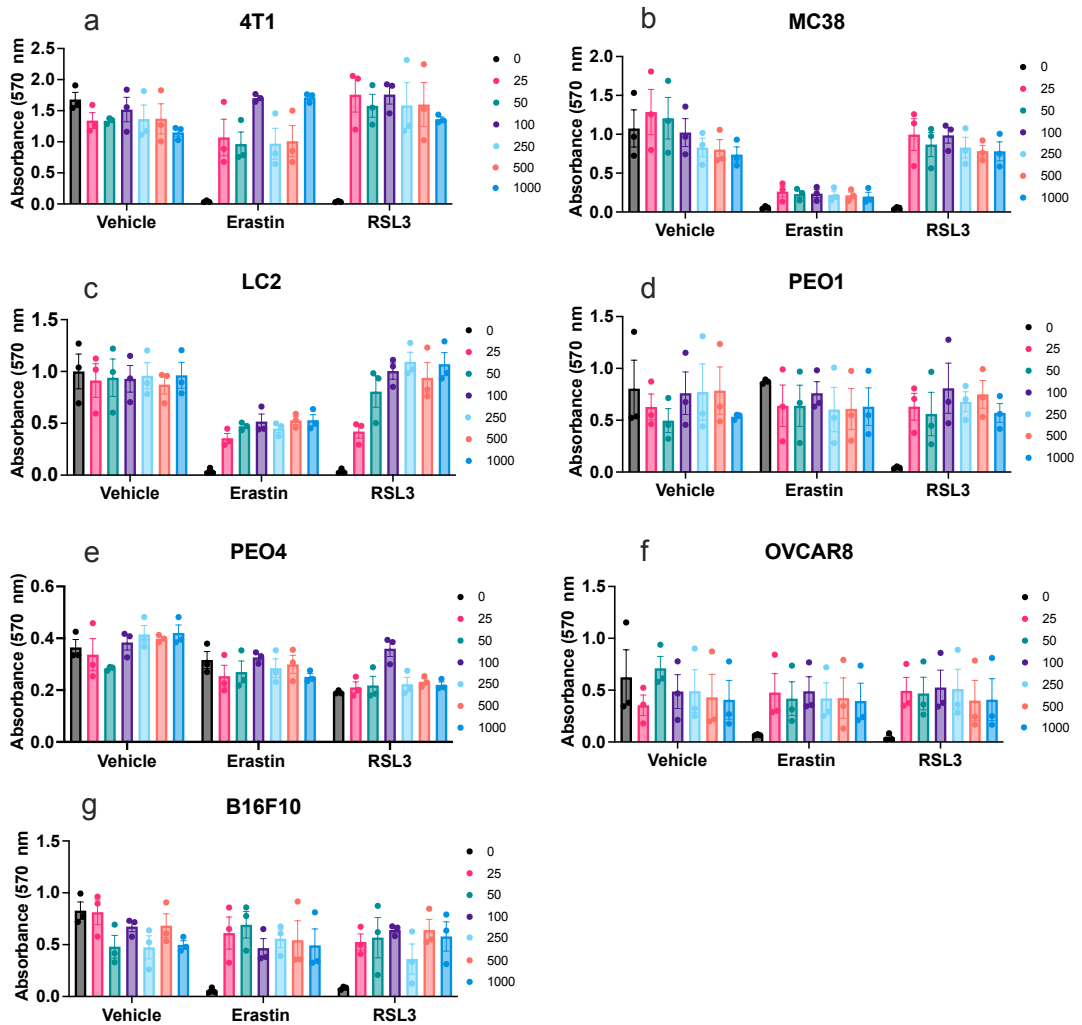


Figure 1: The rescue effect of Liproxstatin-1 treatment against the ferroptosis inducers; Erastin and RSL3. The panel of cancer cells lines were cultured in media containing Vehicle or Liproxstatin1 (25nM-1000nM) or Erastin (2.5 μ M) or RSL3 (0.625 μ M). Cells were treated with Liproxstatin-1 for 30 min prior to treatment with Erastin or RSL3 for 24 h. Cell viability was evaluated using MTT assay after 24 h.

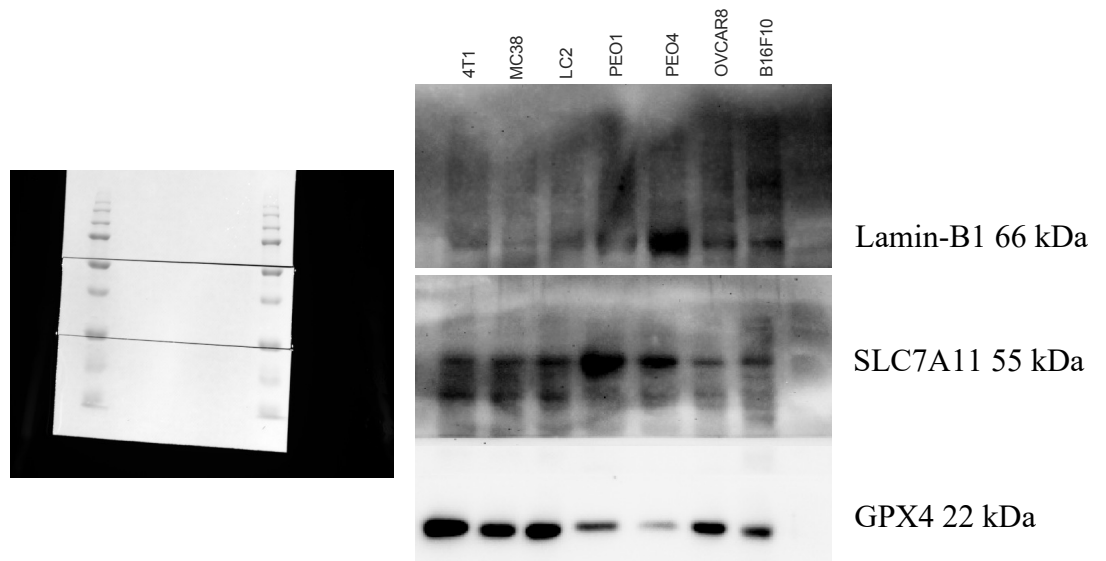


Figure 2: The whole blot was cut at specific bands depending on the protein of interest. The above blot was taken to determine the presence of SLC7A11 and GPX4 in all the cancer cell lines. Lamin-B1 was used as a housekeeping protein due to the size of the proteins of interest. GPX4 was observed at 22 kDa, SLC7A11 was observed at 55 kDa and the housekeeping protein Lamin-B1 was observed at 66 kDa.

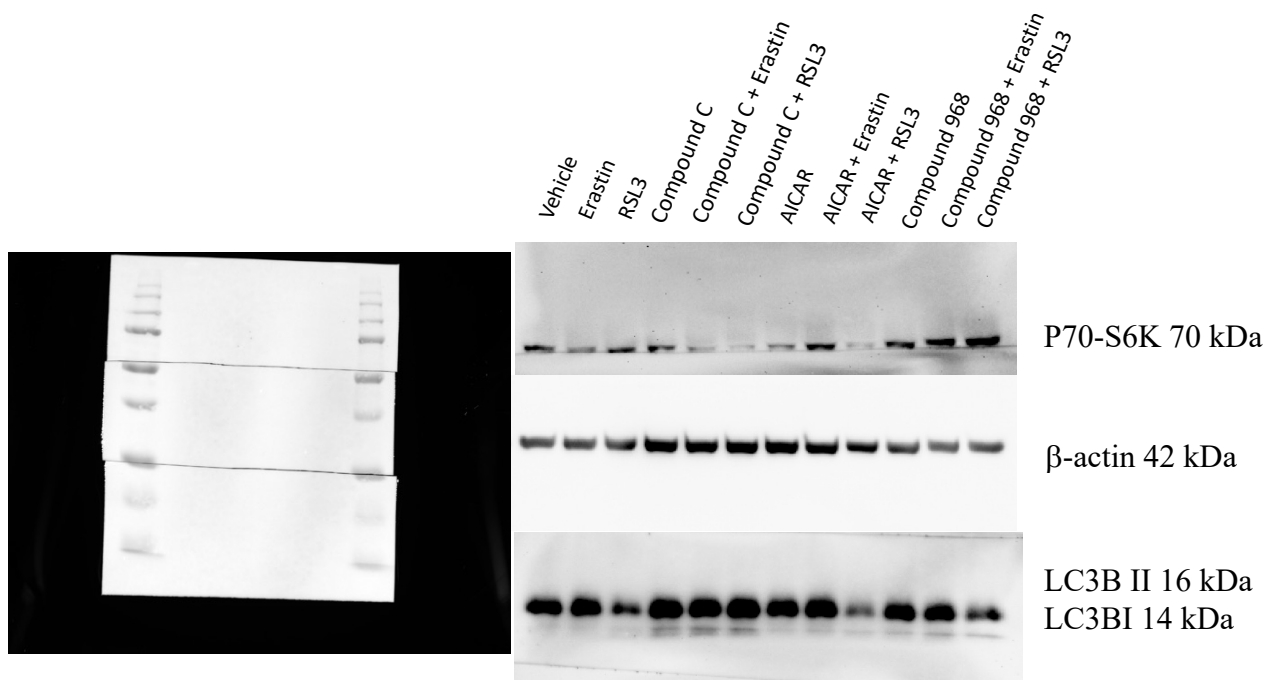


Figure 3: The whole blot was cut at specific bands depending on the protein of interest, this was done for all cancer cell lines individually. Each blot was set up to include all the treatments; compound C (4h), AICAR (4h) and Compound 968 (4h) or 30 min treatment prior to Erastin and RSL3. The phosphorylated proteins were imaged first and then stripped and re-probed for the total protein. The above blot shows P-P70-S6K was observed at 70 kDa prior to the antibody being stripped and re-probed for T-P70-S6K which was also observed at 70 kDa, B-actin was observed at 42 kDa and LC3B-I and LC3B-II were observed at 14 and 16 kDa.

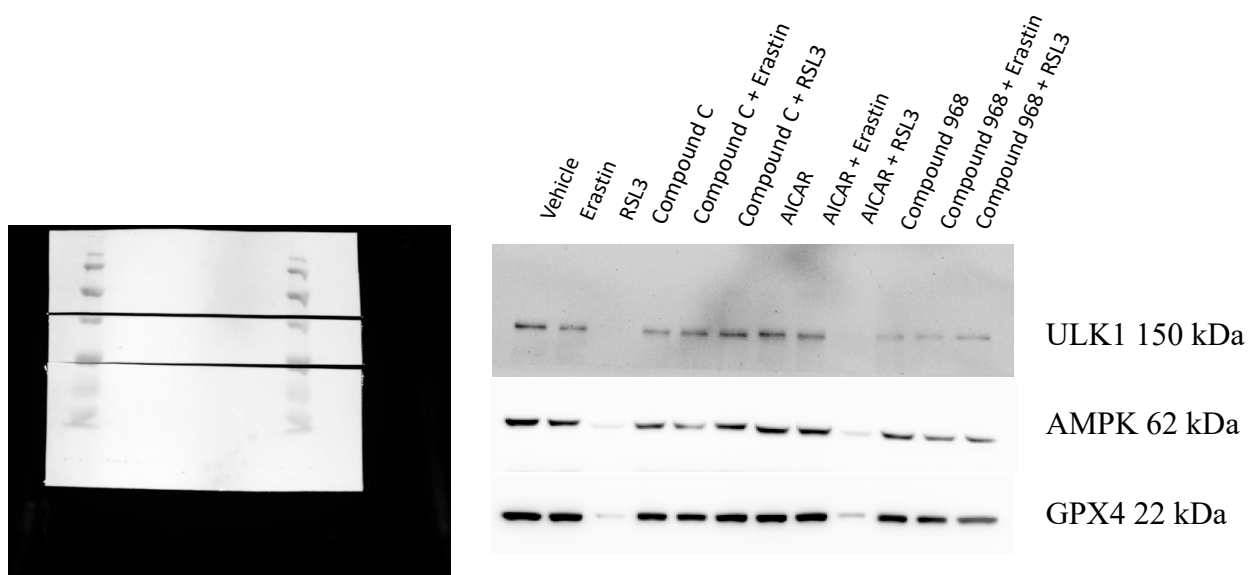


Figure 4: The whole blot was cut at specific bands depending on the protein of interest, this was done for all cancer cell lines individually. Each blot was set up to include all the treatments; compound C (4h), AICAR (4h) and Compound 968 (4h) or 30 min treatment prior to Erastin and RSL3. On two blots SER757 was observed at 140/150 kDa and SER555 which was observed at 112 kDa, both antibodies were then stripped and re-probed for total-ULK1 which was observed at 150 kDa. P-AMPK was observed at 62 kDa prior to the antibody being stripped and re-probed for T-AMPK which was observed at 62 kDa and then re-probed again for B-actin which was observed at 42 kDa. GPX4 was finally observed at 22 kDa.